UNIVERSITY OF STRATHCLYDE
Department of Biomedical Engineering

Design of a wearable LED-based phototherapy device

by

Francesca Ann Farrell

A thesis presented in fulfilment of the
requirements for the degree of
Doctor of Engineering

February 2021

Declaration of Authorship

This thesis is the result of the author's original research. It has been composed by the author and has not been previously submitted for examination which has led to the award of a degree.

The copyright of this thesis belongs to the author under the terms of the United Kingdom Copyright Acts as qualified by University of Strathclyde Regulation 3.50. Due acknowledgement must always be made of the use of any material contained in, or derived from, this thesis.

Signed: ____

Date: ____

Frontispiece

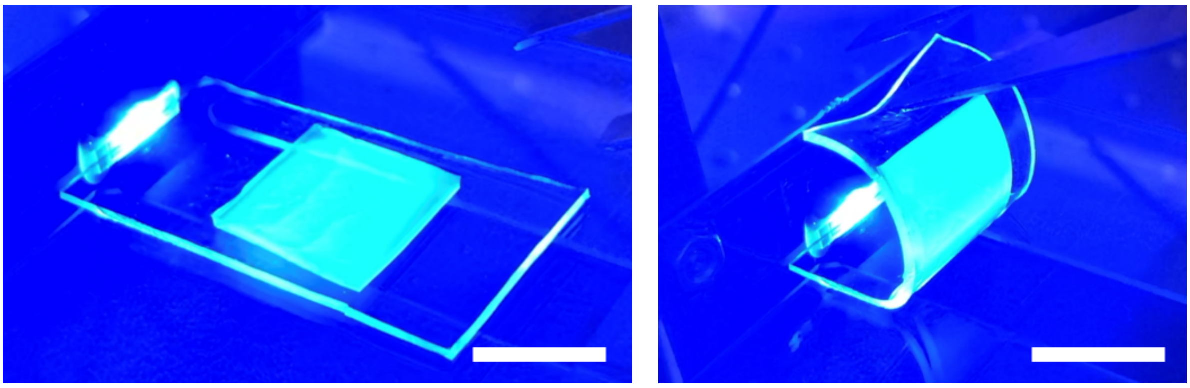

Uniform emission device with blue μLED array shown on a flat surface (left) and flexibility shown (right), scale is 10 mm.

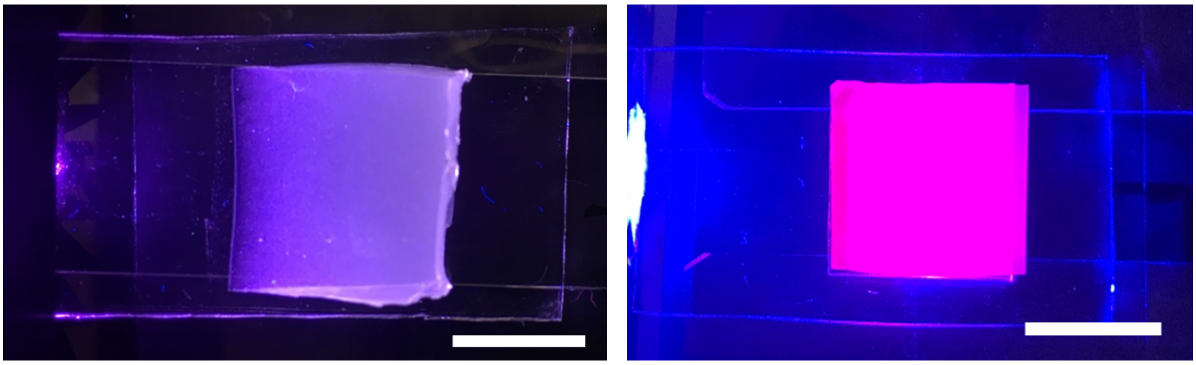

Uniform emission device with UV LED (left) and uniform red emission using blue μLED array and red CQD film, scale is 10 mm.

Abstract

The aim of the work described in this thesis is to design a wearable phototherapy device utilising LEDs. Phototherapy is the use of light to treat medical conditions, such as, eczema, psoriasis and newborn jaundice. Treatment usually takes place in a clinical environment, but a recent focus for phototherapy is the development of at-home devices. Currently available technologies consist of rigid LED arrays; identifying the treatment regime with these devices is difficult due to the non-uniform light distribution. A potential solution to this problem is to create a flexible and conformable device that allows for uniform light distribution over the treatment area by incorporating light scattering features.

Broad area LEDs (UV and blue) and blue micro-sized LEDs are utilised as the light source coupled into the end of a thin polydimethylsiloxane membrane. High refractive index nanoparticles are embedded in a substrate and used to extract light from the surface of the membrane. By changing the size of these substrates, or by changing the nanoparticle concentration inside the substrates, uniform irradiance is demonstrated over an area of 15 x 15 mm^2. Though not demonstrated in this thesis, there is potential for treatment over larger areas.

Colloidal quantum dots can be embedded in elastomeric materials and used to down-convert the LED light into lower energy wavelengths. This is shown with red wavelength emitting quantum dots, producing a uniform red irradiance over the substrate area. A similar technique is shown to produce multi-wavelength blue and red uniform emission over the extraction area.

The output of the device can be optimised by adding flexible reflective layers to one side of the membrane. This increases the light output from the extraction substrates, whilst maintaining the device flexibility. The light output can also be increased by adding secondary embedded waveguides into the membrane. These are coupled to the micro-LED light and can potentially produce structured emission over the treatment area.

The device platform is also shown to be effective as a fluorescent evanescent waveguide sensor, utilising quantum dots as the fluorescent molecules and a smart phone camera to measure the fluorescence.

Acknowledgements

I am very grateful to the CDT and Patricia Connolly for the support and opportunity to undertake the EngD. Consequently, I am also grateful to the IoP and FCAP for the opportunity to carry out this project. It would not have been half as successful or enjoyable without the help of many great people.

Firstly, I would like to thank Nicolas Laurand for his encouragement and great supervision, his enthusiasm for research is infectious. Secondly, thanks to Anne-Marie Haughey for her guidance and support for the EngD project and life outwith the laboratory. I would like to acknowledge the clinical advice received from NHS clinicians, Dr Richard Weller and Dr Colin Morton, and thank them for their continued interest in the project.

I would like to thank all of my IoP and FCAP colleagues for creating an excellent work environment. In particular I would like to thank Benoit Guilhabert for his willingness to share knowledge and help, Enyaun Xie and Xiangyu He for their help with μLED design and fabrication, and Mark Scullion for his photolithography and microfluidic guidance. I have been lucky to make many friends throughout my EngD with our daily discussions ranging from research ideas to existential crises, you all made the EngD even more fun, thank you.

None of this would have been possible without all the administrative support from the different project collaborators. Thank you to Carol McInnes in the CDT for dealing with many purchase requests and questions and to Lisa Flanagan for being my FCAP go-to, cocktail supplier and gym accountability buddy. A massive thanks goes to Sharon Kelly and Lorraine Annand in the IoP, for everything they do for all of the IoP and for always being available for a chat.

A special thank you has to go to my former teachers; Sharon Denham, Claire Carten and Elizabeth Murray. Your love of science was contagious, because of that I am completing an EngD using knowledge of chemistry, physics and biology that I learned from you.

Finally, I want to thank all my family and friends for their love and provision of fun distractions. Mum, Dad, Ewan and Katie, your unconditional support throughout my entire life means more than you could ever know, I am forever grateful. Last, and definitely not least, thank you to my husband Dougie, you have supported me throughout my entire journey with patience, encouragement and unlimited glasses of wine.

Contents

List of Figures

List of Tables

Abbreviations

ALA	Aminolaevulinic acid
AlGaAs	Aluminium gallium arsenide
AlGaInP	Aluminium gallium indium phosphide
CCD	Charge-coupled device
CDT	Centre for Doctoral Training in Medical Devices and Healthcare Technologies
CMOS	Complementary metal-oxide semiconductor
CQD	Colloidal quantum dots
FCAP	Fraunhofer Centre for Applied Photonics
FWHM	Full width at half maximum
GaN	Gallium nitride
$\mathbf{HfO_2}$	Hafnium dioxide
InGaN	Indium gallium nitride
IoP	Institute of Photonics
LIV	Luminosity - current - voltage relationship
λ	Wavelength
LED	Light emitting diodes
MAL	Methyl aminolevulinate
μ**LED**	Micro-LED
MQW	Multiple quantum well
n	Refractive index
NA	Numerical aperture
NIR	Near infrared radiation
NO	Nitric oxide
OLED	Organic light emitting diodes
PCB	Printed circuit board

PDMS	Polydimethylsiloxane
PDT	Photodynamic therapy
POC	Point of care
PUVA	Psoralens ultraviolet radiation
RGB	Red-green-blue
SD	Standard deviation
TiO_2	Titanium dioxide
UV	Ultraviolet radiation
UVA	Ultraviolet-A (320-400 nm)
UVB	Ultraviolet-B (280-320 nm)
UVC	Ultraviolet-C (<280 nm)
ZrO_2	Zirconium dioxide

Chapter 1

Introduction

This chapter describes the rationale and the biomedical and technical background for this work. After a brief presentation of the motivations and outline of the thesis, it introduces the effects of light on skin. Light therapy at a range of wavelengths is discussed including the use of photosensitisers to increase the efficacy. This is followed by an explanation of the benefits of at-home phototherapy devices and a summary of such devices currently available on the market. Our wearable phototherapy device concept is then presented as the basis for this thesis. Finally, the benefits of light-emitting diodes (LEDs) in light therapy, and the engineering basis behind LEDs and micro-LEDs is discussed.

1.1 Motivation and thesis outline

The aim of the work behind this thesis was to create, study and optimise a wearable phototherapy device. Phototherapy is the use of ultraviolet (UV) or visible light to treat medical conditions, in particular skin disorders such as eczema, psoriasis, acne, etc. It is traditionally carried out in a clinical environment utilising large, inefficient fluorescent tubes as the light source. These practices are generally time-consuming, making them inconvenient for both patients and healthcare staff. Consequently, the development of at-home devices for phototherapy applications aims to improve patient convenience and to decrease the demand on healthcare resources [1].

Existing home technologies are either handheld or worn on the body. These give the patient improved comfort, however, the rigidity of these devices make it difficult for clinicians to determine the light dosage [2, 3] due to their limited conformability and the “hot-spots” in their light distribution.

The development of flexible light technologies could be a solution to this problem; a flexible and conformable device would allow for maximum treatment efficiency with a potentially lower power over a longer treatment time. The use of a lower power device has the added benefit of reducing side effects, such as pain, that are common to treatments with high power devices [4].

The aim of this thesis is to design a wearable device that can be utilised in phototherapy applications, producing uniform light over a treatment area. Throughout this thesis, uniform light is described as light with an average irradiance error of less than 15% over an area of at least 1cm^2. This value for uniformity was chosen as it allows a high similarity light output over the treatment area, allowing the clinician to determine the correct treatment dosage. This will be an improvement upon currently used clinic-based devices which have a centre to edge uniformity error of 73%.

This device has an edge-lit configuration, with LED light sources on the edge of an elastomeric membrane and light guided out of the top surface at desired locations. Uniform emission of light at a range of wavelengths is discussed using LEDs, micro-sized LEDs and colour converting films. The device platform also enables another biomedical application as a fluorescent sensor, this is also explored.

Chapter 1 provides an overview of phototherapy and various light interactions with skin. The currently available home-phototherapy devices are discussed. It also introduces light emitting diodes and their key properties related to phototherapy, followed by the development of micro-LEDs. Chapter 2 explains the materials and methods utilised throughout the thesis and in the design of the wearable phototherapy device. The production of uniform irradiance over an area of more than 2 cm^2 using a broad-area blue LED is shown. In Chapter 3, a specially designed micro-sized LED is used as the light source; this chapter focuses on increasing the irradiance output while maintaining uniformity over the emission layer. The use of a UV LED source to produce uniform emission, at a UV wavelength, is shown in Chapter 4, along with the use of colour converting films to produce red and multiwavelength emission. Chapter 5 focuses on the properties of the uniform device produced in Chapter 3, by looking at the effects of curvature on the device output. Flexible reflective films are also added to increase the device emission while maintaining flexibility. The addition of secondary embedded waveguides is discussed to allow increased irradiance as well as offering the capability for structured emission. The use of the elastomeric edge-lit platform as a fluorescent sensor is presented in Chapter 6. Finally, Chapter 7 provides conclusions and possible future work.

1.2 Light and the skin

A range of different wavelengths of light are utilised to treat different medical conditions. The most commonly used wavelengths for phototherapy treatment are ultraviolet-B (280-320 nm), ultraviolet-A (320-400 nm), blue (400-490 nm), red (620-750 nm) and near-infrared (750+ nm). The following discusses the effects of each of these wavelengths on skin. The action of light induces a cellular response, this response is the basis of phototherapy and is dependent on the wavelength and fluence of the light.

1.2.1 Biology of the skin

The skin is the largest human organ that makes up around 16% of a human's total body weight. The skin is made up of tissue layers with different properties. The top layer is known as the epidermis, it is generally 0.1 mm thick and primarily functions as a barrier against pathogens. The layer below the epidermis is called the dermis, this is 2 mm thick on average and protects the body from stress and strain. The innermost layer of skin is called the hypodermis, or cutaneous tissue, and is mainly used to store body fat [5].

Each layer of skin contains different cellular components which provide the layer with its properties. The epidermis contains 95% keratinocytes with the remaining 5% including Langerhans cells, melanin and inflammatory cells [6]. These cells provide a physical barrier against micro-organisms as well as providing mechanical resistance. The dermis is much thicker than the epidermis and is composed of collagen, elastin, extracellular matrix proteins, mast cells and fibroblasts [6]. The hypodermis consists mainly of connective tissue and body fat [5].

1.2.2 Mechanism of action of light on the skin

When light hits the surface of skin a range of different effects can occur, including, reflection, absorption and scattering. Around 4 to 7% of incident light is reflected at the epidermis [7], independent of the wavelength.

The remaining 93 to 96% of light not reflected at the surface will be absorbed or scattered depending upon the wavelength. UV wavelengths are mainly absorbed, while visible and NIR wavelengths are more likely to scatter before absorption. Scattering is characterised as a change in direction of light and is caused when a photon interacts with a particle of differing refractive index from the surrounding media [8].

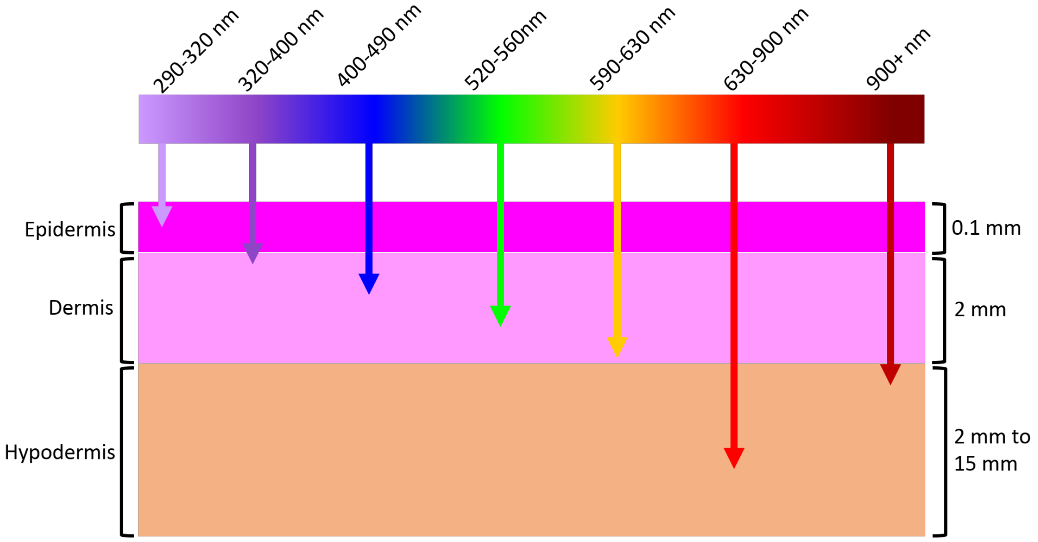

FIGURE 1.1: Schematic showing the different layers of skin and penetration depths of different wavelengths of light

Absorption is the most important effect for light therapy. Different wavelengths of light are absorbed by a variety of materials present in the skin (called chromophores). As the absorption properties of these chromophores differ, the absorption of light through the skin layers varies. Figure 1.1 shows the basic layers of skin and penetration depths for different wavelengths.

1.2.3 Absorption and the skin

The layers of skin contain different chromophores therefore, the absorption of light differs. Chromophores in the skin include, DNA, lipids, amino acids, porphyrins, haemoglobin and melanin [9]. These absorb different wavelengths of light which leads to photochemical or photobiological reactions. These reactions are exploited in phototherapy producing therapeutic effects.

1.2.3.1 UV absorption

UV radiation can be split into three different groups, UVA, UVB and UVC. Wavelengths from 100 to 280 nm fall into the UVC category and have no therapeutical benefits. UVB is described as wavelengths between 280 and 315 nm, while UVA is wavelengths from 315 to 400 nm. Both UVA and UVB wavelengths are used as a method of phototherapy [10]. With UVB being used as broadband 280 to 320 nm, or narrowband, with 310 to 313 nm. The presence of melanocytes in the epidermis accounts for the majority of UV absorption, this decreases the detrimental effects of UV radiation on cells and produces melanin which causes the pigmentation of skin [9].

UVB radiation which is not absorbed by melanocytes is absorbed in the epidermis by keratinocytes, Langerhans cells and lymphocytes. The UVB causes a reduction in DNA synthesis. This makes it beneficial in conditions like psoriasis which has an accelerated DNA synthesis, resulting in the formation of multiple skin layers. [11].

UVA radiation penetrates deeper than UVB, into the start of the dermis. It affects inflammatory cells and endothelial cells. UVA also causes a reduction in DNA synthesis, although four orders of magnitude less is absorbed compared to UVB [9]. This is why UVA radiation is commonly used in combination with a photosensitising compound [12].

UV radiation has also been shown to release nitric oxide (NO) from nitrosated proteins in skin [13, 14]. The effects are not fully understood, however, it has been clinically proven that the release of NO by endothelial cells is an important regulator in resting blood flow rate [15], and also stimulates proliferation and migration of keratinocytes, providing an anti-inflammatory effect.

Repeated exposure to UV radiation, especially at a young age, has been shown to damage cellular DNA leading to tumour formation and premature skin aging [16, 17]. This has led to the study of visible wavelengths as phototherapy treatment. Visible light penetrates deeper into the dermis, and is not absorbed by DNA directly, so has a less harmful effect.

1.2.3.2 Blue light absorption

Blue light penetrates deeper into the dermis than UVA and is absorbed by flavins, cryptochromes and porphyrins [11, 18]. These chromophores release reactive oxygen species which leads to a reduction in proliferation and dendritic cell activation. These effects lead to blue light being a suitable therapy for hyperproliferative skin diseases while minimising the side effects associated with UV radiation (i.e. skin cancer) [19], though there is no significant association of UV phototherapy producing an increased likelihood of skin cancer [20].

Additional effects of blue light irradiation are not fully understood including T-cell induced apoptosis, altered immune response and decreased inflammation. Like other photobiologic responses these effects appear to be wavelength and fluence dependent. With shorter blue wavelengths, less than 440 nm, and high fluences possibly leading to toxicity and oxidative stress [19, 21].

1.2.3.3 Red and NIR light absorption

Red light penetrates the skin by at least 2 mm, deep into the dermis. Red light/near-infrared (NIR) therapy leads to enhancement of enzyme activity, electron transport, mitochondrial respiration and ATP production [18]. It is thought that cytochrome c oxidase absorbs the light and photodissociation of inhibitory NO occurs, leading to the enhancement. This has been shown to increase collagen production and elastic fibres in skin while activating fibroblasts [22]. Hence it is used in wound healing [23] and cosmetically in anti-aging procedures [24].

Infrared radiation is sometimes used in combination with red light as it penetrates further into the skin, to the hypodermis [25]. It is not used clinically as a light therapy treatment, however, is used as a photothermal treatment, converting light energy into heat energy [26].

1.2.3.4 Other visible wavelength absorption

Green, orange and yellow wavelengths of light penetrate deeper than blue, but not as deep as red. These have not been shown to have any clinical benefits in light therapy treatment of skin disorders. Green light is commonly used in photoplethysmography, along with red and NIR light, to measure heart rate by calculating the absorption of oxygen in oxyhaemoglobin [27].

1.3 Summary of light treatment applications

The global light therapy market in 2019 was valued at $790.3 million, split between commercial, domestic and healthcare market segments [28]. Each segment consists of devices that can be utilised to treat skin conditions. Light can be used as a treatment for a range of conditions from acne treatments to cellular rejuvenation and wound care. Bright white light is used to treat depression [29], namely seasonal affective disorder (SAD) or in combination with antidepressants to treat non-seasonal depression [30] or bipolar disorder [31]. However, light therapy is most commonly used to treat newborn jaundice and dermatological conditions, such as psoriasis, acne and vitiligo. Light therapy is also used as a method of photobiomodulation, using low levels of visible/NIR light to induce tissue healing and provide pain relief [32].

UV light therapy is being investigated as a treatment on its own, or in combination with NO delivering nanoparticles to increase the NO levels in the skin [33], producing cardiovascular benefits [34].

1.3.1 Phototherapy

Phototherapy is the term used to describe treating medical conditions with light. Sunlight has been used for centuries to treat skin diseases, known as heliotherapy in ancient Greece [10]. Research by Niels Ryberg Finsen led to the development of modern phototherapy by successfully treating lupus vulgaris with a UV lamp [35]. Antibiotics were not available at this time, consequently phototherapy was a breakthrough. For this work, Finsen was awarded the Nobel prize in medicine in 1903.

In the 1960's, photochemotherapy was introduced through the combination of psoralens and UVA lamps to treat psoriasis and vitiligo [10]. This was the forerunner to photodynamic therapy used today. In the 1980's, this became a treatment option for patients with psoriasis, vitiligo and atopic dermatitis [35].

Light therapy is used for wide range of diseases particularly hyperproliferative skin conditions like psoriasis, acne and keratosis. It is also a treatment for some skin cancers using photosensitisers to increase the effect of the light, discussed in more detail in Section 1.3.3.

1.3.1.1 UV phototherapy

UV phototherapy is used extensively as a psoriasis treatment. Psoriasis is an autoimmune condition and causes rapid growth of the epidermal layer of skin, by hyperproliferation of keratinocytes [36]. It results in inflamed areas of dry, flaky skin, these are often found on the elbows, knees and scalp [11]. Narrowband UVB radiation is the most commonly used wavelength for psoriasis phototherapy, although PUVA and blue light treatment have also been utilised [10, 37]. Topical corticosteroids or biologics are widely used to treat psoriasis in regions where light therapy is not common and in combination with light therapy on severe lesions [38]. Psoriasis is the most common healthcare condition requiring phototherapy, representing almost 70% of the market share and affecting up to 3% of the global population [39].

UV phototherapy can be used to treat vitiligo. This is a condition where patches of skin lose their pigmentation [10]. The UVB light, or psoralens UVA combination leads to the stimulation of melanocyte proliferation and the apoptosis of the immune cells responsible for the decreased melanin production [40].

UV phototherapy is also a treatment option for eczema (atopic dermatitis). This condition results in skin inflammation and may be acute (chemical reaction) or chronic (long term immune response). The treatment can either be narrowband UVB radiation or

UVA radiation. Here the treatment depends on the condition, with UVA shown to be more effective in treating acute flares while UVB is more effective at managing chronic cases [41].

UV phototherapy treatment schedule varies depending on condition and severity [41–43]. However, generally involves treatment a few times a week over the course of many weeks with increasing UV light doses prescribed by the dermatologist, based on the effect of previous sessions.

1.3.1.2 Blue light therapy

Blue light phototherapy has become more common in recent years due to the development of efficient blue light emitting diodes. The most common use of blue light therapy is in neonatal jaundice to convert unconjugated bilirubin to its oxidation products [44]. As bilirubin has a peak absorption at blue wavelengths, they are the most effective at lowering serum bilirubin concentrations [18].

Blue light has been used in the treatment of psoriasis and been shown to be effective in clearing plaques classified as mild/moderate [37, 45]. At higher fluences blue light can produce similar effects to UV light in the clearing of psoriasis plaques. However, the remission period before more treatments are needed is shortened for blue light psoriasis treatment [46]. Blue light treatment is not yet clinically prescribed as psoriasis treatment.

Blue light is also used as a phototherapy treatment for acne [47, 48]. The blue light excites porphyrins leading to formation of reactive oxygen species and resultant destruction of the acne bacteria [12].

1.3.1.3 Red light therapy

As discussed in Section 1.2.3.3, red light penetrates deeper into the dermis than UV and blue wavelengths. This makes it beneficial as a cosmetic treatment for anti-aging [49]. The application of low incident levels of red wavelengths of light results in enhanced action potentials of skin cells and increases blood and lymphatic flow, generating tighter dermal layers. This reduces the effects of wrinkles and brightens the skin surface.

Red light has also been used to stimulate wound healing in chronic wounds [50]. Studies have shown an increase in the growth of epithelial cells and decreased wound healing times when irradiated with red LEDs [50, 51].

Red light therapy is often used in combination with blue light therapy to treat acne. The red light produces anti-inflammatory effects which, when combined with the antibacterial effect of the blue light, leads to a reduction in acne and a decreased scarring [52]. The combination of these wavelengths has also been shown to be effective in treating diabetic skin ulcers [53].

1.3.2 Photochemotherapy

Photochemotherapy is the combination of light therapy and a photosensitising drug that increases the effects of the light. The most common photochemotherapy method is psoralens-UVA (PUVA). A drug that contains psoralens is delivered orally or topically to the treatment area. Psoralens is a compound found in plants that makes the skin more sensitive to UV radiation. The psoralens is activated by UV light and binds strongly to DNA, damaging the cells. Therefore, when applied to psoriatic skin, it can be used as a treatment [10]. PUVA has been found to be more effective at clearing psoriasis lesions and exhibits a longer remission duration than narrowband UVB treatment [54].

1.3.3 Photodynamic therapy

Photodynamic therapy (PDT) is the use of a topical drug that is metabolised to protoporphyrin IX (PpIX). As the drug needs to be metabolised to be effective, it is known as PDT rather than photochemotherapy. The drug is applied topically to the epidermis and is transformed into PpIX through the sebaceous gland [55]. It accumulates higher in malignant tissue compared to normal tissue [56].

Under the presence of oxygen and light absorption, the PpIX generates reactive oxygen species which cause necrosis or apoptosis of cells [58]. The absorption spectrum of PpIX is given in Figure 1.2 [57]. The PpIX absorbs light of different wavelengths, with absorption peaks at 410 nm, 505 nm, 540 nm, 580 nm and 630 nm [4].

Two main types of topical drugs are used, aminolaevulinic acid (ALA) and its methylated ester, methyl aminolevulinate (MAL). Studies have shown that although MAL is more lipophilic, so should penetrate deeper into lesions than the hydrophilic ALA, there is no difference in response [59].

Recent studies have utilised sunlight as the PDT light source, known as daylight therapy [60], this has varying effectiveness. In the Northern Hemisphere it is only viable in summer months and is therefore not commonly prescribed as treatment. Artificial daylight lamps have been fabricated and utilised, however, they have been shown to be less effective than red LEDs in actinic keratosis treatment [61].

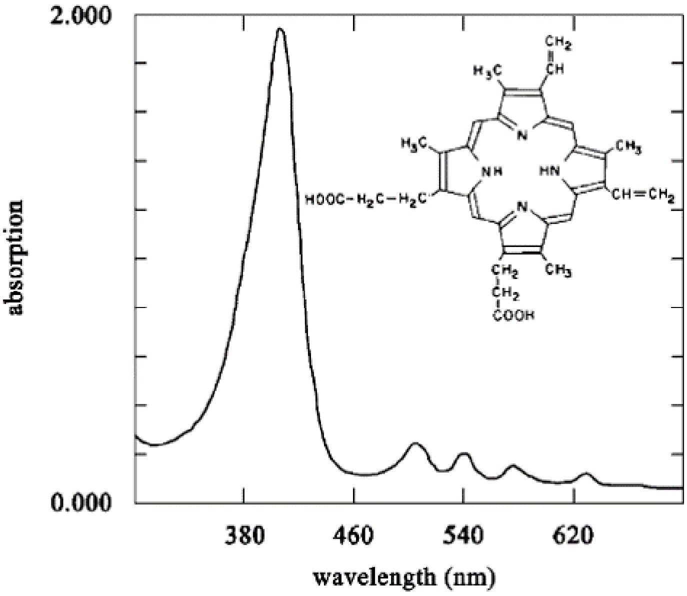

Figure 1.2: Absorption spectrum of PpIX, figure taken from [57]

Dermatological conditions which benefit from PDT include actinic keratosis, non-melanoma skin cancers and Bowen's disease.

1.4 Light therapy treatment

Traditionally phototherapy and photodynamic therapy is carried out in a clinical environment, hospital or dermatologist office. UV phototherapy typically uses narrowband fluorescent UVB lamps or UVA lamps for PUVA [12]. Blue LED arrays are most commonly used now for blue light therapy, previously halogen lamps and fluorescent tubes were utilised with filters [62]. Red light LED devices, like those by Aktilite (CL16 and CL128) are commonly used with ALA or MAL to treat actinic keratosis [2, 63]. These light sources are large bulky systems that require excess space. They also consist of arrays of either fluorescent tubes or LEDs, this results in non-uniform light emission [2]. The designed device described in this thesis uses different emission methods to reduce this uniformity effect, explained in more detail in 1.6.

Clinically prescribed phototherapy usually requires treatment at a hospital or dermatologist office. This is demanding on the healthcare system and on the patients. Depending on the treatment, the patient may have to wait for a long period of time for photosensitiser absorption (PDT) or attend sessions regularly over the course of a few months (UV therapy). Common treatment doses and durations are given in Table 1.1 for NB-UVB, PUVA and PDT. Treatment varies between dermatological condition, wavelength and skin type, these average values are taken from [64], [65] and [66]. The treatment duration depends upon the dosage required and the device irradiance. A low irradiance device has to be used for longer to reach the same light dose as a high irradiance device. This has increased the availability of light therapy devices for home-use.

TABLE 1.1: Table of light therapy treatments and their properties

Treatment type	Conditions treated	Skin type	Initial dose* (J/cm^2)	Maximum dose* (J/cm^2)	Treatment duration	Number of treatments
NB-UVB	Psoriasis, eczema, vitiligo	–	0.2	4.3	15–30 minutes	18–24 treatments with 3 day break between treatments
PUVA	Psoriasis, eczema, vitiligo	I	0.5	15	15–30 minutes	18–24 treatments with 3 day break between treatments
		II	1.0			
		III	1.4			
		IV	2.0			
		V	2.0			
PDT	Actinic keratosis, Bowen's disease, basal cell carcinoma	–	37.5	75	4+ hours	1 treatment minimum

*Note, accepted units of dose in phototherapy are J/cm^2, in contrast to SI units

(a) (b)

Figure 1.3: Home-use narrowband UVB phototherapy devices, (a) SolRx 100 from Solarc [70] and (b) Clarify device and smartphone [71]

1.5 At-home light therapy

Patient issues, such as, time constraints, loss of income and travelling difficulties, are improved by home phototherapy. When home phototherapy was offered to psoriasis patients, there was an increase in compliance and adherence to the treatment compared to clinical phototherapy [67, 68].

Despite these benefits, home phototherapy is not widely used due to multiple challenges. These include safety of home use, patient and clinician training as well as the availability of home phototherapy units. The currently available home use devices, though wearable compared to clinical devices, are still bulky and consist of top-down arrays resulting in similar uniformity issues with the arrays [3]. The device described in this thesis uses different emission methods to reduce this uniformity effect, explained in more detail in 1.7.

Home phototherapy can utilise lower irradiance devices worn/used for a longer time period to obtain the correct light dosage. This method of lower irradiance decreases the pain impact on the patients, whilst maintaining the effectiveness of the treatment [4, 69]. This pain is an inflammatory response of the skin due to the increased production of free radicals at high power densities, the production of these can be reduced by a lower power density.

1.5.1 Home-use devices

UV phototherapy using whole body units at home has been used to treat psoriasis and vitiligo, but issues include transporting the units and the space required in patients'

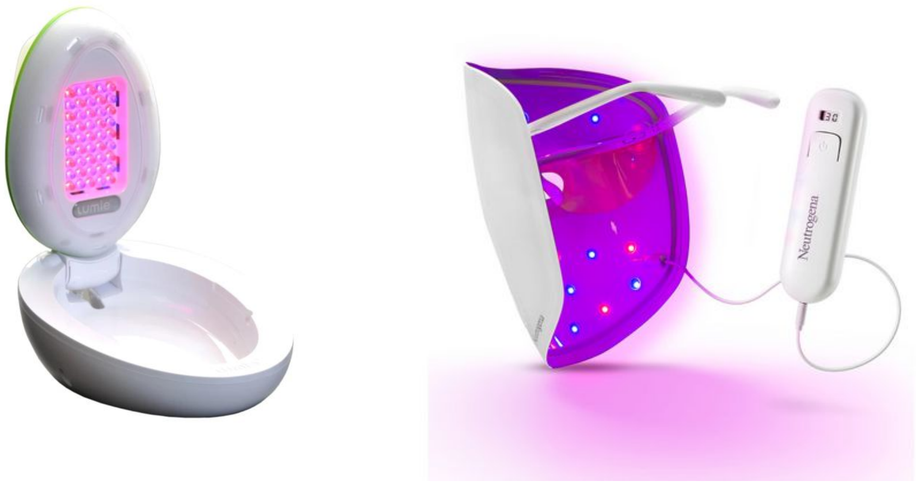
(a) (b)

Figure 1.4: Home phototherapy devices for acne treatment, (a) Lumie® Clear handheld device [74] and (b) Neutrogena® treatment mask [75]

homes. Handheld UV phototherapy lamps have become more popular. These can treat areas of skin up to 12 x 6 cm^2. Trials have shown that these are effective and safe for home phototherapy treatment of psoriasis [72].

1.5.1.1 UV devices

Home UV phototherapy devices include the Solarc handheld, SolRx 100 narrowband UVB lamp [70] and the Clarify Medical handheld, smartphone connected phototherapy device [71]. These both utilise the same narrowband UVB bulbs and require the patient to hold them over the affected area, devices are shown in Figure 1.3. The Clarify device is a therapeutic treatment option in the US. The device is supplied with a smartphone and web-portal which ensures patient adherence and allows clinicians to determine dosage requirements [73]. It has enhanced patient support and FDA medical device clearance for treating psoriasis, vitiligo and atopic dermatitis [71].

1.5.1.2 Visible devices

Available visible wavelength devices are mainly considered phototherapy devices. One previously available device was designed for at-home PDT use. The Ambicare Ambulight device consisted of an array of red LEDs (the original concept utilised organic LEDs). The device was previously offered as a treatment for actinic keratosis, basal cell carcinoma and Bowen's Disease in NHS Tayside [1, 4].

There are a number of at-home phototherapy treatments for acne. Many of these consist of rigid LED arrays with blue and red wavelengths, which have been shown to be effective in treating acne. The blue light destroys the acne causing bacteria, while the red light reduces the inflammation in the surrounding tissue. These devices are generally handheld, like the Lumie® Clear device, Figure 1.4(a), [74]. A more wearable option is the Neutrogena® Acne Mask (Figure 1.4(b)), this is shaped to the contours of the face and has inbuilt eye safety [75].

Downsides to devices like these include the handheld aspect, and the rigidity of the LED arrays. The Lumie® Clear device recommends a treatment time of 15 to 30 minutes when using handheld, close to the treatment area. The use of rigid LED arrays results in non-uniformity, due to treatment areas being different in shape and contour. Therefore, flexible light sources are a better alternative.

1.5.1.3 Flexible devices

There are some flexible LED based devices available on the market, these consist of LED arrays on flexible substrates which increases the wearability of the devices. Celluma light therapy has a range of flexible LED devices that emit in the blue, red and NIR wavelengths [76]. The devices available range from full body LED arrays (Celluma DELUX), to smaller flexible arrays for the back or face (Celluma HOME) (Figure 1.5). These devices are marketed towards acne treatment, pain management and wound healing. Philips previously offered a flexible light therapy device [77]. The BlueTouch used blue LEDs on a flexible substrate as a pain relief device, Figure 1.5(c). The device was supplied with a smartphone application to control treatment parameters.

1.5.1.4 Wearable devices

The commercially available home phototherapy devices are more compact than the clinical alternatives, however, they are still fairly bulky, making them difficult to be worn discreetly. These devices all contain arrays of LEDs as light sources. These arrays are useful at producing high powered light, and with improvements in flexible electronics will become more wearable. However, arrays of LEDs have been shown to produce hotspots in their light distribution [2, 3]. This makes it difficult for light dosages to be determined and is a major reason why at-home phototherapy is not heavily adopted.

Polymer optical fibres are being investigated as an alternative to LED arrays to improve the homogeneity of the emission area. Flexible optical fibres can be woven together with fabric to produce a material with a large diffusing area. A light source can be applied

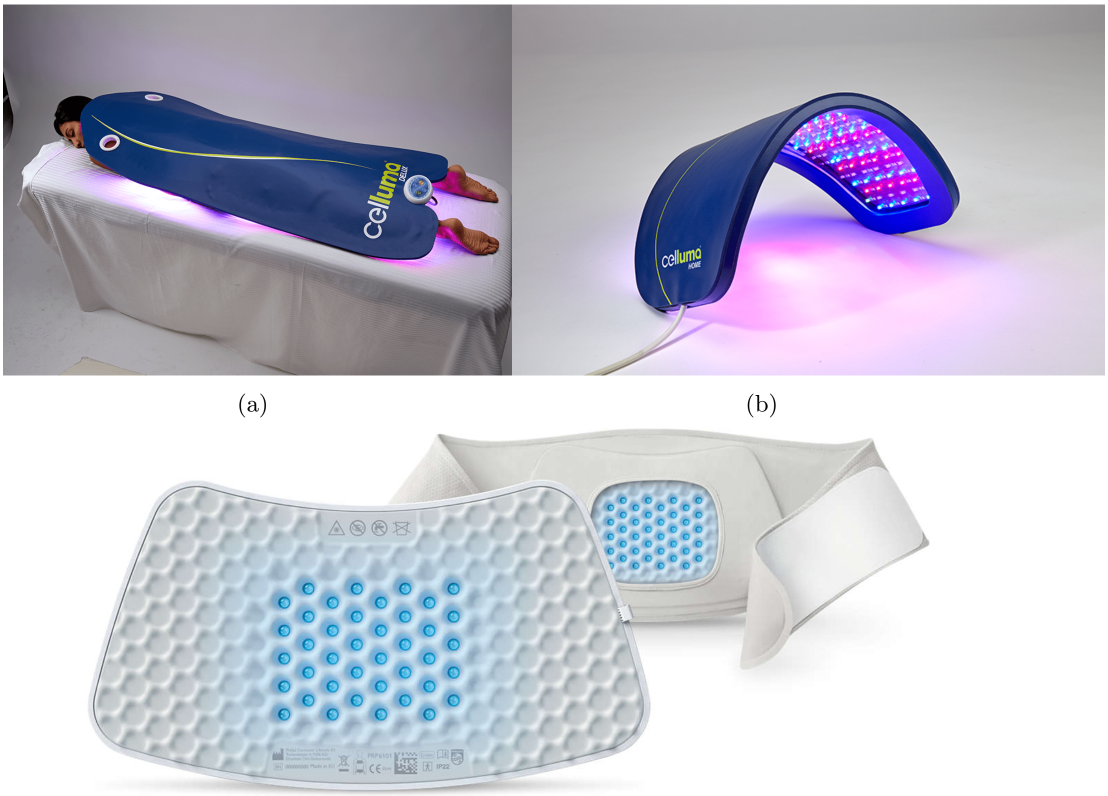

(a) (b)

(c)

FIGURE 1.5: Flexible phototherapy devices, (a) full body Celluma DELUX [76], (b) small area portable Celluma HOME [76] and (c) Philips BlueTouch [77]

to the ends of the optical fibres producing uniform emission over the fabric area. This has been shown in a finger device by Mordon et al., [3], and used clinically as a PDT device for Paget's disease [78]. This device utilised laser sources coupled into the fibres, however, other groups have coupled LEDs to their fibres to produce the same effect. For example, blue LEDs coupled into fibres woven with fabric as a potential treatment device for newborn jaundice [79]. Challenges with these devices include efficient light coupling into the fibres and also maintaining uniform output when weaved with fabric.

1.5.1.5 Emerging technologies

There is a whole range of research dedicated to wearable devices for skin contact, called wearable electronics. These devices are fabricated to have physical properties that resemble skin [80] and are being investigated as long-term options for non-invasive healthcare monitoring, via electrical, optical or piezoelectric transduction methods.

These devices are battery-free, instead they incorporate wireless power supplies, making them lightweight and increasing the flexibility. This wireless energy transfer utilises near-field communications (NFC), with a transmitter on a regular power supply/battery with

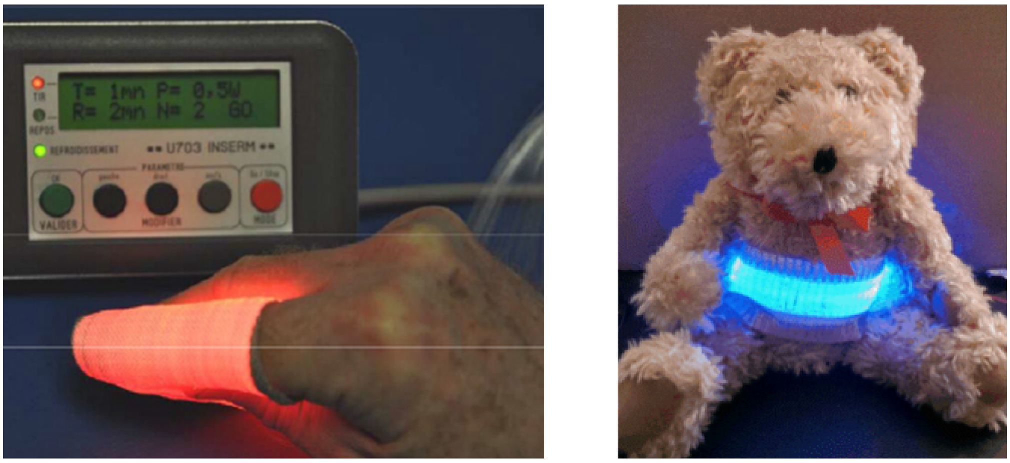

(a) (b)

Figure 1.6: Fibre-based wearable devices, (a) Laser coupled fibres shown around finger [3] and (b) neonatal jaundice fibre patch coupled to blue LEDs, shown on a toy [79]

a receiver antenna on the flexible device [81, 82].

These technologies are facilitated by transfer printing techniques to remove the electronic devices from their rigid substrate and place them on flexible materials, in a method known as "pick and place" [83]. LEDs can be added to flexible substrates using this method. Many of the research methods utilise single LEDs for monitoring purposes, for example, measuring blood oxygen levels [84] or measuring glucose levels in a smart contact lens [85]. The LEDs have also been demonstrated as arrays of micro-sized LEDs on a laboratory coat [81] or arrays of vertical LEDs on a flexible substrate as a method for stimulating hair growth, shown in a mouse model [86]. These flexible electronic technologies are currently small in size and require low electrical powers, but the constant progression in this area should produce larger flexible surfaces with suitable wireless power supplies in the future.

1.5.2 Summary of at-home devices

As described, there is a large range of at-home devices available in different designs and wavelengths. These also have a range of irradiance outputs from 7 mW/cm^2 for the Ambulight device and 2 mW/cm^2 for the Lumie® Clear device [4, 74]. These are much lower in irradiance than the in-clinic devices, reducing the chance of damage to healthy surrounding skin [2]. The maximum light dose limits for UV therapy depends upon the treatment and the number of treatments required, as shown in Table 1.1. The light exposure is gradually increased with each treatment, therefore, this is best utilised with some clinical input as is seen with the Clarify device [71].

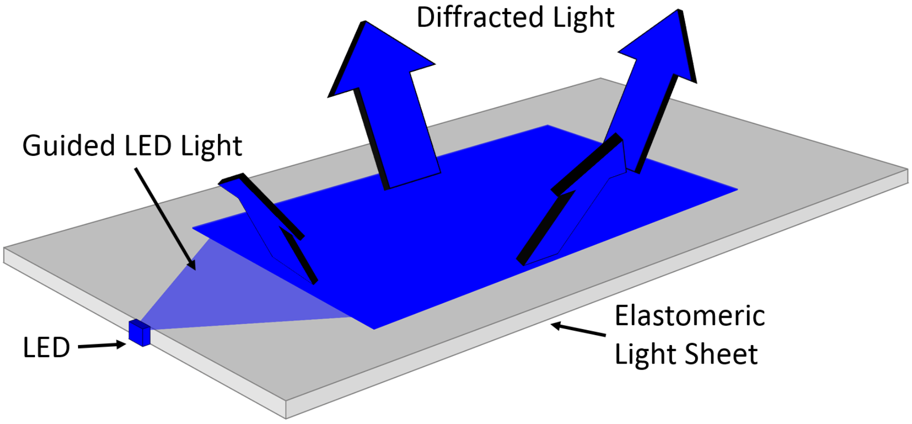

FIGURE 1.7: Schematic of our wearable device design

1.6 Our wearable design

One major issue with current LED based phototherapy devices, is non-uniformity over the treatment area. The LED arrays have non-uniform light distribution [2, 3], which makes it difficult for clinicians to determine treatment dosages. The bulky size of the LEDs limits the fill factor of the devices, preventing uniformity from being achieved using very dense arrays.

Due to their excellent electrical, spectral and cost-effective properties, our device utilises LEDs. However, to avoid the distribution issue seen with LED arrays, the LEDs are coupled to an elastomeric membrane in an edge-lit configuration. The flexibility of this membrane makes it conformable to different contours of the body. Light is guided through the membrane and extracted out of the top surface at a designated position to coincide with the treatment area. A schematic of the device design is shown in Figure 1.7. This method of edge-injection is used in display technology to produce thinner, and flexible displays [87].

This edge-lit design also provides a decreased device thickness compared to current devices; the thickness of the overall device depends only on the size of the LEDs. Smaller LEDs can be utilised to decrease the device thickness further, improving its wearability. These smaller LEDs are called micro-LEDs and are discussed in Section 1.8. The use of an elastomeric membrane will allow for treatment to different regions of the body with high conformability.

The initial device objectives are an irradiance output of at least 1 $\mathrm{mW/cm^2}$ over an area of 1 $\mathrm{cm^2}$ with a uniformity error of less than 15% over the emission area. Although this irradiance value is less than other devices on the market [88], the device is less obtrusive than these other devices, allowing it to be worn for longer to reach the required light dose.

1.7 Light emitting diodes

Several technologies have been utilised as the light source in phototherapy. There is a recent trend towards using LEDs over traditional light sources. They are more compact, energy efficient and low cost compared to other light sources and laser-based sources. Recent developments in UV LEDs makes them even more relevant. Figure 1.8 shows two LED devices utilised for phototherapy in clinics and hospitals. The red LED Aktilite® device from Galderma is used as a light source for PDT [89], while the blue LED BILIPAD device from AVI Healthcare Pvt Ltd is used as an infant phototherapy lamp [90].

1.7.1 LED history

The history of the LED dates back to the early 20th century, but a practical device emitting visible light (red) was not fabricated until 1962 [91]. Initially these LEDs were utilised in indicator lights and calculator displays. A lot of effort was put into broadening the available wavelength spectrum and in 1994, the first blue indium gallium nitride (InGaN) device was fabricated by Nakamura at Nichia. This work later won the 2014 Nobel Prize in Physics, along with Akasaki and Amano. After decades of work it is now possible to fabricate LEDs in a whole range of wavelengths using different semiconductor materials. For example; InGaN for ultraviolet, blue and green, aluminium gallium indium phosphide (AlGaInP) for yellow, orange and red and aluminium gallium arsenide (AlGaAs) for red and infrared [91]. There are gaps in the available wavelength

(a) (b)

Figure 1.8: Light emitting diode based phototherapy devices (a) red LED Aktilite® source for PDT [89] and (b) blue LED BILIPAD source for infant phototherapy of jaundice [90]

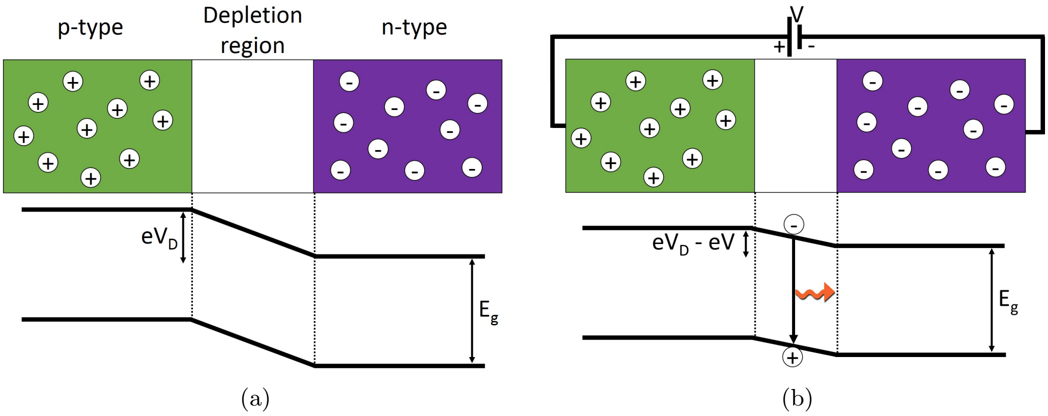

FIGURE 1.9: A simplified p-n junction under (a) no bias and (b) forward bias

spectrum, between green and orange and it is difficult to get fully effective LEDs at these wavelengths.

1.7.2 LED physics

LEDs are fabricated from semiconductors which are a material, in which the electron band structure has a band gap that cannot be occupied by charge carriers. Electroluminescence occurs when electrons from the upper conduction band recombine with holes in the lower valance band, releasing energy as a photon. The energy difference across the band gap determines the wavelength of the emitted photons when a suitable current is supplied.

In order to produce functional devices, the semiconductor materials are doped with acceptor (p-type) or donor (n-type) atoms to increase the number of available carriers. The p-type and n-type materials are grown together to form a p-n junction. Excess electrons and holes diffuse into the opposite material and recombine, producing a depletion region between the p-type and n-type materials. A diffusion voltage, $\mathrm{V_D}$, is formed giving a potential barrier of energy, $e\mathrm{V_D}$, producing the energy band structure shown in Figure 1.9. Under a forward bias, carriers are injected into the depletion region where they can recombine and emit photons [92]. The recombination rate in an LED is dependent upon the density of electrons in the active region, however, electrons and holes will propagate through the material with a characteristic diffusion length, which can be several micrometres, limiting the carrier concentrations [91].

Larger bandgap materials can be grown on either side of a narrow band gap material to form potential barriers. These barriers confine the carriers to a smaller region, therefore, increasing the concentration. To maximise the recombination of carriers, multiple quantum well (MQW) structures are used. These have repeating series of narrow and wide band gap materials and increase the quantum efficiency of the LEDs.

LEDs are grown on different materials depending on the semiconductor properties, gallium nitride (GaN) LED materials are typically grown on sapphire, though research has been carried out on silicon. Sapphire is beneficial as it is transparent so allows for so-called “flip-chip” emission through the sapphire, protecting the semiconductor from physical harm. Silicon substrates are much cheaper than sapphire, and can allow for mass production with integrated electronics, unlike sapphire [93].

1.7.3 Organic LEDs

There is another type of LED, known as organic LEDs (OLEDs). OLEDs have a similar method of action to inorganic LEDs, however, they have an organic semiconductor layer instead of an inorganic semiconductor layer [94]. These have many advantages over inorganic LEDs including the ease of deposition on a range of materials, both flexible and hard and the ability to produce multi-layered devices with organic materials of different band gaps. However, they have emission lifetime issues due to degradation of the organic materials [95].

OLEDs have been utilised as display materials for a number of years now but there has only been one phototherapy device which utilised them. The Ambicare Ambulight device was initially designed using red emitting OLEDs as the light source [96]. This device published good results in a pilot trial but the OLEDs were later swapped for inorganic LEDs for the final device [1, 4]. The reason for this source change has not been published but is perhaps down to degradation issues with the organic semiconductors.

1.7.4 GaN-based LEDs

The devices utilised in this thesis are based on gallium nitride (GaN) materials. The band gap of the material is selected by adjusting the composition of gallium, indium and aluminium in the alloy. These nitride-based materials cover the blue-green range of spectrum wavelengths and extend into the UV. In particular, efficient blue-emitting LEDs fabricated with GaN have enabled white LED lighting by combining with phosphors. The LEDs discussed in this thesis use InGaN/GaN alloys for the active region and are grown on *c*-plane sapphire.

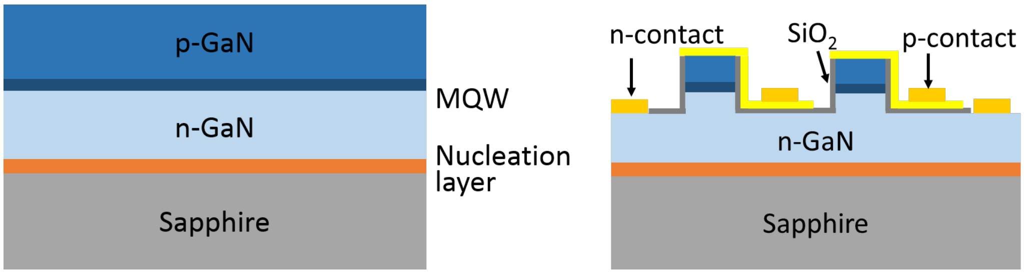

(a) (b)

FIGURE 1.10: (a) Schematic showing the layers of a GaN semiconductor wafer and (b) resulting wafer structure of a fabricated LED array

1.7.5 LED structure and fabrication

The layers of a typical GaN on sapphire wafer are shown in Figure 1.10. The structure has a nucleation/buffer layer of undoped GaN between the sapphire substrate and the n-GaN. This buffer layer is needed to reduce the 16% lattice mismatch between the sapphire and n-GaN, this relaxes the strain and reduces the number of dislocations [97]. The n-GaN layer is followed by the active region, which consists of the MQWs and is generally less than 200 nm in thickness. This is then topped with a thin layer of p-GaN to form the LED wafer [98].

In order to produce LED chips from the GaN wafers, photolithographic and etching techniques are utilised along with material depositions. The fabrication takes place in a cleanroom environment to avoid contamination. A typical fabrication process is described here. Initially, the LED pixels are defined by photolithography and the wafer plasma-etched down to the n-GaN layer. A layer of silicon dioxide is then deposited to electrically insulate each pixel. A thick palladium layer is spread over the top of the p-GaN to act as a contact and mirror, this increases the light extraction efficiency. A final metal deposition of titanium/gold mixture is then added as a metal bonding pad for each of the positive (p) and negative (n) contact pads, allowing for the LED to be electrically driven.

1.8 Micro-LEDs

Micro-LEDs (μLEDs) are LEDs that are less than 100 μm in size. These vary from typical broad-area LEDs that range from 300 μm to 1 mm in size. Terminology now proposes that LEDs between 100 μm and 300 μm should now be known as mini-LEDs [99].

The first μLEDs were fabricated in 2000 from InGaN/GaN wafers [100]. Advances in fabrication and application driven research of these devices has led to many publications of

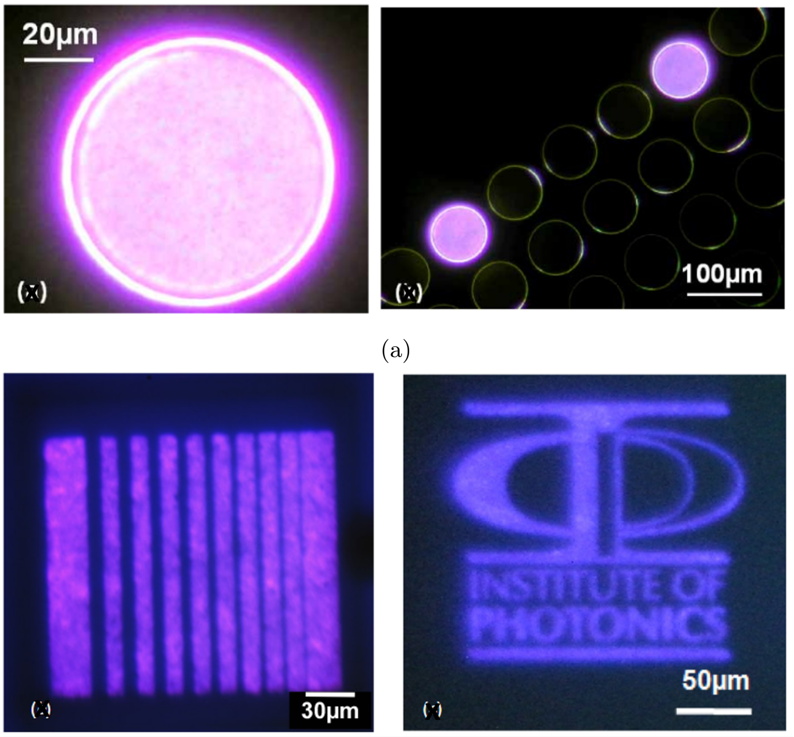

(a)

(b)

Figure 1.11: Microscope images of μLEDs fabricated in the IoP (a) round UV pixels with diameters of 72 μm [102] and (b) a 1D array of violet bars (left) with the laboratory logo shown with microstructured pixels [103]

large arrays of μLEDs and broad areas of usage [101]. Examples of μLEDs fabricated in the Institute of Photonics are shown in Figure 1.11, these are taken from [102] and [103].

The small size and high optical power density of μLEDs make them an ideal light source for a wearable phototherapy device as is shown in Chapter 3.

1.8.1 Micro-LED fabrication

The μLED devices utilised throughout this work are based on commercially grown GaN on sapphire wafers with a 300 μm thick sapphire substrate. The devices are fabricated as described in Section 1.7.5. Photolithographic techniques, chemical and physical etching and material deposition are undertaken in a cleanroom environment to avoid any contamination.

The devices can be fabricated to have individually addressable pixels [93], or they can be connected to a common p-contact and n-contact and connected in series or parallel [93, 101]. In series connected μLEDs, each pixel receives the same current and the supply voltage is divided between the number of pixels in the circuit. Whereas, in a parallel connected circuit, each μLED pixel receives the same voltage and the supply current is shared between them. So, the same number of pixels will have a lower supply voltage and higher supply current in a parallel circuit compared to a series connected circuit.

The devices fabricated for this thesis have a common p-contact and n-contact. Therefore, all of the pixels are either on or off depending on the power supplied. The pixels are connected in parallel, therefore the supplied current is shared between each pixel. Parallel connected pixels have the disadvantage of a higher supply current being required; this increases the risks of damage from overheating but they have the advantage of a lower voltage requirement to power the pixels. For a wearable device this means a smaller number of batteries can be connected, minimising the device footprint. Another benefit for parallel connectivity is that a short circuit at a single pixel will not result in full device breakdown, unlike in a series circuit.

1.9 Summary

This chapter introduced the application of phototherapy and the mechanism of action of different wavelengths of light on the layers of the skin. A brief summary of available at-home phototherapy devices was given as was an introduction to the future possibilities of devices with flexible fibre-woven designs and flexible electronic-based wearables. Finally, the engineering background behind LED devices was presented alongside the benefits of micro-sized LEDs.

The motivation behind this work is to design a wearable phototherapy device suitable for treatments using different wavelengths. The work herein discussed throughout this thesis utilises an elastomeric membrane, edge-lit with LEDs or μLEDs, to produce a flexible emissive area.

References

[1] S. H. Ibbotson and J. Ferguson, “Ambulatory photodynamic therapy using low irradiance inorganic light-emitting diodes for the treatment of non-melanoma skin cancer: an open study,” *Photodermatology, photoimmunology & photomedicine*, vol. 28, no. 5, pp. 235–239, 2012.

[2] H. Moseley, “Light distribution and calibration of commercial PDT LED arrays,” *Photochemical & Photobiological Sciences*, vol. 4, no. 11, pp. 911–914, 2005.

[3] C. Cochrane, S. R. Mordon, J. C. Lesage, and V. Koncar, “New design of textile light diffusers for photodynamic therapy,” *Materials Science and Engineering: C*, vol. 33, no. 3, pp. 1170–1175, 2013.

[4] C. Morton, R.-M. Szeimies, A. Sidoroff, and L. Braathen, "European guidelines for topical photodynamic therapy part 1: treatment delivery and current indications - actinic keratoses, bowen's disease, basal cell carcinoma," *Journal of the European Academy of Dermatology and Venereology*, vol. 27, no. 5, pp. 536–544, 2013.

[5] F. Martini, J. L. Nath, E. F. Bartholomew, W. C. Ober, C. E. Ober, K. Welch, and R. T. Hutchings, *Fundamentals of anatomy & physiology*, vol. 7. Pearson Benjamin Cummings San Francisco, CA, 2006.

[6] G. K. Menon, "New insights into skin structure: scratching the surface," *Advanced drug delivery reviews*, vol. 54, pp. S3–S17, 2002.

[7] R. R. Anderson, J. A. Parrish, *et al.*, "The optics of human skin.," *Journal of investigative dermatology*, vol. 77, no. 1, pp. 13–19, 1981.

[8] C. Ash, M. Dubec, K. Donne, and T. Bashford, "Effect of wavelength and beam width on penetration in light-tissue interaction using computational methods," *Lasers in medical science*, vol. 32, no. 8, pp. 1909–1918, 2017.

[9] A. R. Young, "Chromophores in human skin," *Physics in Medicine & Biology*, vol. 42, no. 5, p. 789, 1997.

[10] A. Campanati and A. Offidani, *Phototherapy in Dermatology.* Nova Biomedical, Nova Science Publishers, Inc, 2017.

[11] T. Bhutani, W. Liao, and M. Nakamura, *Evidence-Based Psoriasis: Diagnosis and Treatment.* Springer, 2018.

[12] J. Krutmann, H. Hönigsmann, C. A. Elmets, and P. R. Bergstresser, *Dermatological phototherapy and photodiagnostic methods.* Springer, 2009.

[13] A. N. Paunel, A. Dejam, S. Thelen, M. Kirsch, M. Horstjann, P. Gharini, M. Mürtz, M. Kelm, H. de Groot, V. Kolb-Bachofen, *et al.*, "Enzyme-independent nitric oxide formation during UVA challenge of human skin: characterization, molecular sources, and mechanisms," *Free Radical Biology and Medicine*, vol. 38, no. 5, pp. 606–615, 2005.

[14] C. V. Suschek, T. Schewe, H. Sies, and K.-D. Kröncke, "Nitrite, a naturally occurring precursor of nitric oxide that acts like a 'prodrug'," *Biological chemistry*, vol. 387, no. 5, pp. 499–506, 2006.

[15] M.-M. Cals-Grierson and A. Ormerod, "Nitric oxide function in the skin," *Nitric oxide*, vol. 10, no. 4, pp. 179–193, 2004.

[16] U. P. Kappes, D. Luo, M. Potter, K. Schulmeister, and T. M. Rünger, "Short-and long-wave UV light (UVB and UVA) induce similar mutations in human skin cells," *Journal of Investigative Dermatology*, vol. 126, no. 3, pp. 667–675, 2006.

[17] F. Trautinger, "Mechanisms of photodamage of the skin and its functional consequences for skin ageing," *Clinical and experimental dermatology*, vol. 26, no. 7, pp. 573–577, 2001.

[18] B. H. Mahmoud, C. L. Hexsel, I. H. Hamzavi, and H. W. Lim, "Effects of visible light on the skin," *Photochemistry and photobiology*, vol. 84, no. 2, pp. 450–462, 2008.

[19] J. Liebmann, M. Born, and V. Kolb-Bachofen, "Blue-light irradiation regulates proliferation and differentiation in human skin cells," *Journal of Investigative Dermatology*, vol. 130, no. 1, pp. 259–269, 2010.

[20] R. Hearn, A. Kerr, K. Rahim, J. Ferguson, and R. Dawe, "Incidence of skin cancers in 3867 patients treated with narrow-band ultraviolet B phototherapy," *British Journal of Dermatology*, vol. 159, no. 4, pp. 931–935, 2008.

[21] C. Opländer, S. Hidding, F. B. Werners, M. Born, N. Pallua, and C. V. Suschek, "Effects of blue light irradiation on human dermal fibroblasts," *Journal of Photochemistry and Photobiology B: Biology*, vol. 103, no. 2, pp. 118–125, 2011.

[22] S. Y. Lee, K.-H. Park, J.-W. Choi, J.-K. Kwon, D. R. Lee, M. S. Shin, J. S. Lee, C. E. You, and M. Y. Park, "A prospective, randomized, placebo-controlled, double-blinded, and split-face clinical study on LED phototherapy for skin rejuvenation: clinical, profilometric, histologic, ultrastructural, and biochemical evaluations and comparison of three different treatment settings," *Journal of Photochemistry and Photobiology B: Biology*, vol. 88, no. 1, pp. 51–67, 2007.

[23] M. E. d. A. Chaves, A. R. d. Araújo, A. C. C. Piancastelli, and M. Pinotti, "Effects of low-power light therapy on wound healing: LASER v LED," *Anais brasileiros de dermatologia*, vol. 89, no. 4, pp. 616–623, 2014.

[24] J. Bhat, J. Birch, C. Whitehurst, and S. W. Lanigan, "A single-blinded randomised controlled study to determine the efficacy of Omnilux Revive facial treatment in skin rejuvenation," *Lasers in medical science*, vol. 20, no. 1, pp. 6–10, 2005.

[25] P. Avci, A. Gupta, M. Sadasivam, D. Vecchio, Z. Pam, N. Pam, and M. R. Hamblin, "Low-level laser (light) therapy (LLLT) in skin: stimulating, healing, restoring," in *Seminars in cutaneous medicine and surgery*, vol. 32, p. 41, NIH Public Access, 2013.

[26] J. Zhou, Z. Lu, X. Zhu, X. Wang, Y. Liao, Z. Ma, and F. Li, "NIR photothermal therapy using polyaniline nanoparticles," *Biomaterials*, vol. 34, no. 37, pp. 9584–9592, 2013.

[27] D. Castaneda, A. Esparza, M. Ghamari, C. Soltanpur, and H. Nazeran, "A review on wearable photoplethysmography sensors and their potential future applications in health care," *International journal of biosensors & bioelectronics*, vol. 4, no. 4, p. 195, 2018.

[28] Technavio, *Light Therapy Market by End-user and Geographic Landscape - Forecast and Analysis 2020-2024*. 2020.

[29] G. Pail, W. Huf, E. Pjrek, D. Winkler, M. Willeit, N. Praschak-Rieder, and S. Kasper, "Bright-light therapy in the treatment of mood disorders," *Neuropsychobiology*, vol. 64, no. 3, pp. 152–162, 2011.

[30] C. Even, C. M. Schröder, S. Friedman, and F. Rouillon, "Efficacy of light therapy in nonseasonal depression: a systematic review," *Journal of affective disorders*, vol. 108, no. 1-2, pp. 11–23, 2008.

[31] F. Benedetti, R. Riccaboni, C. Locatelli, S. Poletti, S. Dallaspezia, and C. Colombo, "Rapid treatment response of suicidal symptoms to lithium, sleep deprivation, and light therapy (chronotherapeutics) in drug-resistant bipolar depression.," *The Journal of clinical psychiatry*, 2014.

[32] L. F. de Freitas and M. R. Hamblin, "Proposed mechanisms of photobiomodulation or low-level light therapy," *IEEE Journal of selected topics in quantum electronics*, vol. 22, no. 3, pp. 348–364, 2016.

[33] M. T. Pelegrino, R. B. Weller, A. Paganotti, and A. B. Seabra, “Delivering nitric oxide into human skin from encapsulated S-nitrosoglutathione under UV light: An in vitro and ex vivo study,” *Nitric Oxide*, vol. 94, pp. 108–113, 2020.

[34] J. Loscalzo and G. Welch, “Nitric oxide and its role in the cardiovascular system,” *Progress in cardiovascular diseases*, vol. 38, no. 2, pp. 87–104, 1995.

[35] H. Hönigsmann, “History of phototherapy in dermatology,” *Photochemical & photobiological sciences*, vol. 12, no. 1, pp. 16–21, 2013.

[36] J. E. Gudjonsson and J. T. Elder, “Psoriasis: epidemiology,” *Clinics in dermatology*, vol. 25, no. 6, pp. 535–546, 2007.

[37] S. Pfaff, J. Liebmann, M. Born, H. F. Merk, and V. Von Felbert, “Prospective randomized long-term study on the efficacy and safety of UV-free blue light for treating mild psoriasis vulgaris,” *Dermatology*, vol. 231, no. 1, pp. 24–34, 2015.

[38] M. Lebwohl, P. Ting, and J. Koo, “Psoriasis treatment: traditional therapy,” *Annals of the rheumatic diseases*, vol. 64, no. suppl 2, pp. ii83–ii86, 2005.

[39] A. Ighani, A. C. Partridge, N. H. Shear, C. Lynde, W. P. Gulliver, C. Sibbald, and P. Fleming, “Comparison of management guidelines for moderate-to-severe plaque psoriasis: a review of phototherapy, systemic therapies, and biologic agents,” *Journal of cutaneous medicine and surgery*, vol. 23, no. 2, pp. 204–221, 2019.

[40] J. M. Bae, H. M. Jung, B. Y. Hong, J. H. Lee, W. J. Choi, J. H. Lee, and G. M. Kim, “Phototherapy for vitiligo: a systematic review and meta-analysis,” *JAMA dermatology*, vol. 153, no. 7, pp. 666–674, 2017.

[41] N. B. Meduri, T. Vandergriff, H. Rasmussen, and H. Jacobe, “Phototherapy in the management of atopic dermatitis: a systematic review,” *Photodermatology, photoimmunology & photomedicine*, vol. 23, no. 4, pp. 106–112, 2007.

[42] V. K. Jain, K. Aggarwal, K. Jain, and A. Bansal, “Narrow-band UV-B phototherapy in childhood psoriasis,” *International journal of dermatology*, vol. 46, no. 3, pp. 320–322, 2007.

[43] S. S. Yones, R. A. Palmer, T. M. Garibaldinos, and J. L. Hawk, “Randomized double-blind trial of treatment of vitiligo: efficacy of psoralen-UV-A therapy vs narrowband-UV-B therapy,” *Archives of dermatology*, vol. 143, no. 5, pp. 578–584, 2007.

[44] M. J. Maisels and A. F. McDonagh, “Phototherapy for neonatal jaundice,” *New England Journal of Medicine*, vol. 358, no. 9, pp. 920–928, 2008.

[45] M. Kleinpenning, M. Otero, P. van Erp, M. Gerritsen, and P. van de Kerkhof, “Efficacy of blue light vs. red light in the treatment of psoriasis: A double-blind, randomized comparative study,” *Journal of the European Academy of Dermatology and Venereology*, vol. 26, no. 2, pp. 219–225, 2012.

[46] A. Weinstabl, S. Hoff-Lesch, H. F. Merk, and V. Von Felbert, “Prospective randomized study on the efficacy of blue light in the treatment of psoriasis vulgaris,” *Dermatology*, vol. 223, no. 3, pp. 251–259, 2011.

[47] C. Morton, R. Scholefield, C. Whitehurst, and J. Birch, "An open study to determine the efficacy of blue light in the treatment of mild to moderate acne," *Journal of dermatological treatment*, vol. 16, no. 4, pp. 219–223, 2005.

[48] R. Akaraphanth, W. Kanjanawanitchkul, and P. Gritiyarangsan, "Efficacy of ALA-PDT vs blue light in the treatment of acne," *Photodermatology, photoimmunology & photomedicine*, vol. 23, no. 5, pp. 186–190, 2007.

[49] M. A. Trelles, "Phototherapy in anti-aging and its photobiologic basics: a new approach to skin rejuvenation," *Journal of cosmetic dermatology*, vol. 5, no. 1, pp. 87–91, 2006.

[50] H. T. Whelan, R. L. Smits Jr, E. V. Buchman, N. T. Whelan, S. G. Turner, D. A. Margolis, V. Cevenini, H. Stinson, R. Ignatius, T. Martin, *et al.*, "Effect of NASA light-emitting diode irradiation on wound healing," *Journal of clinical laser medicine & surgery*, vol. 19, no. 6, pp. 305–314, 2001.

[51] B. J. Erdle, S. Brouxhon, M. Kaplan, J. Vanbuskirk, and A. P. Pentland, "Effects of continuous-wave (670-nm) red light on wound healing," *Dermatologic Surgery*, vol. 34, no. 3, pp. 320–325, 2008.

[52] D. J. Goldberg and B. A. Russell, "Combination blue (415 nm) and red (633 nm) LED phototherapy in the treatment of mild to severe acne vulgaris," *Journal of Cosmetic and Laser Therapy*, vol. 8, no. 2, pp. 71–75, 2006.

[53] K. H. Beckmann, G. Meyer-Hamme, and S. Schröder, "Low level laser therapy for the treatment of diabetic foot ulcers: a critical survey," *Evidence-Based Complementary and Alternative Medicine*, vol. 2014, 2014.

[54] E. Archier, S. Devaux, E. Castela, A. Gallini, F. Aubin, M. Le Maître, S. Aractingi, H. Bachelez, B. Cribier, P. Joly, *et al.*, "Efficacy of psoralen UV-A therapy vs. narrowband UV-B therapy in chronic plaque psoriasis: a systematic literature review," *Journal of the European Academy of Dermatology and Venereology*, vol. 26, pp. 11–21, 2012.

[55] D. J. Piacquadio, D. M. Chen, H. F. Farber, J. F. Fowler Jr, S. D. Glazer, J. J. Goodman, L. L. Hruza, E. W. Jeffes, M. R. Ling, T. J. Phillips, *et al.*, "Photodynamic therapy with aminolevulinic acid topical solution and visible blue light in the treatment of multiple actinic keratoses of the face and scalp: Investigator-blinded, phase 3, multicenter trials," *Archives of dermatology*, vol. 140, no. 1, pp. 41–46, 2004.

[56] C. Fritsch, B. Homey, W. Stahl, P. Lehmann, T. Ruzicka, and H. Sies, "Preferential relative porphyrin enrichment in solar keratoses upon topical application of aminolevulinic acid methylester," *Photochemistry and photobiology*, vol. 68, no. 2, pp. 218–221, 1998.

[57] K. König, M.-T. Wyss-Desserich, Y. Tadir, U. Haller, B. Tromberg, M. W. Berns, and P. Wyss, "Modifications of protoporphyrin IX fluorescence during ALA-based photodynamic therapy of endometriosis," *Medical Laser Application*, vol. 21, no. 4, pp. 291–297, 2006.

[58] J. C. Kennedy and R. H. Pottier, "New trends in photobiology: endogenous protoporphyrin IX, a clinically useful photosensitizer for photodynamic therapy," *Journal of Photochemistry and Photobiology B: Biology*, vol. 14, no. 4, pp. 275–292, 1992.

[59] F. Moloney and P. Collins, “Randomized, double-blind, prospective study to compare topical 5-aminolaevulinic acid methylester with topical 5-aminolaevulinic acid photodynamic therapy for extensive scalp actinic keratosis,” *British Journal of Dermatology*, vol. 157, no. 1, pp. 87–91, 2007.

[60] C. Morton, H. Wulf, R. Szeimies, Y. Gilaberte, N. Basset-Seguin, E. Sotiriou, S. Piaserico, R. Hunger, S. Baharlou, A. Sidoroff, *et al.*, “Practical approach to the use of daylight photodynamic therapy with topical methyl aminolevulinate for actinic keratosis: a European consensus,” *Journal of the European Academy of Dermatology and Venereology*, vol. 29, no. 9, pp. 1718–1723, 2015.

[61] S. R. Wiegell, J. Heydenreich, S. Fabricius, and H. C. Wulf, “Continuous ultra-low-intensity artificial daylight is not as effective as red LED light in photodynamic therapy of multiple actinic keratoses,” *Photodermatology, photoimmunology & photomedicine*, vol. 27, no. 6, pp. 280–285, 2011.

[62] E. W. Jeffes, J. L. McCullough, G. D. Weinstein, R. Kaplan, S. D. Glazer, and J. R. Taylor, “Photodynamic therapy of actinic keratoses with topical aminolevulinic acid hydrochloride and fluorescent blue light,” *Journal of the American Academy of Dermatology*, vol. 45, no. 1, pp. 96–104, 2001.

[63] S. Wiegell, M. Hædersdal, P. Philipsen, P. Eriksen, C. Enk, and H. C. Wulf, “Continuous activation of PpIX by daylight is as effective as and less painful than conventional photodynamic therapy for actinic keratoses; a randomized, controlled, single-blinded study,” *British Journal of Dermatology*, vol. 158, no. 4, pp. 740–746, 2008.

[64] R. A. Palmer, S. Aquilina, P. J. Milligan, S. L. Walker, J. L. Hawk, and A. R. Young, “Photoadaptation during narrowband ultraviolet-B therapy is independent of skin type: A study of 352 patients,” *Journal of Investigative Dermatology*, vol. 126, no. 6, pp. 1256 – 1263, 2006.

[65] T. Ling, T. Clayton, J. Crawley, L. Exton, V. Goulden, S. Ibbotson, K. McKenna, M. Mohd Mustapa, L. Rhodes, R. Sarkany, *et al.*, “British association of dermatologists and british photodermatology group guidelines for the safe and effective use of psoralen–ultraviolet a therapy 2015,” *British Journal of Dermatology*, vol. 174, no. 1, pp. 24–55, 2016.

[66] “Service Guidance and Standards for Phototherapy Units - NICE Accredited,” Standard, British Photodermatology Group/British Association of Dermatologists, UK, Oct. 2016.

[67] M. B. Koek, E. Buskens, H. van Weelden, P. H. Steegmans, C. A. Bruijnzeel-Koomen, and V. Sigurdsson, “Home versus outpatient ultraviolet b phototherapy for mild to severe psoriasis: pragmatic multicentre randomised controlled non-inferiority trial (PLUTO study),” *Bmj*, vol. 338, p. b1542, 2009.

[68] B. V. Nolan, “Review of home phototherapy,” *Dermatology online journal*, vol. 16, no. 12, p. 2, 2010.

[69] K. Langmack, R. Mehta, P. Twyman, and P. Norris, “Topical photodynamic therapy at low fluence rates–theory and practice,” *Journal of Photochemistry and Photobiology B: Biology*, vol. 60, no. 1, pp. 37–43, 2001.

[70] “SolRx 100-Series handheld UVB-narrowband home phototherapy device.” `https://solarcsystems.com/en/product/solrx-hand-held/`. Accessed: 22-04-2020.

[71] "How Clarify's Phototherapy Treatment Works." `https://www.clarifymed.com/clarify-system/`. Accessed: 22-04-2020.

[72] V. Eleftheriadou and K. Ezzedine, "Portable home phototherapy for vitiligo," *Clinics in dermatology*, vol. 34, no. 5, pp. 603–606, 2016.

[73] A. Cline, E. L. Unrue, A. Collins, and S. R. Feldman, "Adherence to a novel home phototherapy system with integrated features," *Dermatology online journal*, vol. 25, no. 3, 2019.

[74] "Lumie Clear." `https://www.lumie.com/collections/featured-products/products/clear`. Accessed: 23-04-2020.

[75] "Red & blue light therapy acne mask: NEUTROGENA®." `https://www.neutrogena.com/skin/skin-acne/red-and-blue-light-therapy-acne-mask/6810124.html`. Accessed: 23-04-2020.

[76] "Celluma Light Therapy Products." `https://www.celluma.com/collections/all`. Accessed: 23-04-2020.

[77] "Phillips BlueTouch controlled pain relief patch." `https://www.philips.co.uk/c-p/PR3743_00/bluetouch-app-controlled-pain-relief-patch`. Accessed: 23-04-2020.

[78] C. Vicentini, O. Carpentier, F. Lecomte, E. Thecua, L. Mortier, and S. R. Mordon, "Treatment of a vulvar Paget's disease by photodynamic therapy with a new light emitting fabric based device," *Lasers in surgery and medicine*, vol. 49, no. 2, pp. 177–180, 2017.

[79] B. M. Quandt, M. S. Pfister, J. F. Lübben, F. Spano, R. M. Rossi, G.-L. Bona, and L. F. Boesel, "POF-yarn weaves: controlling the light out-coupling of wearable phototherapy devices," *Biomedical optics express*, vol. 8, no. 10, pp. 4316–4330, 2017.

[80] Y. Liu, M. Pharr, and G. A. Salvatore, "Lab-on-skin: a review of flexible and stretchable electronics for wearable health monitoring," *ACS nano*, vol. 11, no. 10, pp. 9614–9635, 2017.

[81] H. E. Lee, D. Lee, T.-I. Lee, J. H. Shin, G.-M. Choi, C. Kim, S. H. Lee, J. H. Lee, Y. H. Kim, S.-M. Kang, *et al.*, "Wireless powered wearable micro light-emitting diodes," *Nano Energy*, vol. 55, pp. 454–462, 2019.

[82] A. J. Bandodkar, P. Gutruf, J. Choi, K. Lee, Y. Sekine, J. T. Reeder, W. J. Jeang, A. J. Aranyosi, S. P. Lee, J. B. Model, *et al.*, "Battery-free, skin-interfaced microfluidic/electronic systems for simultaneous electrochemical, colorimetric, and volumetric analysis of sweat," *Science advances*, vol. 5, no. 1, p. eaav3294, 2019.

[83] C. Linghu, S. Zhang, C. Wang, and J. Song, "Transfer printing techniques for flexible and stretchable inorganic electronics," *npj Flexible Electronics*, vol. 2, no. 1, pp. 1–14, 2018.

[84] J. Kim, P. Gutruf, A. M. Chiarelli, S. Y. Heo, K. Cho, Z. Xie, A. Banks, S. Han, K.-I. Jang, J. W. Lee, *et al.*, "Miniaturized battery-free wireless systems for wearable pulse oximetry," *Advanced functional materials*, vol. 27, no. 1, p. 1604373, 2017.

[85] J. Park, J. Kim, S.-Y. Kim, W. H. Cheong, J. Jang, Y.-G. Park, K. Na, Y.-T. Kim, J. H. Heo, C. Y. Lee, *et al.*, "Soft, smart contact lenses with integrations of wireless circuits, glucose sensors, and displays," *Science advances*, vol. 4, no. 1, p. eaap9841, 2018.

[86] H. E. Lee, J. Choi, S. H. Lee, M. Jeong, J. H. Shin, D. J. Joe, D. Kim, C. W. Kim, J. H. Park, J. H. Lee, *et al.*, "Monolithic flexible vertical GaN light-emitting diodes for a transparent wireless brain optical stimulator," *Advanced Materials*, vol. 30, no. 28, p. 1800649, 2018.

[87] G. Harbers, W. Timmers, and W. Sillevis-Smitt, "LED backlighting for LCD HDTV," *Journal of the Society for Information Display*, vol. 10, no. 4, pp. 347–350, 2002.

[88] D. R. Opel, E. Hagstrom, A. K. Pace, K. Sisto, S. A. Hirano-ALi, S. Desai, and J. Swan, "Light-emitting diodes: a brief review and clinical experience," *The Journal of clinical and aesthetic dermatology*, vol. 8, no. 6, p. 36, 2015.

[89] "Galderma Aktilite lamp for PDT in dermatology." `https://www.galderma.com/se/sites/g/files/jcdfhc271/files/inline-files/Produktblad_Aktilite_SE-FI-eng-2018`. Accessed: 30-04-2020.

[90] "AVI Healthcare BILIPAD LED phototherapy unit." `http://avihealthcare.com/bilipad`. Accessed: 29-04-2020.

[91] E. F. Schubert, *Light-Emitting Diodes.* Cambridge University Press, 2 ed., 2006.

[92] B. E. Saleh and M. C. Teich, *Fundamentals of photonics.* john Wiley & sons, 2019.

[93] P. Tian, J. J. McKendry, Z. Gong, S. Zhang, S. Watson, D. Zhu, I. M. Watson, E. Gu, A. E. Kelly, C. J. Humphreys, *et al.*, "Characteristics and applications of micro-pixelated GaN-based light emitting diodes on Si substrates," *Journal of Applied Physics*, vol. 115, no. 3, p. 033112, 2014.

[94] H. Sasabe and J. Kido, "Development of high performance oleds for general lighting," *Journal of Materials Chemistry C*, vol. 1, no. 9, pp. 1699–1707, 2013.

[95] D. Kondakov, W. Lenhart, and W. Nichols, "Operational degradation of organic light-emitting diodes: Mechanism and identification of chemical products," *Journal of Applied Physics*, vol. 101, no. 2, p. 024512, 2007.

[96] S. Attili, A. Lesar, A. McNeill, M. Camacho-Lopez, H. Moseley, S. Ibbotson, I. Samuel, and J. Ferguson, "An open pilot study of ambulatory photodynamic therapy using a wearable low-irradiance organic light-emitting diode light source in the treatment of nonmelanoma skin cancer," *British Journal of Dermatology*, vol. 161, no. 1, pp. 170–173, 2009.

[97] S. Nakamura and S. F. Chichibu, *Introduction to nitride semiconductor blue lasers and light emitting diodes.* CRC Press, 2000.

[98] E. Xie, M. Stonehouse, R. Ferreira, J. J. McKendry, J. Herrnsdorf, X. He, S. Rajbhandari, H. Chun, A. V. Jalajakumari, O. Almer, *et al.*, "Design, fabrication, and application of GaN-based micro-LED arrays with individual addressing by N-electrodes," *IEEE Photonics Journal*, vol. 9, no. 6, pp. 1–11, 2017.

[99] T. Wu, C.-W. Sher, Y. Lin, C.-F. Lee, S. Liang, Y. Lu, S.-W. Huang Chen, W. Guo, H.-C. Kuo, and Z. Chen, "Mini-LED and micro-LED: promising candidates for the next generation display technology," *Applied Sciences*, vol. 8, no. 9, p. 1557, 2018.

[100] S. Jin, J. Li, J. Li, J. Lin, and H. Jiang, "GaN microdisk light emitting diodes," *Applied Physics Letters*, vol. 76, no. 5, pp. 631–633, 2000.

[101] M. D. Dawson and M. A. Neil, "Micro-pixellated LEDs for science and instrumentation," *Journal of Physics D: Applied Physics*, vol. 41, no. 9, p. 090301, 2008.

[102] H. Zhang, D. Massoubre, J. McKendry, Z. Gong, B. Guilhabert, C. Griffin, E. Gu, P. Jessop, J. Girkin, and M. Dawson, "Individually-addressable flip-chip AlInGaN micropixelated light emitting diode arrays with high continuous and nanosecond output power," *Optics express*, vol. 16, no. 13, pp. 9918–9926, 2008.

[103] D. Massoubre, E. Xie, B. Guilhabert, J. Herrnsdorf, E. Gu, I. M. Watson, and M. D. Dawson, "Micro-structured light emission from planar InGaN light-emitting diodes," *Semiconductor Science and Technology*, vol. 29, no. 1, p. 015005, 2013.

Chapter 2

Device design and experimental methods

This chapter introduces the materials and methods utilised in the design and characterisation of the wearable phototherapy device. It also includes a ‘first validation’ of the platform using an off the shelf broad LED (whereas in following chapters micro-LEDs are used). The platform is based on an elastomeric waveguide membrane, with a structure for light extraction, that is injected from its side with light from a LED (see Chapter 1). Characterisation methods used throughout latter chapters are explained and demonstrated using the broad LED.

In the following, the elastomeric membrane properties and fabrication is discussed followed by the properties of a broad area LED as the light source. The coupling efficiency of the LED to the membrane is calculated via optical simulations. The LED is coupled to the membrane and the irradiance from the top surface of the device is then measured experimentally. The irradiance change with the addition of a scatter substrate, consisting of a membrane doped with high refractive index nanoparticle to extract light, is determined as is the concentration effect of these nanoparticles on the extracted light. Irradiance mapping of the scatter substrates is determined using a CCD and an image analysis code. Finally, the chapter closes with a description of a method of extracting uniform light from the device.

2.1 Elastomeric light sheet

As discussed in Chapter 1, our device consists of an elastomeric light sheet edge-lit by μLEDs. An elastomer is a polymer with very weak inter-molecular forces, low Young’s modulus and high failure strain, it also has both viscosity and elasticity (viscoelasticity) properties [1]. This viscoelastic nature allows the polymer to be mechanically flexible. There are a range of different elastomers commercially available, however, in order to guide light in a phototherapy device, they also have to be transparent to UV and visible light and biocompatible with human skin. Elastomers transparent to UV/visible light include polyurethanes, silicones and fluorelastomers. Polyurethanes are a versatile material used for a vast array of applications. Although considered an inert material when correctly fabricated, the process requires the use of isocyanites which are toxic [2]. Fluorelastomers have excellent chemical resistivity but have a complex and expensive fabrication process [3]. Silicones are a silicon-based polymer with low toxicity and low thermal conductivity [4]. The most common silicone is polydimethylsiloxane (PDMS) which is used in contact lenses [5], medical devices [6] and as an antifoaming agent in food [4]. PDMS is commonly used in microfluidic devices due to its low cost, ease of fabrication and non-reactivity with biomaterials. Its inert nature makes PDMS a biocompatible material suitable for use in medical devices [6, 7]. PDMS also has a higher refractive index than skin, this allows light to be guided through the PDMS to the treatment area. Due to these properties, PDMS was chosen as the material for the elastomeric membrane.

2.1.1 Polydimethylsiloxane

PDMS is a two-part polymer consisting of silicone and a cross-linking material; it is commonly used in casting and moulding processes [8]. PDMS is highly transparent to visible wavelengths, with published transmission values of 95% for 2 mm thick PDMS at 400 nm [9]. The PDMS membranes described throughout this thesis are fabricated from a ratio of 5:1 silicone to cross-linker and are cut in slabs of 40 x 20 x 1 mm^3, unless otherwise stated.

2.1.2 PDMS fabrication

Momentive RTV615 PDMS was obtained from Techsil, this two-part polymer is comprised of a silicone base and platinum cross-linker. This particular formulation of PDMS was chosen as it is FDA approved for use in food contact applications and is transparent down to 250 nm [10]. The two-parts are combined at a ratio of 10:1 and cured at room temperature or higher to produce an elastomeric material. The ratio of base to cross-linker can be adjusted to change the resultant properties of the elastomeric material. For example, increasing the ratio to 20:1 results in more deformable polymer, whereas a ratio of 5:1 produces a firmer polymer. As this work utilises thin PDMS membranes of

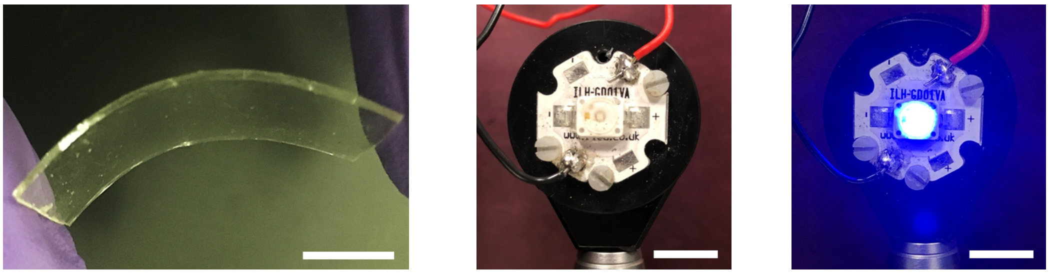
(a) (b) (c)

Figure 2.1: Images of the device components (a) a fabricated PDMS membrane under tension, (b) the broad LED utilised throughout this chapter and (c) the LED with a 20 mA supply current, scale is 10 mm

1 mm or less, a ratio of 5:1 was used, to get a flexible membrane that is easy to handle. Calculated weights of PDMS base and cross-linker were mixed for 3 minutes to ensure homogeneity of the two-parts. The resultant liquid PDMS was added to a petri-dish to form a 1 mm thick film, this was de-gassed for 2 hours and then cured at 80°C for 4 hours. A membrane 40 x 20 mm^2 was then cut from the petri-dish using a scalpel. A fabricated membrane is shown under flex in Figure 2.1(a).

2.2 Light source

The edge-lit light sheet design is primarily used in displays to decrease the overall thickness of devices [11]. The light sources employed are generally LEDs [11, 12], however, historically cold-cathode fluorescent lamps [13, 14] were utilised. These are usually placed along one end of the light sheet, however, can also be placed at one corner of the sheet [15, 16].

Flexible edge-lit devices are becoming more common, for displays and other uses. For example, Kim et al. utilised a flexible PDMS light sheet as an optical cuff for stimulating neurons [17]. As discussed in Section 1.7, LEDs are becoming a more common light source in phototherapy devices due to their high efficiencies, low-cost design and miniaturisation capability. These features, as well as the availability of different wavelengths, make LEDs an ideal source for a wearable phototherapy device.

2.2.1 Broad-area LED

The LED utilised for this chapter was a broad-area blue Golden Dragon LED by Osram Semiconductors [18]. The device consists of an LED chip (1 x 1 mm^2) encased in a silicone dome for protection, this is then packaged and bonded to a power star and heat sink for optimum thermal management. The silicone dome surrounding the LED was

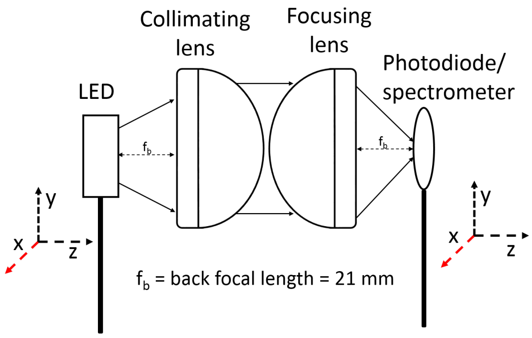

FIGURE 2.2: Schematic showing the optical setup used to characterise the LEDs

filed down using very fine sandpaper to produce a flat surface for better coupling to the membrane. The LED used is shown in Figure 2.1 with no current supplied (b) and 20 mA supplied (c).

2.2.2 LED characteristics

An optical setup, depicted in Figure 2.2, was employed to measure the electrical and optical properties of the LED. The LED is mounted on a small translation stage allowing for movement in the x, y and z-directions, and coupled into a pair of collimating lenses. These aspheric condenser lenses (ACL4532-A, Thorlabs) have a 45 mm diameter and a focal length of 32 mm. The collimated light is then coupled into a focusing lens allowing for the LED light to be focused onto a detector. The detector is also mounted on a small translation stage to allow for movement. The LED placement and detector placement are adjusted until the LED light is focused at the detector. Both the LED and the detector are situated around 21 mm from the lenses, this is the back focal length of the lenses.

To measure the optical power, a silicon detector (Thorlabs, S120VC) coupled to an optical power meter (Thorlabs, PM100D) was used. The power meter is adjusted to the peak wavelength of the LED to allow a correction factor to be applied to the measured power based on the detector's properties. Based on the manufacturers information, the LED can be run at currents of 100 mA to 1000 mA. The optical power from the LED and voltage supplied with this range of currents was recorded to obtain a graph of power-current-voltage (LIV) shown in Figure 2.3(a). Optical powers of 50–140 mW ± 5% can be obtained with supply voltages ranging from 3.0 V to 3.8 V.

For the remainder of this chapter, the LED was run at 350 mA, resulting in an output optical power of 102 ± 5 mW. The detector was replaced with an optical fibre (100 μm core size, 0.22 NA) connected to a spectrometer (OceanOptics, USB4000) to obtain the spectral response of the LED. Figure 2.3(b) shows the emission spectrum of the

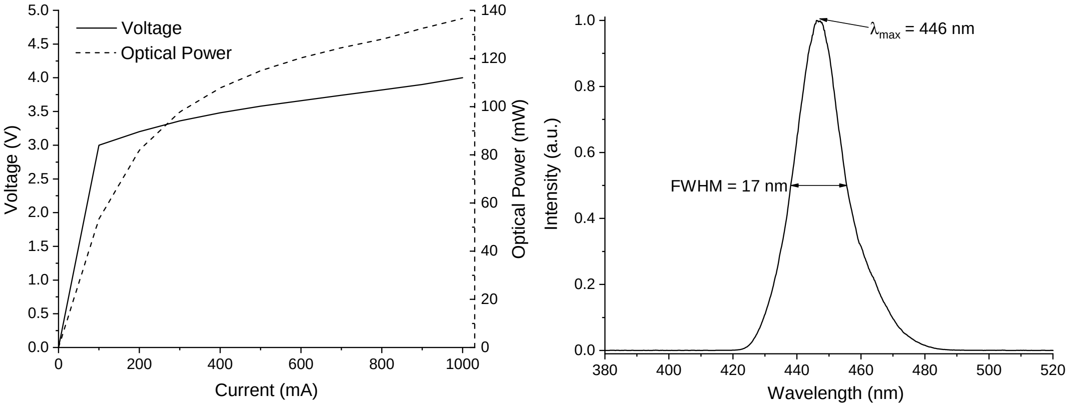

(a) (b)

Figure 2.3: Broad LED electronic and spectral properties (a) LED LIV data (b) wavelength spectrum of the LED run at a current of 350 mA

LED at 350 mA. The device has a peak blue wavelength of 446 nm, with a full-width half-maximum (FWHM) of 17 ± 1.6 nm, typical for GaN-based LED sources [19].

The setup used to determine optical power has associated errors. Stray light analysis was not carried out on the lenses, as the same optical setup was employed to measure the optical power from all sources used throughout this thesis it was deemed suitable for comparison. A calculable error associated with the measurements is in the optical detector, which has an inherent error of 5% at blue and UVA wavelengths, this error is included with all optical power measurements taken with the optical detector.

2.3 Simulated optical coupling

As described in Section 1.6, the LED is to be placed in contact with the 1 mm thick PDMS membrane edge. In order to estimate how much light is coupled into the membrane from the LED, optical design software can be used. Optical design software performs simulations of optical systems, allowing for system performance to be predicted before fabrication. The software uses a mathematical description of the optical elements including the materials, location and shape. There are three main methods used in optical design software, sequential ray tracing, non-sequential ray-tracing and finite difference time-domain. Sequential ray-tracing is where rays are traced through a pre-defined sequence of surfaces while travelling from the object source to the image surface, primarily used for design and analysis of imaging and afocal systems. Non-sequential ray tracing is where there is no pre-defined sequence of surfaces that the rays must hit as they are being traced. This method allows for rays to be split, scattered and reflected through optical components in any order. This makes non-sequential mode ideal for analysing stray light and illumination systems, and it predicts the real-world behaviour of systems more accurately. Finite difference time-domain software allows for micro- and nano- systems to be simulated, primarily used to predict performance of wavelength scale objects.

The phototherapy device being designed relies primarily on scattering effects of light, and as the objects (excluding the nanoparticles) are macro-scale, non-sequential ray-tracing would be the most suitable method for optical simulations. An optical design software that utilises non-sequential ray-tracing methods is Zemax OpticStudio [20], which is used primarily for the design and analysis of illumination and imaging systems.

2.3.1 Zemax simulations

OpticStudio light sources can be a point, diode, data file or user-defined type, the emission characteristics of the source can be added, as can the spectral output. A chosen number of rays can be traced from the source and a power value is given to those rays. OpticStudio uses Monte Carlo ray tracing methods to determine the power associated with a ray as it makes its way through the components. The LED described in Section 2.2.1, is supplied with Zemax rayfiles of 100,000 rays, 1 million rays and 5 million rays. The PDMS membrane can be added as a rectangular volume, 40 x 20 x 1 mm^3. This volume then has to be set as a PDMS material. OpticStudio is supplied with a vast array of material properties in the glass catalogue, most common optical system materials are available, but PDMS is not. A material can be added to the catalogue if its optical properties are known. PDMS is added to the glass catalogue using the refractive index data listed in Table 2.1, from [21]. Along with the transmission-thickness data shown in Table 2.2, from [9, 22]. OptisStudio takes these data points and creates a trend for the refractive index and transmission of light within the given wavewlengths.

Table 2.1: Table of refractive index data for PDMS used in optical simulations taken from [21]

Wavelength (nm)	Refractive index
350	1.4525
405	1.448
532	1.435
635	1.429
905	1.418
1321	1.403
1554	1.399

Table 2.2: Table of transmittance data for varying PDMS thickness used in optical simulations taken from [9, 22]

Wavelength (nm)	Transmittance (%)	Thickness (mm)
300	89.0	1.37
300	80.5	3.35
400	96.1	0.3
400	94.5	1.37
400	91.5	3.35
500	96.7	0.3
600	96.6	0.3
700	96.5	0.3
800	96.0	0.3

The PDMS membrane was coupled close to the LED, adding a 0.5 mm space to account for the lens over the LED pixel and 50 rays were added to the layout from the LED. Simulated images showing the effect of these rays, undergoing scattering, splitting and reflecting in the PDMS membrane is shown in Figure 2.4.

In OpticStudio, a virtual detector plane can be used to measure how much of the LED light is coupled in to the PDMS membrane. The LED rayfile with 5 million rays was loaded and simulations carried out using 5 million trace rays, the initial power of the rays was set to 100 mW. The power of each ray of light that crosses the detector plane is counted, and the results given as a map of irradiance over the detector area, with the peak irradiance and total power highlighted.

A detector is placed at the LED coupled end of the PDMS membrane. This detector is 20 mm long and 1 mm wide to match the size of the membrane end. The detector contains 200 x 10 pixels to measure the total power of light from the LED coupled to the PDMS membrane. The detector map is shown in Figure 2.5, the red pixels correspond to areas of high irradiance as seen in the centre of the LED, this decreases down to areas

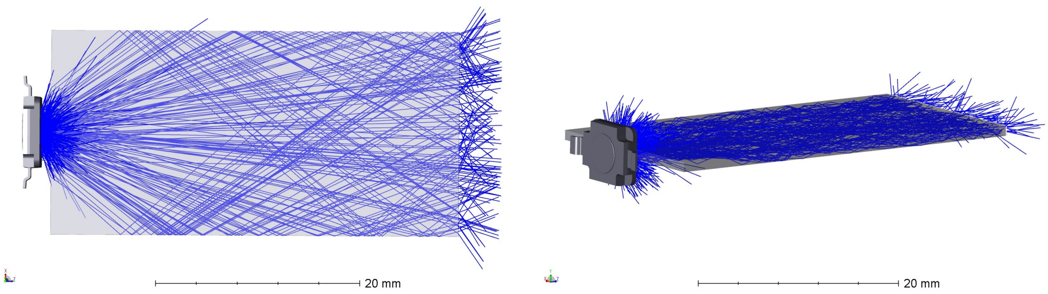

(a) (b)

Figure 2.4: Images from Zemax OpticStudios non-sequential 3D viewer with 50 rays from the LED (a) top-down view and (b) side-on view

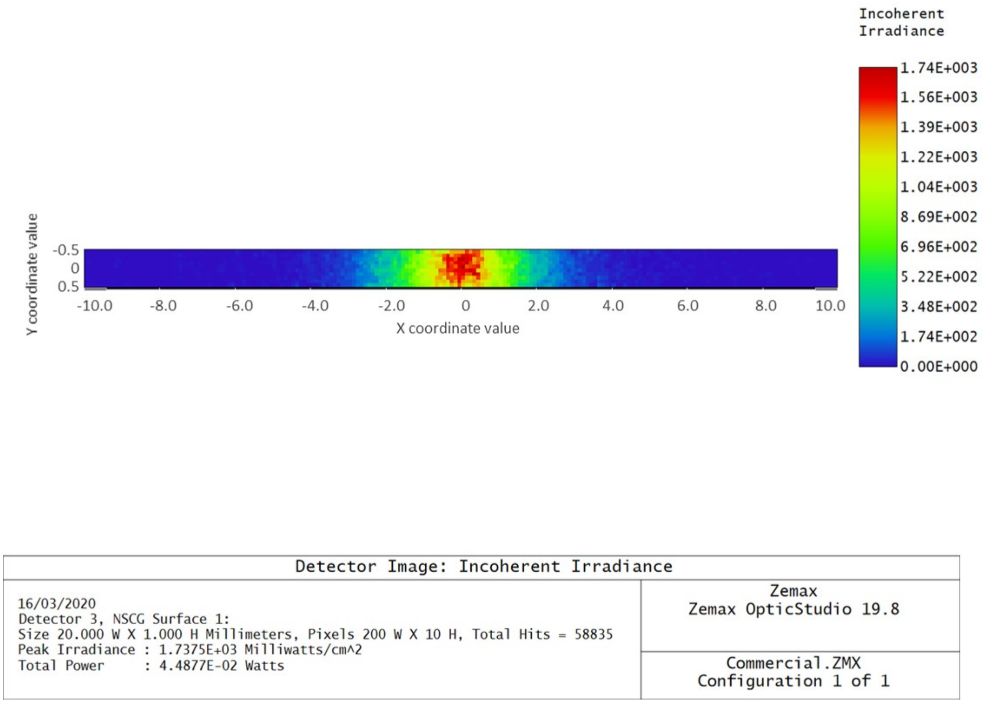

```
Detector Image: Incoherent Irradiance

16/03/2020
Detector 3, NSCG Surface 1:
Size 20.000 W X 1.000 H Millimeters, Pixels 200 W X 10 H, Total Hits = 58835
Peak Irradiance : 1.7375E+03 Milliwatts/cm^2
Total Power     : 4.4877E-02 Watts

Zemax
Zemax OpticStudio 19.8

Commercial.ZMX
Configuration 1 of 1
```

Figure 2.5: OpticStudio detector viewer of the LED light coupled to the PDMS membrane

of low/no irradiance which is represented by blue pixels. From the detector viewer, it can be seen that a total power of 45 mW is measured. Comparing the light that enters the PDMS membrane to the overall light output of the LED, it can be seen that a maximum of 45% of the LED light will be coupled into the membrane. From the detector profile it can be seen that the majority of the most intense light will be coupled into the membrane. However, less of the median intensity light will be coupled into the PDMS membrane due to it being thinner than the emissive area of the LED. This results in a large amount of LED light not being coupled into the PDMS membrane.

2.4 Experimental optical coupling

The LED described in Section 2.2.1 was coupled to the end of a 1 mm thick PDMS membrane. The experimental setup is described here in detail to measure the light scattered through the top surface of the membrane.

2.4.1 Experimental setup

The PDMS membrane was fabricated as described in Section 2.1.2 to produce a 1 mm thick slab, 40 mm long and 20 mm wide. The 20 mm wide edge of the PDMS membrane

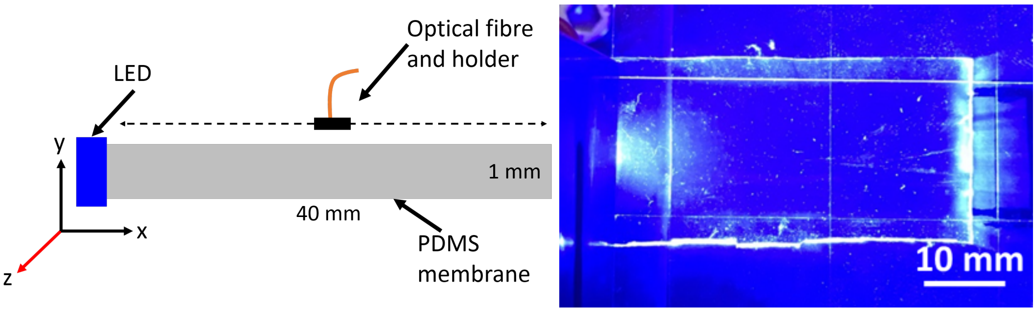

(a) (b)

Figure 2.6: (a) Schematic of experimental setup showing the coupling and how the irradiance is measured and (b) image of the edge-illuminated membrane

was placed in contact with the centre of the LED, like shown in schematic form in Figure 2.6(a). The PDMS membrane was placed on a translation platform that allows for movement in the x, y and z-direction. To avoid the PDMS sticking to the platform, glass microscope slides are used to hold the membrane. Two glass slides were used with a distance of 16 mm between them, seen in Figure 2.3(b). Only the edges of the PDMS are held, reducing the amount of lost light through the glass while keeping the PDMS flat and above the platform surface. Due to the PDMS membrane acting as a waveguide, most of the light coupled can be seen to travel directly through the device and out the other end.

The output from the top surface of the device will be measured as this is to be the emissive area. There are a number of different methods that can be used to measure light. In light therapy devices, the output light characteristic is usually given as irradiance, also called power density, typically given in units of mW/cm^2. The most popular method for measuring irradiance in light therapy literature is by using a photodiode which after absorbing a photon of sufficient energy, will generate a photocurrent proportional to the light power [23, 24]. Photodiodes are advantageous due to their ability to measure very small optical powers, however, the irradiance is crudely measured by these devices based on the sensor size. The spectral information is also not taken in to account and the sensitivity of the photodiode differs with wavelength, which may cause the power to be under- or over-estimated for broadband light sources. Another method of measuring irradiance from light sources is to use spectrometers [23]. Spectrometers can be calibrated to known light sources to then measure spectral irradiance in μW/cm^2/nm. The spectral irradiance can then be integrated over a wavelength range to calculate the irradiance in μW/cm^2. Calibration light sources are carefully characterised to deliver a known quantity of light at each wavelength with a very low uncertainty error.

The remainder of the work discussed in this thesis uses a calibrated spectrometer (OceanOptics, USB4000) to measure the irradiance of devices. The spectrometer is calibrated to a tungsten-halogen light source (OceanOptics, HL2000), itself radiometrically calibrated to a NIST standard so its absolute irradiance spectrum is known. The spectral response from 350 nm to 1150 nm is recorded using the spectrometer. The true spectral response of the light source is then uploaded to the system and the response of the spectrometer corrected to the actual irradiance output of the lamp. This produces a calibration file which is then used for every measurement, ensuring the spectrum obtained is the true absolute irradiance spectrum and therefore the irradiance can be calculated. The benefits of using this spectrometer is the small size of the collection fibre, which allows accurate irradiance measurements to be made over very small distances.

The optical fibre is positioned closely to the device surface (1 mm) and fixed in the x-axis to remain in line with the central width of the PDMS membrane. The fibre is translated in the z-direction at 1 mm intervals to measure the spectral irradiance along the device surface with increasing distance from the LED. The spectral irradiance is then integrated over the wavelengths of 400 to 500 nm to calculate the irradiance at that specific distance from the LED. These measurements were carried out using the bare optical fibre as the collection source, resulting in the measurement field of view being only 25°. In order to determine an accurate output from the surface of the device, a cosine corrector can be attached to the optical fibre. Cosine correctors are optical diffusers that have 180° field of view with a theoretical response close to Lambert's cosine law. This states that the irradiance measured will vary with respect to the cosine angle between the detector and the source. The calculation of the correction factor for the broad LED was found to be 34.77. The corrected irradiance values can then be plotted against the distance from the LED to produce a graph showing the irradiance trend. An absorbing block was placed above the PDMS membrane very close to the LED to minimise non-coupled light reaching the detector and therefore over-estimating the device output.

2.4.2 Irradiance from a PDMS membrane

The irradiance from the surface of the PDMS membrane is shown in Figure 2.7. The irradiance is an average of three PDMS membranes, each measured in triplicate, the SD of the average is also given. The mean SD of the irradiance for one membrane was found to be 6% and between the three membranes was calculated as 7%. These error values are consistent with all irradiance measurements undertaken and discussed throughout this thesis.

It can be seen that the irradiance of a PDMS membrane, injected with the broad area blue LED in an edge-lit configuration, decreases with increasing distance from the LED. Due to the size of the fibre holder and LED package, the first measurement possible

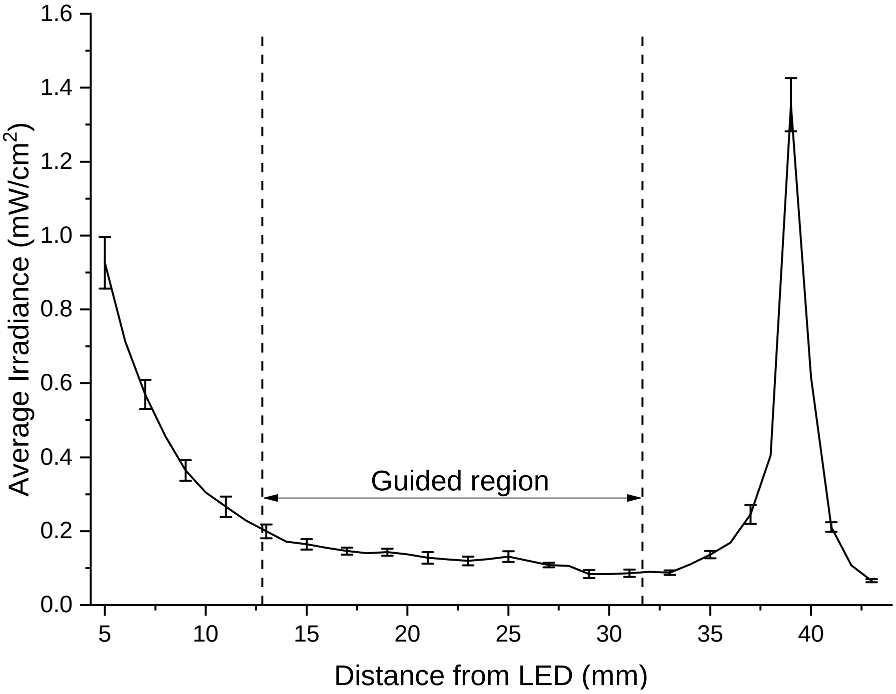

FIGURE 2.7: Average irradiance trend with increasing distance from the LED. The highlighted region is where most of the light in the waveguide is undergoing total internal reflection

is 4 mm from the coupled end of the membrane. As shown in Figure 2.7 there is a large loss of light within the first 13 mm which corresponds to leaky modes within the membrane [25]. The increase in irradiance after 37 mm is caused by edge effect. As the PDMS membrane is cut from a mould, the edges are not optically smooth, the roughness of the edges results in light exiting the membrane becoming scattered and therefore getting detected above the membrane [26]. The middle highlighted region of the irradiance graph shows a relatively low irradiance output (0.12 mW/cm^2). This region with low irradiance is where most of the light is guided in the membrane. This is the most important region of the membrane as this is where light behaves predictably, therefore it can be manipulated to allow for light extraction.

2.5 Light extraction

When light enters the edge-lit membrane, the latter acts as a slab waveguide. This means that the light undergoes total internal reflection inside the membrane as long as the refractive index of the guide is larger than that of the surrounding material. In this case, the surrounding material is air with a refractive index of 1, compared to the PDMS membrane with a refractive index of 1.42 at 460 nm [27]. In a slab waveguide, light incident at an angle larger than a certain value will not be coupled, this is called the acceptance angle α. The acceptance angle of a waveguide given in Equation 2.1 depends on the refractive index of the guide, n_1, and of the surrounding medium, n_0. The PDMS membrane has an acceptance angle of 57.7°, and a full acceptance of 115.4°. Therefore, light that enters the PDMS membrane at an angle larger than this will not be coupled.

$$sin\alpha = \sqrt{n_1^2 - n_0^2} \tag{2.1}$$

For light to undergo total internal reflection inside a waveguide, the angle of light that hits the internal surface of the guide has to be larger than the critical angle, θ_c. The critical angle also depends on the refractive index of the waveguide n_1, and the surrounding medium n_0. The critical angle equation is given in Equation 2.2. The PDMS membrane has a critical angle of 45°, therefore only light that hits the surface at an angle larger than this will undergo total internal reflection. A schematic of light in a waveguide is given in Figure 2.8(a). In order to extract light from the surface of the waveguide, the total internal reflection has to be disrupted. This can be done by adding features to the surface of the waveguide, when light hits these features the angle will change, if smaller than the critical angle, light will be extracted.

$$sin\theta_c = \frac{n_2}{n_1} \tag{2.2}$$

2.5.1 Methods of light extraction

There are multiple methods utilised to extract light from an edge-lit light guide. The most common method used in displays and automotive lighting [11, 15] is to have a diffractive pattern on the surface of the light guide. These patterned features can have a range of different designs including pyramids, cones or cylinders. These features are specially designed using optical simulation software such as Zemax OpticStudio [20]. Another method employed is to use high refractive index spherical particles inside the waveguide to scatter the light [14, 28]. These methods are shown in Figure 2.8.

The pattern extraction method is fairly common to use, however, requires a different pattern for different areas of extraction, and each of these will require a large number of processing and simulation steps to determine the ideal patterns. Using spherical particles to extract the light is an experimentally faster technique, particles can be mixed with PDMS to form extraction films that can be added to the surface of the PDMS membrane like shown in Figure 2.8(d) to extract light [29].

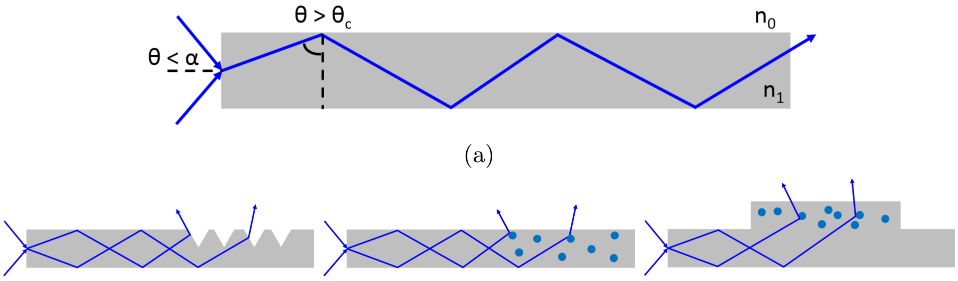

(a)

(b) (c) (d)

FIGURE 2.8: (a) Light undergoing total internal reflection in a waveguide and methods of extracting light from a waveguide; (b) extracting pattern, (c) extracting nanoparticles inside the waveguide and (d) extracting films of nanoparticles on top of the waveguide

2.6 Light extraction using TiO_2 nanoparticles

Due to the ease of adaptability, a particle extraction film will be utilised to extract light from the surface of a PDMS membrane. Titanium dioxide (TiO_2) nanoparticles are a widely used material in a range of applications, due to their high refractive index, brightness and resistance to discolouration. TiO_2 is commonly used as a pigment for example; as whiteners in paint, abrasives in cosmetics and colourants in foods [30, 31]. It is also utilised as a charge transfer material in dye sensitised solar cells due to its high electronic mobility and stability under a wide range of conditions [32]. More recently, TiO_2 has been used as a light scattering layer in organic LEDs [33, 34] due to its transparency and high refractive index.

2.6.1 TiO_2 film fabrication

TiO_2 nanoparticles averaging 20 nm in size (Sigma Aldrich) are utilised, these have a refractive index of 2.71 almost double that of PDMS at 460 nm. The nanoparticles are dispersed in liquid PDMS and mixed thoroughly to achieve a uniform matrix. The solution is then cured to produce 1 mm thick films, these are cut into regions of 15 x 15 mm^2.

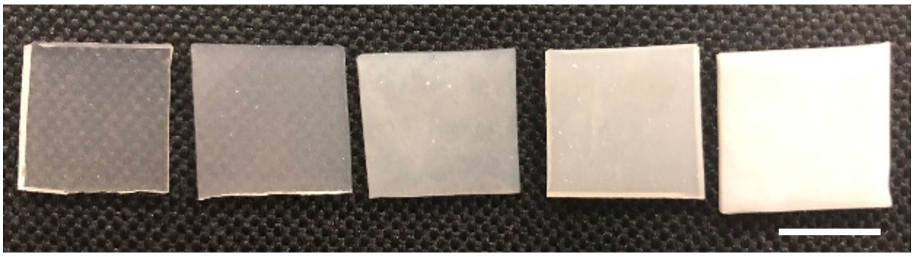

FIGURE 2.9: Image of scattering membranes with increasing nanoparticle concentration, from 0% to 2%, scale is 10 mm

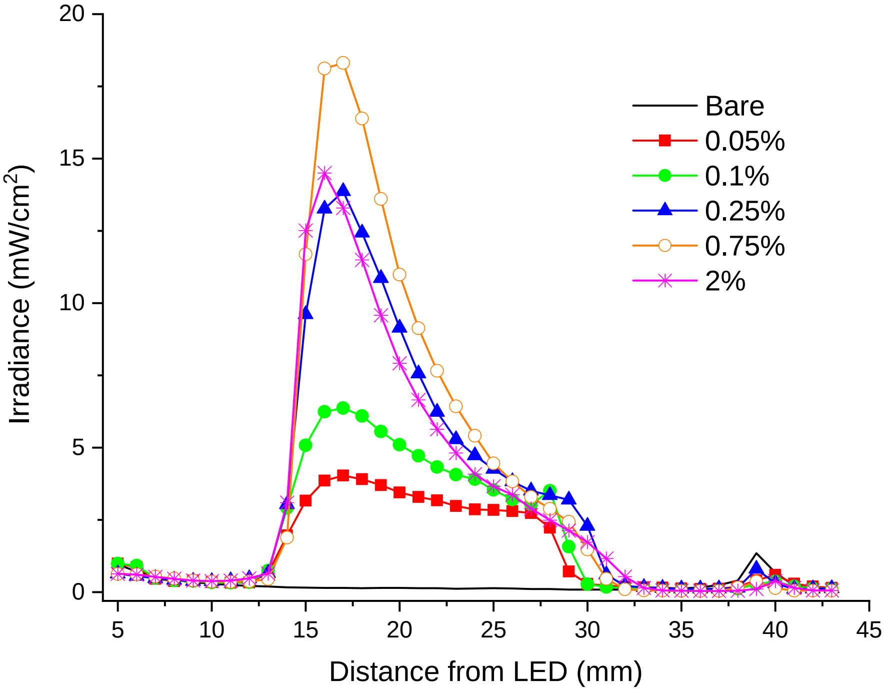

Figure 2.10: Irradiance of different scatter substrates with increasing distance from the LED, the bare PDMS irradiance is given for reference

The scatter films are fabricated with different weight ratios of TiO_2 to PDMS, ranging from 0.04% to 2%. With increasing TiO_2 concentration, the scatter film becomes more opaque due to multiple scattering, as shown in Figure 2.9. The scatter films are added to the top surface of the PDMS, at a distance of 15 mm from the LED edge and placed centrally across the width. The LED is then run at 350 mA, as before, and the irradiance measured as described in Section 2.4.1.

2.6.2 Irradiance of PDMS membrane with TiO_2 films

Figure 2.10 shows the irradiance profiles for different weight concentrations of scatter films added to the membrane surface and compared to the irradiance from the membrane alone. It can be seen that all of the scatter films cause an increase in irradiance over the emissive region from 15 to 30 mm. There is a decrease in the edge effect with the scatter substrates, this is because more light is extracted from the membrane surface. Therefore, there is less light leaving the end of the membrane. From the figure it can be seen that as the TiO_2 concentration increases, the maximum irradiance value increases until a maximum irradiance of 18 mW/cm^2 is obtained at 0.75%. At higher concentrations (e.g. 2%), the increased opacity of the films reduces the amount of extracted light, resulting in a decreased irradiance maximum. This is due to multiple scattering events taking place within the scatter substrate, reducing the intensity of the extracted light.

As well as an increased irradiance maximum, higher concentrations of TiO_2 have a steeper drop off in irradiance with increasing distance from the LED. For example, the 28 mm irradiance is 16% of the 16 mm irradiance for 0.75% TiO_2 sample, whereas this value increases to 56% for the 0.1% TiO_2 sample. It can be seen that the lower concentrations provide a more uniform irradiance over the length of the scatter substrate but lower irradiance maximum values of 4 mW/cm^2 and 6 mW/cm^2 for the 0.05% and 0.1% respectively.

2.6.3 CCD imaging

The irradiance measured with the spectrometer only considers a central linear region of the device - it does not show the trend across the whole scatter substrate. Theoretically, it would be possible to use the spectrometer and take multiple measurements across the whole scatter area, however, this would be very time-consuming. Alternatively, the irradiance over the whole scatter substrate can be seen visually and through camera images, however, this is not directly quantifiable. In order to quantify the irradiance over the whole scatter substrate, a charge-coupled device (CCD) imaging system was implemented.

Using a monochrome CCD (DCU224M, Thorlabs), an imaging lens and neutral density filters, images were taken of the scatter substrates, these images were taken with 824 x 824 pixels and represented an effective field of view of 18 x 18 mm^2. An image of

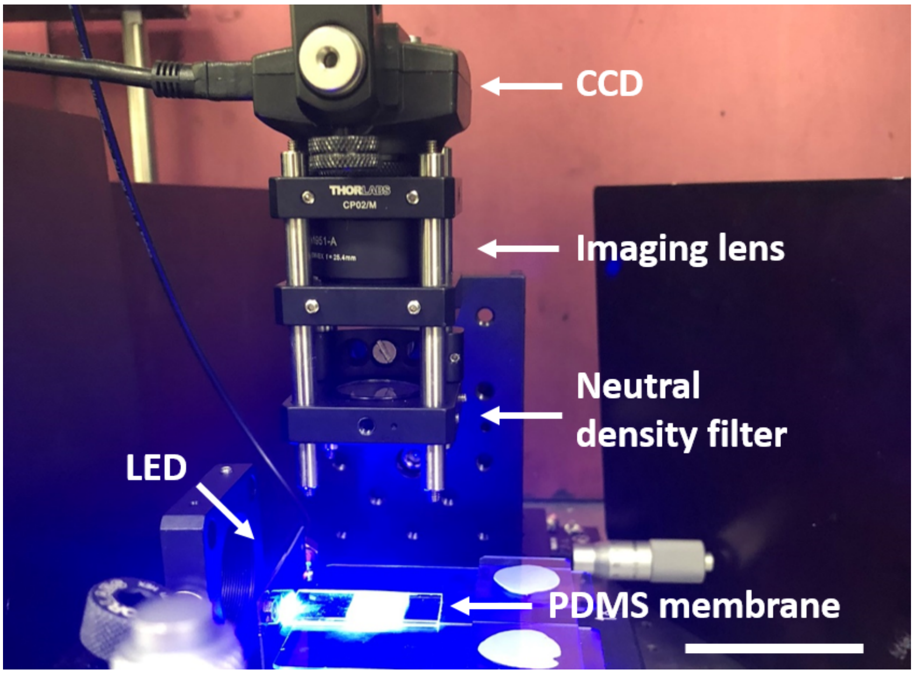

Figure 2.11: Image of the CCD imaging setup, scale is 50 mm

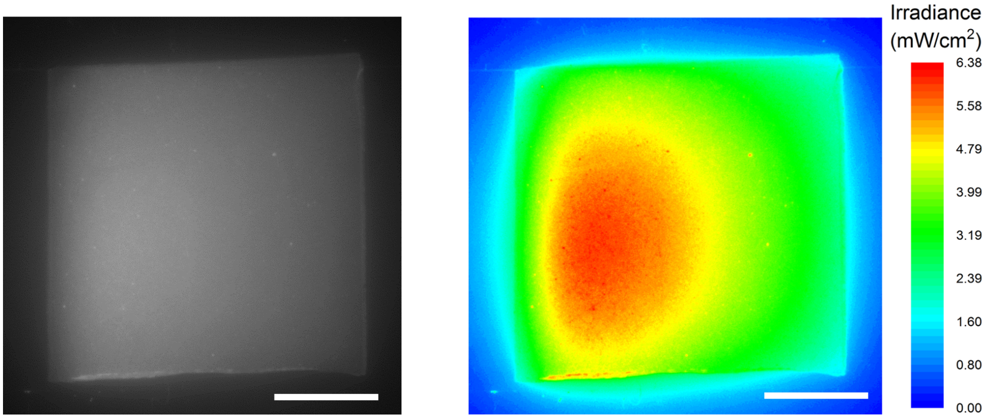

(a) (b)

FIGURE 2.12: (a) CCD image of 0.1% TiO_2 and (b) the resultant analysed irradiance map, scale is 5 mm

the setup is shown in Figure 2.11. The CCD is placed above the centre of the scatter substrate at a distance of 18 cm. This was followed by an imaging lens and neutral density filters ranging from 0.5 to 4.0. These filters were used to avoid over-saturation of the sensitive detector. The CCD settings remained constant throughout the imaging, with a gain of 0 and an exposure time of 100 ms. Each scatter substrate is imaged ten times and the resultant images averaged, ten dark images (with the LED off) are then averaged and this dark average is subtracted from the image average, producing a new image. The new images ranged in pixel intensity from 0 to 255, these intensity values were normalised to the experimentally measured irradiance results obtained with the fibre-coupled spectrometer apparatus on the same membrane. After applying this normalisation, a 2D irradiance map can be produced, wherein each pixel represents an irradiance in mW/cm^2.

Figure 2.12 shows the CCD image for the 0.1% TiO_2 sample and the resultant irradiance map for this sample. The resultant map is a colour gradient of irradiance, also called a 'heat map'. Red regions of the maps correspond to where the irradiance is highest and blue is where the irradiance is low, each map has a corresponding irradiance colour scale. The irradiance map is produced in Origin® 2018, graphing and analysis system from OriginLab®. From the irradiance maps of the scatter substrates, the power in mW associated with each pixel can be calculated. These power values can be summed to provide a total power output of light from the scatter substrate. The efficiency of the scatter substrate at extracting light through the top surface can be calculated as a percentage using the LED optical power as the initial value.

2.6.4 Irradiance maps

From the irradiance maps we can calculate the total power output of each scatter sample in mW; using this and the LED output power the extraction efficiency of the scatter samples can be calculated. This extraction efficiency is based on the total LED output power, not the light coupled into the membrane, so therefore is an underestimate of the real extraction efficiency of the scatter film. Table 2.1 contains the peak irradiance, total output power and extraction efficiency for a range of TiO_2 concentrations. The most efficient device at extracting light is the 0.75% TiO_2, which also produces the highest peak irradiance. It can also be seen that although 2% TiO_2 has a higher maximum irradiance than 0.25% TiO_2, 14.5 mW/cm^2 cf. 13.9 mW/cm^2, 0.25% has a higher extraction efficiency of 19.9% compared to 17.1%. This is due to the higher % concentrations of TiO_2 being less efficient at extracting light due to more scattering occurring inside the substrate.

Table 2.3: Table of peak irradiance values, total power output and efficiency based on an input power of 103 mW for different weight ratios of TiO_2 with SD errors

TiO_2 concentration (wt%)	Peak average irradiance (mW/cm^2)		Total power (mW)		Efficiency %	
0.04	2.3	±0.05	2.7	±0.07	2.6	±0.1
0.05	4.0	±0.05	4.4	±0.10	4.3	±0.1
0.1	6.4	±0.07	9.0	±0.19	8.7	±0.2
0.25	13.9	±0.17	18.4	±0.41	17.9	±0.4
0.75	18.3	±0.26	21.8	±0.51	21.2	±0.5
1	17.2	±0.09	20.2	±0.41	19.6	±0.4
2	14.5	±0.25	17.6	±0.43	17.1	±0.5

The irradiance maps produced for each sample show the trend in light output across the entire substrate, and allow for further comparison between the samples, the produced maps are shown in Figure 2.13. As can be seen for 0.05% the irradiance is intense over a broad region of the scatter substrate width and length which decreases with increasing distance from the LED. The intense region of the 0.1% TiO_2 is smaller than that of the 0.05% in both length and width, this decreasing trend is seen with increasing concentration. The regions of high and medium irradiance decrease in size, proving the decreased uniformity with increased concentration.

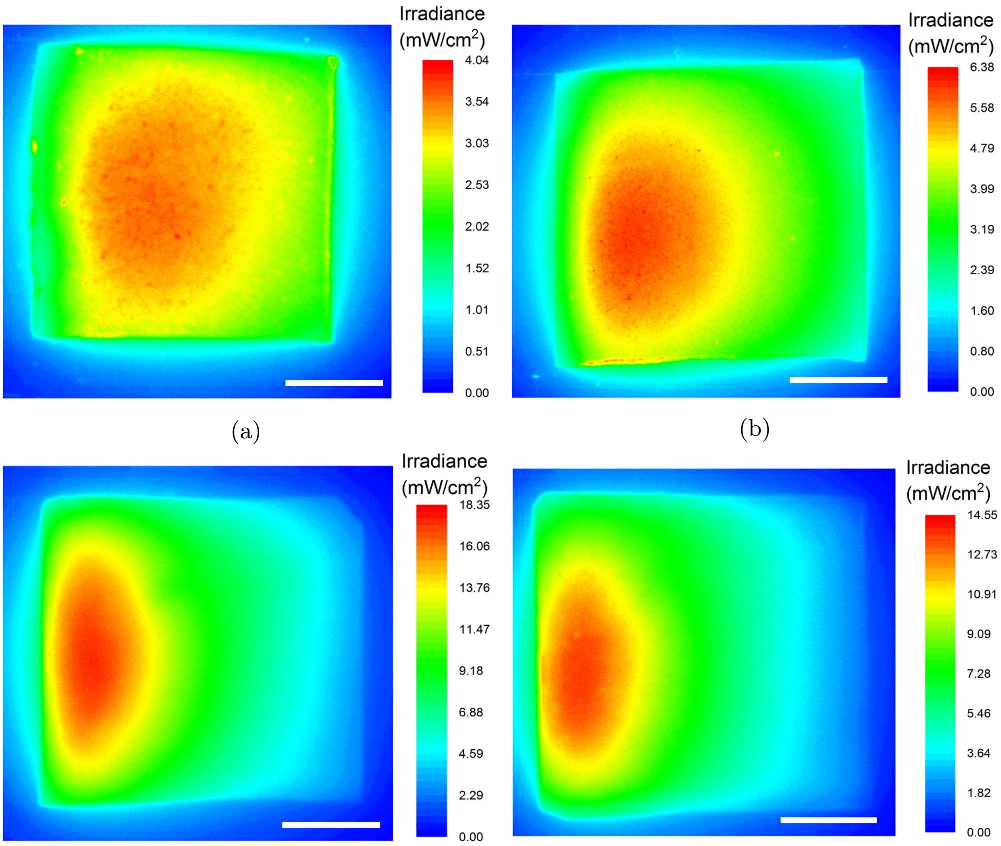

(a) (b)

(c) (d)

FIGURE 2.13: Irradiance maps of TiO_2 scatter substrates (a) 0.05%, (b) 0.1%, (c) 0.75% and (d) 2%, the maps represent an intensity gradient with red regions producing highest irradiance and blue regions refer to low irradiance values, scale is 5 mm

2.7 Uniform irradiance

Although the scattering films extract light from the PDMS membrane, the output emission is non-uniform. In order to obtain uniform emission, the scatter substrate has to increase the probability of light scattering out of the membrane with increasing distance from the LED.

2.7.1 Methods for uniform light extraction

For uniform light extraction from an edge-lit membrane, the extraction features have to increase in density or frequency with increasing distance from the light source [15, 35]. A similar effect can be obtained by decreasing the thickness of the waveguide with increasing distance from the LED [16].

To obtain uniform extraction from the TiO_2 films, the size of the nanoparticles could be increased with increasing distance from the LED. This would be difficult to achieve

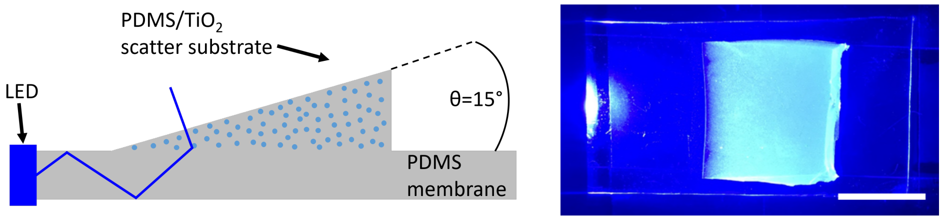

(a) (b)

FIGURE 2.14: (a) Schematic showing the tapered scatter substrate effect and (b) image of the tapered 0.05% TiO_2 scatter film on the PDMS membrane, scale is 10 mm

without specially fabricating the nanoparticles; there is not a large size range of commercially available TiO_2 particles. Another method would be to increase the density of nanoparticles with increased distance from the LED. This could be done by producing an increasing gradient in the concentration of TiO_2 in the extraction substrates, which is the chosen approach in our final device design as reported in Section 3.6. Another method could be increasing the thickness of the extraction substrate with increasing distance from the LED, producing a tapered substrate. This was the method we chose to use initially.

2.7.2 TiO_2 tapered scatter substrate fabrication

For initial testing, tapered extraction substrates were fabricated. In order to fabricate tapered substrates, the PDMS/TiO_2 matrix was produced as before, however, it was left to cure at an angle of 15° to produce a substrate that increases in thickness along the length, from 0.5 mm to a maximum of 4 mm. This angle was chosen as it was easy to reproduce in in the laboratory using available equipment. This was carried out on the lower concentrations of TiO_2, as these naturally were more uniform than the high concentration samples. A schematic of the method and an image of a 0.05% TiO_2 tapered substrate on the membrane are shown in Figure 2.14. The tapered substrate was added to the PDMS membrane in the same format as the flat substrates. Relying on the tacky nature of PDMS to hold the substrate in place.

2.7.3 TiO_2 tapered scatter substrate irradiance

Tapered scatter substrates of 0.04, 0.05 and 0.1% were fabricated and added to the top surface of the membrane, with the thinnest end closest to the LED as shown in Figure 2.14. Irradiance measurements were then carried out as described in Section 2.6.2 and the irradiance results from these samples compared to the bare membrane are given in Figure 2.15. Throughout this thesis, the uniformity is measured using the irradiance

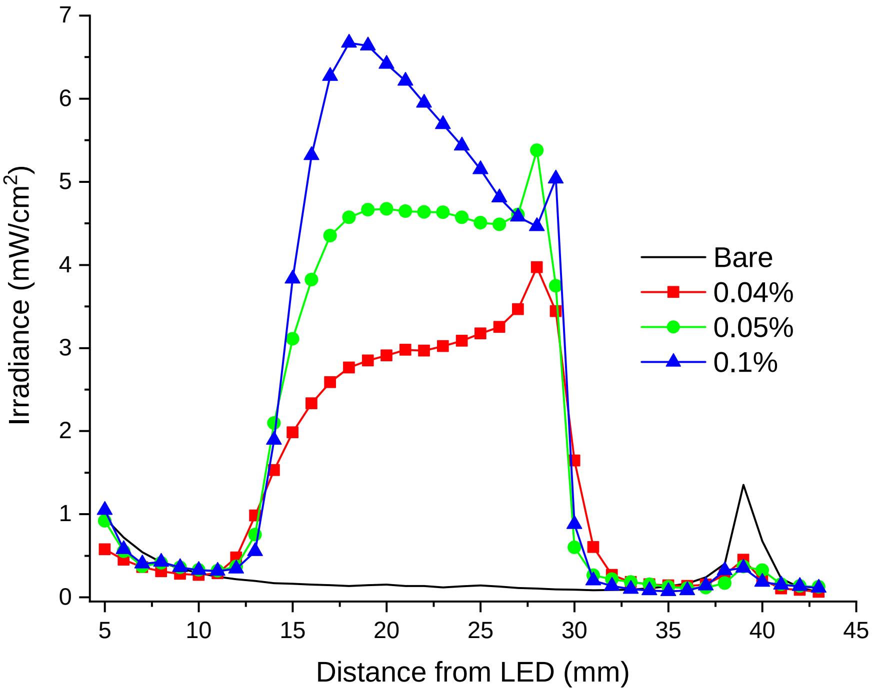

FIGURE 2.15: Irradiance of different tapered scatter substrates with increasing distance from the LED, the bare PDMS irradiance is given for reference

profile of the devices. The region of the scatter substrates, from 15 mm to 30 mm is identified and the central field of view is utilised. The uniformity is then measured as the average irradiance over 75% of the data points in this region, with the error being the SD of this value.

From these results we can see that a taper angle of 15° results in a maximum irradiance of 3.9 mW/cm^2 at the far end of the substrate, for the 0.04% sample. This value is relatively low while the irradiance trend increases across the length of the scatter substrate. From these results, using a smaller taper angle over the length of scatter substrate would result in a more uniform irradiance profile, however, the irradiance values are deemed too low for effective use. We can see that a curing angle of 15° is too low for 0.1% TiO_2. The irradiance reaches a maximum close to the LED, then decays similar to the trend seen with the flat scatter substrate. The increase in irradiance at the end of the substrate is due to the roughly cut surface scattering more light which is recorded above the device. An angle of 15° is an ideal angle for obtaining uniform emission from a 0.05% TiO_2 sample, here the irradiance is virtually uniform at 4.5 ± 0.8 mW/cm^2 over the entire length of the scatter substrate excluding the end where we again see a peak due to edge effect.

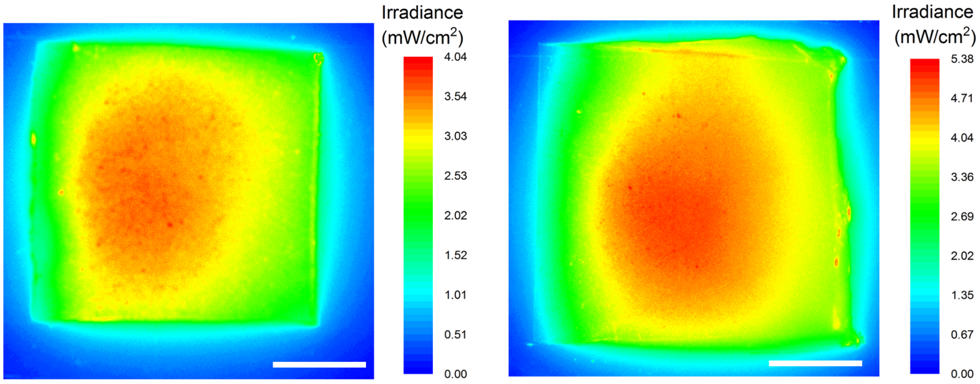

(a) (b)

Figure 2.16: Irradiance maps of the (a) 0.05% TiO_2 flat scatter substrate and (b) 0.05% TiO_2 tapered scatter substrate cured at an angle of 15°, scale is 5 mm

2.7.4 Irradiance maps of tapered substrates

Images of the tapered samples were taken with the CCD setup to produce irradiance maps and to determine the total power output from the substrates, these are compared to the flat samples in Table 2.4. It can be seen that for each of the concentrations of TiO_2, the tapered samples produce an increase in extraction efficiency of at least 2%.

Comparing the irradiance maps of the 0.05% TiO_2 samples, both the flat sample (cured at 0° angle) and the tapered sample (cured at 15°), it can be seen that the area of high irradiance is larger with the tapered sample. It can also be seen that the irradiance is more centralised over the entire scatter substrate. However, a lot of light is lost at the edges of the scatter substrate, this is due to both the increased thickness and the rough surface edges caused by cutting it to shape with a scalpel.

Table 2.4: Table of peak irradiance values, total power output and efficiency based on an input power of 103 mW for the tapered scatter substrates of different TiO_2 concentrations compared to the flat samples with SD errors

Curing angle °	TiO_2 concentration (wt%)	Peak average irradiance (mW/cm^2)		Total power output (mW)		Efficiency %	
15	0.04	3.9	± 0.05	4.8	±0.20	4.6	± 0.2
0	0.04	2.3	±0.05	2.7	±0.07	2.6	±0.1
15	0.05	5.3	±0.21	8.6	±0.40	8.4	±0.4
0	0.05	4.0	±0.05	4.4	±0.10	4.3	±0.1
15	0.1	6.7	±0.05	11.1	±0.45	10.7	±0.5
0	0.1	6.4	±0.07	9.0	±0.19	8.7	±0.2

2.8 Discussion

Although a uniform irradiance of 4.5 mW/cm^2 can be obtained with the tapered scatter substrate it still corresponds to a low extraction efficiency with a large portion of light being lost at the sides and end of the tapered substrate. Theoretically the extraction efficiency is likely higher than that calculated as not all of the LED light is coupled into the membrane due to the size disparity and emission profile of the LED. From the optical simulations it was shown that a maximum of 45% of the LED light will be coupled in to a 1 mm thick membrane. A smaller LED would allow for more light to be coupled into the membrane and hence increase the extraction efficiency. A smaller LED would also require a smaller package, the commercial LED utilised requires a large heat sink and power star for energy efficiency and to extend its operational life.

The technique for producing uniform emission with the tapered scatter substrate, although effective, is not very efficient and it also increases the thickness of the elastomeric region of the device 5-fold, from 1 mm to 5 mm. The increased thickness also decreases the flexibility of the device making it less wearable. Other extraction methods with scattering particles could be used to produce uniform emission, for example, changing the size of the particles with increased distance from the LED, as the size of the particles increases the light is more likely to be scattered. The effect of the tapered substrates is to increase the density of scattering particles with increased distance from the LED, this could be obtained by increasing the concentration of nanoparticles with increasing distance from the LED (i.e. a concentration gradient). The benefit of this is that a uniform thickness of 1 mm or less could be utilised allowing for an overall thinner device subject to the identification and fabrication of the gradient.

2.9 Summary

In this Chapter, the potential of an LED-based elastomeric membrane for uniform emission has been demonstrated. The fabrication of the PDMS membrane and the properties of a broad LED were described. Optical design software was utilised to estimate that a maximum of 45% of LED light can in principle be coupled to the PDMS membrane with the broad LED device used in this first validation of the platform. The experimental techniques utilised to characterise the elastomeric membranes were explained in detail. The effect of scattering nanoparticle concentration on the output emission is discussed with an increased TiO_2 concentration resulting in a higher irradiance output and extraction efficiency, however, causing a decrease in the uniformity of the 15 x 15 mm^2

emission area. By fabricating tapered scatter substrates to produce an increased probability of light scattering with increased distance from the LED, uniform irradiance of 4.5 mW/cm^2 can be obtained from the scatter substrate, resulting in an overall device efficiency of 8% based on the LED output power of 103 mW.

The effectiveness of the edge-illuminated technique has been demonstrated, and the discussion highlights the improvements that could be made to ensure the wearability of the device, this will be explored throughout the rest of this thesis.

References

[1] C. A. Harper, *Handbook of plastics, elastomers, and composites*, vol. 4. McGraw-Hill New York, 2002.

[2] C. Hepburn, *Polyurethane elastomers.* Springer Science & Business Media, 2012.

[3] F. Duvalsaint and A. L. Moore, "Process for producing fluorelastomers," Aug. 21 2001. US Patent 6,277,937.

[4] W. Noll, *Chemistry and technology of silicones.* Elsevier, 2012.

[5] P. C. Nicolson and J. Vogt, "Soft contact lens polymers: an evolution," *Biomaterials*, vol. 22, no. 24, pp. 3273–3283, 2001.

[6] S. H. Kim, J.-H. Moon, J. H. Kim, S. M. Jeong, and S.-H. Lee, "Flexible, stretchable and implantable PDMS encapsulated cable for implantable medical device," *Biomedical Engineering Letters*, vol. 1, no. 3, p. 199, 2011.

[7] V. Gubala, L. F. Harris, A. J. Ricco, M. X. Tan, and D. E. Williams, "Point of care diagnostics: Status and future," *Analytical Chemistry*, vol. 84, no. 2, pp. 487–515, 2012.

[8] D. C. Duffy, J. C. McDonald, O. J. Schueller, and G. M. Whitesides, "Rapid prototyping of microfluidic systems in poly (dimethylsiloxane)," *Analytical chemistry*, vol. 70, no. 23, pp. 4974–4984, 1998.

[9] W. Li and G. Huber, "Optical characterization of RTV615 silicone rubber compound," *Journal of Instrumentation*, vol. 9, no. 07, p. P07012, 2014.

[10] "Momentive RTV615 silicone." `https://www.techsil.co.uk/momentive-rtv615-11lb`. Accessed: 22-02-2020.

[11] G. Harbers, W. Timmers, and W. Sillevis-Smitt, "LED backlighting for LCD HDTV," *Journal of the Society for Information Display*, vol. 10, no. 4, pp. 347–350, 2002.

[12] T.-C. Teng and M.-F. Kuo, "Highly precise optical model for simulating light guide plate using LED light source," *Optics express*, vol. 18, no. 21, pp. 22208–22214, 2010.

[13] T. Okumura, A. Tagaya, Y. Koike, M. Horiguchi, and H. Suzuki, "Highly-efficient backlight for liquid crystal display having no optical films," *Applied physics letters*, vol. 83, no. 13, pp. 2515–2517, 2003.

[14] B.-Y. Joo, J. J. Kang, and J.-P. Hong, "Analysis of the light-scattering power of patterned dot material printed on the light guide plate in liquid crystal display," *Displays*, vol. 33, no. 4-5, pp. 178–185, 2012.

[15] J.-G. Chang and Y.-B. Fang, "Dot-pattern design of a light guide in an edge-lit backlight using a regional partition approach," *Optical Engineering*, vol. 46, no. 4, p. 043002, 2007.

[16] C.-J. Li, Y.-C. Fang, and M.-C. Cheng, "Study of optimization of an LCD light guide plate with neural network and genetic algorithm," *Optics express*, vol. 17, no. 12, pp. 10177–10188, 2009.

[17] M. Kim, M. Kim, J. Hwang, C. Joo, J. Kang, and Y. Kim, "A light guide plate based flexible optical cuff for optogenetic stimulation of motor units," in *2015 Transducers-2015 18th International Conference on Solid-State Sensors, Actuators and Microsystems (TRANSDUCERS)*, pp. 1653–1656, IEEE, 2015.

[18] "Osram Semiconductors." `https://www.osram.com`. Accessed: 23-01-2020.

[19] E. F. Schubert, *Light-Emitting Diodes.* Cambridge University Press, second ed., 2006.

[20] "Zemax OpticStudio." `https://www.zemax.com/products/opticstudio`. Accessed: 22-01-2020.

[21] F. Schneider, J. Draheim, R. Kamberger, and U. Wallrabe, "Process and material properties of polydimethylsiloxane (PDMS) for optical MEMS," *Sensors and Actuators A: Physical*, vol. 151, no. 2, pp. 95–99, 2009.

[22] G. S. Rajan, G. S. Sur, J. E. Mark, D. W. Schaefer, and G. Beaucage, "Preparation and characterization of some unusually transparent poly (dimethylsiloxane) nanocomposites," *Journal of Polymer Science Part B: Polymer Physics*, vol. 41, no. 16, pp. 1897–1901, 2003.

[23] M. A. Hadis, S. A. Zainal, M. J. Holder, J. D. Carroll, P. R. Cooper, M. R. Milward, and W. M. Palin, "The dark art of light measurement: accurate radiometry for low-level light therapy," *Lasers in medical science*, vol. 31, no. 4, pp. 789–809, 2016.

[24] I. Sinclair, *Electronics Simplified.* Newnes, third ed., 2011.

[25] R. G. Hunsperger, "Acousto-optic modulators," in *Integrated Optics*, pp. 201–220, Springer, 2009.

[26] I. L. Fabelinskii, "Molecular scattering of light," in *Molecular Scattering of Light*, pp. 483–532, Springer, 1968.

[27] Z. Cai, W. Qiu, G. Shao, and W. Wang, "A new fabrication method for all-PDMS waveguides," *Sensors and Actuators A: Physical*, vol. 204, pp. 44–47, 2013.

[28] A. Colombo, F. Tassone, F. Santolini, N. Contiello, A. Gambirasio, and R. Simonutti, "Nanoparticle-doped large area PMMA plates with controlled optical diffusion," *Journal of Materials Chemistry C*, vol. 1, no. 16, pp. 2927–2934, 2013.

[29] J.-Y. Zhang, J. R. Baran Jr, T. L. Smith, W. J. Schultz, W. B. Kolb, C. A. Patnaude, S. A. Lamansky, B. K. Nelson, N. Jing, B. U. Kolb, *et al.*, "Light extraction film with nanoparticle coatings," June 7 2011. US Patent 7,957,621.

[30] A. Weir, P. Westerhoff, L. Fabricius, K. Hristovski, and N. von Goetz, "Titanium dioxide nanoparticles in food and personal care products," *Environmental Science & Technology*, vol. 46, no. 4, pp. 2242–2250, 2012. PMID: 22260395.

[31] Y. Dan, H. Shi, C. Stephan, and X. Liang, "Rapid analysis of titanium dioxide nanoparticles in sunscreens using single particle inductively coupled plasma–mass spectrometry," *Microchemical Journal*, vol. 122, pp. 119 – 126, 2015.

[32] R. Govindaraj, M. S. Pandian, P. Ramasamy, and S. Mukhopadhyay, "Sol-gel synthesized mesoporous anatase titanium dioxide nanoparticles for dye sensitized solar cell (DSSC) applications," *Bulletin of Materials Science*, vol. 38, no. 2, pp. 291–296, 2015.

[33] H.-W. Chang, K.-C. Tien, M.-H. Hsu, Y.-H. Huang, M.-S. Lin, C.-H. Tsai, Y.-T. Tsai, and C.-C. Wu, "Organic light-emitting devices integrated with internal scattering layers for enhancing optical out-coupling," *Journal of the Society for Information Display*, vol. 19, no. 2, pp. 196–204, 2011.

[34] D. Riedel, T. Wehlus, T. C. Reusch, and C. J. Brabec, "Polymer-based scattering layers for internal light extraction from organic light emitting diodes," *Organic Electronics*, vol. 32, pp. 27 – 33, 2016.

[35] Y. C. Kim, "Optimize pattern design for the thin LGP," *Optik*, vol. 124, no. 15, pp. 2171–2173, 2013.

Chapter 3

Micro-LED results

In this chapter a μLED array is utilised as the source in the edge-lit PDMS membrane. The small size of the source allows for more light to be coupled to a PDMS membrane 1 mm thick or less. The extraction effect of different concentrations of TiO_2 scatter substrates is measured and compared to the results of the same substrates using the broad LED as the source. Scatter substrates with a gradient in concentration were designed, and bonded to the PDMS membrane in an effort to produce uniform emission from a thin device. Lastly, a method of obtaining a suitable concentration gradient for different lengths of scatter substrates is discussed to allow for uniform emission over larger areas.

3.1 Micro-LED design and properties

The broad LED was effective in showing the device proof of concept, however, the large size of the LED reduces the wearability of the device. In order to design a thin, flexible device that couples the majority of the source light, micro-sized LEDs (μLEDs) can be utilised. As described in Chapter 1, these are devices that have at least one dimension smaller than 100 μm and can be fabricated into a variety of pixel shapes and sizes [1, 2]. Micro-LEDs can be driven at higher current and optical power densities than conventional broad-area LEDs [3]. Consequently, they are promising for applications that benefit from high intensity light, e.g. displays and projection [2]. A further benefit of the high current density is a reduction of the carrier lifetime making micro-LEDs an attractive source for high speed data transmission using visible light, i.e. visible light communications (VLC) [4, 5]. The small size and high current density of micro-LEDs, make them promising sources for small scale applications such as neural stimulation [6] and optical cochlear implants [7]. The small size and high optical power density of

μLEDs also make them an ideal source for a wearable phototherapy device as is shown here.

3.1.1 Design and fabrication of μLED

The μLEDs were designed as linear arrays of pixels and two different designs were produced. Design A consists of ten pixels, 100 x 100 μm^2, with a pitch of 720 μm. Design B consists of forty 100 x 100 μm^2, in two rows of twenty, with a 360 μm pitch and a 30 μm spacing between the two rows. In the centre of the device on either side of the pixels, are two large contact pads for wire bonding to a printed circuit board (PCB). These designs were chosen as thin, long sources to couple as much light as possible into the thin PDMS membrane. The final design consisted of three devices, two of device A and one of device B.

The designed devices are flip-chip, which means they emit through the sapphire substrate. As the light is emitted through the sapphire, the overall pixel size is increased to account for the scattering through the sapphire. The emissive area has been shown as dependent on the thickness of the sapphire layer [8]. The 300 μm thick sapphire layer here results in the pixel size through the sapphire surface being closer to 300 x 300 μm^2. This is also shown in the optical simulations of the μLED design in Section 3.2. It is possible to thin the sapphire layer to 150 μm and maintain the same fabrication process. This would result in a smaller emissive area for each pixel, resulting in more light being coupled to the thin membrane.

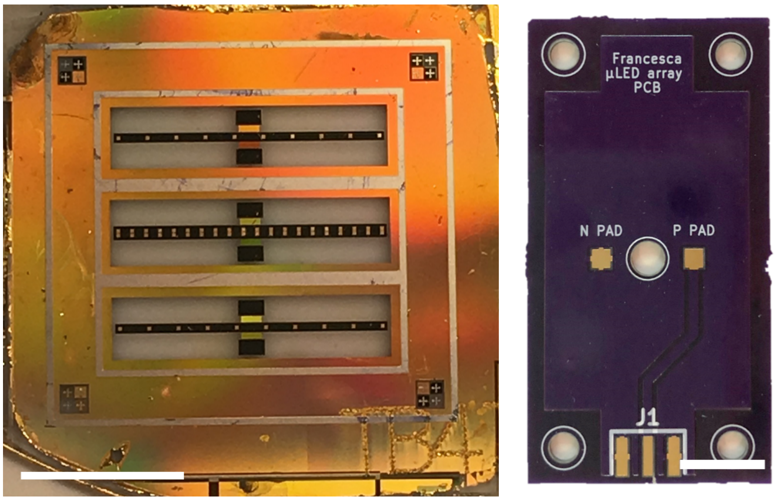

(a) (b)

FIGURE 3.1: (a) Image of the fabricated μLED devices before they were diced into the separate arrays, the image is taken of the gold contact side, not the emissive sapphire side, scale is 5 mm and (b) Image of the PCB designed for the μLED arrays, scale is 10 mm

A photomask was produced with the different layers required for etching and depositing of materials to fabricate the μLED devices. The devices were fabricated on a GaN on sapphire wafer, with the fabrication steps described in Section 1.8.1. An image of the final devices before they were diced is given in Figure 3.1(a), with the gold contact side facing upwards. The devices were diced to produce three individual μLED arrays.

3.1.2 PCB design

To power the μLED a PCB was designed using KiCAD [9]. The PCB was 25 x 50 mm^2 to allow the μLED device to be easily and accurately held in place in an optical setup, an image of the PCB is given in Figure 3.1(b). The PCB is one-sided and consists of p-type and n-type ohmic contact pads, each 2 x 2 mm^2, these are wire bonded to the equivalent device contact. The PCB is made from copper due to its high conductivity and the contacts are electroless nickel immersion gold (ENIG) which is corrosion resistant and an effective surface for both wire bonding and soldering. The PCB surface is connected to the n-type contact pad, down to the two outer prongs of an edge SMA connector. The p-type contact is connected to the middle SMA prong via an isolated track through the circuit board.

The designed PCBs were purchased from OshPark [10], the resultant boards were 1.6 mm thick, 25 mm wide and 50 mm long with a layer of 1 oz copper as the current spreader. The μLED is glued on to the underside of the PCB using a transparent epoxy with the sapphire side facing out, the contacts are then wire bonded to the corresponding pads on the PCB with three wires to spread the current and avoid wire-burnout. The delicate wire bonds are then protected with a small glass coverslip tacked on to the PCB, alternatively the bonds can be protected by a polymer.

3.1.3 Micro-LED properties

The electrical properties of the devices on the PCBs were determined. Both device A arrays switched on, with a turn-on voltage of 2.9 V, device B did not work under any supplied power. It is suspected that during dicing, the contact metal tracks on device B that allow for the current to spread along the pixels were bent, causing a short circuit to occur. No further testing could be carried out on device B. An image of both design A devices with a 5 mA supply current is given in Figure 3.2. It can be seen that not all of the pixels are responsive in device A1. There are five bright pixels, three less bright and two very dim. This is thought to be due to poor contact issues with the thin metal connector tracks. Device A2 consisted of 10 fully responsive pixels as seen in Figure 3.2(b). As device A1 still worked, it was utilised for experimental testing, with

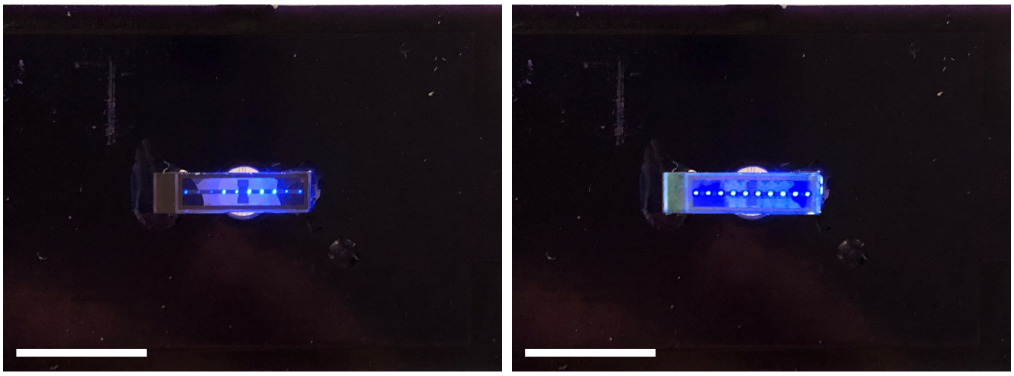

(a) (b)

Figure 3.2: Images of the array A devices with a 5 mA supply current, (a) device A1 and (b) device A2, scale is 10 mm

device A2 being saved for a potential prototype device and as a backup device in case A1 was broken. Device A1 has fewer working pixels and the majority of light is centred in the middle of the device. Device A2 has all pixels working and all have similar pixel intensity values. Therefore, device A2 will likely produce a more uniform emission across the width of an extraction substrate than device A1. This may not be noticeable with the 1 cm wide extraction substrate, but could potentially produce more uniform light across the width of a wider substrate. This has to be taken into account with the given results. With a fully working μLED device, the irradiance will have increased unifomity across the width of the emissive area.

The μLED device A1 was added to the setup described in Section 2.2.2 and the electrical and optical properties recorded. The device was run at increasing current values from 10 to 500 mA, the voltage and output optical power at each current was recorded and the results given in Figure 3.3(a). The device has a turn on value of 2.9 V, and the output optical power ranges from 1 mW at 10 mA to 22 mW at 450 mA, after this

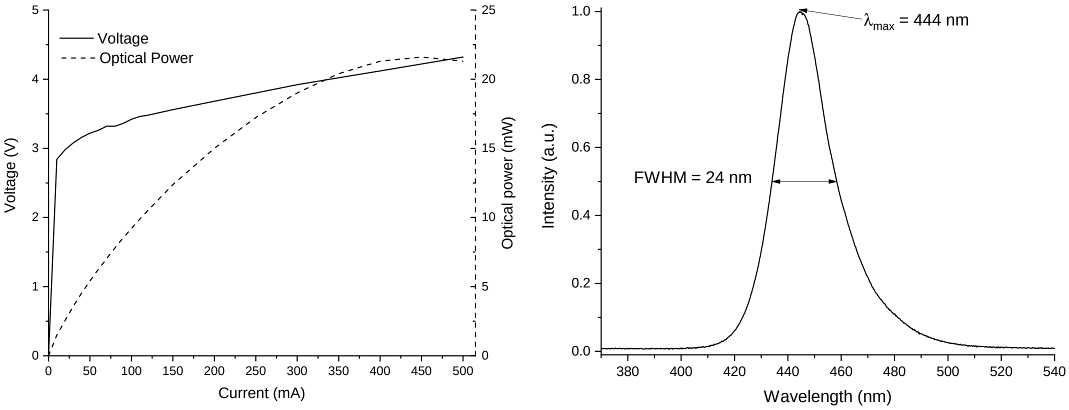

(a) (b)

Figure 3.3: μLED electronic and spectral properties (a) LIV data (b) wavelength spectrum of the μLED run at a current of 110 mA

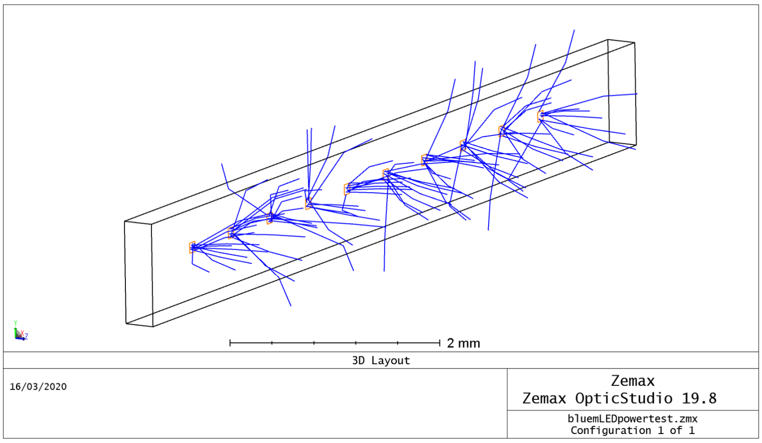

FIGURE 3.4: Simulation of the μLED device in OpticStudio, each pixel is shown with 10 trace rays inside a 300 μm thick sapphire substrate

current, thermal rollover occurs. In order to allow for easy comparison to the broad LED, the input current to the device was set at 120 mA producing an output optical power of 10 mW. Figure 3.3(b) shows the spectral response of the μLED at 120 mA. As can be seen, the device has a peak wavelength of 444 nm, resulting in a blue light output, with a full-width half-maximum (FWHM) of 24 nm.

3.2 Simulated optical coupling of μLED

The μLED device was added to the optical simulation discussed in Section 2.3.1. The device was simulated as an array of LED pixels (100 x 100 μm^2) with a spacing of 720 μm. The emission profile from the pixels was set as a Lambertian source [11]. These pixels were placed in contact with a sapphire rectangular volume (10 x 1 x 0.3 mm^3). A 3D OpticStudio render of this device with 10 trace rays from each pixel is shown in Figure 3.4. The device was placed with the sapphire in contact with the 1 mm thick PDMS membrane. Each pixel was set to have an optical power of 2.5 mW, producing a total output optical power of 21 mW through the main surface of the sapphire substrate. The remaining 4 mW is reflected within the sapphire substrate and not coupled out through the top surface. For the raytrace, the pixels were set to have 500,000 trace rays each so the total number of trace rays (5 million) matched that of the broad LED.

A detector was added to the PDMS surface, in contact with the sapphire substrate and a raytrace carried out. A detector map is shown in Figure 3.5. The red pixels correspond to areas of high irradiance while the blue pixels correspond to areas of low/no irradiance. From the detector viewer it can be seen that a total power of 18.45 mW is coupled into the PDMS membrane. With an output power of 21 mW through the sapphire surface, this provides a coupling efficiency of 88%. Much higher than the coupling efficiency for

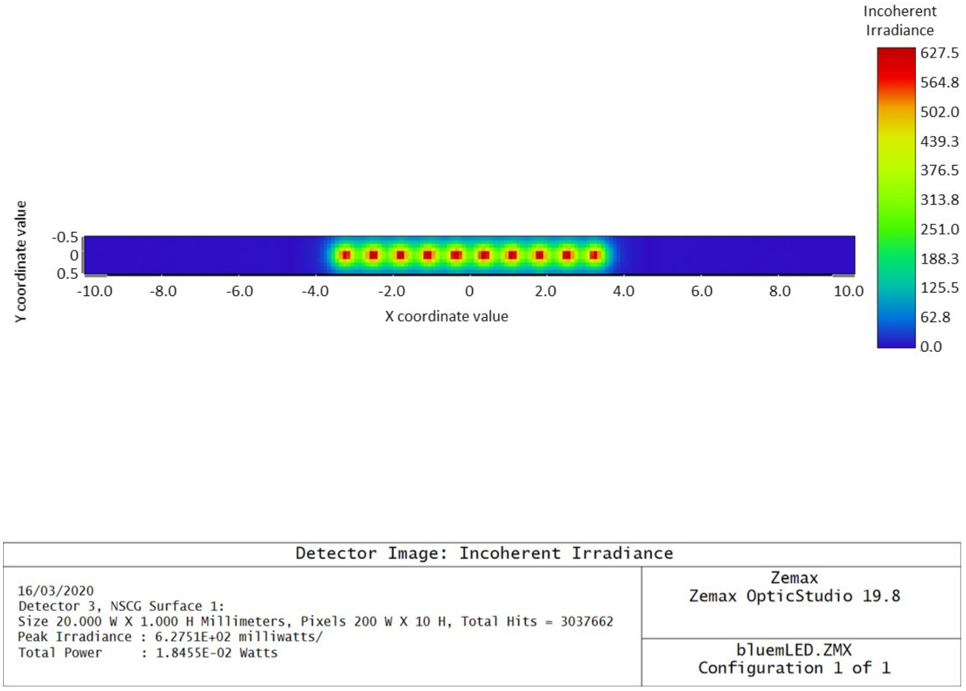

```
Detector Image: Incoherent Irradiance

16/03/2020
Detector 3, NSCG Surface 1:
Size 20.000 W X 1.000 H Millimeters, Pixels 200 W X 10 H, Total Hits = 3037662
Peak Irradiance : 6.2751E+02 milliwatts/
Total Power     : 1.8455E-02 Watts

Zemax
Zemax OpticStudio 19.8

bluemLED.ZMX
Configuration 1 of 1
```

FIGURE 3.5: OpticStudio detector viewer of the μLED light coupled to the PDMS membrane

the broad LED (45%). This is due to the small pixel size, as can be seen in the detector viewer, all of the intense light and most of the less intense light is coupled into the PDMS membrane.

3.3 Coupling μLED and PDMS membrane

The μLED array is mounted on a 3-axis translation stage and the PDMS membrane is butt-coupled directly to the sapphire side of the array, an image of the setup is shown in Figure 3.7(a). To ensure the device is coupled centrally to the membrane the optical fibre, described in Section 2.4.1, is fixed above the membrane 40 mm from the μLED. The height of the μLED array is then adjusted until a maximum irradiance is measured. The irradiance is measured at one μLED position in height with respect to the membrane input and then the height is adjusted until a maximum is obtained. The μLED is then placed in contact with the membrane when irradiance is maximised. This maximum corresponds to a maximum amount of light being coupled in the membrane. This coupling test was carried out every time the PDMS membrane was removed from the setup.

The irradiance trend of the bare PDMS is given in Figure 3.7(b). This is very similar to the irradiance trend seen with the broad LED in Chapter 2. A maximum irradiance is

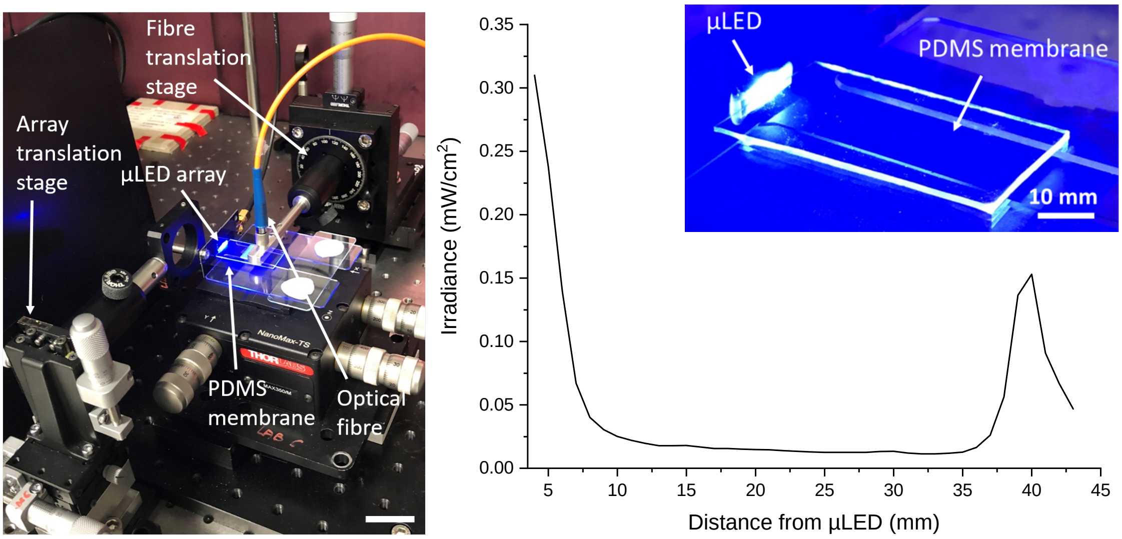

(a) (b)

Figure 3.6: (a) Image of the μLED irradiance setup, scale is 25 mm. (b) Irradiance trend of a bare PDMS membrane with increasing distance from the μLED, inset is an image of the μLED device coupled to the PDMS membrane

measured close to the LED that is due to non-guided light leaking from the membrane. This non-guided light interacts at the surface between the PDMS and air at an angle smaller than the critical angle, resulting in the light exiting the membrane [12, 13]. After 35 mm (from the μLED/membrane input), the irradiance increases due to edge effect, peaking at the very end of the membrane, 40 mm from the μLED. The middle guided region of the device from 13 to 35 mm has an average irradiance of $10.0 \pm 1.4\ \mu\text{W/cm}^2$. With the broad-area LED it was visually easy to ensure it was aligned to the PDMS membrane, and as the source was larger than the membrane a slight misalignment would still result in similar irradiance values. However, as the μLED array is much smaller than the broad LED, it is more difficult to visually see the coupling, and a misalignment may have a large effect on the amount of coupled light.

3.3.1 μLED alignment

To measure the effect of μLED position on the coupled light into the membrane, alignment tests were carried out. The fibre was placed at the end of the PDMS membrane opposite to the μLED, like shown in Figure 3.7(a). The μLED was then moved in the z- and y-direction to find the position with the maximum irradiance, this becomes the origin for the alignment measurements. The irradiance is recorded at the origin and the μLED is moved by a minimum of 100 μm in the z-direction and the irradiance recorded once more. This was repeated at a range of displacements to a maximum of 2 mm. The LED was then moved back to the origin and the above steps repeated in the y-direction

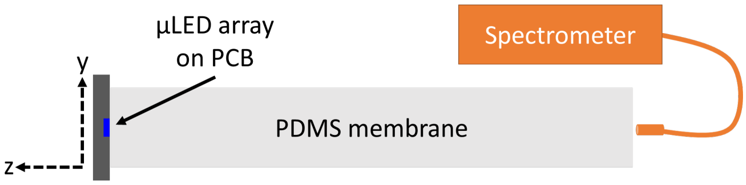

(a)

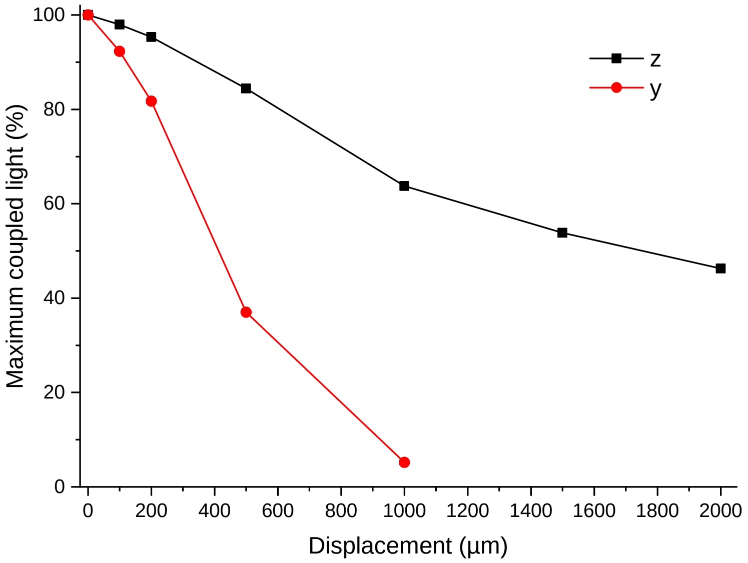

(b)

FIGURE 3.7: (a) Schematic of the alignment setup with the optical fibre measuring irradiance at the end of the PDMS membrane and (b) percentage decrease in coupled light when the LED is misaligned by specific values in the z- and y-directions

up to a distance of 1 mm. The resultant irradiance is plotted as a percentage of the original value versus the displacement from the origin shown in Figure 3.7(b).

As can be seen in Figure 3.7(b), the percentage of coupled light decreases when the μLED array is moved away from the PDMS membrane. By moving the LED in the z-direction, there is a slow decrease in the coupled light, with a 2% decrease occurring with a gap of 100 μm. The coupled light decreases by a further 13% when the μLED is moved 500 μm away from the PDMS membrane. Moving the LED in the y-direction has a much larger effect on the coupled light, with an 8% decrease at a distance of 100 μm from the centre. This decreases even further by 35% when the μLEDs are moved 500 μm from the centre of the PDMS membrane.

Moving the μLED in the z-direction has less of an effect on the % coupled light. By increasing this gap between the device and the PDMS membrane, the intensity of light that reaches the surface of the membrane is decreased, resulting in the decreased efficiency. A larger effect occurs when moving the μLED in the y-direction. Moving in this direction means the device is no longer central to the membrane, this causes the angle of light at the entrance of the membrane to change, resulting in more of the light being smaller than the critical angle and therefore being extracted close to the μLED. As the device is moved further from the central plane of the membrane, more light is scattered close to the LED, decreasing the amount of light coupled through to the end of the membrane. From these alignment tests, it is shown that the μLED array can be misaligned by a maximum of 500 μm in the z-direction or a maximum of 200 μm in the y-direction and the coupled light will be within 80% of the maximum. As the μLED device is placed in direct contact with the PDMS membrane in the z-direction, the effect of misalignment in both directions was not considered. It is more important to ensure accurate coupling on the y-direction as this has a larger effect on the coupled light and is also more difficult to achieve without measuring irradiance.

3.4 Light extraction using TiO_2 nanoparticles

Scatter substrates of different TiO_2 concentrations in PDMS, described in Section 2.6.1, are added to the surface of the PDMS membrane. The irradiance is measured from the top surface of the membrane as before. Irradiance maps were taken to determine the power and efficiency values of the different concentrations. These results are compared to those obtained with the broad LED.

3.4.1 Irradiance results of flat scatter substrates with μLED

The scatter substrates were added to the membrane 15 mm from the μLED device and the device run at a current of 120 mA, producing an optical power of 10 mW. The irradiance along the central region of the membrane was recorded at millimetre interval distances from the μLED.

Figure 3.8 shows the irradiance profiles of different weight concentrations of scatter substrates added to the membrane surface, the black solid line represents the irradiance from a bare PDMS membrane. It can be seen that all of the scatter substrates produce an increase in irradiance over the emissive region from 15 to 30 mm. The scatter substrates also cause a decrease in the edge effect, this is because more light is extracted from the membrane surface therefore, there is less light scattered when leaving the end of the membrane. From the figure it can be seen that as the TiO_2 concentration increases, the maximum irradiance increases until a maximum irradiance of 2.1 mW/cm^2 is obtained at 0.75%. At higher concentrations (e.g. 2%), the increased opacity of the films reduces the amount of scattered light extracted through the top surface of the membrane, this results in a decreased irradiance maximum. As well as an increased irradiance maximum, higher

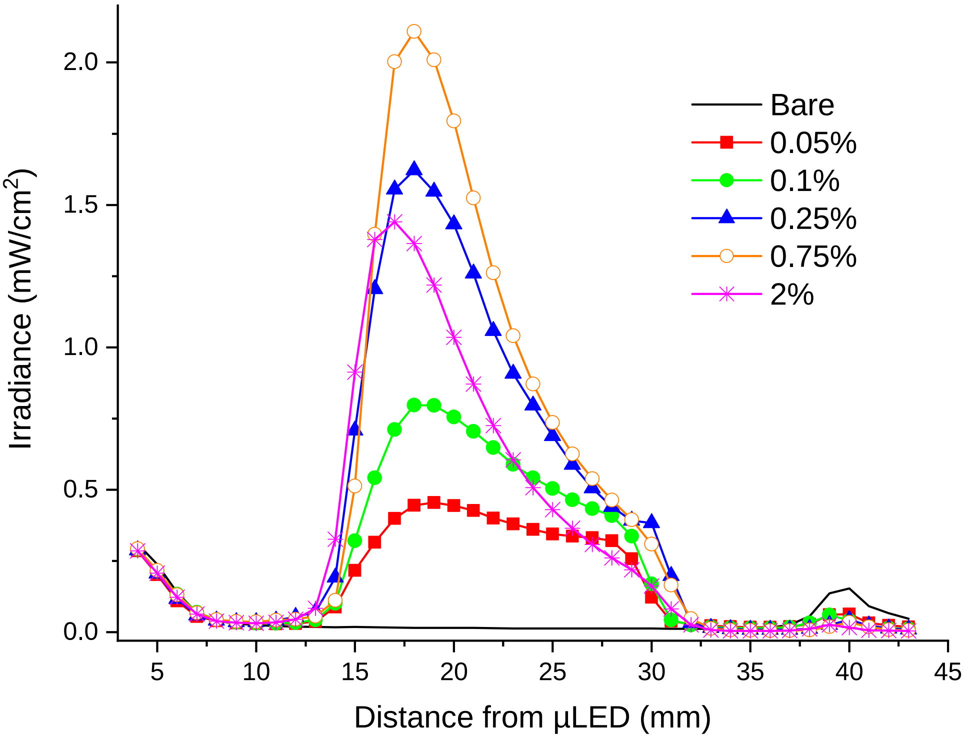

FIGURE 3.8: Irradiance of different concentrations of TiO_2 scatter substrates with increasing distance from the LED, the irradiance of the bare PDMS is given for reference

concentrations of TiO_2 have a steeper drop off in irradiance with increasing distance from the LED. For example, the 28 mm irradiance is 23% of the 17 mm irradiance for 0.75% TiO_2 sample, whereas this value increases to 57% for the 0.1% TiO_2 sample. It can be seen that the lower concentrations provide a more uniform irradiance over the length of the scatter substrate, however, produce lower maximum irradiance values. For example, 0.5 mW/cm^2 and 0.8 mW/cm^2 for the 0.05% and 0.1% respectively.

3.4.2 Output power of μLED samples

CCD images were taken of the scatter substrates to produce irradiance maps, as described in Section 2.6.3. The irradiance maps produced for each sample show the trend in light output across the entire substrate, and allow for further comparison between the samples. The maps for the TiO_2 concentrations of 0.1% and 0.75% are shown in Figure 3.9. The red regions of the maps correspond to where the irradiance is highest and blue is the lowest irradiance values. As can be seen for 0.1%, the irradiance is intense over a broad region of the scatter substrate width and length which decreases with increasing distance from the LED, as is seen in the irradiance graph. The intense region of the 0.75% TiO_2 is smaller than that of the 0.1% in both length and width, this

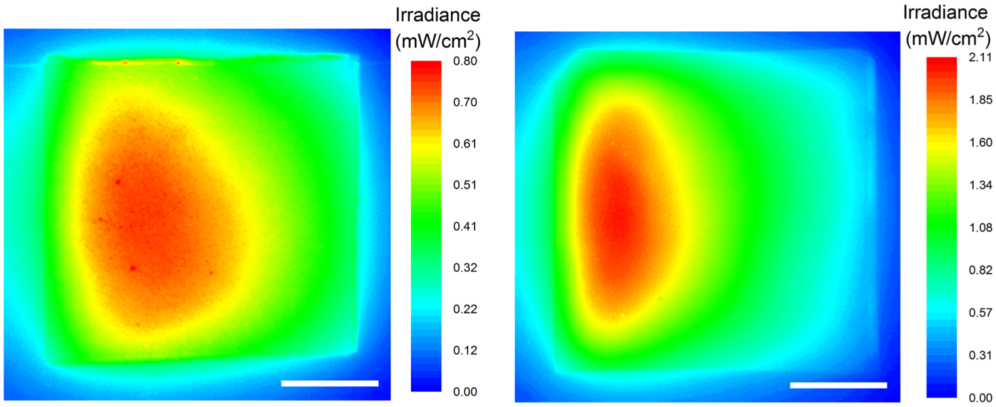

(a) (b)

FIGURE 3.9: Irradiance maps from CCD images of (a) 0.1% and (b) 0.75% TiO_2 scatter substrates, scale is 5 mm

decreasing trend is seen with increasing concentration, with both the high and medium irradiance areas decreasing.

From the irradiance maps we can calculate the total power output of each scatter sample in mW; using this and the μLED optical power of 10 mW, the overall optical efficiency of the devices can be calculated. The actual extraction efficiency of the substrates will be higher as not all of the μLED light is coupled into the PDMS membrane. Table 3.1 lists the peak irradiance, total output power and extraction efficiency for a range of TiO_2 concentrations. From these results it can be seen that the total output power increases with increasing concentration up to 0.75%, greater concentrations lead to reduced output power. This follows the same trend as the maximum irradiance. The most efficient device at extracting light is the 0.75% TiO_2, which extracts more than 26% of the input power.

TABLE 3.1: Table of maximum irradiance values, total power output and efficiency for different weight ratios of TiO_2, based on an input optical power of 10 mW with SD errors

TiO_2 (wt%)	Peak average irradiance (mW/cm^2)		Total power (mW)		Efficiency %	
0.04	0.3	±0.008	0.5	±0.020	4.8	±0.3
0.05	0.5	±0.003	0.7	±0.028	7.4	±0.2
0.1	0.8	±0.016	1.2	±0.043	12.2	±0.8
0.25	1.6	±0.007	2.1	±0.08	20.8	±1.8
0.75	2.1	±0.02	2.6	±0.110	26.6	±1.6
1	1.9	±0.019	2.4	±0.098	24.4	±1.9
2	1.4	±0.011	1.8	±0.073	18.3	±1.6

3.4.3 Comparison between broad and μLED

Comparing the broad LED irradiance (Section 2.6) with the μLED, the irradiance trend of the different TiO_2 scatter substrates remains similar. As the concentration of scatter substrate increases, the maximum irradiance increases until after 0.75% where less scattered light is extracted and the irradiance decreases. In order to better compare the different sources, the broad LED irradiance values obtained from an input power of 100 mW are reduced by 90% assuming that the trend between input power and irradiance is linear. A 90% reduction of the LED optical power would be 10 mW, the optical power of the μLEDs.

Table 3.2: Table comparing the maximum irradiance, total power output and efficiency for TiO_2 scatter substrates with the μLED and broad LED

TiO_2 concentration	Maximum irradiance mW/cm^2		Power output mW		Efficiency %			
	μLED	LED*	μLED	LED*	μLED		LED	
0.05	0.5	0.4	0.7	0.4	7.4	±0.2	4.3	±0.1
0.1	0.8	0.6	1.2	0.9	12.2	±0.8	8.7	±0.2
0.25	1.6	1.4	2.1	1.8	20.8	±1.8	17.9	±0.4
0.75	2.1	1.8	2.6	2.1	26.6	±1.6	21.2	±0.5
1	1.9	1.7	2.4	2.0	24.4	±1.9	19.6	±0.4
2	1.4	1.4	1.8	1.7	18.3	±1.6	17.1	±0.5

*estimated results based on an optical power of 10 mW

Table 3.2 gives a comparison between the two sources. In order to compare effectively, it is assumed that the irradiance and power values from the broad LED can be scaled to estimate what values would be obtained if the LED optical power was 10 mW compared to the experimental results obtained with an optical power of 102 mW. From the table it can be seen that the peak irradiance is slightly higher for the μLED compared to the estimated broad LED irradiance, with an average increase of 0.17 mW/cm^2 in the maximum irradiance. This increase on its own could be due to measurement errors, however, the effect is also seen in the extraction efficiency. Comparing the extraction efficiency of each sample with both of the devices, there is an average increase of 3.5% in the extraction efficiency samples with the μLED compared to the broad LED. Although the effect is not obvious in the irradiance graphs, when comparing the irradiance maps it can be seen that the samples with the μLED produce a more intense irradiance over a larger area than that of the broad LED. This effect is seen across the entire range of concentrations.

Figure 3.10 shows the irradiance maps of the 0.1% TiO_2 sample with both the μLED (a) and the broad LED (b). It can be seen that the irradiance is broader across both the width and the length of the scatter substrate when imaged with the μLED as the source.

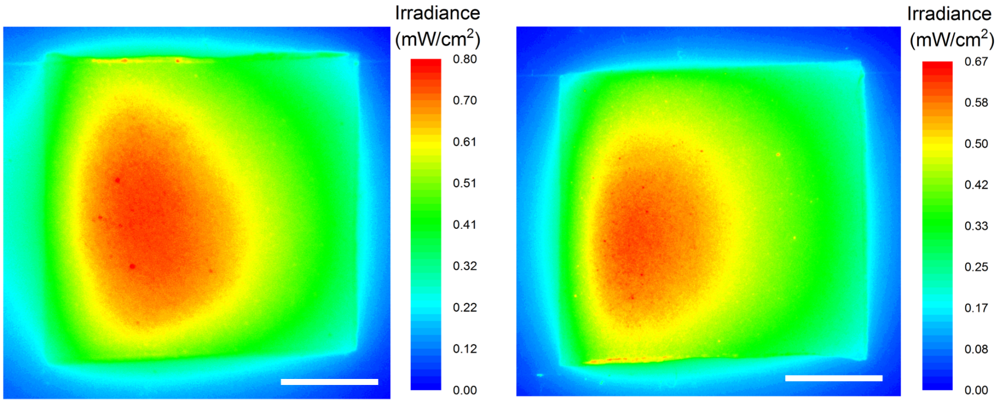

(a) (b)

FIGURE 3.10: Irradiance maps of the 0.1% TiO_2 scatter sample with the (a) μLED and (b) broad LED, scale is 5 mm

The increased irradiance across the width is because the μLED source is longer in the lateral direction compared to the broad LED.

3.5 Light extraction using tapered scatter substrates

The tapered scatter substrates described in Section 2.7.2 are utilised here. They consist of 0.04%, 0.05% or 0.1% TiO_2 in PDMS cured at an angle to produce a substrate with increasing thickness with distance from the LED. These substrates have a taper angle of 15°, producing a substrate that is 0.5 mm thick at one end and 4 mm thick at the other. The surface of the substrate remains as 15 x 15 mm^2.

3.5.1 Irradiance results of tapered scatter substrates with μLED

The tapered scatter substrates were added to the PDMS membrane surface, 15 mm from the μLED. The thinnest end of the substrate was placed closest to the LED, with the thickness increasing with distance from the μLED. Irradiance measurements were carried out as before, with the fibre being held at a distance of 5 mm from the surface of the waveguide to allow for measurements over the whole length of the scatter substrate. Figure 3.11(b) shows the irradiance results from these samples compared to the bare membrane. From these results we can see that a curing angle of 15° is not high enough for the 0.1% TiO_2 sample. The irradiance maximum of 0.8 mW/cm^2 occurs at the start of the scatter substrate, the irradiance then decays providing a non-uniform emission profile as observed with the flat samples. The irradiance of the 0.04% sample increases with distance from the LED, reaching a peak irradiance of 0.35 mW/cm^2 at the furthest end of the scatter substrate. Although this profile is close to being uniform, the low concentration of TiO_2 results in a very low irradiance. An angle of 15° is an ideal angle for obtaining uniform emission from a 0.05% TiO_2 sample. Here the irradiance remains uniform at 0.5 ± 0.04 mW/cm^2 over the entire length of the scatter substrate excluding the end where we see a peak due to light scattering from the roughly cut sample edges.

3.5.2 Irradiance maps of tapered scatter substrates

As before, CCD images were taken of the tapered scatter substrates and these used with the irradiance data to produce irradiance maps over the surface area of the substrates. The calculated total power and extraction efficiency of these samples is shown in Table 3.3. Comparing these to the flat scatter samples of the same concentration, the power output increased by at least 2 mW resulting in increased extraction efficiencies of 2% for the tapered samples.

TABLE 3.3: Table of maximum irradiance values, total power output and efficiency for different weight ratios of tapered TiO_2, based on an input optical power of 10 mW

TiO_2 concentration (wt%)	Peak average irradiance (mW/cm^2)		Total power (mW)		Efficiency %	
0.04	0.3	±0.002	0.6	±0.02	5.6	±0.3
0.05	0.5	±0.004	1.0	±0.04	9.7	±0.6
0.1	0.8	±0.021	1.4	±0.06	14.1	±1.1

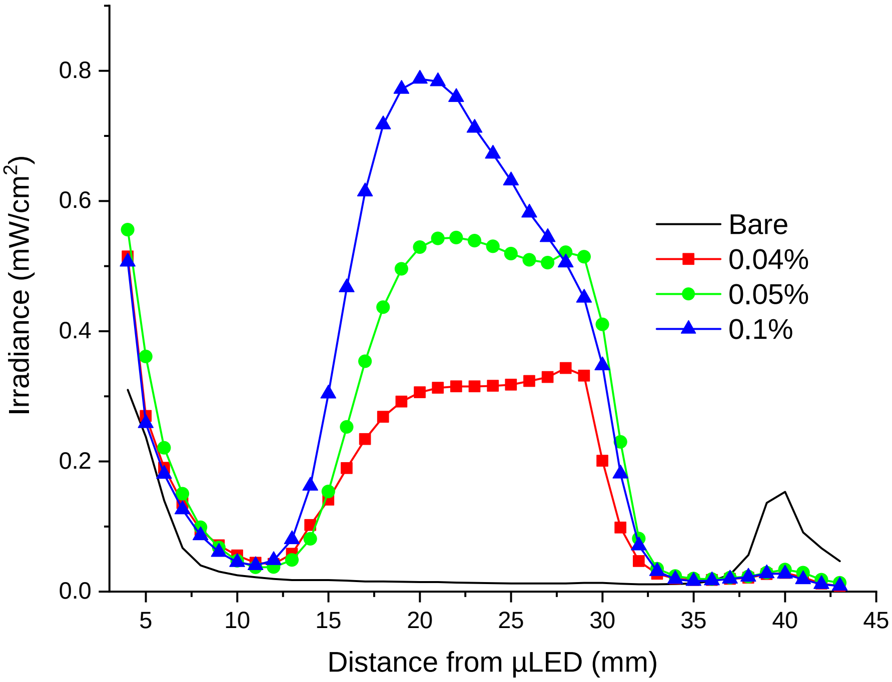

FIGURE 3.11: Irradiance of the tapered scatter substrates cured at an angle of 15°, the irradiance of the bare PDMS membrane is given for reference

3.5.3 Comparison of tapered scatter substrates with the broad LED and μLED

The tapered results can be compared to the flat results in a similar manner. It can be seen that the μLED irradiance is higher than the estimated broad LED irradiance for an optical power of 10 mW. As shown in Section 3.4.2, the irradiance results from the broad LED can be reduced by 90% to assume the effect with an input power of 10 mW. This allows for easier comparisons between the two types of LEDs. Table 3.4 compares the maximum irradiance, power output and extraction efficiency of each of the tapered scatter substrates.

Table 3.4: Table comparing the maximum irradiance, total power output and efficiency for TiO_2 scatter substrates with the μLED and broad LED

TiO_2 concentration	Maximum irradiance mW/cm^2		Power output mW		Efficiency %			
	μLED	LED*	μLED	LED*	μLED		LED	
0.04	0.3	0.4	0.6	0.5	5.6	±0.3	4.6	±0.2
0.05	0.5	0.5	1.0	0.9	9.7	±0.6	8.4	±0.4
0.1	0.8	0.7	1.4	1.1	14.1	±1.1	10.7	±0.5

*estimated results based on an optical power of 10 mW

From the estimated values for the broad LED, it can be seen that the maximum irradiance is very similar for each of the devices. The estimated power output is higher for the μLED devices and the extraction efficiency of each sample is shown to be at least 1% higher than the broad LED, with the 0.01% sample producing a 2.4% increase. Figure 3.12 shows the irradiance maps of the 0.05% tapered sample with the μLED (a) and the broad LED (b). The high intensity irradiance is over a larger area on the μLED sample compared to the broad LED, this results in the increased efficiency for the μLED.

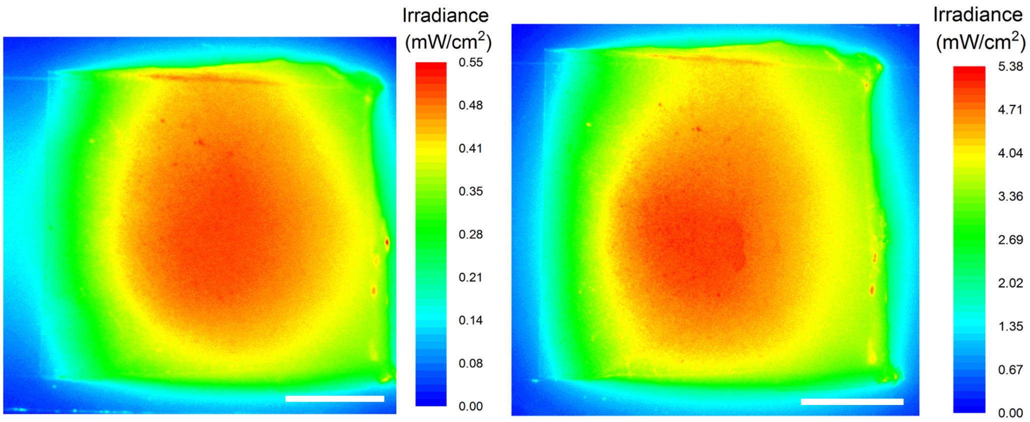

(a) (b)

Figure 3.12: Irradiance maps of the tapered 0.05% TiO_2 scatter sample with the (a) μLED and (b) broad LED, scale is 5 mm

3.6 Using a concentration gradient to achieve uniformity

As mentioned in Section 2.7, to achieve uniform output emission the probability of light being extracted has to increase with increasing distance from the LED. In Sections 2.7.3 and 3.5, this effect was shown using a tapered TiO_2 scatter substrate. This substrate got thicker with increasing distance from the light source. It has been shown that increasing the TiO_2 concentration in the scatter substrates results in an increase in the extracted light. This effect can be utilised by fabricating a scatter substrate with increasing concentration as the distance from the μLED increases. Another benefit of this method would be the reduced thickness of the device, a flat scatter substrate can be employed instead of the tapered design which causes an increased thickness of the overall device.

3.6.1 Fabrication of concentration gradients

In order to extract uniform light from the PDMS membrane, the concentration of TiO_2 has to increase with increasing distance from the LED. For ease of fabrication it was decided that 4 discrete concentrations would be utilised in an attempt to produce uniform extraction. The scatter substrates were fabricated as 15 x 15 x 1 mm^3 slabs.

Concentration gradient scatter substrates require a different fabrication method to the other scatter substrates, a schematic of this method is shown in Figure 3.13. Firstly, a 15 x 15 mm^2 area is cut into a 1 mm thick PDMS mould (a), this mould is then divided into four regions of pre-chosen widths (b). The PDMS from the first region is removed and the required amount and concentration of TiO_2/PDMS blend is added to this empty region (d, e). This region may then be cured partially or left as is depending on the specific fabrication steps for each sample. After, the next strip of PDMS is removed and the process repeated with the next concentration chosen (f, g), this is repeated from steps (h)-(i) until each strip has been removed and replaced. The resultant substrate with the increasing concentration gradient is cut from the PDMS mould (m) ready to be tested (n). The overall aim of this method is for the gradient substrate to look like (o), which has a mixed concentration gradient rather than distinct regions of different concentrations.

A range of different concentration gradients were fabricated and tested, these are given below in Sections 3.6.2 - 3.6.5. In these case samples there is a difference in the concentrations and in the width of each of the concentrations. There is also a difference in some of the fabrication steps which will be discussed for each sample.

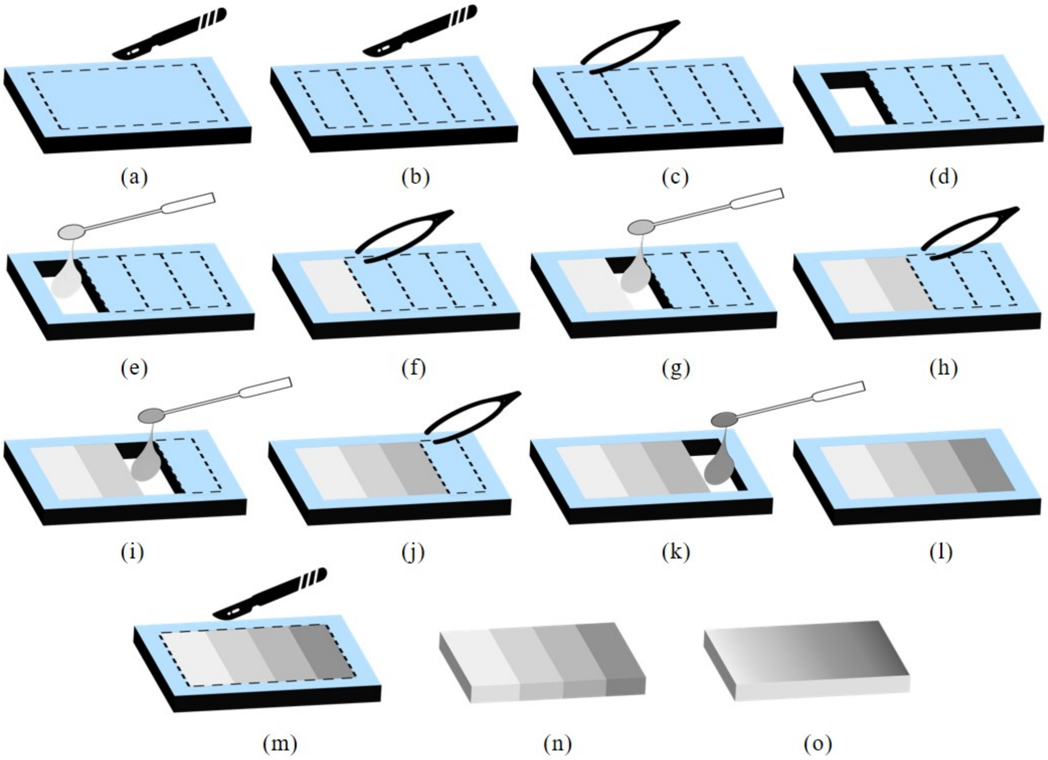

Figure 3.13: The fabrication method of concentration gradient scatter substrates, described in detail in Section 3.6.1

3.6.2 Concentration gradient 1

For the first concentration gradient membrane, a concentration range from 0.1% to 0.7% was utilised. The concentrations chosen for gradient 1 and the width of each concentration is shown schematically in Figure 3.14(a). A maximum concentration of 0.7% was chosen as it is close to the maximum concentration for light extraction (0.75%). A minimum of 0.1% was utilised as it produced a good maximum irradiance while also remaining more uniform for a longer distance from the LED, this first section has a length of 5 mm. Section 2 was 0.2% in concentration and 4.5 mm long, followed by section 3 which was 0.4% in concentration and 3 mm long. The final region (section 4) was 2.5 mm long with a concentration of 0.7%. From the single concentration extraction substrate results, an increasing concentration of TiO_2 resulted in a sharper irradiance peak of decreased uniformity. Therefore, the width of each region was chosen to decrease with increasing concentration in an attempt to produce uniform emission.

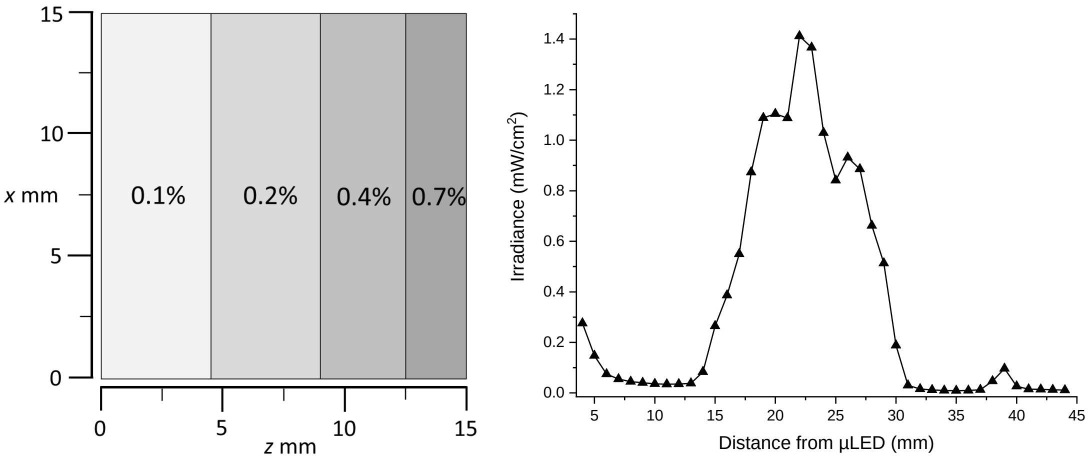

(a) (b)

FIGURE 3.14: (a) Schematic showing the different TiO_2 concentrations utilised in concentration gradient 1 and a scale showing the length of each concentration, (b) Irradiance trend of concentration gradient 1 with increasing distance from the LED

3.6.2.1 Fabrication

As uncured PDMS is a viscous liquid, in order to successfully add the different concentrations it was determined that each strip should be partially cured before adding the next concentration. This is to avoid the previous concentration running in to the next region before its concentration has been added. Each strip was cured at 80°C for 2 minutes to produce a sticky material that no longer spread. When PDMS is stirred or poured, air can get trapped within the mixture resulting in air bubbles if cured too quickly [14]. In order to avoid air bubbles inside the individual strips, the sample is placed under vacuum for 20 minutes to release the trapped air before being partially cured. This resulted in very rigid sticky strips of concentrations that were solid rather than liquid. After all strips have been added to the sample it is then left to fully cure for 4 hours at 80°C. The resultant gradient sample is then cut from the mould ready for irradiance testing.

3.6.2.2 Irradiance

Figure 3.14(b) shows the irradiance of a PDMS membrane with gradient 1 added 15 mm from the μLED. It can be seen that the irradiance increases initially from 15 to 20 mm with the 0.1% concentration, the change to 0.2% results in a further increase in the irradiance to a maximum of 1.4 mW/cm^2. After this increase the irradiance decreases to 0.8 mW/cm^2, before increasing again after 25 mm due to the 0.4% concentration, this then decreases to the end of the 15 mm long scatter substrate. A small shoulder is seen in the irradiance profile at 28 mm due to the 0.7% region of the substrate.

From the irradiance profile of this concentration gradient it can be seen that the 0.2% concentration resulted in too high an extraction of light, which then causes there to be less light further down the membrane, reducing the effect of the increased concentrations. The 0.7% has a minimal effect on the extracted light, although it broadens the decay profile.

3.6.3 Concentration gradient 2

As the concentration increase from 0.1% to 0.2% resulted in too much light getting extracted at that region close to the LED, the concentrations were altered in gradient 2. A lower initial concentration of 0.08% was chosen for 3 mm followed by 5 mm of 0.1%. 0.25% was then added for 4.5 mm and finally a maximum concentration of 0.45% for 2.5 mm.

3.6.3.1 Fabrication

This gradient sample was fabricated similarly to gradient 1, however, the partial cure was only for 90 seconds in an effort to increase the viscosity of the samples while still remaining liquid to allow for more potential mixing rather than the well-defined interface between the regions found in gradient 1. The resultant samples were still very stiff, so limited mixing between the concentration gradients occurs. The final sample with all concentrations was cured for 4 hours at 80°C, then removed from the mould for irradiance testing.

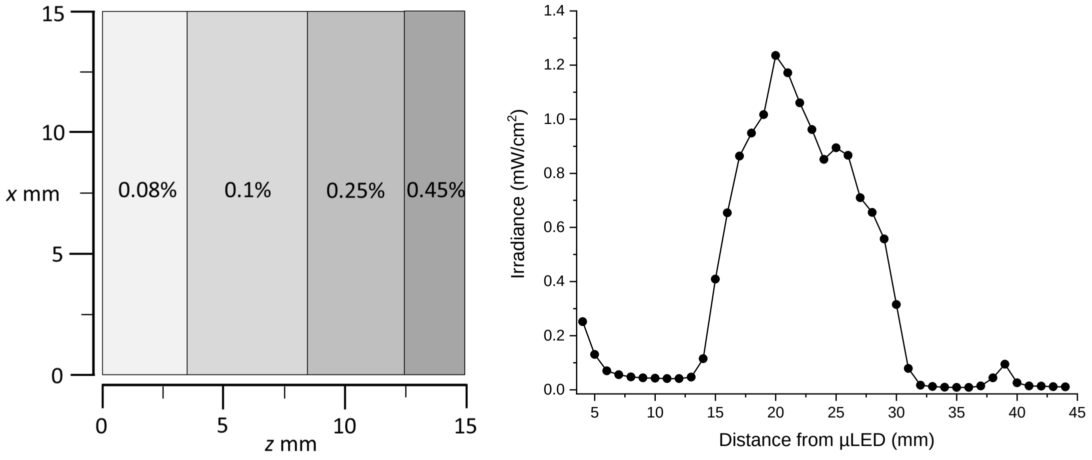

(a) (b)

FIGURE 3.15: (a) Schematic showing the different TiO_2 concentrations utilised in concentration gradient 2 and a scale showing the length of each concentration, (b) Irradiance trend of concentration gradient 2 with increasing distance from the LED

3.6.3.2 Irradiance

The sample was added to a PDMS membrane 15 mm from the μLED and the irradiance measured from the top surface of the device. It can be seen that the irradiance increases gradually until 18 mm, where there is a large irradiance increase due to the concentration change to 0.1%, with a maximum irradiance of 1.2 mW/cm^2. The irradiance then decreases until 24 mm from the μLED where an increase occurs due to the concentration increasing to 0.25%. The irradiance continued to decrease though there was a small shoulder at 28 mm corresponding to the 0.45% concentration.

In the case of this sample it can be seen that the initial 0.08% concentration does not extract enough light and the change to 0.1% causes too high an increase in scattered light.

3.6.4 Concentration gradient 3

For gradient 3, the initial concentration was increased once more to 0.1% to produce a higher initial irradiance over a length of 2.5 mm. Followed by a 5 mm stretch of 0.16% which is a small concentration increase thought to avoid the sharp peaks seen in gradients 1 and 2. This is then followed by 4.5 mm of 0.25% and a maximum concentration of 0.45% for the final 3 mm.

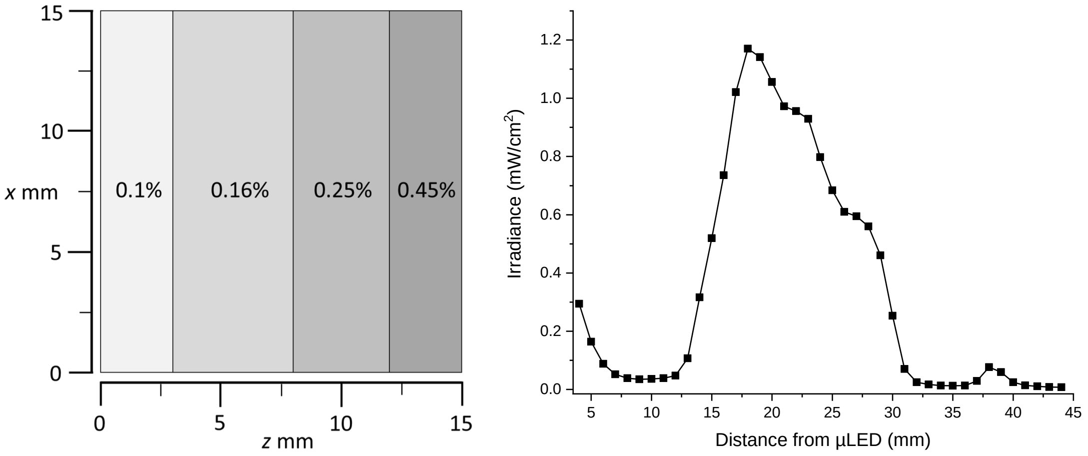

(a) (b)

FIGURE 3.16: (a) Schematic showing the different TiO_2 concentrations utilised in concentration gradient 3 and a scale showing the length of each concentration, (b) Irradiance trend of concentration gradient 3 with increasing distance from the LED

3.6.4.1 Fabrication

In order to streamline the process and reduce the "hands-on" fabrication time utilised in gradient 1 and 2, the partially curing and de-gassing steps were removed from the fabrication of gradient 3. Instead the samples were left in their liquid form for two hours after producing the concentration mixes, this is very near the end of the PDMS working time, so the samples were more viscous, however, still a liquid capable of mixing.

3.6.4.2 Irradiance

The irradiance was measured as before and is given in Figure 3.16. There was a gradual increase in the irradiance to a maximum of 1.2 mW/cm^2 at the region for 0.16%. This decreases to a shoulder at 0.25% followed by another shoulder at 27 mm due to 0.45%. Although this trend is not uniform, the irradiance change is much smoother over the whole extraction region compared to the effect seen with the distinct regions in gradients 1 and 2.

3.6.5 Concentration gradient 4

One issue seen with the previous gradient samples, is that the initial incline in irradiance leads to a maximum that then drops continuously even with increased concentration. In order to counteract this the first section of lowest concentration was made longer (5 mm) to allow a natural maximum to be reached with its concentration before moving to the next concentration of 0.16% for 4.5 mm. In gradients 2 and 3, the two final concentrations were not high enough to produce uniform irradiance further from the μLED, however the final two concentrations in gradient 1 were too high. Therefore, 0.3% was utilised for 3.5 mm followed by a maximum of 0.5% for the final 2 mm of the extraction substrate. This is shown as a schematic in Figure 3.17(a).

3.6.5.1 Fabrication

Similar fabrication steps were carried out as for gradient 3. All concentrations were produced separately and allowed to increase in viscosity for 2 hours before being added to the mould strip by strip. The resultant sample was cured at 80°C for 4 hours before being cut from the mould for irradiance testing.

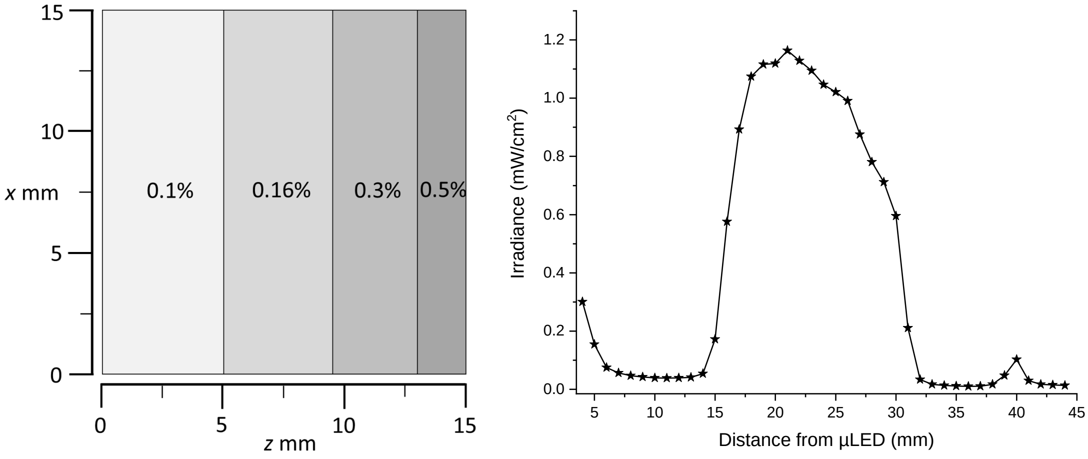

(a) (b)

Figure 3.17: (a) Schematic showing the different TiO_2 concentrations utilised in concentration gradient 4 and a scale showing the length of each concentration, (b) Irradiance trend of concentration gradient 4 with increasing distance from the LED

3.6.5.2 Irradiance

The irradiance profile for gradient 4 is given in Figure 3.17(b) with increasing distance from the LED. For the first 5 mm of the extraction substrate from 15 mm the irradiance increases to a maximum of 1.2 mW/cm^2 at the boundary between the 0.1% region and the 0.16% region. The irradiance slowly decays down to 25 mm where the decay slows down due to the 0.3% region followed by another slow decay through the 0.5% region to the end of the sample.

3.6.6 Comparison of gradient samples

In order to determine the uniformity of the different gradient samples, the main information from each irradiance profile is given below in Table 3.5. From the irradiance results, the maximum irradiance value can be taken. The mean irradiance is measured over the central 13 mm of the scatter substrate, ignoring the initial increase at 15 mm and the final decay at 30 mm. The standard deviation of this mean value is calculated. The maximum irradiance of gradient 1 is higher than the other samples at 1.4 mW/cm^2, however, the mean irradiance is similar. This results in a relatively high SD on the mean of 25%. The mean irradiance for gradients 2 and 3 is 0.9 mW/cm^2 over the 13 mm length, with SDs of 18 and 21% respectively.

The most promising of the concentration gradient extraction substrates is gradient 4. This sample has a mean irradiance of 1.0 mW/cm^2 ± 13% along the length of the

TABLE 3.5: Table of the irradiance results of the different concentration gradient samples with maximum irradiance values, mean irradiance values and the associated standard deviation of the irradiance

Concentration gradient	Maximum irradiance (mW/cm^2)		Mean irradiance (mW/cm^2)	Uniformity SD %
1	1.4	±0.08	1.0	25
2	1.2	±0.07	0.9	18
3	1.2	±0.08	0.9	21
4	1.2	±0.05	1.0	13

substrate. Due to its low error value and uniform shaped irradiance profile, gradient 4 is the chosen uniform concentration gradient sample.

3.7 Comparison of the uniform methods

Two different methods have been employed to produce uniform extracted light; the tapered method utilised in Sections 2.7.2 and 3.5 and the concentration gradient method shown in Section 3.6. The irradiance profiles, the irradiance maps and the uniformity of the two different methods will be compared here.

3.7.1 Irradiance comparison of the uniform methods

The irradiance of each of the methods, and a bare PDMS membrane with increasing distance from the μLED are given in Figure 3.18. The initial irradiance values close to the μLED, from 5 to 10 mm are higher for the tapered substrate due to the fact the fibre is held at a higher distance above the membrane in order to translate along the device without touching the surface. This increase in fibre y-placement of 3 mm causes a higher irradiance value to be recorded as light not guided is then collected by the higher placed fibre. This therefore means that the measured light output from the tapered device is not fully comparable with the flat substrate due to the varying distance from the detector. As this method was not utilised any further, this difference has not been taken into account.

It can be seen that the irradiance of the concentration gradient sample is much higher than that of the tapered sample. The mean irradiance of the tapered sample is 0.5 mW/cm^2 compared to a mean irradiance of 1.0 mW/cm^2 for the concentration gradient. The mean SD values are also different for the samples, with the tapered sample having a lower SD of 11% compared to the 13% SD seen with the gradient sample. In order to compare the full effect of each method, the irradiance across the entire scatter substrate also has to be determined.

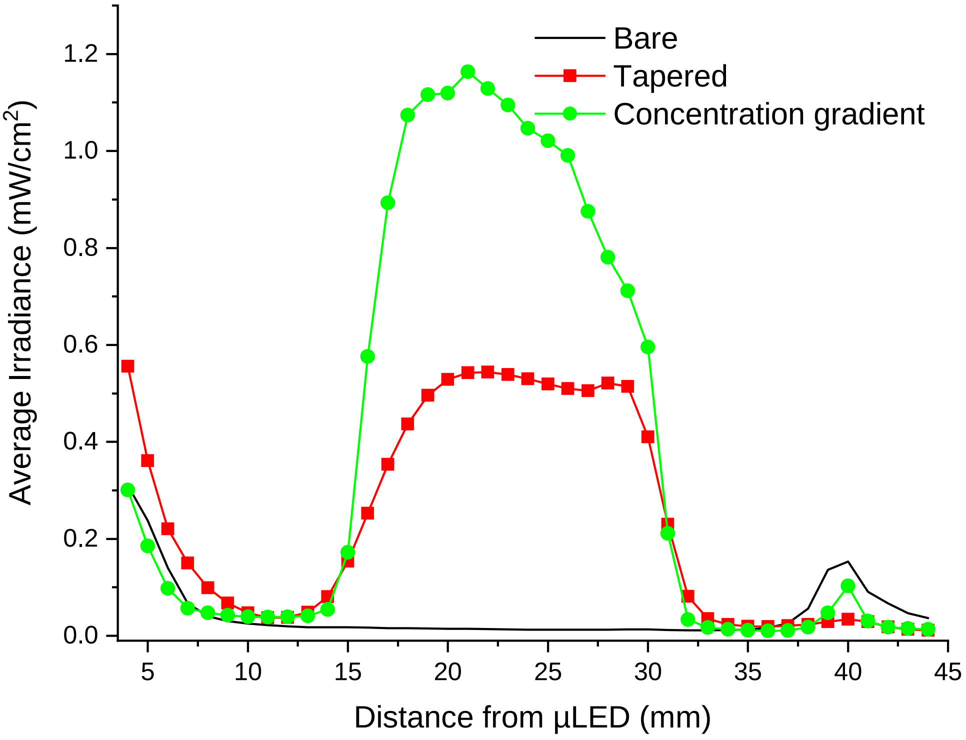

FIGURE 3.18: Irradiance of the different TiO_2 scatter substrate methods for uniform light extraction, irradiance of the bare PDMS membrane is given as a reference

3.7.2 Irradiance maps of the uniform methods

Irradiance maps were produced for each scatter substrate using the method described in Section 2.6.3. The maps of both the tapered and concentration gradient samples are given in Figure 3.19. It can be seen that both methods provide large regions of high irradiance over the scatter substrate. The tapered substrate (Figure 3.19(a)), has a slow build up to the high irradiance region, placing it further from the LED, this is also seen in the irradiance profile. Smaller regions of high irradiance also appear along one edge and at the end of the substrate, this is due to rough edges obtained when cutting the samples to the required size. The irradiance map for the concentration gradient substrate, shown in Figure 3.19(b), places the high irradiance region closer to the LED, with a bigger decay in irradiance produced at the end of the substrate. Again, a rough edge is seen at the top of the map with a small high irradiance region. Comparing the two maps, the high irradiance regions are similar in size, both along the length as shown in the irradiance profile, but also across the width of the substrates, showing that the irradiance is uniform over the majority of the extraction substrates.

Looking closely at the high intensity regions, it can be seen that the concentration gradient sample has a much higher intensity with a high irradiance region (deep red on the map) covering more of the area. The tapered substrate has a smaller maximum

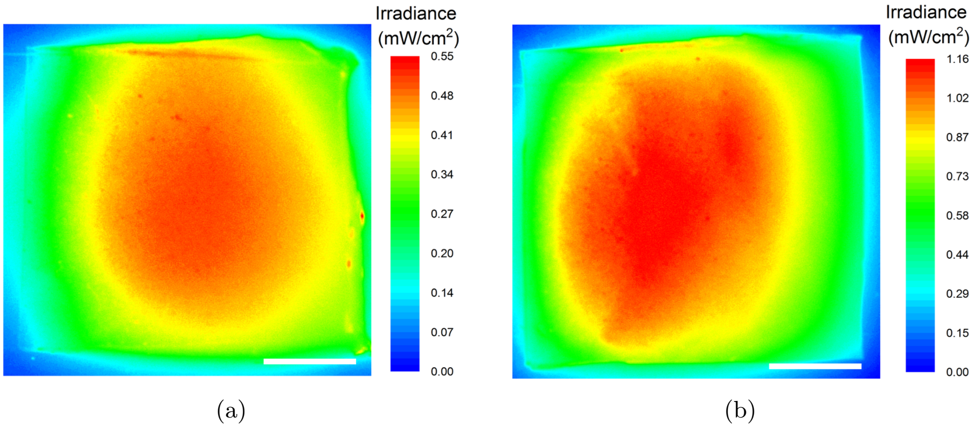

FIGURE 3.19: Irradiance maps of the (a) tapered 0.05% TiO_2 scatter substrate and (b) the concentration gradient substrate, scale is 5 mm

intensity region, with more of the area being a burnt orange intensity corresponding to a lower irradiance.

From the irradiance maps, the total output power of the extraction substrates can be calculated. Table 3.6 gives the maximum irradiance, total output optical power and extraction efficiency for each method of light extraction. It can be seen that the concentration gradient sample has a higher maximum irradiance, output power and efficiency. With a μLED optical power of 10 mW, the gradient sample provides an output power of 2.3 mW giving the device an efficiency above 23%. The tapered sample has an efficiency close to 10%.

TABLE 3.6: Table of maximum irradiance values, total power output and efficiency for the different methods of uniform light extraction, based on an input power of 10 mW

TiO_2 concentration (wt%)	Peak average irradiance (mW/cm^2)		Total power (mW)		Efficiency %	
Tapered	0.5	±0.004	1.0	±0.04	9.7	±0.6
Concentration gradient	1.2	±0.050	2.3	±0.098	23.3	±1.2

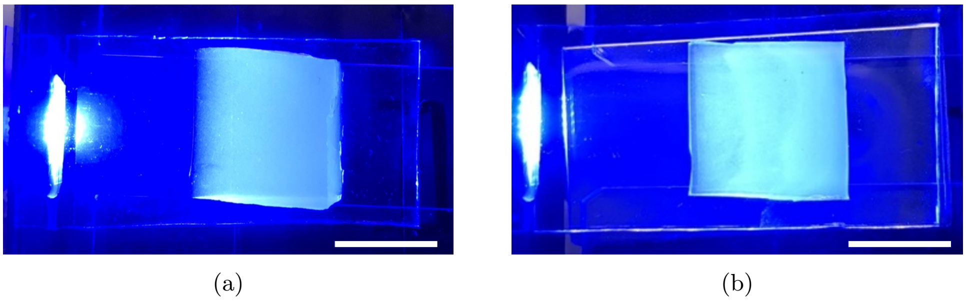
(a) (b)

FIGURE 3.20: Image of each method of uniform extraction with the μLED output power at 10 mW (a) tapered device, (b) concentration gradient device, scale is 10 mm

3.7.3 Most effective uniform extraction method

From the comparison it can be seen that the concentration gradient sample provides a higher uniform irradiance than the tapered sample. Although the mean irradiance SD is higher for the gradient sample, this could be improved by further fabrication/design amendments. The tapered sample, although easier to fabricate loses a large amount of light at the thick end of the substrate, causing a decreased efficiency. The increased device thickness with the tapered sample is not desirable. As well as making the final device more obtrusive, the thick shape of the scatter substrate decreases the flexibility of the overall device, making the device less wearable. The 1 mm thick concentration gradient substrate is uniform over the whole length and only increases the thickness of the overall device by 1 mm, allowing the device to still be wearable. The concentration gradient sample is also much more efficient, at 23% compared to the tapered sample. These properties of the concentration gradient make it a more suitable substrate for producing uniform extraction, with a small drawback being the decrease in uniformity compared to the tapered sample.

3.8 Method for different sizes of concentration gradient

The initial outset of this research is to provide uniform irradiance over an area 1 cm^2. Section 3.6 showed this is possible using a scatter substrate with a gradient in concentration. However, not all lesions that require phototherapy are 1 cm^2, there are many different sizes possible. Therefore, in order to be effective, the wearable phototherapy device must be designed to provide uniform irradiance to a range of treatment areas. The concentration gradient for uniform extraction over a substrate 15 x 15 mm^2 was determined experimentally. In order to adapt the gradient for other sizes of treatment areas a mathematical model can be designed. Such a model is phenomelogically derived next.

It is assumed that the light output is uniform over any width of scatter substrate. This is due to the fact the light from the μLEDs fills the PDMS waveguide, multiple arrays could also be utilised at the end of the membrane without affecting the flexibility.

3.8.1 Light intensity in PDMS

In order to measure the decay of light in the PDMS membrane due to waveguide losses, irradiance measurements were taken at the end of the membrane (opposite the LED), like shown in Figure 3.7(a). The bare PDMS membrane, with no extraction substrate then had a strip 5 mm long cut from the end and the irradiance measured again. This was repeated multiple times until the PDMS membrane was only 5 mm long. This method is widely used to measure propagation losses in waveguides and is known as the cut-back method [15]. The end-facet irradiance at each length of membrane was then calculated as a percentage based on coupled irradiance at the μLED/PDMS membrane surface. This percentage value was plotted against the length of the PDMS membrane, given in Figure 3.21. An exponential fit was applied to the data which provided a decay rate of 0.016 mm^{-1} which is related to the intensity by Equation 3.1. The calculated decay in intensity is mainly due to scattering losses at the edges of the membrane. These membranes are cut by hand using a scalpel; therefore the edges are rough causing scattering.

$$I_\mathrm{z} = I_0 e^{-0.016z} \tag{3.1}$$

Where I_z is the irradiance in the membrane at distance z from the μLED and I_0 is the irradiance of the light coupled into the membrane at $z=0$. This trend is common for edge-lit waveguides [16, 17], where the intensity drops off exponentially with increasing length of membrane. Depending on the cut-edge roughness, this equation should hold true for any length of PDMS membrane, not taking the width of the membrane into

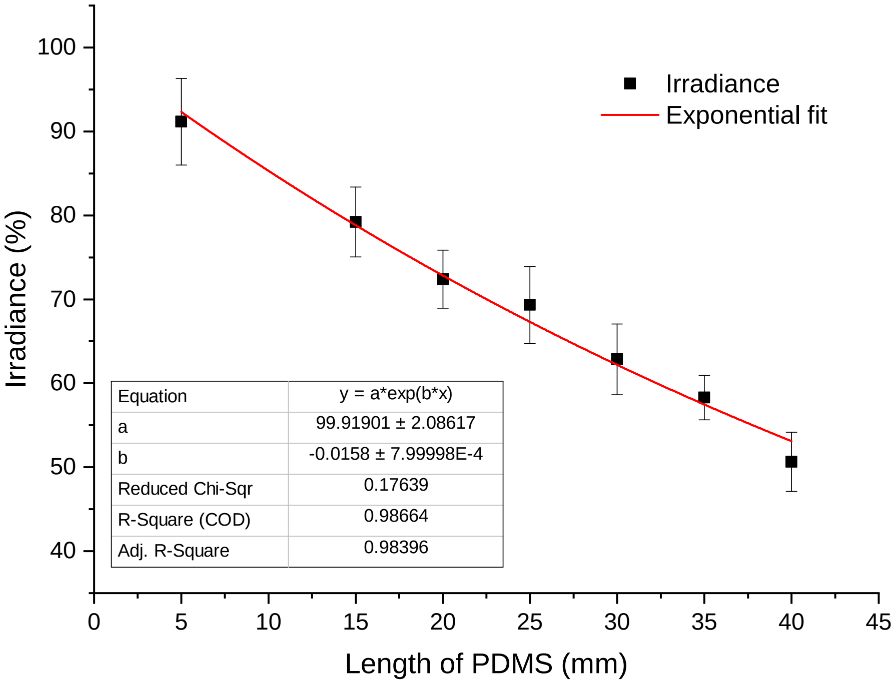

Equation	y = a*exp(b*x)
a	99.91901 ± 2.08617
b	-0.0158 ± 7.99998E-4
Reduced Chi-Sqr	0.17639
R-Square (COD)	0.98664
Adj. R-Square	0.98396

FIGURE 3.21: Decreasing percentage irradiance in a PDMS membrane with increasing length

account. The addition of a scatter substrate changes the irradiance of light in the membrane and therefore the above equation will change.

3.8.2 Effect of an extraction substrate

When an extraction substrate is added to the membrane, the above model no longer holds true. The substrate causes light to be extracted from the PDMS membrane, changing the irradiance (I) after the extraction point. When determining the intensity of light remaining inside the membrane at a certain position, the new equation is given in Equation 3.2[1].

$$I_{\mathrm{z}} = I_0 e^{-0.016z} - S_{(\mathrm{n})} \tag{3.2}$$

Where S_n represents the extracted irradiance at distance n mm from the start of the scatter substrate (see Figure 3.22). The substrate consists of discrete 1 mm intervals, n. The value of n ranges from 0 to L, which is the length of the extraction substrate in millimetres. These discrete regions, and the resultant extracted irradiance, S_n, are shown schematically in Figure 3.22. The irradiance within the PDMS membrane changes to accommodate the additional light lost from every millimetre of the extraction substrate as shown in Equation 3.3, where z is the distance in the PDMS membrane from the LED and n is the discrete region on the extraction substrate.

$$I_{\mathrm{z}} = I_0 e^{-0.016z} - \sum_{n=0}^{n} Sn \tag{3.3}$$

The amount of extracted irradiance, S_n, depends on the irradiance in the membrane at that point I_z. It also depends on the efficiency of the extraction substrate to extract light, E_n. An equation for S_n is given in Equation 3.4.

$$S_n = E_n \times I_{\mathrm{z}} \tag{3.4}$$

For uniform emission, S_n should remain constant over the length of the scatter substrate. Therefore, using Equation 3.4, the efficiency of light extraction would have to increase with distance from the LED, as the irradiance inside the membrane decreases with distance.

---

[1] This method considers the addition of the scatter substrate as simply adding a loss term to the light guided within the membrane to keep our phenomelogical approach simple. This is not physically true as the addition of the scatter substrate disturbs the light guiding as it spreads between the membrane and scatter substrate.

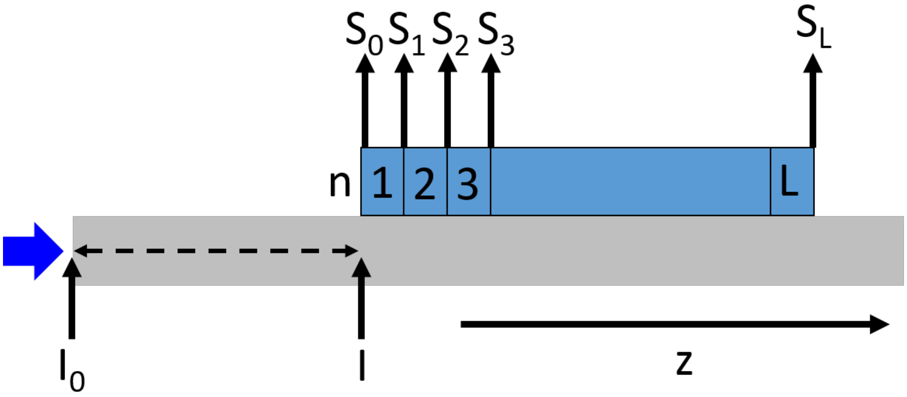

FIGURE 3.22: Schematic of light entering the edge of the PDMS membrane with an extraction substrate on top

3.8.3 Efficiency of light extraction

From Section 3.4.1, we know that the extracted irradiance is dependent upon the concentration of TiO_2. Using these experimental results and combining them with the calculated equation for irradiance inside the PDMS membranes (Equation 3.1), the extraction efficiency, E_n, of different concentrations of TiO_2 can be determined.

The μLED array is run at an output power of 10 mW. By using the experimental data from Section 3.8.1, the irradiance results, in mW/cm^2, can be extrapolated to estimate

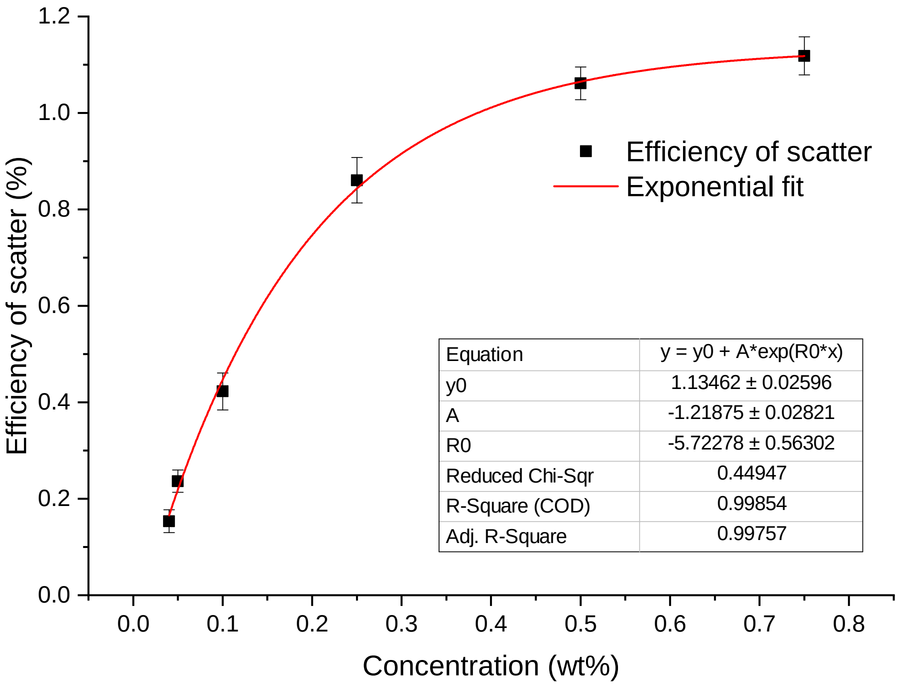

Equation	y = y0 + A*exp(R0*x)
y0	1.13462 ± 0.02596
A	-1.21875 ± 0.02821
R0	-5.72278 ± 0.56302
Reduced Chi-Sqr	0.44947
R-Square (COD)	0.99854
Adj. R-Square	0.99757

FIGURE 3.23: The efficiency of light extraction versus the concentration of TiO_2 in a scatter substrate

the initial irradiance within the PDMS membrane, I_0. The irradiance from the μLED array itself cannot be used as it does not take into account the coupling effect to the PDMS membrane. As shown in optical simulations, Section 3.2, there is a maximum coupling of 88% to the PDMS membrane under ideal conditions. Experimentally this will be less due to the surface of the PDMS membrane not being optically smooth, resulting in light scattering. From extrapolating the experimental data, I_0 was determined to be 220 mW/cm^2 when the μLED was run at 10 mW. The irradiance was measured as 290 mW/cm^2 at the surface of the μLED.

Therefore, using Equation 3.1, at a distance of 18 mm from the LED, the irradiance inside the membrane is calculated to be 165 mW/cm^2. The 18 mm measurement was utilised due to its high irradiance results for each concentration of extraction substrate in the experiments discussed in Section 3.4.1. This value can be used to determine the extraction efficiency of each TiO_2 concentration at the 18 mm measurement. Although the extraction substrate was placed 15 mm from the μLED, the first 3 mm of the substrate is a transition region, therefore, this is ignored for this phenomenological approach to work. A plot of efficiency of scatter (%) versus concentration of TiO_2 in PDMS, is shown in Figure 3.23. The trend shows that with increasing concentration of TiO_2, the extraction efficiency increases until 0.75%. An exponential fit can be applied to this data to produce an asymptote value of 1.1%, from this it can be seen that the maximum amount of light that can be extracted from a substrate at any given z is 1.1%.

For uniform emission, S_n should remain constant over the length of the scatter substrate. As the total amount of light available in the membrane for extraction only changes with I_0, the S_n value will be different for different lengths of extraction substrate, L. For example, a substrate with a shorter length can have a higher extracted irradiance value than a longer substrate for the same input irradiance.

$$E_n = \frac{S_n}{I_{\mathrm{z}}} \tag{3.5}$$

By rearranging Equation 3.4, an equation for E_n can be given. However, this equation, Equation 3.5, does not take the length of the extraction substrate and the position on the PDMS membrane into account. In order to determine the E_n values for different lengths of scatter substrate, Equation 3.6 can be used for each region of an extraction substrate when the z and z_{max} values are known. The z_{max} value is the position in the PDMS membrane at the end of the extraction substrate with length, L. This equation is used as it is found to give a comparable trend to the experimentally produced data, discussed further in Section 3.8.5.

$$E_n = \frac{S_\mathrm{n}}{I_\mathrm{z}} \times \frac{z}{z_{max}} \tag{3.6}$$

From Figure 3.23 it can be seen that the values for E_n have to range between 0 and 1.1% in order to maintain an increasing trend. A length of scatter substrate, L was fixed and theoretically placed 15 mm from the μLED, allowing for z_{max} to equal *15 + L*. The S_n value was then adjusted and E_n calculated until the efficiency of extraction ranged between 0 and 1.1%. This was repeated for different lengths of extraction substrate, L. This iterative calculation process produced the resultant calculated S_n values required for different lengths of extraction substrate are given in Table 3.7.

TABLE 3.7: Calculated $\mathrm{S_n}$ values for different lengths of extraction substrates

Length of extraction substrate mm	Measured $\mathrm{S_n}$ mW/cm^2
5	0.00737
10	0.00647
15	0.0057
20	0.00445
30	0.00394
40	0.00311
50	0.00277

The calculated S_n values in Table 3.7 were plotted against the length of the extraction substrate and the data fitted to obtain a relationship between the extracted irradiance, the initial irradiance in the membrane and the length of the extraction substrate. This produces a plot with an exponential relationship given in Equation 3.7. Different initial irradiance values and lengths of extraction substrates can be input to this equation and the resultant extracted irradiance for uniform emission calculated.

$$S_n = I_0 \times 0.0082e^{-0.024L} \tag{3.7}$$

3.8.4 Equation for a concentration gradient

Using Equation 3.3, 3.6 and 3.7 the extraction efficiency values for uniform light extraction over different lengths of substrate can be calculated. In order to fabricate these extraction substrates, the efficiency values have to be converted to a concentration of $\mathrm{TiO_2}$. Applying an exponential fit to the data in Figure 3.23 results in Equation 3.8. Where, E_n is the efficiency of extraction depending on the concentration, *C*.

$$E_n = 1.1 - 1.23e^{-5.77C} \tag{3.8}$$

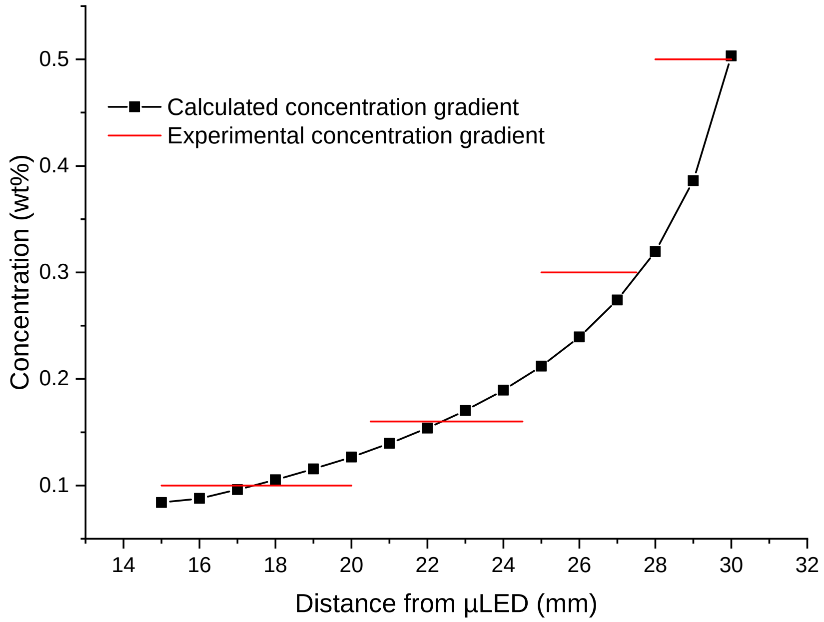

FIGURE 3.24: The calculated and experimental concentration gradients for uniform light extraction from a 15 mm long scatter substrate

By rearranging Equation 3.8, the concentration of TiO_2 required for a calculated extraction efficiency is given in Equation 3.9.

$$C_n = \frac{-ln\left(\frac{1.1-E_n}{1.23}\right)}{5.77} \tag{3.9}$$

Using these equations, the concentration gradient for uniform light over a scatter substrate of length, L, can be calculated. The resultant concentration gradients increase exponentially with increasing distance from the LED. The trend of increasing light extracting features is commonly used in edge-lit backlight displays, for example with scattering pyramids [18] or with dot patterns [19, 20].

These calculations consider only the extracted light from the top surface of the substrate; scattered light in other directions has not been considered. Equation 3.7 only holds true when the scatter substrate is placed 15 mm from the μLED, this would have to be adjusted if the substrate is to be placed at a different distance from the light source. The measured efficiency of the TiO_2 scatter substrates is true for 1 mm thick substrates, increasing or decreasing the thickness of the scatter substrate results in a change in the efficiency. The calculated concentration gradients remain true for 1 mm thick substrates, changing the thickness could result in a non-uniform irradiance being observed. Another limitation to these equations is they only consider the length of the scatter substrate; different widths have not been experimented.

3.8.5 Comparison of experimental and calculated concentration gradient

The validity of the calculated concentration gradients can be compared to the experimental uniform concentration gradient for a 15 mm long scatter substrate. Figure 3.24 contains the calculated concentration gradient and the concentration gradient of the experimental sample, which consisted of four regions of different concentrations like shown.

It can be seen that both methods follow a similar trend in concentration with the maximum and minimum concentration values being very similar. Further experimental work would have to be carried out on different lengths of scatter substrates to truly ensure the validity of the calculated gradients for producing uniform irradiance. A similar method has been used to produce uniform emission in [21]. This method resulted in a linear trend due to the waveguide loss being linear. As the loss within the PDMS membrane utilised here is exponential, the trend in increasing concentration is therefore also exponential.

3.9 Summary

In this chapter, the use of a μLED array and elastomeric membrane as an edge-injected light guide has been demonstrated. The μLED design and subsequent electrical and spectral properties were described in detail, as was the design of the PCB for the μLED. The efficiency of the device with TiO_2 nanoparticles in PDMS was measured and compared to that of the broad-area LED in Chapter 2. Extraction substrates with a gradient concentration of TiO_2 were fabricated and tested to produce uniform emission using a substrate 15 x 15 mm^2. A uniform irradiance of 1 mW/cm^2 was obtained over an area more than 1 cm^2. With a μLED optical power of 10 mW, the overall output power measured was 2.3 mW, resulting in an extraction efficiency of 23%. This is an increase compared to the tapered extraction method. Finally, experimental data was utilised to determine a mathematical method of calculating concentration gradients for different lengths of extraction substrates.

References

[1] M. S. Islim, R. X. Ferreira, X. He, E. Xie, S. Videv, S. Viola, S. Watson, N. Bamiedakis, R. V. Penty, I. H. White, *et al.*, “Towards 10 Gb/s orthogonal frequency division multiplexing-based visible light communication using a GaN violet micro-LED,” *Photonics Research*, vol. 5, no. 2, pp. A35–A43, 2017.

[2] T. Wu, C.-W. Sher, Y. Lin, C.-F. Lee, S. Liang, Y. Lu, S.-W. Huang Chen, W. Guo, H.-C. Kuo, and Z. Chen, “Mini-LED and micro-LED: promising candidates for the next generation display technology,” *Applied Sciences*, vol. 8, no. 9, p. 1557, 2018.

[3] Z. Gong, S. Jin, Y. Chen, J. McKendry, D. Massoubre, I. M. Watson, E. Gu, and M. D. Dawson, “Size-dependent light output, spectral shift, and self-heating of 400 nm InGaN light-emitting diodes,” *Journal of Applied Physics*, vol. 107, no. 1, p. 013103, 2010.

[4] D. Tsonev, H. Chun, S. Rajbhandari, J. J. McKendry, S. Videv, E. Gu, M. Haji, S. Watson, A. E. Kelly, G. Faulkner, *et al.*, “A 3-Gb/s single-LED OFDM-based wireless VLC link using a gallium nitride micro-LED,” *IEEE Photonics Technology Letters*, vol. 26, no. 7, pp. 637–640, 2014.

[5] R. X. Ferreira, E. Xie, J. J. McKendry, S. Rajbhandari, H. Chun, G. Faulkner, S. Watson, A. E. Kelly, E. Gu, R. V. Penty, *et al.*, “High bandwidth GaN-based micro-LEDs for multi-Gb/s visible light communications,” *IEEE Photonics Technology Letters*, vol. 28, no. 19, pp. 2023–2026, 2016.

[6] N. McAlinden, E. Gu, M. D. Dawson, S. Sakata, and K. Mathieson, “Optogenetic activation of neocortical neurons in vivo with a sapphire-based micro-scale LED probe,” *Frontiers in neural circuits*, vol. 9, p. 25, 2015.

[7] C. Goßler, C. Bierbrauer, R. Moser, M. Kunzer, K. Holc, W. Pletschen, K. Köhler, J. Wagner, M. Schwaerzle, P. Ruther, *et al.*, “GaN-based micro-LED arrays on flexible substrates for optical cochlear implants,” *Journal of Physics D: Applied Physics*, vol. 47, no. 20, p. 205401, 2014.

[8] J. Herrnsdorf, Y. Wang, J. J. McKendry, Z. Gong, D. Massoubre, B. Guilhabert, G. Tsiminis, G. A. Turnbull, I. D. Samuel, N. Laurand, *et al.*, “Micro-LED pumped polymer laser: A discussion of future pump sources for organic lasers,” *Laser & Photonics Reviews*, vol. 7, no. 6, pp. 1065–1078, 2013.

[9] “KiCad EDA.” `https://kicad-pcb.org/`. Accessed: 28-02-2020.

[10] “OSH Park.” `https://oshpark.com/`. Accessed: 28-02-2020.

[11] C. Griffin, E. Gu, H. Choi, C. Jeon, J. Girkin, M. Dawson, and G. McConnell, “Beam divergence measurements of InGaN/GaN micro-array light-emitting diodes using confocal microscopy,” *Applied Physics Letters*, vol. 86, no. 4, p. 041111, 2005.

[12] F. Payne and J. Lacey, “A theoretical analysis of scattering loss from planar optical waveguides,” *Optical and Quantum Electronics*, vol. 26, no. 10, pp. 977–986, 1994.

[13] A. W. Snyder and J. Love, *Optical waveguide theory.* Springer Science & Business Media, 2012.

[14] X. Ye, H. Liu, Y. Ding, H. Li, and B. Lu, “Research on the cast molding process for high quality PDMS molds,” *Microelectronic Engineering*, vol. 86, no. 3, pp. 310–313, 2009.

[15] R. G. Hunsperger and J. R. Meyer-Arendt, “Integrated optics: theory and technology,” *Applied Optics*, vol. 31, p. 298, 1992.

[16] Y. C. Kim, “Optimize pattern design for the thin LGP,” *Optik*, vol. 124, no. 15, pp. 2171–2173, 2013.

[17] S.-f. Lin, C.-y. Su, Z.-y. Feng, and X.-d. Li, “Microstructure density generation for backlight display using probability analysis method,” *Journal of Physics D: Applied Physics*, vol. 50, no. 43, p. 435601, 2017.

[18] M. Kusko, C. Kusko, and D. Cristea, “Method of determination of light-scatterer distribution in edge-lit backlight units using an analytical approach,” *JOSA A*, vol. 27, no. 9, pp. 2015–2020, 2010.

[19] J.-G. Chang and Y.-B. Fang, “Dot-pattern design of a light guide in an edge-lit backlight using a regional partition approach,” *Optical Engineering*, vol. 46, no. 4, p. 043002, 2007.

[20] B.-L. Huang, J.-t. Lin, Y. Ye, S. Xu, E.-g. Chen, and T.-L. Guo, “Pattern optimization of compound optical film for uniformity improvement in liquid-crystal displays,” *Optics & Laser Technology*, vol. 97, pp. 254–259, 2017.

[21] Z. Pan and L. Wondraczek, “Light extraction from fundamental modes in modulated waveguides for homogeneous side-emission,” *Scientific reports*, vol. 8, no. 1, pp. 1–11, 2018.

Chapter 4

Other wavelengths and dual-wavelength operation

Previous chapters utilised a broad LED and μLED array that both emit at blue wavelengths. In this chapter, different emission wavelengths and a combination of multiple wavelengths are shown. Firstly, a UV LED is used as the light source and its electrical and spectral properties are discussed. Previously described scatter substrates are used to produce uniform emission and this is compared to the results with the blue LED. Emission at a red wavelength is obtained by adding colour converting quantum dots to a PDMS membrane coupled to the blue μLED. The effect of colour converter concentration is shown as is uniform red emission. Finally, multiwavelength capability is shown by combining colour converters and scatter substrates, producing uniform blue and red emission over the same extraction area.

4.1 Why other wavelengths?

As discussed in Chapter 1, different wavelengths of light are used in phototherapy to treat different dermatological conditions. UV phototherapy is the most common technique, having been utilised medically towards the start of the 20th century [1]. UV light is used clinically, on its own or with a photosensitiser to treat psoriasis [2], vitiligo [3] and eczema [4]. More recently treatment with visible wavelengths is becoming common. Blue light is used to treat infant jaundice [5], mild psoriasis [6], acne [7] or in some cases with a photosensitiser to treat actinic keratosis [8]. Red wavelengths are used for anti-aging [9], to help with wound healing [10], or with a photosensitiser to treat actinic keratosis [11]. Multiple wavelengths of light are desirable for phototherapy devices to treat the vast array of different medical conditions.

4.2 UV LED device

UV phototherapy is typically carried out in a clinical environment and uses large fluorescent lamps. Recently, the use of these devices at-home has become more popular due to the convenience for patients and the decreased demand on healthcare resources. At-home devices are available, however, these still utilise fluorescent lamps [12]. LEDs would make a more compact, energy-efficient, at-home device. UV LEDs are becoming more common in devices as their fabrication and efficiency improves. They have been utilised in a study to treat psoriasis [13]. UV LEDs can be purchased commercially with wavelengths from 360 nm in the UVA to 400 nm. Higher energy wavelengths, UVB and UVC, can be purchased from specialised suppliers.

4.2.1 UV LED properties

The LED utilised for this chapter was a broad area Luxeon UV LED by LumiLEDS [14]. The device consists of an LED chip (1 x 1 mm^2) bonded to a power star as shown in Figure 4.1(a). The LED has poor thermal properties compared to the blue LED [15]. Therefore, when turned on, even at low supply currents, there is a decay in output optical power with time. In order to reduce this decay, the LED has to be bonded to an aluminium alloy heat sink that is 50 mm in diameter and 20 mm thick, shown from the side in Figure 4.1(b).

To measure the electrical and optical properties of the LED, the technique and setup described in Section 2.2.2 was utilised. The LED can be run at currents up to 1000 mA based on the manufacturers data sheet. The output optical power and supplied voltage

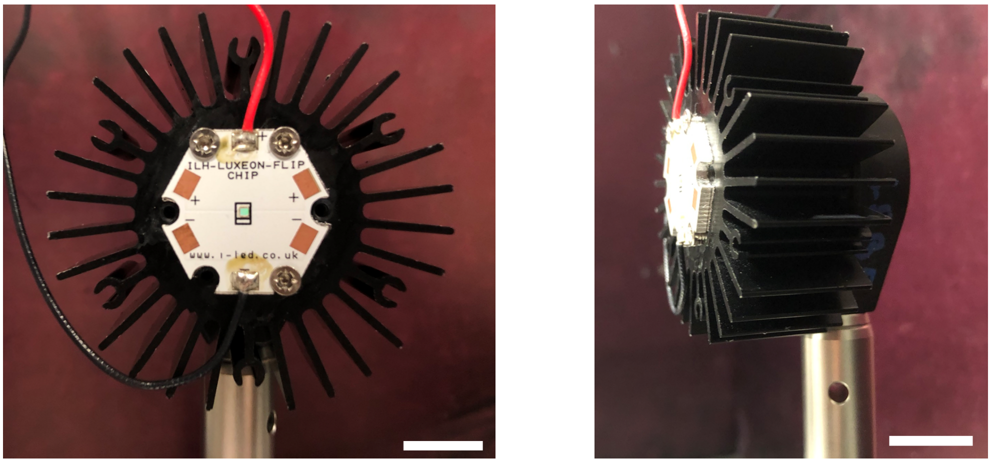

(a) (b)

FIGURE 4.1: Images of the UV LED on its required heatsink, scale is 10 mm

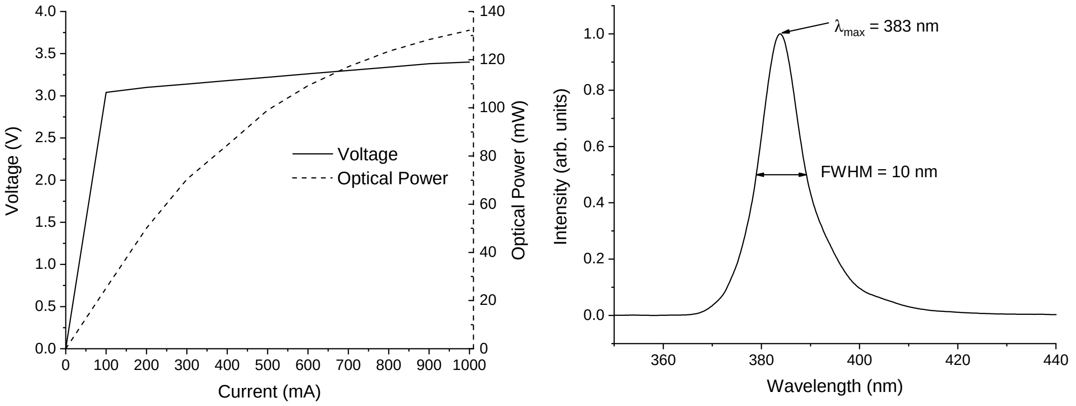

(a) (b)

Figure 4.2: UV LED electronic and spectral properties (a) LIV data and (b) wavelength spectrum of the LED run at a current of 500 mA

for a range of currents from 100 mA to 1000 mA was recorded and a graph of power-current-voltage shown in Figure 4.2(a). Optical powers of 20 mW to 130 mW can be obtained with supply voltages ranging from 2.9 V to 3.3 V. When coupled to the PDMS membrane the LED was run at 500 mA, resulting in an output optical power of 99 mW. Figure 4.1(b) shows the emission spectrum of the LED at 500 mA. The device has a peak wavelength of 383 nm, with a FWHM of 10 nm. This output is in the UVA region of the electromagnetic spectrum.

4.2.2 Simulated coupling

The UV LED can be modelled in the optical simulation, similarly to the blue LED and the μLED, with the main difference being the chief wavelength. There is no rayfile available with the LED therefore, it has to be added into the simulation based on the properties supplied with the manufacturers data sheet. As the angular properties of the emission are given, the LED can be added as a radial source 1 x 1 mm^2 in size. As shown in Sections 2.3.1 and 3.2, a detector was added to the PDMS surface and this placed in contact with the LED source. A ray trace with 5 million trace rays was carried out with an LED optical power of 100 mW and a map of irradiance over the detector surface is recorded. This helps to show the efficiency of the device at coupling light into the membrane.

The detector map is shown in Figure 4.3, the red pixels correspond to areas of high irradiance as seen in the centre of the LED, this decreases down to areas of low/no irradiance which is represented by blue pixels. From the detector viewer, it can be seen that a total power of 55 mW is measured. Comparing the light that enters the PDMS membrane to the overall light output of the LED, it can be seen that a maximum of

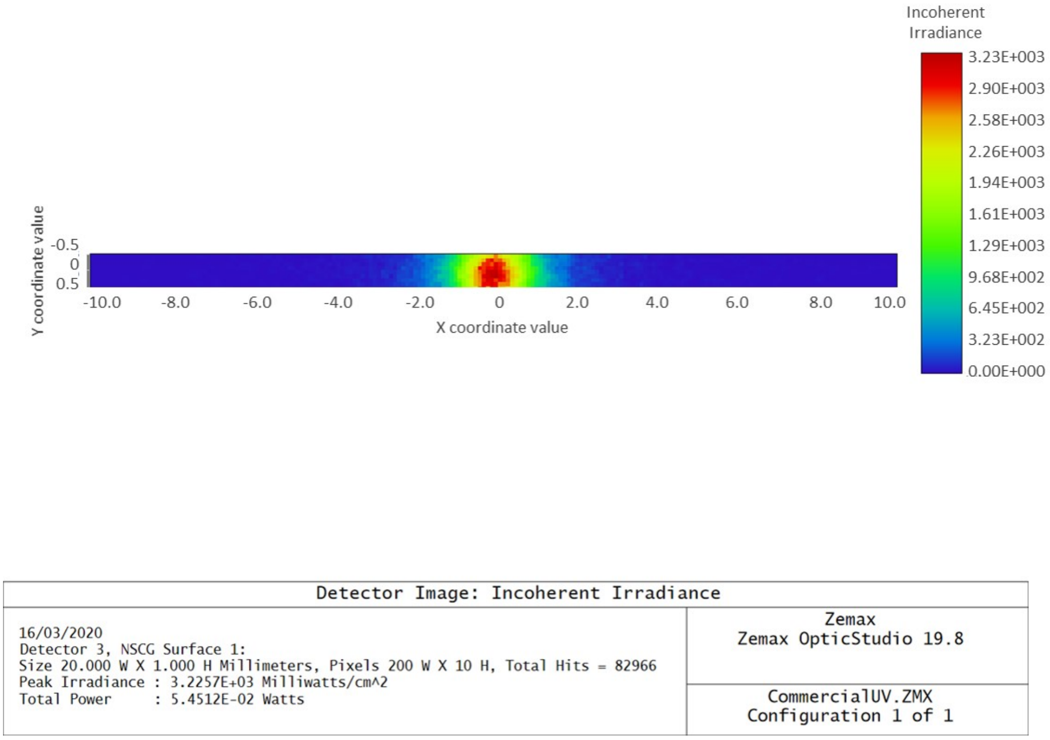

```
Detector Image: Incoherent Irradiance

16/03/2020
Detector 3, NSCG Surface 1:
Size 20.000 W X 1.000 H Millimeters, Pixels 200 W X 10 H, Total Hits = 82966
Peak Irradiance : 3.2257E+03 Milliwatts/cm^2
Total Power     : 5.4512E-02 Watts

Zemax
Zemax OpticStudio 19.8

CommercialUV.ZMX
Configuration 1 of 1
```

FIGURE 4.3: Ray trace detector viewer of UV LED light coupled into the PDMS membrane

55% of the LED light will be coupled into the membrane. The majority of the most intense light (red pixels) will be coupled into the membrane. However, less of the median intensity light (yellow/green) will be coupled into the PDMS membrane due to it being the same thickness as the LED chip. This contributes to the 45% loss in LED coupled light to the membrane.

4.2.3 Experimental coupling

The LED is butt-coupled to the PDMS membrane and the irradiance from the top surface of the membrane is recorded, as in Section 2.4.1. The irradiance trend of the bare PDMS is given in Figure 4.4(a). This is very similar to the irradiance trend seen with the blue LED in Chapter 2 and μLED in Chapter 3. However, the maximum irradiance is measured at the end of the 40 mm long PDMS membrane, rather than initially close to the LED. There is a small initial decay in irradiance at 5 to 12 mm from the LED, this is due to non-guided light leaking from the membrane. The middle guided region of the device from 13 to 35 mm has an average irradiance of 96.0 ± 12 μW/cm^2. An image of the bare PDMS device coupled to the UV LED is shown in Figure 4.4(b). Similarly, as for the same image with the blue LED (Figure 2.6(b)), it can be seen most of the coupled light is emitted at the edges and end of the PDMS membrane.

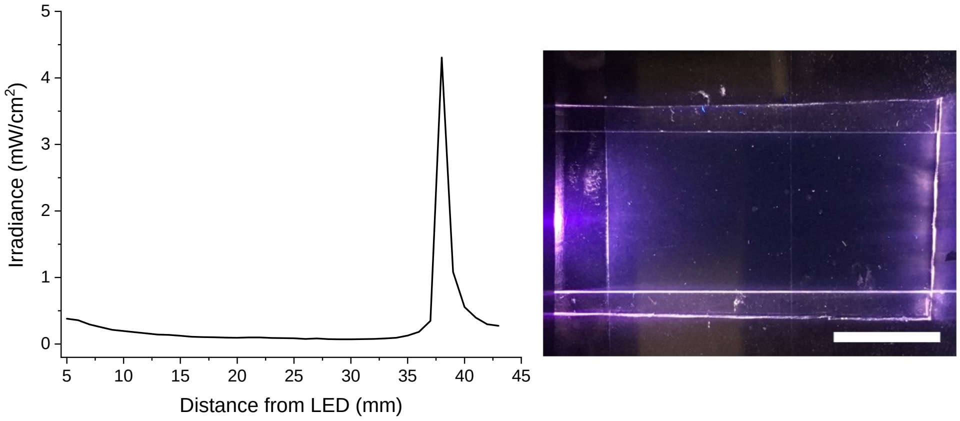

(a)

(b)

FIGURE 4.4: (a) Irradiance graph of bare PDMS membrane and (b) image of PDMS membrane coupled to the UV LED, scale is 10 mm

4.2.4 Effect of flat scatter substrates and UV LED

The same TiO_2/PDMS scatter substrates fabricated in Section 2.6.1 were added to the surface of the PDMS membrane. These were added in the centre width of the membrane, 15 mm distance from the LED. The irradiance at millimetre intervals along the length of the membrane was recorded for the different concentrations of TiO_2, and is shown in Figure 4.5. The black solid line in the graph represents the irradiance from a bare PDMS membrane for comparison.

It can be seen that, as with the blue LEDs, the scatter substrates produce an increase in irradiance over the emissive region from 15 to 30 mm. The scatter substrates also cause a decrease in the edge effect. This is because more light is extracted from the membrane surface, therefore, there is less light scattered when leaving the end of the membrane. From the figure it can be seen that as the TiO_2 concentration increases, the maximum irradiance increases until a maximum irradiance of 17 mW/cm^2 is obtained for 0.25%. At higher concentrations (e.g. 2%), the increased opacity of the films reduces the amount of scattered light extracted through the top surface of the membrane, this results in a decreased irradiance maximum. As well as an increased irradiance maximum, higher concentrations of TiO_2 have a steeper drop off in irradiance with increasing distance from the LED. For example, the 28 mm irradiance is 13% of the 17 mm irradiance for 0.75% TiO_2 sample, whereas this value increases to 47% for the 0.05% TiO_2 sample. It can be seen that the lower concentrations provide a more uniform irradiance over the length of the scatter substrate, however, they also produce lower maximum irradiance values. For example, 3.5 mW/cm^2 and 4.6 mW/cm^2 for the 0.05% and 0.1% TiO_2 substrates respectively.

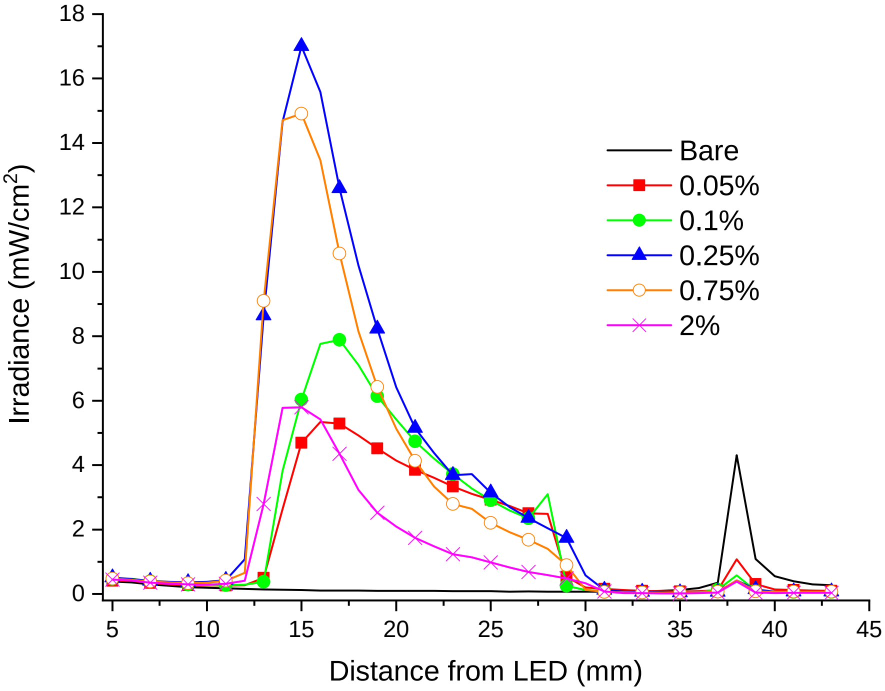

FIGURE 4.5: Irradiance of different concentrations of TiO_2 scatter substrates with increasing distance from the UV LED, the irradiance of the bare PDMS irradiance is given for reference

CCD images were taken of the scatter substrates to produce irradiance maps, as described in Section 2.6.3. The irradiance maps produced for each sample show the trend in light output across the entire substrate, and allow for further comparison between the samples. The maps for the TiO_2 concentrations of 0.05% and 0.75% are shown in Figure 4.6. As can be seen for 0.05% the irradiance is intense over a broad region of the scatter substrate width and length and decreases with increasing distance from the LED, as is seen in the irradiance graph. The intense region of the 0.75% TiO_2 is smaller than that of the 0.05% in both length and width, this decreasing trend is seen with increasing concentration, with both the high and medium irradiance areas decreasing.

From the irradiance maps we can calculate the total power output of each scatter sample in mW; using this and the LED optical power of 99 mW, the efficiency of the devices can be calculated. The actual extraction efficiency of the scatter substrates will be higher than what is calculated here as not all of the LED light is coupled into the PDMS membrane. Table 4.1 lists the peak irradiance, total output power and efficiency for a range of TiO_2 concentrations using the UV LED. From these results, it can be seen that the total output power increases with increasing concentration up to 0.25% and then decreases at higher concentrations. This follows the same trend as the maximum irradiance. The most efficient device at extracting light is the 0.25% TiO_2, which extracts more than 23% of the input power.

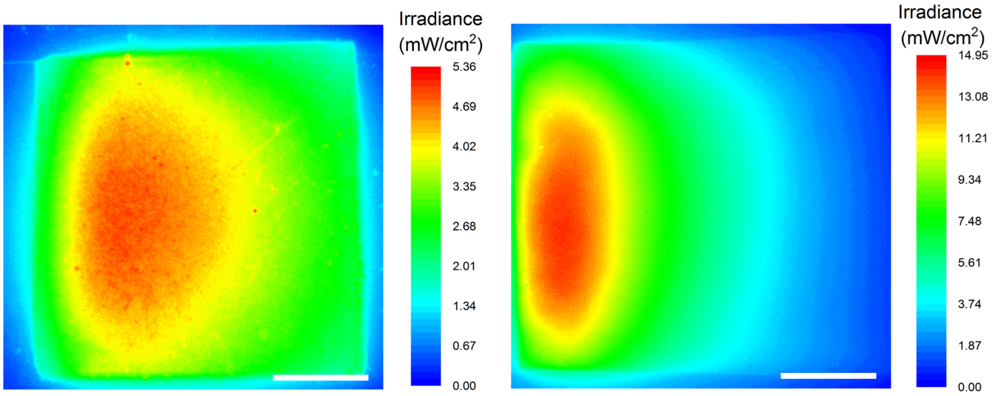

(a) (b)

Figure 4.6: Irradiance maps from CCD images of (a) 0.05% and (b) 0.75% TiO_2 scatter substrates, scale is 5 mm

Table 4.1: Table of maximum irradiance values, total power output and efficiency for different weight ratios of TiO_2, based on the UV LED optical power at 500 mA

TiO_2 concentration (wt%)	Peak average irradiance (mW/cm^2)		Total power (mW)		Efficiency %	
0.04	3.3	±0.03	5.9	±0.24	6.1	±0.3
0.05	5.3	±0.13	9.5	±0.40	9.7	±0.4
0.1	7.9	±0.06	11.8	±0.48	12.1	±0.5
0.25	17.0	±0.28	22.7	±0.95	23.2	±1.0
0.75	14.9	±0.24	18.4	±0.77	18.7	±1.1
1	11.6	±0.05	14.0	±0.56	14.3	±0.9
2	5.8	±0.16	7.9	±0.35	8.1	±0.9

4.2.5 Uniform light extraction with UV LED

The tapered substrates fabricated in Section 2.7.2 were added to the surface of the PDMS membrane, 15 mm from the LED. Irradiance measurements were carried out as before, with the fibre being held at a distance of 5 mm from the surface of the waveguide to allow for measurements over the whole length of the scatter substrate. Figure 4.7(a) shows the irradiance results from these samples compared to the bare membrane. From these results, we can see that with a curing angle of 15°, the 0.05% and 0.1% samples show a decrease in irradiance with increased distance from the LED. The 0.04% sample, however, shows an average uniform irradiance of 2.5 ± 0.1 mW/cm^2 along the length of the scatter substrate followed by an increase to 2.8 mW/cm^2 at the furthest end of the substrate due to light scattering from the rough edges. An image of the 0.04% sample is given in Figure 4.7(b).

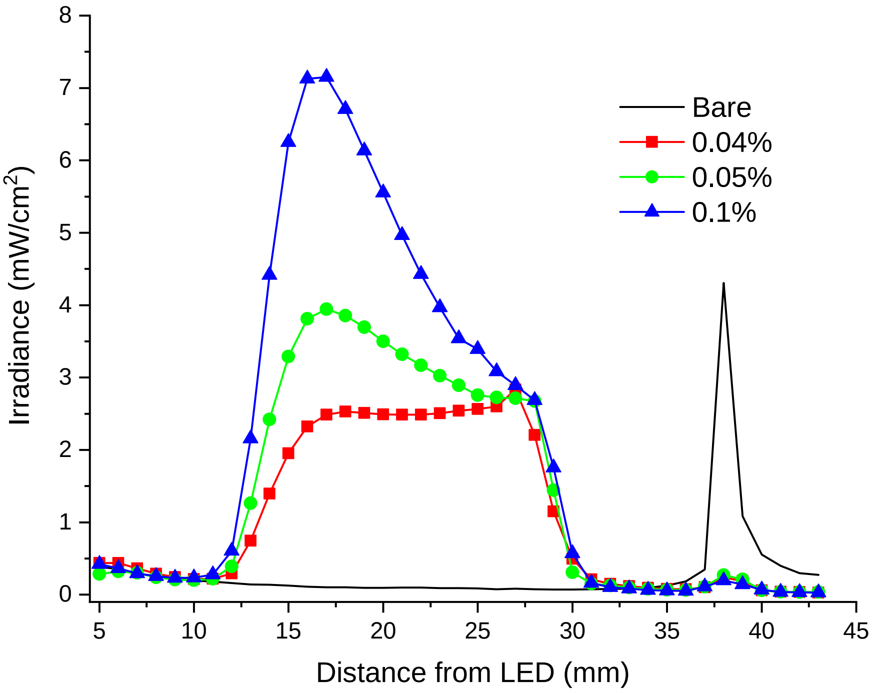

(a)

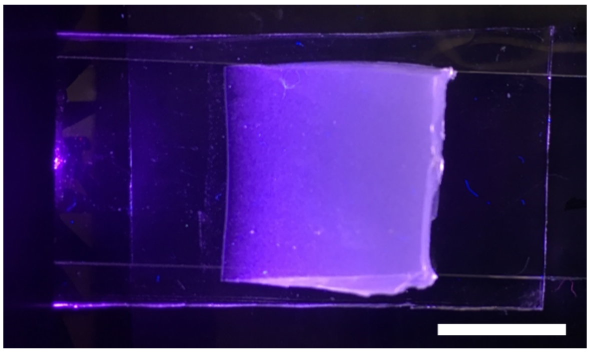

(b)

Figure 4.7: (a) Irradiance of different concentrations of tapered TiO_2 scatter substrates with increasing distance from the UV LED, the irradiance of the bare PDMS irradiance is given for reference and (b) an image of the tapered 0.04% TiO_2 on the PDMS membrane, scale is 10 mm

As before, the output power from these extraction substrates is calculated, along with the efficiency of the overall devices based on the LED input power. Table 4.2, lists the maximum irradiance, power output and efficiency for the different tapered samples. For the uniform sample it can be seen that the total output power over the extraction area was 5.8 mW, resulting in an overall device efficiency of 6%, not considering the lost light that is not coupled into the PDMS membrane initially.

Table 4.2: Table of maximum irradiance values, total power output and efficiency for different weight ratios of tapered TiO_2, based on an input UV LED optical power of 99 mW

TiO_2 concentration (wt%)	Peak average irradiance (mW/cm^2)		Total power (mW)		Efficiency %	
0.04	2.8	±0.03	5.8	±0.23	6.0	±0.3
0.05	3.9	±0.08	7.4	±0.31	7.6	±0.6
0.1	7.1	±0.08	10.3	±0.42	10.5	±0.4

4.2.6 Comparison of device with UV and blue LEDs

From the optical simulations, it has been shown that the UV LED couples more LED light into the membrane (55%), compared to the blue broad LED (45%). This is due to the design of the LEDs, the blue LED has a silicone lens over the chip, increasing the emission area, therefore decreasing the light intensity coupled into the PDMS membrane. The UV LED has no lens, the PDMS can coupled directly to the chip therefore more light is coupled.

The irradiance from a bare PDMS membrane is very similar for both source wavelengths and light is extracted from both by adding TiO_2/PDMS scatter substrates to the PDMS membrane. There is a difference in the effect of concentration on extracted light between the two wavelengths. A comparison for the flat TiO_2 scatter substrates is given in Table 4.3.

Table 4.3: Table comparing the maximum irradiance, total power output and efficiency for TiO_2 scatter substrates with the UV and blue wavelength broad LEDs

TiO_2 concentration	Maximum irradiance mW/cm^2		Power output mW		Efficiency %			
	μLED	LED*	μLED	LED*	μLED		LED	
0.05	5.3	4.0	9.5	4.4	9.7	±0.4	4.3	±0.1
0.1	7.9	6.4	11.8	9.0	12.1	±0.5	8.7	±0.2
0.25	17.0	13.9	22.7	18.4	23.2	±1.0	17.9	±0.4
0.75	14.9	18.3	18.4	21.8	18.7	±1.1	21.2	±0.5
1	11.6	17.4	14.0	20.2	14.3	±0.9	19.6	±0.4
2	5.8	14.5	7.9	17.6	8.1	±0.9	17.1	±0.5

The wavelengths follow a similar trend of increased maximum irradiance and power output with increased concentration. However, the values are higher for the UV wavelength, so more light is extracted compared to the blue LED. Both sources have similar maximum power outputs with 22.7 mW for the UV LED and 0.25% TiO_2, and 21.8 mW for the blue LED and 0.75% TiO_2. Both wavelengths reach a limit of maximum extraction,

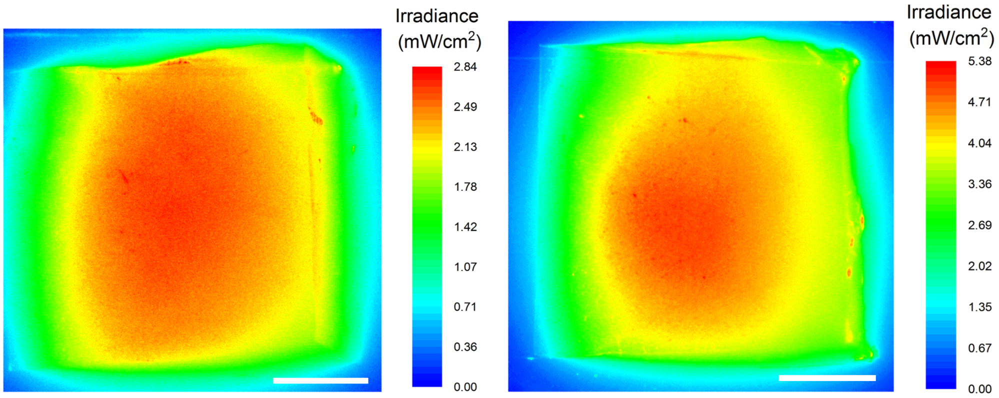

(a) (b)

Figure 4.8: Irradiance maps from CCD images of uniform devices at different wavelengths (a) UV LED and 0.04% tapered TiO_2 and (b) blue LED with 0.05% tapered TiO_2, scale is 5 mm

after which the extracted light decreases although the concentration of nanoparticles increases. This is caused by multiple scattering events taking place within the substrate, reducing the intensity of light extracted. This maximum extraction value is different for the different wavelengths, with the UV LED limit being 0.25% and the blue LED limit being 0.75%. This change in extraction with wavelength is due to the scattering of light depending upon the wavelength [16]. Shorter wavelengths are scattered more strongly than longer wavelengths, hence the increase in extracted light with the UV LED compared to the blue LED, with the same concentration of TiO_2.

Due to the difference in extracted light, a different concentration of TiO_2 is required to produce uniform emission with the tapered substrates. The blue LED produced a uniform irradiance of 4.5 mW/cm^2 (Section 2.7.3) using the tapered 0.05% TiO_2 substrate. For uniform irradiance from the UV LED membrane, the 0.04% tapered TiO_2 substrate had to be used. Producing an average irradiance of 2.5 mW/cm^2 over the length of the substrate. The irradiance maps for both samples are shown in Figure 4.8. It can be seen that both have intense irradiance in the centre of the substrate, covering most of the width. Comparing the maps, it can be seen that the UV device is more uniform over a slightly larger area than the blue, seen in the SD of the means, with the UV having a deviation of 0.1 mW/cm^2 compared to the SD of 0.8 mW/cm^2 for the blue device. Due to the larger maximum irradiance and higher output power, the blue device is more efficient based on the input optical power. The blue device has an efficiency of 8.4% compared to the UV efficiency of 6%.

4.2.7 UV LED summary

Uniform emission was shown in the UV using a tapered TiO_2 scatter substrate. Based on the similarities between this and the blue LED, a similar formula for the concentration gradient could be used to produce uniform emission from a flat substrate. The gradient would need to consist of a lower concentration for the maximum than that seen with the blue LED. This is due to the strong wavelength dependence of scattering [16]. In the optical simulation, more of the broad UV light is coupled into the membrane, 55% compared to 45% for the blue broad LED, despite the LED chips being the same size. This is due to the silicone casing surrounding the blue LED, increasing the extraction profile of the LED [17]. The UV LED has an exposed LED chip which has a decreased extraction profile and allows for a physically better coupling to the PDMS membrane.

4.3 Colour convertors for red emission

As well as using different LED sources, colour converters can be utilised to produce a different emission wavelength. Common colour converters are colloidal quantum dots (CQDs), these act as down-converters, absorbing short wavelength light and emitting light of a higher wavelength [18, 19]. CQDs can be encapsulated in polymer matrices to enhance the stability and protect the dots from environmental effects [18].

4.3.1 Fabrication of colour converter membranes

Red CQDs (630nm-emitting CdSSe/ZnS, 6nm mean diameter) were diluted at different concentrations in toluene before being added to a set weight of uncured PDMS. The calculations used in our lab depend on 20% of CQD solution being added to a known mass of uncured PDMS. There is a limit on the amount of CQDs that can be added to the uncured PDMS, above 0.5% CQDs to PDMS mass ratio results in the PDMS not curing. The PDMS polymerisation process utilises a platinum-based catalyst for a hydrosilylation reaction, this process can be inhibited by electron deficient molecules [20]. Although the exact ligands in the CQDs utilised are unknown, many ligand types are electron-deficient [21].

Table 4.4: Table of CQD concentration in toluene and resulting concentration in PDMS converter substrates

CQD concentration in toluene (mg/ml)	CQD concentration in PDMS (%)
5	0.1
10	0.2
15	0.3
25	0.5

The CQDs were added to the uncured PDMS and the mixture stirred to fully homogenise. The resultant solution was added to a mould to produce 1 mm thick substrates. These were cured at 80°C for 6 hours, before being cut to produce substrates 15 x 15 x 1 mm^3. The concentrations of CQDs utilised, and the resulting weight ratio of CQDs to PDMS in the substrates is given in Table 4.4. Images of the substrates under white light are shown in Figure 4.9(a).

The emission of the CQD substrate being excited with the μLED array is shown in Figure 4.9(b). The samples have a peak red wavelength at 634 nm with a FWHM of 29 nm.

4.3.2 Irradiance of colour converters

The CQD substrates are added to the PDMS membrane similarly to the TiO_2 substrates, in the centre of the membrane width, 15 mm from the μLED. The μLED is run at a current of 120 mA, producing an output optical power of 10 mW. Spectral irradiance is measured as before at millimetre intervals along the length of the membrane. The

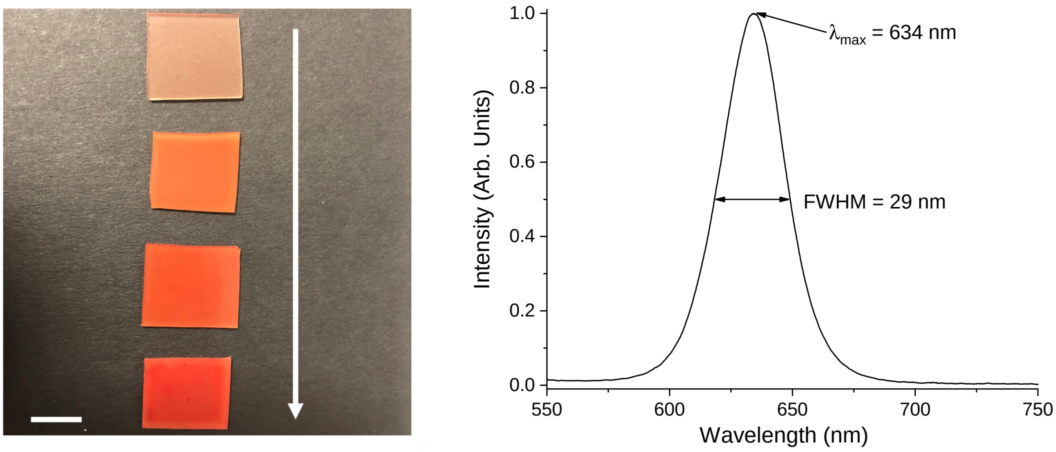

(a) (b)

Figure 4.9: (a) Image of CQD substrates in white light, arrow represents increasing CQD concentration from 0.1% to 0.5%, scale is 10 mm and (b) emission spectrum of CQDs in PDMS substrate

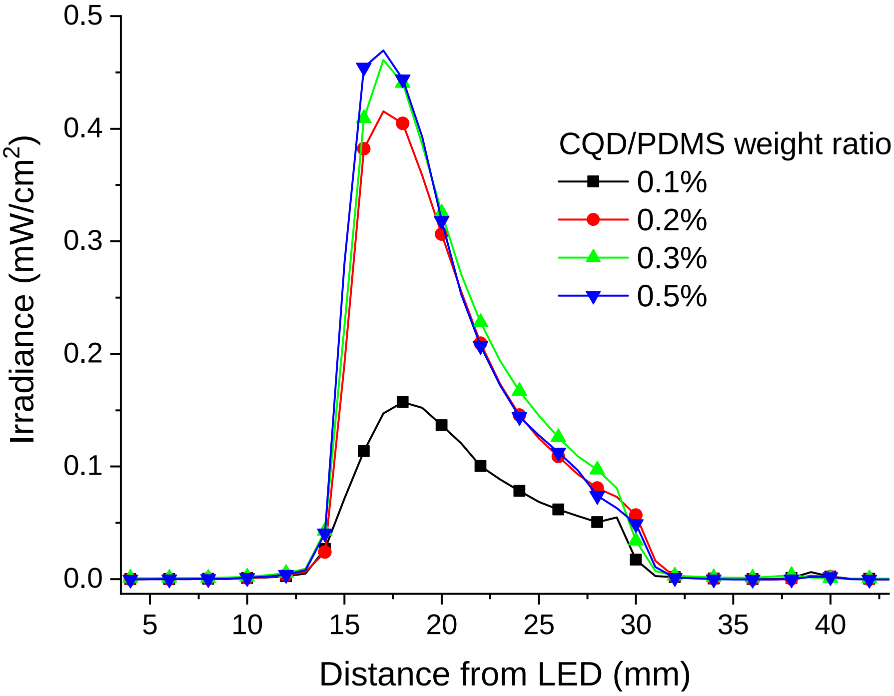

FIGURE 4.10: Irradiance from PDMS membrane with CQD substrates added

irradiance is obtained by integrating over the region of 550 nm to 700 nm. Therefore, the irradiance recorded is only associated with the CQD substrate emission. The irradiance of the different concentrations of CQD substrates is shown in Figure 4.10.

CQD substrates show a similar irradiance profile to the TiO_2 substrates. Initially, close to the LED (15 mm), an irradiance maximum for the sample is measured, the irradiance then decays along the remaining length of the substrate. It can be seen that a low CQD concentration (0.1%) produces a lower irradiance maximum at 0.16 mW/cm^2, however, the profile is broader and more uniform along the length than the higher concentrations. For the other substrates, there is a slight increase in irradiance maximum with increasing concentration with a maximum of 0.47 mW/cm^2 being obtained for the 0.5% CQD substrate. As for the TiO_2 samples, a higher irradiance maximum leads to a quicker drop in irradiance over the length (or a decreased uniformity). This is due to the blue light decreasing along the length of the CQD substrate due to absorption.

4.3.3 Uniform red emission

Similarly to the scattering effect with TiO_2, the concentration of CQDs in the substrate could be decreased further to obtain uniform emission. However, this would result in a very low value for the irradiance. Light scattering substrates can be used along with the CQDs to scatter more light further from the μLED, which can then be absorbed and

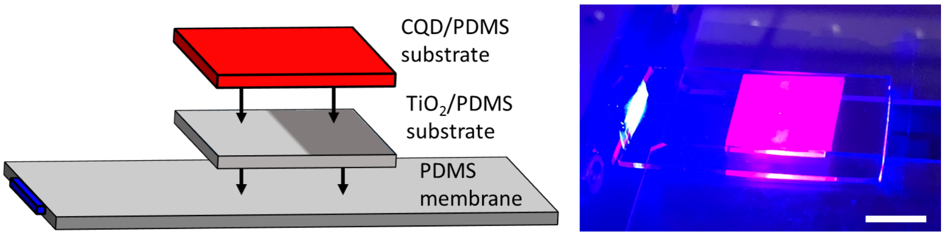

(a) (b)

FIGURE 4.11: (a) Method for obtaining uniform red emission from device and (b) image of this method being tested, scale is 10 mm

down-converted by the CQDs further along the length of the membrane. This is shown in schematic form in Figure 4.11(a).

4.3.3.1 Fabrication

Substrates with a TiO_2 concentration gradient were fabricated similarly to Section 3.6.5. However, there were only two regions of different TiO_2 concentration for simplicity. Region 1, 7.5 mm in length consisted only of PDMS, region 2, also 7.5 mm in length, consisted of either 0.1, 0.2 or 0.5% TiO_2 in PDMS.

4.3.3.2 Method

These cured samples, 15 x 15 x 1 mm^3, were added to the centre of the PDMS membrane, 15 mm from the μLED. The CQD substrates were then added to the top of the scatter substrate and the irradiance measured, as per Section 4.3.2.

4.3.3.3 Uniform red irradiance

The irradiance from the 0.5% CQD substrate was measured when added to the three different scattering substrates on the PDMS membrane. The irradiance results are shown in Figure 4.12(a). It can be seen that compared to the irradiance from the CQD substrates alone (Figure 4.10), the irradiance values are lower than that of 0.5% CQD. This is because there is less light in the scatter substrate than in the PDMS membrane, therefore there is less that can be converted into red light. The irradiance values are still higher than the low concentration CQD sample (0.1%). When the scatter sample has a concentration increase to 0.1% or 0.2% TiO_2, the irradiance from the CQD substrate still decays with distance, although this decay is less harsh than with the CQD substrates alone. Having an increase to 0.5% TiO_2, however, results in a uniform profile of red irradiance being obtained from the device. An average irradiance of 270 ± 32 $\mu W/cm^2$

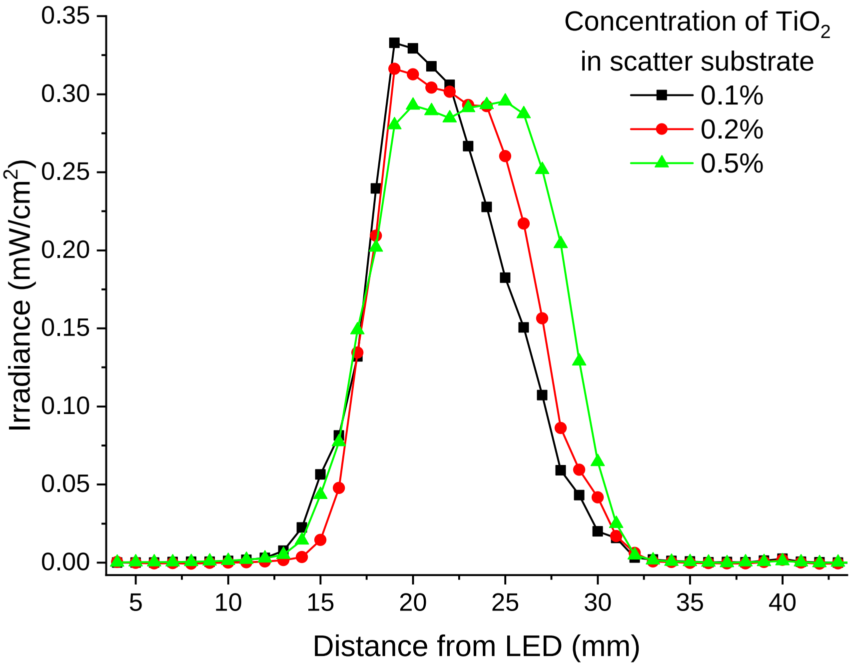

(a)

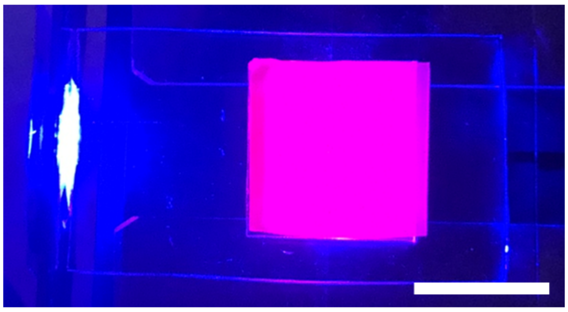

(b)

FIGURE 4.12: (a) Irradiance of 0.5% CQD converter substrate with scattering films of different concentration added between membrane and substrate and (b) image of uniform red device, scale is 10 mm

is achieved with the 0.5% CQD substrate and a scatter substrate of PDMS and 0.5% TiO_2/PDMS.

A CCD image of this sample can be taken to produce an irradiance map, as shown in Section 2.6.3. However, a long-pass filter (Thorlabs, FEL0500) is added to the setup, with a cut-on wavelength of 500 nm. This is to remove any scattered μLED light, to ensure the map contains only information at red wavelengths.

The irradiance map of the uniform red emitting device is shown in Figure 4.13. As was shown in the irradiance graphs, the irradiance is uniform over the centre of the substrate. It can also be seen that it is uniform across the width of the CQD substrate. From this map, the total output power of the substrate is calculated to be 0.6 mW.

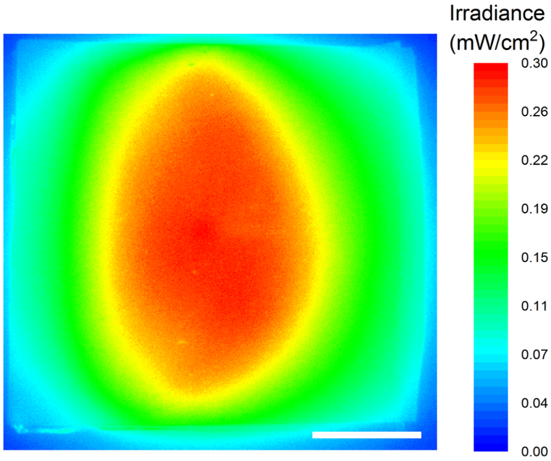

FIGURE 4.13: Irradiance map of uniform red device using a scatter substrate and 0.5% CQD substrate, scale is 5 mm

Based on an input μLED optical power of 10 mW, this results in an overall device efficiency of 6%. Again, this efficiency value is realistically higher considering not all of the μLED light will be coupled into the PDMS membrane. The output power is much lower for this device with colour converters than for the concentration gradient uniform blue device (Section 3.7.1). This is due to the colour conversion process not being 100% efficient [22]. As the absorption profile of the CQDs overlaps with the emission profile, some of the converted light is not reabsorbed by the quantum dots. Some LED light is also not converted at all and scatters/reflects based on the laws of total internal reflection. Although this device produces uniform red irradiance, there is still blue irradiance being extracted over the emissive region.

4.4 Multiwavelength capability

For some dermatological conditions, multiwavelength emission is beneficial. For example, utilising the antibacterial effects of blue light with the anti-inflammatory effects of red light has been shown to increase skin healing [23, 24]. This combination of wavelengths has also been used to treat diabetic skin ulcers for the same properties [25]. The device platform with the blue μLED array combined with TiO_2 scatter substrate and CQD converter substrate has the capability to produce a multiwavelength output.

4.4.1 Obtaining multiwavelength emission

In Section 4.3, the device was utilised to produce uniform red emission using a colour converter substrate (15 x 15 x 1 mm^3), with a CQD concentration of 0.5%. Between the PDMS membrane and CQD substrate a scatter film was added (15 x 15 x 1 mm^3).

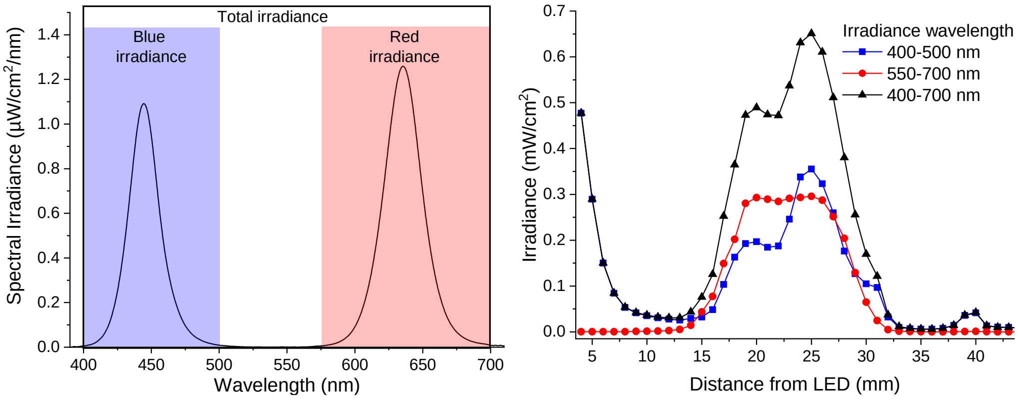

(a) (b)

FIGURE 4.14: (a) Spectral irradiance from uniform red device, measured at 23 mm from μLED and (b) irradiance of the uniform red device at blue and red wavelengths, along with the total irradiance

The first 7.5 mm of this film was PDMS, followed by 7.5 mm of 0.5% TiO_2 in PDMS. This combination allowed uniform red emission to be obtained over the scatter substrate (Section 4.3.3.3).

As the irradiance is obtained from the spectral irradiance (Section 2.4.1), the irradiance from different regions of the spectrum can be measured at the same time. Figure 4.14(a) shows the spectral irradiance, 23 mm from the μLED, for the uniform red device. Integrating over the highlighted wavelengths, gives a blue irradiance of 0.25 mW/cm^2 and a red irradiance of 0.3 mW/cm^2. The overall irradiance across the visible spectrum at that measurement point was 0.55 mW/cm^2.

The blue and red irradiance for the uniform red device is given in Figure 4.14(b), as is the total irradiance from 400 to 700 nm. It can be seen that, although the red irradiance is uniform, the blue irradiance (and in turn the total irradiance) is not uniform. The extracted blue light increases with distance from the μLED, plateauing between 18 mm and 22 mm from the μLED. The irradiance then increases further with a maximum of 0.35 mW/cm^2 being recorded 25 mm from the μLED. This sudden increase in irradiance is due to more blue light being scattered by the increase in TiO_2 nanoparticles in the scatter substrate. Not all of the scattered blue light is converted to red light by the CQDs resulting in an increase in the blue emission.

4.4.2 Multiwavelength uniformity

Different combinations of scatter substrates and concentrations of CQD converting substrates were tested to determine the effect on both the red and blue irradiance. By using a scatter substrate of the same design as Section 4.3.3, but with a lower concentration of

TiO_2 (0.2% compared to 0.5%) and combining this with a lower concentration of CQD in the converting substrate (0.2% compared to 0.5%) a uniform irradiance of both blue and red wavelengths can be obtained. The irradiance results are shown in Figure 4.15.

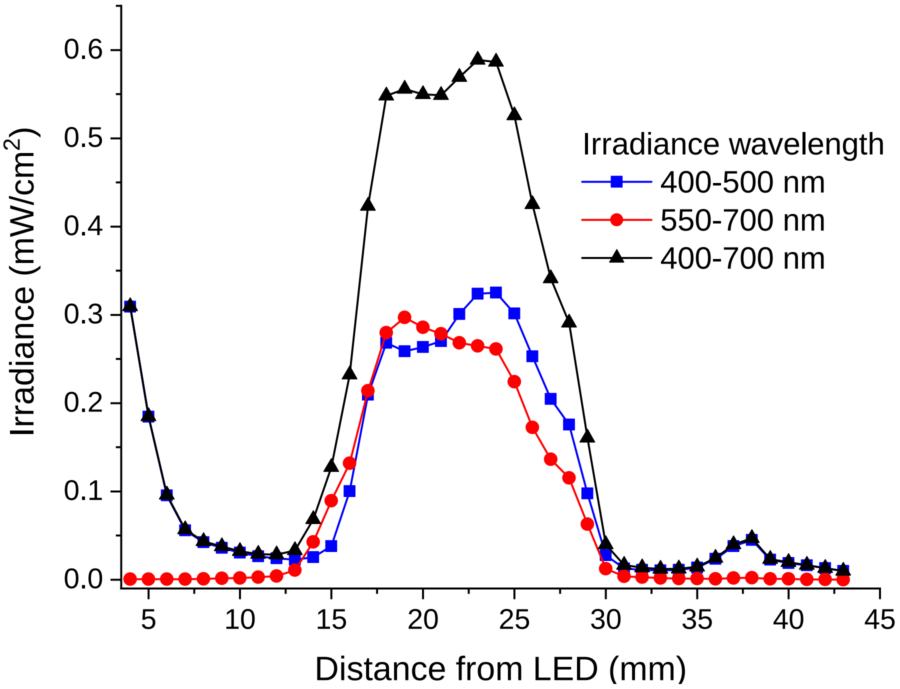

Figure 4.15: Irradiance of a PDMS membrane, with an extraction substrate consisting of PDMS and 0.2% TiO_2 PDMS and a CQD converter substrate of 0.2%

From this it can be seen that a uniform total irradiance of 0.53 mW/cm^2 can be obtained, comprised of a uniform red irradiance of 0.26 mW/cm^2 and a uniform blue irradiance of 0.27 mW/cm^2. Irradiance maps can be used to observe the irradiance over the entire extraction region. The total irradiance map can be produced following the steps in Section 2.6.3. In order to view the irradiance maps for the red and blue irradiance separately, filters have to be added to the imaging setup to block out the other wavelength. For the blue irradiance, a short-pass filter (Thorlabs, FES500) is added to the setup with a cut-off wavelength of 500 nm, stopping any light above this wavelength being imaged. For the red irradiance, a long-pass filter (Thorlabs, FEL0500) is added to the setup with a cut-on wavelength of 500 nm, any light below this wavelength will be absorbed/reflected.

The irradiance maps of the uniform multiwavelength device are shown in Figure 4.16 along with an image of the device. From these the power output of the device at each wavelength has been calculated, as has the total power output regardless of wavelength. The blue extracted light has an optical power of 0.54 mW and the red extracted light has an optical power of 0.51 mW. This then leads to a total optical power of 1.1 mW, giving the device an efficiency of 11% based on the μLED input power.

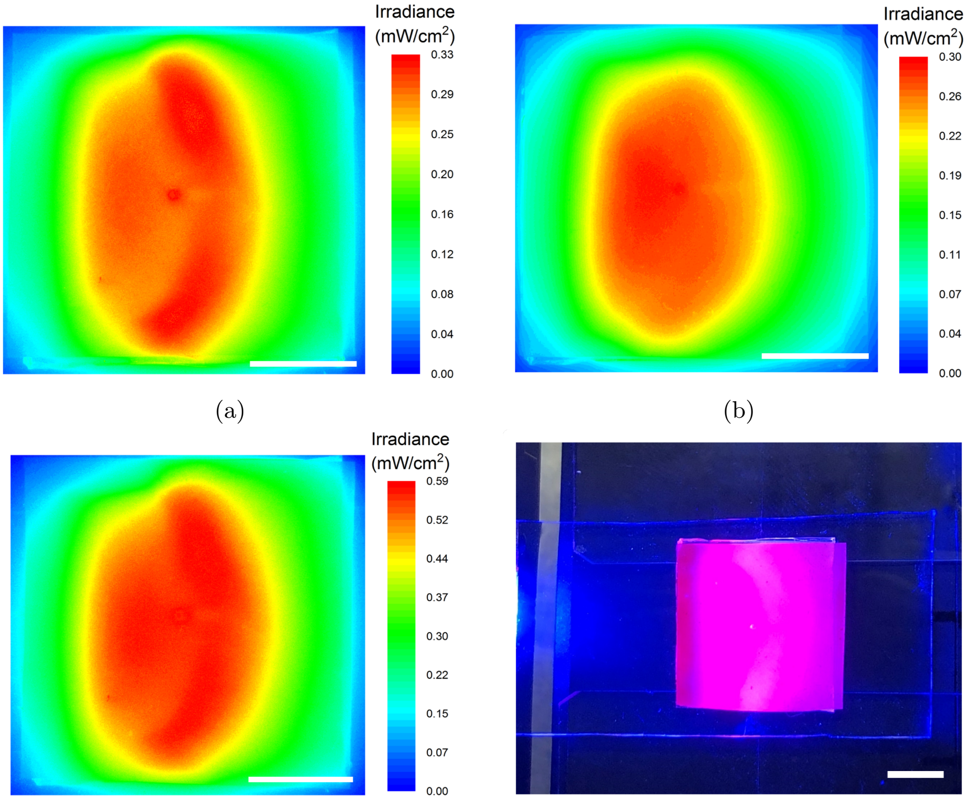

(a) (b)

(c) (d)

FIGURE 4.16: Irradiance maps from the multiwavelength device, (a) blue wavelength map, (b) red wavelength maps, (c) all visible wavelengths map and (d) an image of the multiwavelength device, 5 mm scale

4.5 Summary

In this chapter, the ability of the device design to be utilised at other wavelengths has been realised. The source wavelength can be changed and the irradiance extracted from the PDMS light guide using scattering nanoparticles. The concentration of these particles has to change to produce uniform emission due to the wavelength dependency of light scattering. Uniform emission at a UVA wavelength of 383 nm was obtained using a tapered nanoparticle substrate. Although not tested, theoretically the concentration gradient method utilised in Section 3.6 could be adapted for this lower wavelength, to achieve a higher irradiance with a thinner device structure. If lower wavelengths have to be realised, for example narrowband UVB, the nanoparticles utilised to extract light may have to change due to increased TiO_2 absorption at UV wavelengths [26]. Possible nanoparticles include zirconium dioxide (ZrO_2) or hafnium dioxide (HfO_2). These have similar properties to TiO_2, however, their larger band gap means less UV light will be absorbed [27]. ZrO_2 has even been shown to be dispersed in a PDMS matrix to produce a high refractive index composite [28]. An alternative solution to nanoparticles would be to utilise a porous PDMS extraction substrate. This would scatter light in a similar method to the high refractive index nanoparticles, with the difference of the pores being low refractive index (air).

This chapter also utilised substrates of CQDs in PDMS to convert the blue μLED light into red light. The substrate fabrication and effect of different concentrations was discussed. The combination of TiO_2/PDMS scatter substrates with CQD converting substrates produced a uniform red irradiance over the extraction area. By adjusting the concentrations of CQDs and TiO_2 a device with uniform multiwavelength irradiance was obtained. One major challenge of the colour converting device is the use of cadmium-based quantum dots. These are encapsulated in a polymer matrix which helps decrease the degradation of the quantum dots, caused by oxygenation and thermal effects. However, the use of them in a biological capacity is restricted due to their toxicity [29]. Many studies have been carried out to produce alternative materials, so called cadmium-free quantum dots [30]. These alternative materials do not yet meet the optical properties of their cadmium-based counterparts, although they are progressively improving [31].

References

[1] H. Hönigsmann, "History of phototherapy in dermatology," *Photochemical & photobiological sciences*, vol. 12, no. 1, pp. 16–21, 2013.

[2] H. Hönigsmann, "Phototherapy for psoriasis," *Clinical and experimental dermatology*, vol. 26, no. 4, pp. 343–350, 2001.

[3] J. M. Bae, H. M. Jung, B. Y. Hong, J. H. Lee, W. J. Choi, J. H. Lee, and G. M. Kim, "Phototherapy for vitiligo: a systematic review and meta-analysis," *JAMA dermatology*, vol. 153, no. 7, pp. 666–674, 2017.

[4] N. J. Reynolds, V. Franklin, J. C. Gray, B. L. Diffey, and P. M. Farr, "Narrow-band ultraviolet B and broad-band ultraviolet A phototherapy in adult atopic eczema: a randomised controlled trial," *The Lancet*, vol. 357, no. 9273, pp. 2012–2016, 2001.

[5] M. J. Maisels and A. F. McDonagh, "Phototherapy for neonatal jaundice," *New England Journal of Medicine*, vol. 358, no. 9, pp. 920–928, 2008.

[6] S. Pfaff, J. Liebmann, M. Born, H. F. Merk, and V. Von Felbert, "Prospective randomized long-term study on the efficacy and safety of UV-free blue light for treating mild psoriasis vulgaris," *Dermatology*, vol. 231, no. 1, pp. 24–34, 2015.

[7] T.-Y. Tzung, K.-H. Wu, and M.-L. Huang, "Blue light phototherapy in the treatment of acne," *Photodermatology, photoimmunology & photomedicine*, vol. 20, no. 5, pp. 266–269, 2004.

[8] D. J. Piacquadio, D. M. Chen, H. F. Farber, J. F. Fowler Jr, S. D. Glazer, J. J. Goodman, L. L. Hruza, E. W. Jeffes, M. R. Ling, T. J. Phillips, *et al.*, "Photodynamic therapy with aminolevulinic acid topical solution and visible blue light in the treatment of multiple actinic keratoses of the

face and scalp: Investigator-blinded, phase 3, multicenter trials," *Archives of dermatology*, vol. 140, no. 1, pp. 41–46, 2004.

[9] M. A. Trelles, "Phototherapy in anti-aging and its photobiologic basics: a new approach to skin rejuvenation," *Journal of cosmetic dermatology*, vol. 5, no. 1, pp. 87–91, 2006.

[10] B. J. Erdle, S. Brouxhon, M. Kaplan, J. Vanbuskirk, and A. P. Pentland, "Effects of continuous-wave (670-nm) red light on wound healing," *Dermatologic Surgery*, vol. 34, no. 3, pp. 320–325, 2008.

[11] D. M. Pariser, N. J. Lowe, D. M. Stewart, M. T. Jarratt, A. W. Lucky, R. J. Pariser, and P. S. Yamauchi, "Photodynamic therapy with topical methyl aminolevulinate for actinic keratosis: results of a prospective randomized multicenter trial," *Journal of the American Academy of Dermatology*, vol. 48, no. 2, pp. 227–232, 2003.

[12] S. Lim, "Phototherapy and the benefits of LEDs," *Journal of the Society for Information Display*, vol. 19, no. 12, pp. 882–887, 2011.

[13] L. Kemény, Z. Csoma, E. Bagdi, A. Banham, L. Krenacs, and A. Koreck, "Targeted phototherapy of plaque-type psoriasis using ultraviolet B–light-emitting diodes," *British Journal of Dermatology*, vol. 163, no. 1, pp. 167–173, 2010.

[14] "Lumileds UV LEDs." `https://www.lumileds.com/products/uv-leds`. Accessed: 2020-04-17.

[15] F. Arques-Orobon, N. Nuñez, M. Vazquez, C. Segura-Antunez, and V. González-Posadas, "High-power UV-LED degradation: Continuous and cycled working condition influence," *Solid-State Electronics*, vol. 111, pp. 111–117, 2015.

[16] A. Cox, A. J. DeWeerd, and J. Linden, "An experiment to measure Mie and Rayleigh total scattering cross sections," *American Journal of Physics*, vol. 70, no. 6, pp. 620–625, 2002.

[17] W. H. Smits, R. F. Hendriks, G. Basin, F. H. Konijn, R. S. West, P. S. Martin, and G. Harbers, "Wide emitting lens for LED useful for backlighting," Apr. 1 2008. US Patent 7,352,011.

[18] N. Laurand, B. Guilhabert, J. Mckendry, A. Kelly, B. Rae, D. Massoubre, Z. Gong, E. Gu, R. Henderson, and M. Dawson, "Colloidal quantum dot nanocomposites for visible wavelength conversion of modulated optical signals," *Optical Materials Express*, vol. 2, no. 3, pp. 250–260, 2012.

[19] F. Zhang, X. Feng, Y. Zhang, L. Yan, Y. Yang, and X. Liu, "Photoluminescent carbon quantum dots as a directly film-forming phosphor towards white LEDs," *Nanoscale*, vol. 8, no. 16, pp. 8618–8632, 2016.

[20] L. N. Lewis, J. Stein, Y. Gao, R. E. Colborn, and G. Hutchins, "Platinum catalysts used in the silicones industry," *Platinum Metals Review*, vol. 41, no. 2, pp. 66–75, 1997.

[21] J. Zhou, Y. Liu, J. Tang, and W. Tang, "Surface ligands engineering of semiconductor quantum dots for chemosensory and biological applications," *Materials Today*, vol. 20, no. 7, pp. 360–376, 2017.

[22] S. Nizamoglu and H. V. Demir, "Excitation resolved color conversion of CdSe/ZnS core/shell quantum dot solids for hybrid white light emitting diodes," *Journal of Applied Physics*, vol. 105, no. 8, p. 083112, 2009.

[23] P. Papageorgiou, A. Katsambas, and A. Chu, "Phototherapy with blue (415 nm) and red (660 nm) light in the treatment of acne vulgaris," *British journal of Dermatology*, vol. 142, no. 5, pp. 973–978, 2000.

[24] D. J. Goldberg and B. A. Russell, "Combination blue (415 nm) and red (633 nm) led phototherapy in the treatment of mild to severe acne vulgaris," *Journal of Cosmetic and Laser Therapy*, vol. 8, no. 2, pp. 71–75, 2006.

[25] K. H. Beckmann, G. Meyer-Hamme, and S. Schröder, "Low level laser therapy for the treatment of diabetic foot ulcers: a critical survey," *Evidence-Based Complementary and Alternative Medicine*, vol. 2014, 2014.

[26] M. M. Khan, S. A. Ansari, D. Pradhan, M. O. Ansari, J. Lee, M. H. Cho, *et al.*, "Band gap engineered TiO_2 nanoparticles for visible light induced photoelectrochemical and photocatalytic studies," *Journal of Materials Chemistry A*, vol. 2, no. 3, pp. 637–644, 2014.

[27] S. Tkachev, M. Manghnani, A. Niilisk, J. Aarik, and H. Mändar, "Raman and Brillouin scattering spectroscopy studies of atomic layer-deposited ZrO_2 and HfO_2 thin films," *Spectrochimica Acta Part A: Molecular and Biomolecular Spectroscopy*, vol. 61, no. 10, pp. 2434–2438, 2005.

[28] S. Lee, H.-J. Shin, S.-M. Yoon, D. K. Yi, J.-Y. Choi, and U. Paik, "Refractive index engineering of transparent Zro_2 polydimethylsiloxane nanocomposites," *Journal of Materials Chemistry*, vol. 18, no. 15, pp. 1751–1755, 2008.

[29] I. Corazzari, A. Gilardino, S. Dalmazzo, B. Fubini, and D. Lovisolo, "Localization of CdSe/ZnS quantum dots in the lysosomal acidic compartment of cultured neurons and its impact on viability: Potential role of ion release," *Toxicology in Vitro*, vol. 27, no. 2, pp. 752–759, 2013.

[30] G. Xu, S. Zeng, B. Zhang, M. T. Swihart, K.-T. Yong, and P. N. Prasad, "New generation cadmium-free quantum dots for biophotonics and nanomedicine," *Chemical reviews*, vol. 116, no. 19, pp. 12234–12327, 2016.

[31] M. K. Choi, J. Yang, T. Hyeon, and D.-H. Kim, "Flexible quantum dot light-emitting diodes for next-generation displays," *npj Flexible Electronics*, vol. 2, no. 1, pp. 1–14, 2018.

Chapter 5

Design Optimisation

In this chapter, the optimisation of the device from Chapter 3 is discussed in more detail. The effect of adding a reflective layer on one side of the device (opposite to the illumination area) is shown using a flexible mirror-like material. The effect of curvature on the device is studied by measuring the irradiance at different percentage curvatures. Secondary waveguides are fabricated and embedded in PDMS membranes in an attempt to move the extraction area further from the light source, to increase the extracted irradiance and to offer the possibility of structured illumination. The μLED light is coupled into a 500 μm thick membrane to test the effect of coupling to thinner membranes. Finally, injection of μLED light at both ends of the PDMS membrane is demonstrated as a method of increasing the extracted irradiance.

5.1 Utilising a reflective layer

The device discussed throughout this thesis has consisted of a PDMS membrane and an extraction substrate (sometimes with a colour converter). Looking at images of the device, it can be seen that light that is not extracted is guided out of the opposite end of the membrane from the source. Furthermore, as the scattering in the extraction film can be assumed to be isotropic [1], it is likely that a similar amount of light is extracted out of the bottom of the device as from the top. There is therefore scope for improving the extracted irradiance by using solutions to recycle these ‘lost’ photons.

5.1.1 Extraction effect on either side of the PDMS membrane

The extracted irradiance from both sides of the PDMS membrane was measured to confirm if a similar effect is seen on both sides. A schematic of the methods for comparison

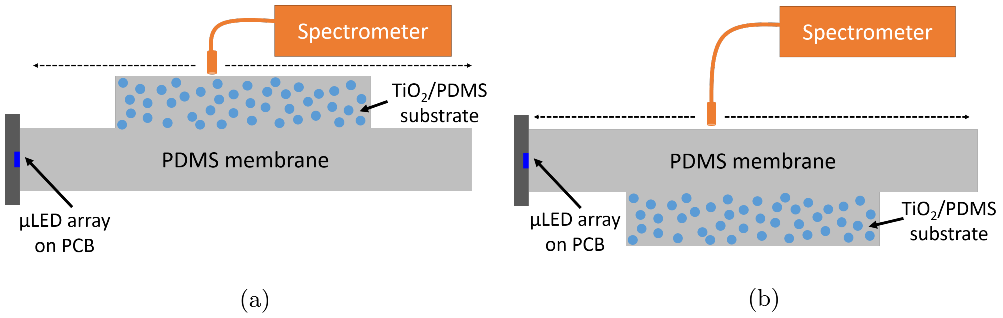

FIGURE 5.1: Schematics of the different geometries for irradiance measurements, (a) with the extraction substrate facing upwards and irradiance measured from this substrate and (b) with the extraction substrate facing down and irradiance measured from the PDMS

is shown in Figure 5.1. The measurement method used previously, measured the irradiance from the extraction substrate side of the membrane (Figure 5.1(a)). To measure the irradiance on the other side of the PDMS membrane, the device is turned upside down with the extraction substrate on the bottom of the device. The irradiance is then measured through the PDMS membrane as in Figure 5.1(b).

The irradiance of different concentrations of TiO_2 extraction substrates was measured and compared, the results of the 0.5% TiO_2 are given in Figure 5.2. From the irradiance results it can be seen that a similar irradiance is seen with both methods. With the substrate down sample, the maximum irradiance is slightly higher with a value of 2.1 mW/cm^2 compared to 2.0 mW/cm^2 with the substrate up. This slight increase is less than 5% which is within the 15% error specifications utilised throughout this thesis. This allows measurements to be taken from either side of the membrane and compared. From these results, it stands to reason that the use of a reflective layer on one side of the membrane would increase the extracted light.

5.1.2 Reflective materials

There are a range of materials that can be utilised for reflecting the light. A metal layer deposited on the membrane surface, like silver or aluminium, would reflect the majority of light, however, this is an expensive method and the material would likely be prone to cracks and delamination [2]. Other reflective substrates include reflective paints and varnishes, these generally consist of small glass particles that act as a prism to reflect light back towards the source, a technique known as retro-reflectivity [3]. These are used in applications like street signs and road markings, and visibility markers on bicycles [4]. However, as these paints are water or oil based, they are unable to form effective films on the hydrophobic PDMS surface. There are methods which can be employed to temporarily make the PDMS surface hydrophilic including treatment with

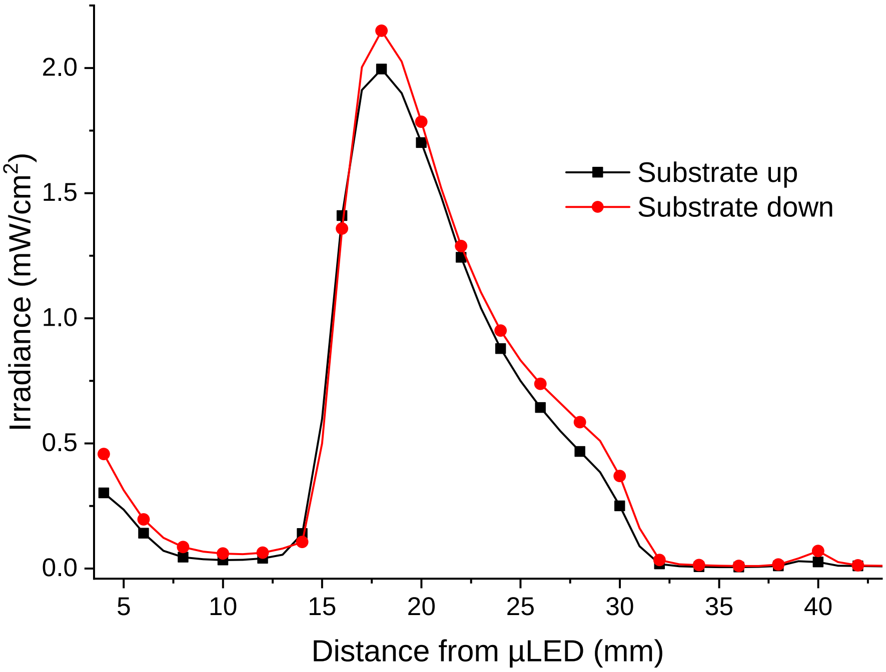

FIGURE 5.2: Irradiance results of 0.5% TiO_2 scatter substrate measured with the substrate facing upwards and facing down

oxygen plasma or chemicals [5]. This would allow for the PDMS membrane to be painted/varnished. However, the resultant reflective film would be rigid. Therefore, cracks would form in the film if the membrane was bent over a curved surface, multiple cracks could result in delamination of the film and reduced reflectivity properties. There are flexible reflective films that can be fabricated from nanoparticles, including graphene oxide sheets [6] and silk clay films [7], however, these are expensive to fabricate. A more cost-effective alternative is to use off-the-shelf flexible reflective materials. These consist of a flexible substrate, like paper or plastic, coated in a reflective paint [8]. These materials are commonly available for interior design or crafting purposes.

5.1.3 Reflective methods

Flexible mirror-like tiles were purchased (Amazon) to be utilised as the reflective material. These are coated polyethylene terephthalate sheets that can be cut to size and bent to any shape while maintaining an optically smooth surface. The extraction substrate down method was used with the reflective layer to measure the increase in irradiance. By placing the mirror in contact with the extraction substrate and measuring through the PDMS, the irradiance increase occurs more at the extraction substrate area, rather than over the entire membrane.

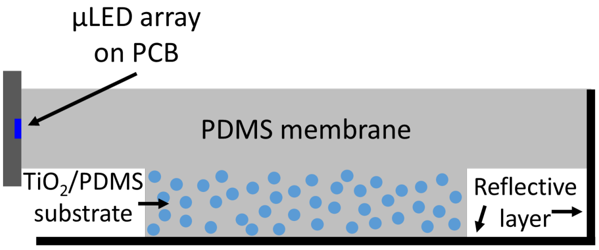

FIGURE 5.3: Schematic of the membrane setup for the reflective tests using a flexible mirror-like material

The reflective material is cut to the size of the membrane (20 x 40 mm^2) and placed underneath in contact with the extraction substrate, this contact holds the reflective film in place under the PDMS membrane. The reflective material for the end is cut slightly larger (20 x 2 mm^2) to cover the end of the membrane and fill the gap between the PDMS and the mirror at the end of the membrane, shown in Figure 5.3.

5.1.4 Highlights of irradiance with reflective layer

The reflective mirrors were added to the membrane with different concentrations of TiO_2. The irradiance was measured and compared to the same devices without the reflective mirror. The results are shown in Figure 5.4. For each concentration the irradiance increased by at least 90%. With the lower concentrations, 0.05% and 0.1% the peak irradiance more than doubles.

Irradiance maps were taken of these substrates using the method from Section 2.6.3. From these maps the total output power and efficiency based on the input LED optical power can be measured. These are given in Table 5.1, with the results from the same devices with no reflective material for reference.

TABLE 5.1: Table comparing the maximum irradiance, total power output and efficiency for TiO_2 scatter substrates with the bare PDMS membrane and the reflective layer

TiO_2 concentration	Maximum irradiance mW/cm^2		Power output mW		Efficiency %			
	Bare	Reflective	Bare	Reflective	Bare		Reflective	
0.05	0.5	1.2	0.7	2.2	7.4	±0.2	22.4	±0.8
0.1	0.8	1.9	1.2	3.5	12.2	±0.8	35.7	±0.7
0.5	1.9	3.6	2.4	5.7	24.2	±1.3	57.6	±1.2

As well as increasing the peak irradiance, the reflective layer increases the irradiance over the entire extraction substrate. This is seen in the increased power output calculated from the irradiance maps. This results in increased efficiencies based on the μLED

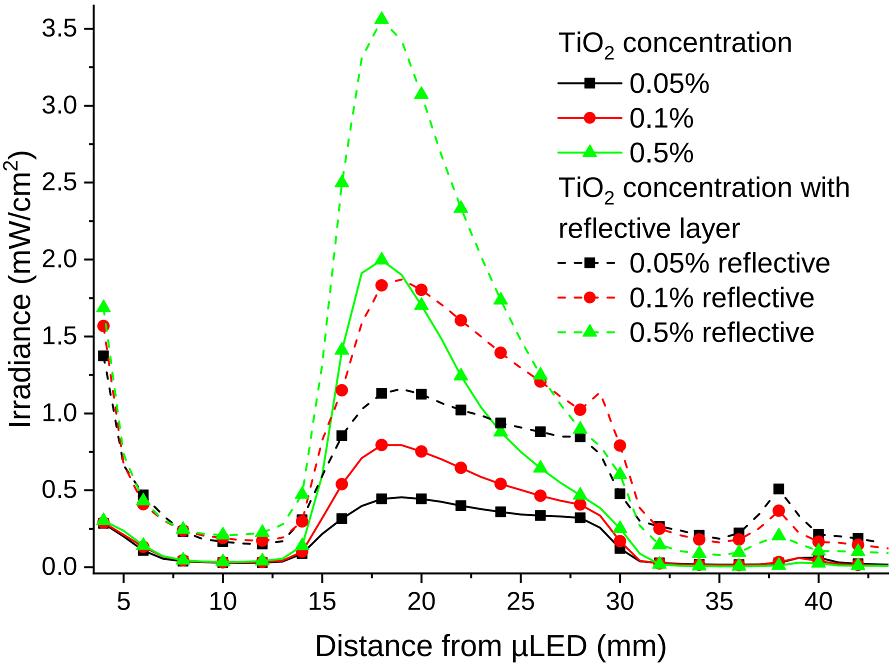

FIGURE 5.4: Irradiance results of different TiO_2 extraction substrates on a PDMS membrane with and without the reflective layer on one side of the membrane

optical power. The efficiencies are all 100% higher than without the reflective layer with a maximum efficiency of almost 57% with the 0.5% TiO_2 extraction substrate. The increase in efficiency is less, as the concentration of TiO_2 in the extraction substrate increases. This is likely due to light being scattered more within the substrate. Multiple scattering events leads to less light being extracted out of the top surface, similar to the effect of increasing the TiO_2 concentration above 1%. It is worth noting that the actual extraction efficiency of the substrates will be higher as not all of the 10 mW μLED optical power is coupled into the PDMS membrane.

5.1.5 Uniform irradiance with reflective layer

The reflective material was added to the uniform device from Section 3.7.1. The irradiance was measured from the top surface of the membrane, the side opposite the extraction substrate. This is shown in Figure 5.5 comparing it to the same device with no reflective layer. It can be seen that the addition of the reflective layer increases the irradiance over the entire PDMS membrane with a high irradiance increase close to the μLED, this is due to reflection of the non-guided leaky mode light. The average irradiance over the extraction substrate increases to 1.7 mW/cm^2, an increase of 80%, similar to the reflective effect on the single-concentration substrates. Irradiance maps were taken as in Section 2.6.3, the resultant maps are given in Figure 5.6. It can be seen that, the addition of the reflective layer increases the uniformity across the scatter

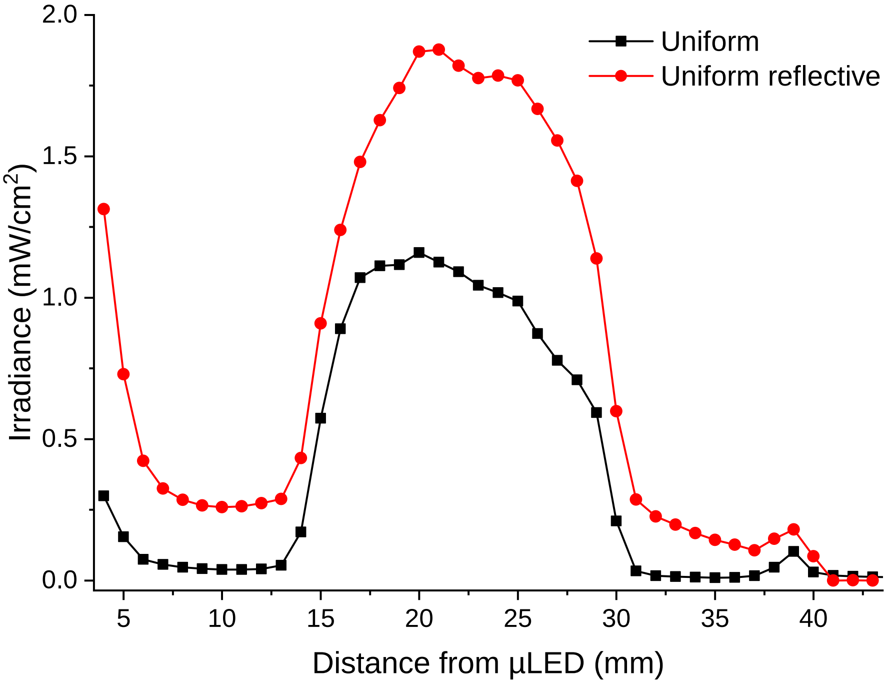

FIGURE 5.5: Irradiance results of the uniform irradiance producing concentration gradient extraction substrate with and without the reflective layer

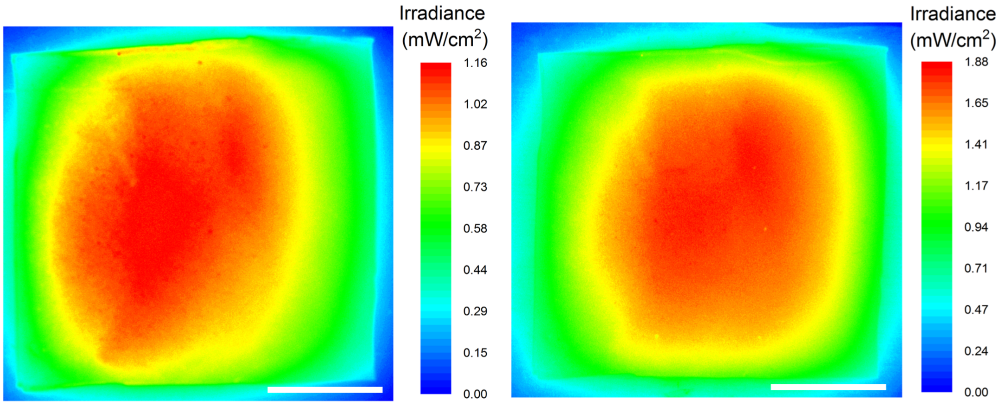

(a) (b)

FIGURE 5.6: Irradiance maps of the uniform irradiance producing concentration gradient extraction substrate (a) without the reflective layer and (b) with the reflective layer, scale is 5 mm

substrate as well as increasing the mean irradiance. This can also be seen in the SD of the mean irradiance values, with the reflective method giving a mean irradiance of 1.7 mW/cm^2 ± 8.9% while the same sample without a reflective layer produces a mean irradiance of 1.0 mW/cm^2 ± 13.2%.

The irradiance map shows that the total power output from the device is 4.8 mW, giving the device an efficiency of 48% based on the output optical power of the μLED device. The same sample, without the reflective layer, has an output power of 2.3 mW and an efficiency of 23%. The reflective layer more than doubles the efficiency of the uniform extraction substrate.

5.2 The effect of curvature

One main benefit of our device design is the flexibility of the PDMS membrane. Phototherapy treatment is carried out on many areas of the human body, most of which are not flat [9]. The device designed in Section 3.7.1 has been shown to produce uniform emission when flat, however, to be used therapeutically, the device also has to produce uniform irradiance over curved surfaces. Therefore, the irradiance of the device under different curvatures needs to be examined.

5.2.1 Design of experiment

Curved objects were obtained at three different curvatures, shown in Figure 5.7. The pieces are made from brushed aluminium as it was available to us. Each curve generally relates to a different body area and is described as a percentage where, 0% is a flat substrate and 100% would be a substrate bent at 180° in the centre. Piece (a) has a small curve of 33%, which generally would correspond to the curvature of a large body area, like a thigh or the skull. Piece (b) has a larger curve corresponding to a smaller body area like an arm with a curvature of 55%. The third piece, (c) has a much steeper curve of 85%, on a body this would correspond to a finger. These samples had curvature radii of 27 mm, 18 mm and 6 mm, respectively. It is worth noting that although these pieces are suitable for measuring curvature at different radii, the effect on a patient's skin would not be identical. In particular, these pieces allow measurements to be made on the outer side of the device whilst on a patient's body, it would be light on the inner side of the device that has an effect. Although this is suitable to estimate effects of curvature to be more accurate the experiment should be repeated with curvatures in the opposite direction to measure the light output on the inside of the bend.

5.2.2 Curvature method

The membrane has to be stuck to the curved piece to maintain the curved shape throughout the experiment. Double-sided sticky tape is used along the length of the membrane, at either side and at the end opposite the μLED array. The glue in the tape has a higher refractive index than PDMS [10], therefore, some of the light will be guided through it, as seen in Figure 5.8. In order to ensure any measured irradiance changes are due to the

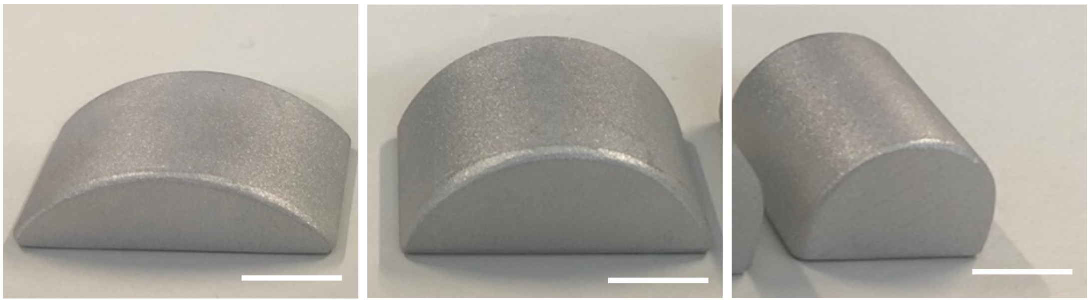

(a) (b) (c)

FIGURE 5.7: The brushed aluminium pieces used for curvature measurements, (a) 33%, (b) 55% and (c) 85%, scale is 10 mm

curvature effect, an initial measurement is carried out with the membrane held flat on a flat piece of the same brushed aluminium. Any changes corresponding to the metallic base and the taped edges is then cancelled out between the different curvatures. Images of each of the curvatures with the μLED turned on, is shown in Figure 5.8. The 0% curvature picture is not with the aluminium piece underneath, this was taken at a different time, on the traditional setup.

In order to measure the irradiance at the membrane surface as in Section 2.4.1, the optical fibre has to be rotated, as well as translated in the y and z directions.

The optical setup shown in Figure 3.7 contains a rotation stage, this allows the angle of the optical fibre to be moved 360° in a radial direction. Using the curvature of the metal pieces, the angle of fibre and the height and lateral positions required, can be

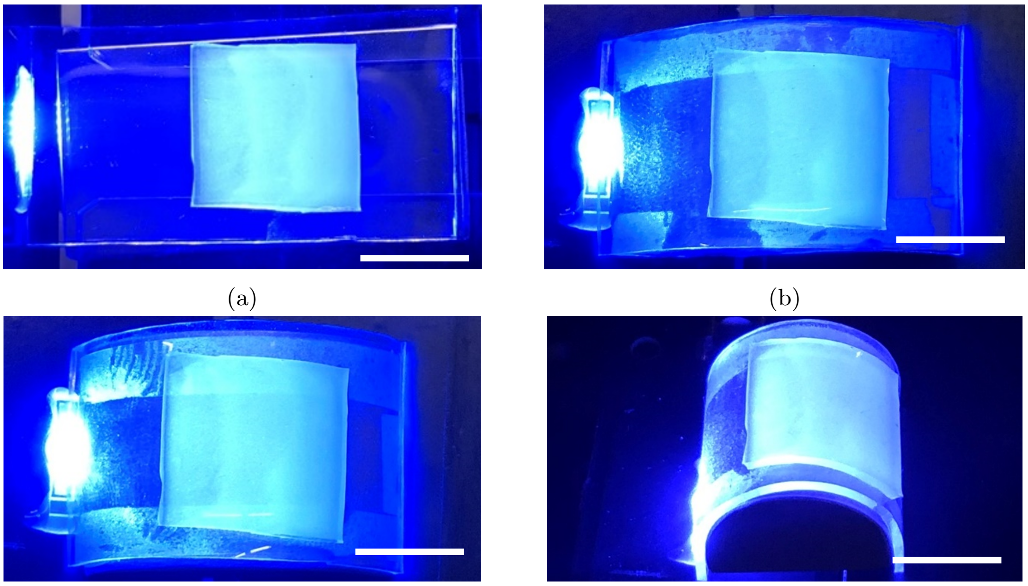

(a) (b)

(c) (d)

FIGURE 5.8: Images of the uniform extraction substrate under different percentages of curvature, (a) 0%, (b) 33%, (c) 55% and (d) 85%, scale is 10 mm

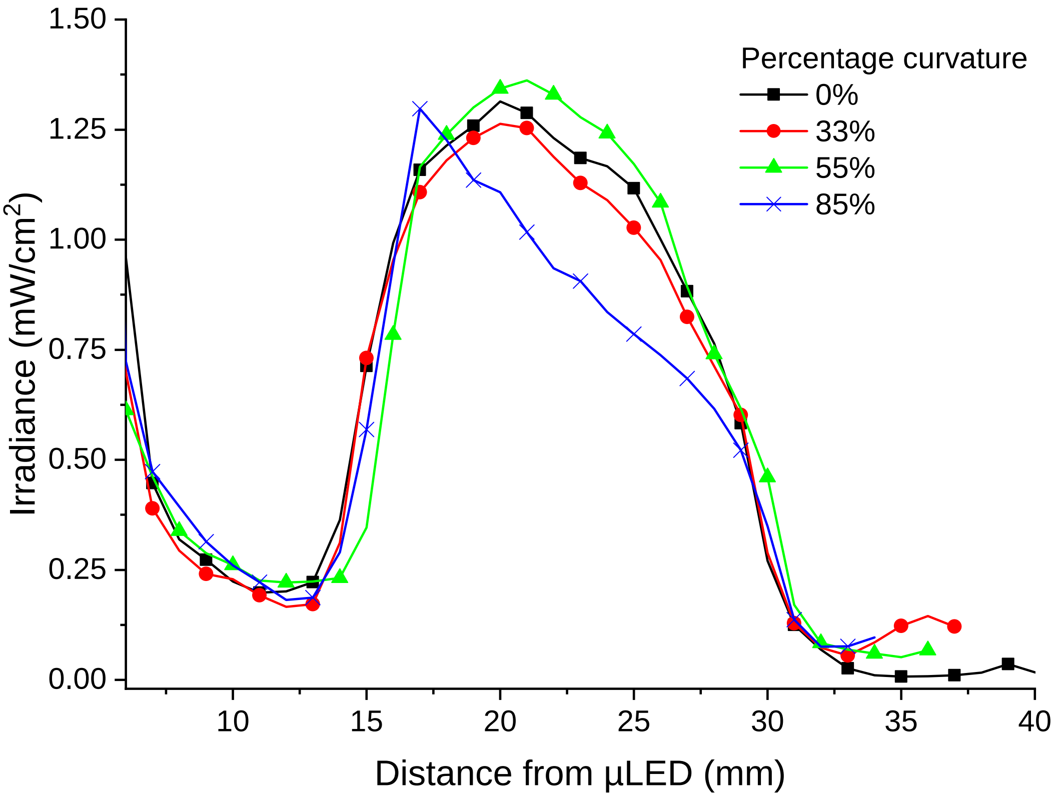

Figure 5.9: Irradiance results of the uniform extraction membrane under different percentage curvatures

calculated to measure the irradiance at each millimetre distance from the μLED along the length of the membrane. Allowing for an accurate comparison of the irradiance from the different curvatures.

5.2.3 Irradiance results at different curvatures

The irradiance for each curvature at millimetre intervals from the μLED array was taken and is shown in Figure 5.9. As can be seen, the irradiance remains fairly similar for the flat sample and the 33% and 55% curvature samples. The slight decrease in 33% and increase in 55% are likely due to small differences in coupling to the μLEDs. It is difficult to ensure the coupling is accurate at each curvature, so slight deviations are likely to occur. This accounts for the small differences in the irradiance values. The device with 85% curvature shows a much different irradiance profile. There is a peak irradiance close to the μLED, and the irradiance then decreases over the length of the scatter substrate, resulting in a non-uniform emission profile.

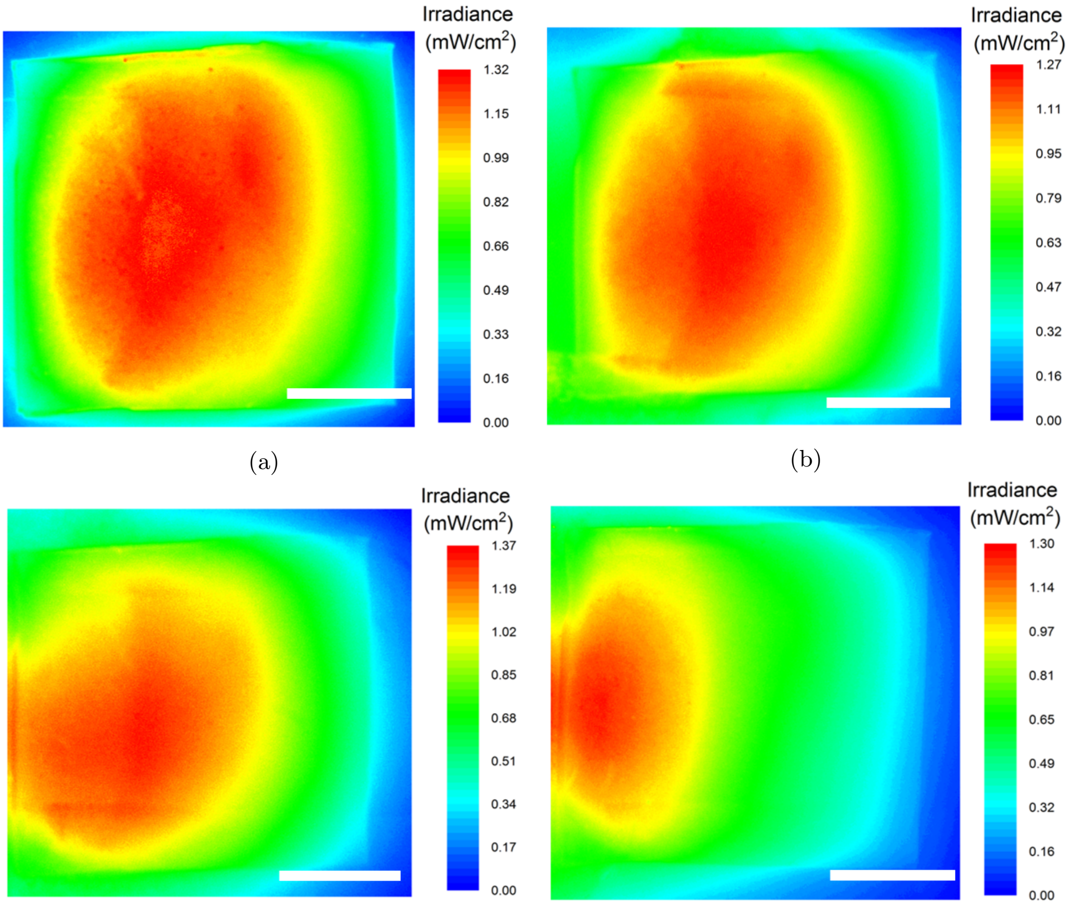

(a) (b)

(c) (d)

Figure 5.10: Irradiance maps of the uniform extraction membrane under different percentage curvatures, (a) 0%, (b) 33%, (c) 55% and (d) 85%, scale is 5 mm

5.2.4 Irradiance maps and power

CCD images of the device at each curvature were taken and irradiance maps were produced. These maps are shown in Figure 5.10. These maps show similar irradiance trends to those observed in the irradiance results.

Looking at the irradiance maps for the 55% and 85% an initial high irradiance is seen at the start of the samples; this is actually scattered μLED light that is observed due to the curvature effect. From the irradiance maps, the total power output can be estimated using the same technique as in Section 2.6.3. With the total output power, the efficiency of the devices based on the μLED optical power can be determined, shown in Table 5.2. The flat device produces the highest power, resulting in an efficiency of 26%. The 33% curvature and 55% curvature have efficiency of 25%, just 1% lower than the flat device. The efficiency of the 85% curved device has a decreased efficiency down to 20%.

TABLE 5.2: Table comparing the peak irradiance, total power output and efficiency for the uniform TiO_2 extraction substrate at different percentage curvatures

Curvature (%)	Peak average irradiance (mW/cm^2)		Total power (mW)		Efficiency %	
0	1.3	±0.07	2.6	±0.08	26	±0.8
33	1.3	±0.02	2.5	±0.04	25	±0.6
55	1.4	±0.04	2.5	±0.06	25	±0.7
85	1.3	±0.05	2.0	±0.09	20	±1.4

From these results, it can be seen that curvatures of 33% and 55% still produce uniform irradiance outputs. However, by increasing the curvature to 85%, the device loses its uniformity over the 15 x 15 mm^2 extraction area. This shows that the device can produce uniform emission when placed over contours up to at least 55%. The decrease in uniformity at the small curvature radius is likely due to a change in the waveguiding conditions due to bending loss. If the device is to be used at smaller curvatures than 55%, the concentration gradient of TiO_2 along the length of the substrate would have to be changed to produce uniform light.

5.3 The addition of a secondary waveguiding layer

A secondary array of waveguides can be utilised to guide the μLED light in a 2-dimensional format further down the PDMS membrane. Increasing the distance from the source to the treatment area, while maximising brightness. Herein, these waveguides are embedded within the PDMS membranes and consist of areas of higher refractive index that have a rectangular cross-section.

5.3.1 Waveguide design

In order to couple a light from the μLEDs, the embedded waveguides need to have a higher refractive index than the PDMS membrane. A number of materials can be used as the waveguiding material, including a lower ratio PDMS, shown experimentally in [11] and [12]. Other materials, such as epoxies can also be used, these are available with a higher refractive index [13]. These are a more suitable material for the secondary waveguides, the PDMS membrane used already has a low PDMS ratio, making the refractive index change less suitable. For effective coupling, the waveguide ends have to be large enough to couple light from the μLEDs.

The waveguide contact area was chosen to be 180 x 180 μm^2, this is larger than the μLED pixel size (100 x 100 μm^2), however, smaller than the emissive area of the μLED pixels,

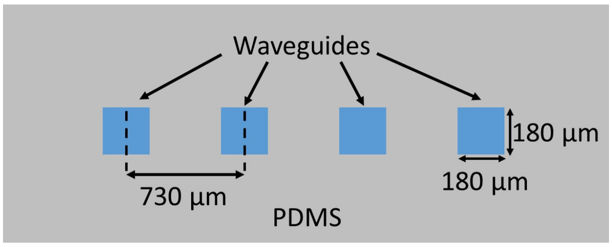

(a)

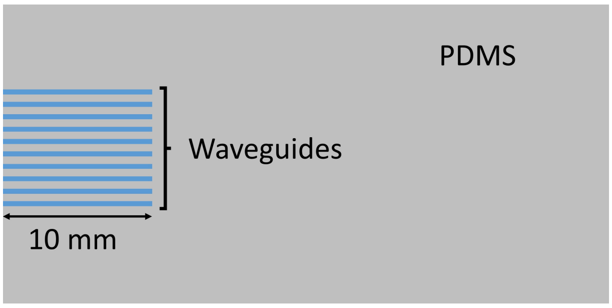

(b)

FIGURE 5.11: Design of secondary waveguides in the PDMS membrane, (a) a side view of the membrane edge, showing the size and pitch of the waveguides and (b) top-down view of the membrane showing the waveguide length

which is dependent on the thickness of the sapphire substrate [14]. The waveguides should therefore couple a large portion of the emitted μLED light, allowing the method to be demonstrated. The waveguides were chosen to have a length of 10 mm. This value was chosen as it allowed the waveguide ends to be far enough away from the μLEDs ensuring that any measured light was not caused by the initial leaky modes in the PDMS membrane. Schematics showing the design of these waveguides in the PDMS membrane are given in Figure 5.11.

5.3.2 Fabrication of waveguide mould

A waveguide mask was produced with ten waveguides, these have a width of 180 μm and length of 10 mm, with a pitch of 730 μm. This design allows for the waveguides to couple to the μLED array (Section 3.1.3). This mask design produced the features required for the waveguides, but not the thickness. For this, a thick photoresist had to be utilised. Photoresists are polymeric materials that either cure after reaction with UV light (negative resists) or do not cure upon reaction with UV light (positive resists) [15]. A commonly used photoresist is SU8 (MicroChem [16]), this has many formulations with varying viscosities, the different viscosities allow for different thicknesses of resist to be spin-coated onto substrates. For thick photoresist films, of more than 100 μm, SU8-100 is utilised [17].

Silicon substrates were solvent cleaned, dried to remove any moisture and treated with oxygen plasma to help the photoresist adhere to the surface. SU8-100 was spin-coated on the surface of the silicon at a speed of 2700 rpm for 30 seconds to produce a photoresist layer 180 μm thick. The sample was then soft-baked for 1 hour at 95°C to harden the photoresist before being exposed to UV light with the waveguide mask layer, cross-linking the photoresist over the waveguide areas. A 20 minute post-exposure bake step at 95°C was then carried out before the substrate was developed in 1-methoxy-2-propanol acetate to remove the uncrosslinked resist. The substrate was then hard-baked at 200°C for 20 minutes. This resulted in ten SU8 waveguides 0.18 x 0.18 x 10 mm^3 on a silicon substrate.

5.3.3 Fabrication of PDMS membrane with secondary waveguides

The fabrication steps for the secondary waveguides within the primary PDMS membrane are given in Figure 5.12. The silicon and SU8 waveguides were used as a mould for a PDMS membrane (a). Uncured PDMS was added to the mould to fill a volume of 20 x 40 x 0.6 mm^3 (b). The PDMS was cured at 80°C for 4 hours and carefully peeled from the mould generating a negative with empty waveguides (c). This PDMS negative was then exposed to oxygen plasma to increase the surface reactivity of the PDMS surface, allowing the waveguiding material to adhere [5]. The waveguides were then filled with a UV-curable epoxy (NOA65, Norland Adhesives) using the doctor blade technique [18]. This epoxy was chosen for its high refractive index compared to PDMS, its flexibility when cured, its transparency to UV and visible wavelengths and its ability to bond to plastic [13].

The epoxy was cured under a UV lamp for 3 minutes, producing a partial membrane with the secondary waveguides (d). Uncured PDMS was then added to the top of the waveguide surface to produce the top half of the membrane, 20 x 40 x 0.4 mm^3 (e). The resultant membrane was 20 x 40 x 1 mm^3 with epoxy filled waveguides in the centre (f). This method was effective in producing the secondary waveguide membranes.

5.3.4 Coupling to secondary waveguides

In order to check the effectiveness of each waveguide, they are coupled to a single μLED pixel, from LED B in [19]. This pixel is trapezoid shaped with a long edge of 45 μm in length (smaller than our pixels of 100 μm). To check how well the waveguides coupled light, an extraction substrate (0.1% TiO_2) was added to the membrane, at the end of the secondary waveguides, 10 mm from the μLED. This is shown for different waveguides in Figure 5.13.

The CCD imaging system was used to image the scatter surface, in order to determine if the μLED was coupled into the waveguides. If the waveguide was efficient at guiding light, the light should start to scatter as it comes out of the waveguide end, producing a linear shaped emission with increasing width as light from the waveguide end diffracts in the PDMS membrane. This can be seen in the extraction substrate. When not coupled into a waveguide the light should fill the PDMS membrane and the entire substrate should scatter light, like seen without the secondary membrane.

The results of the individual waveguide coupling tests are shown in Figure 5.14. A CCD image was taken of each waveguide coupled into the single μLED pixel. Each waveguide is numbered and shown on the same scale of intensity map. It can be seen that light

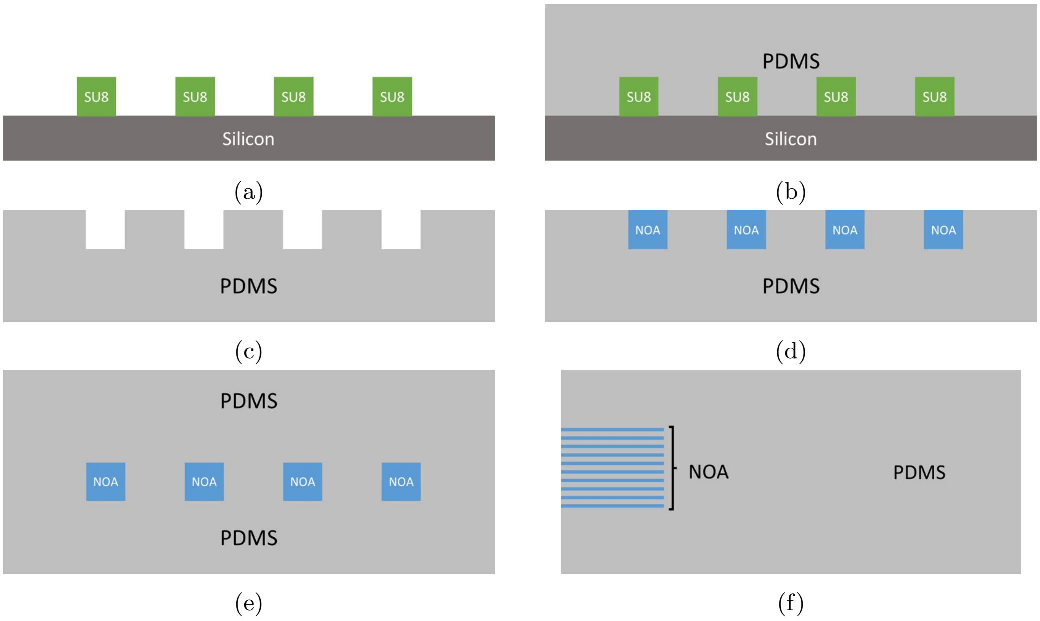

(a) (b) (c) (d) (e) (f)

FIGURE 5.12: Schematic of the fabrication steps required to produce the secondary waveguides within the PDMS membrane

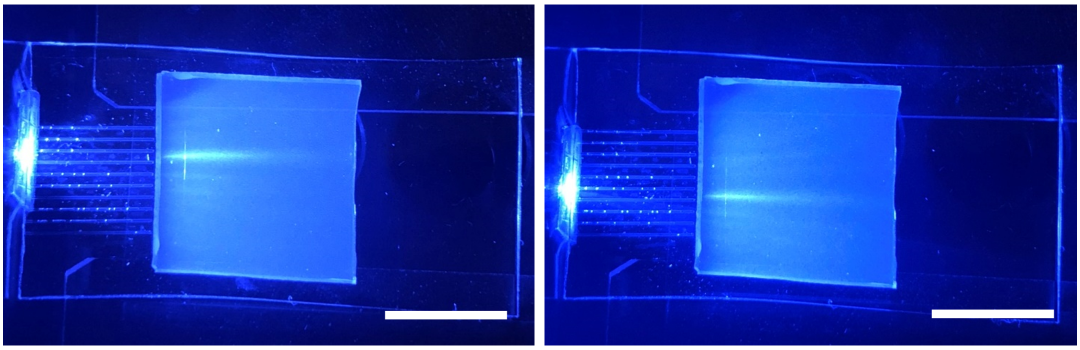

(a) (b)

FIGURE 5.13: Image of the single μLED pixel coupled to different waveguides, the 0.1% extraction substrate is added to see the emission from waveguide ends, a) μLED at waveguide 7 and b) μLED at waveguide 4, scale is 10 mm

is extracted over the entire surface of the scatter substrate, but the most intense light is seen coming from the end of each waveguide. Waveguides 8 and 9 result in much more light being extracted over a larger area, this is either due to the μLED light not being coupled correctly into the waveguide, or the waveguides themselves may have defects resulting in a lot of scatter. In order to ensure the μLED was coupled into each waveguide, the sensor was allowed to saturate. This results in the majority of pixels surrounding the waveguide emission reading 255 counts, the maximum. This means that although these images allow for comparison of the quality of each waveguide, no quantitative comparison can be determined. As this attempt at secondary waveguides is purely proof-of-concept the qualitative information was the main requirement. In order to obtain quantitative information this would have to be repeated below the sensor saturation limit.

These results from the individual tests can be added together to estimate the effect with ten μLED pixels shown in Figure 5.15(b), like the μLED array. The μLED array was then coupled to the waveguides, using the CCD imaging system to identify coupling and a CCD image taken as before. As there are ten waveguides, μLED array A2 was utilised, this array emits light from all 10 pixels unlike μLED array A1 in which only some of the pixels were fully functioning.

An intensity map of the extraction substrate is shown in Figure 5.15(b). It can be seen that the shape of the irradiance profile is very similar to the combined individual pixels, however, light extraction from the substrate with the μLED array is much higher as there are more μLEDs emitting at the same time. From the intensity map, there are strips of more intense light from light that is guided through the waveguides.

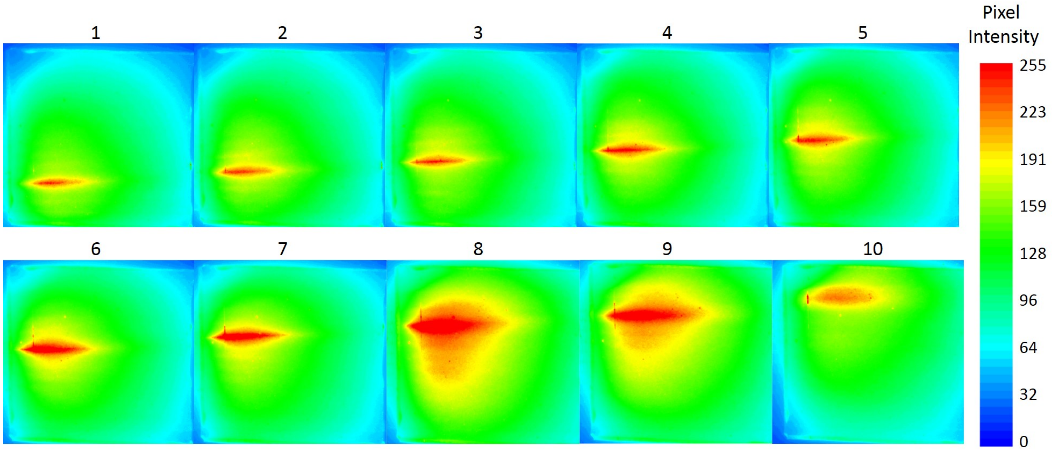

FIGURE 5.14: Intensity maps of the emission from the single μLED pixel coupled into each of the ten waveguides

The use of the CCD imaging system allows the coupling to waveguides to be identified. A more sophisticated method would have to be employed to truly ensure each waveguide is coupled to the pixels of the μLED array. Similar to what is seen in [20] where arrays of μLEDs are coupled into fibre arrays. However, for the purposes of proof of concept, there is enough coupling to the waveguides to determine if there is a difference in the irradiance from an extraction substrate when a secondary waveguide is utilised.

5.3.5 Extraction effect with secondary waveguides

A concentration gradient extraction substrate was added to the PDMS membrane with the secondary waveguides, in the centre of the membrane, 15 mm from the μLED. The irradiance was measured from the top surface as described in Section 2.4.1. The irradiance along the membrane is shown in Figure 5.16 with the irradiance of the same sample on a membrane with no secondary waveguides embedded, given as a comparison.

The irradiance from the extraction substrate is higher with the secondary waveguide membrane, by a maximum of 0.7 mW/cm^2. There is a slight increase in irradiance, 12 mm from the μLED in the secondary waveguide sample, this is due to a thin edge of epoxy causing a change in the refractive index, leading to the small increase in irradiance. It can also be seen that the increase from the secondary waveguide membrane is higher closest to the waveguide ends, and decreases at a higher rate than what is seen without the secondary membrane. This makes the previously uniform sample, non-uniform due to the irradiance in the secondary waveguide membrane at 15 mm being higher than that of the PDMS membrane.

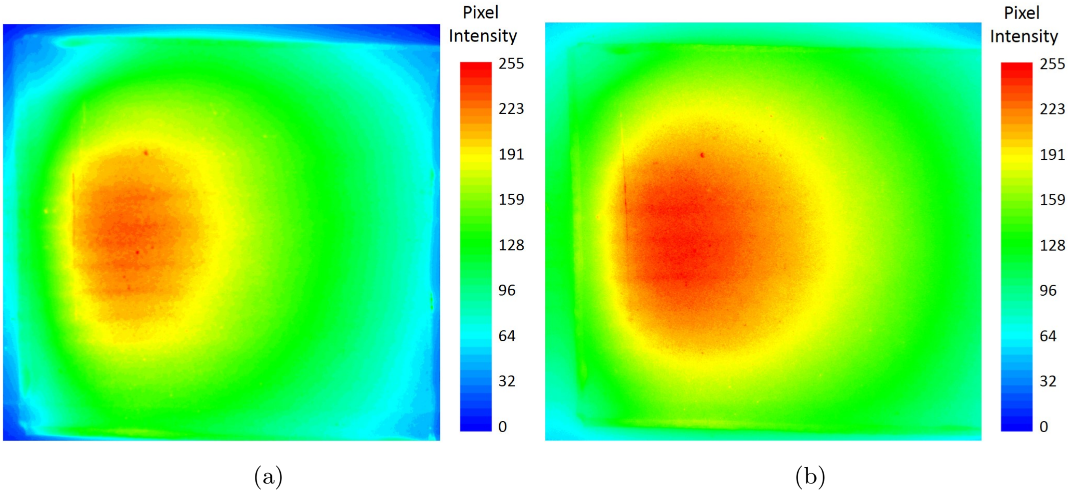

(a) (b)

Figure 5.15: Intensity maps of the 0.1% TiO_2 extraction substrate on the secondary waveguide PDMS membrane (a) combined map from each waveguide coupled to a single μLED pixel and (b) the waveguides coupled to the μLED array consisting of 10 pixels at the same time

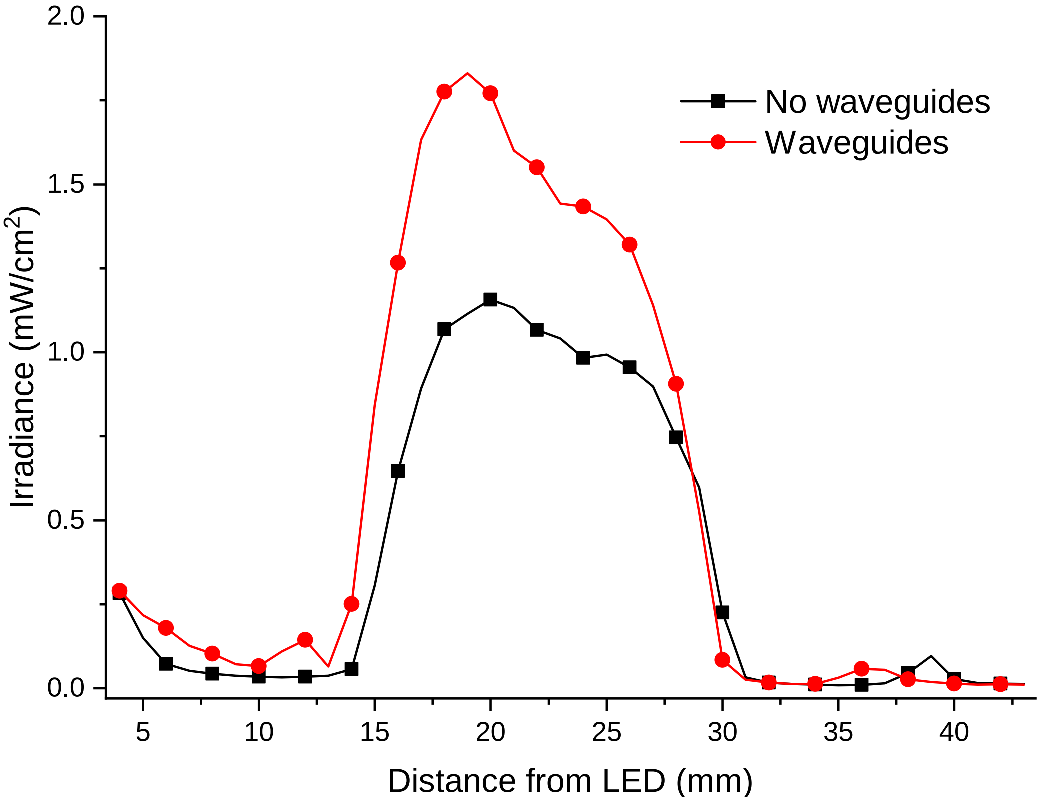

FIGURE 5.16: Irradiance results from the uniform extraction substrate on a primary PDMS membrane and on a membrane with secondary waveguides coupled to the μLEDs

These results show that the use of secondary waveguides is an effective way to increase the extraction of light further down the membrane than without the secondary waveguides. The waveguides propagate a percentage of the light further down the PDMS membrane with minimal loss of brightness, leading to an overall increase in the extracted irradiance.

5.4 Decreasing device thickness

Based on the μLED design, the PDMS membrane could be fabricated as thin as 300 μm before the coupling efficiency would decrease due to the emission area of the pixels through the sapphire substrate being 300 μm [14]. Smaller μLEDs could be fabricated to go even thinner in membrane thickness. However, as the membrane gets thinner, it becomes more difficult to align the μLEDs and the membrane. This makes it more challenging to achieve the maximum coupling efficiency in the centre of the membrane [20], requiring precise apparatus.

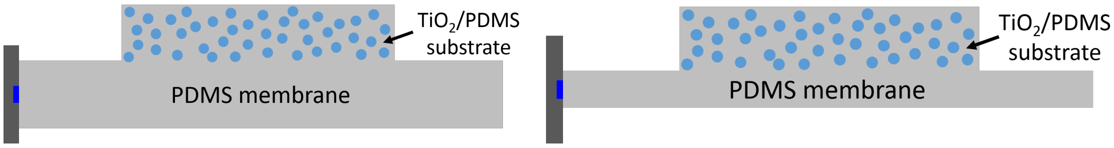

(a) (b)

Figure 5.17: Schematic of the device design at different PDMS membrane thicknesses (a) 1 mm thick PDMS membrane and (b) 500 μm thick PDMS membrane

5.4.1 Coupling of thinner PDMS membranes

A PDMS membrane 20 x 40 x 0.5 mm^3 was fabricated, as in Section 2.1.2. This membrane is half the thickness of a the previously studied PDMS membranes, as shown with schematics in Figure 5.17. A range of different extraction substrates, the flat 0.1% TiO_2 and 0.5% TiO_2 and the tapered 0.05% TiO_2 were added to the surface of the PDMS membrane 15 mm from the μLED.

5.4.2 Membrane comparison

The results are shown in Figure 5.18, along with the results from the 1 mm thick PDMS membrane for comparison. It is expected that the irradiance from the thinner membrane should be similar to the 1 mm thick membrane as the membrane thickness is larger than the μLED pixel size emission area and the numerical aperture stays the same. However, the results show that the irradiance is higher for the thinner membrane.

The irradiance is 15% to 20% higher for the 0.5 mm thick PDMS membrane. Theoretically, the coupling of the thinner membrane should produce similar irradiance values. Therefore, the edges of both membranes were inspected under a microscope to determine if there is a difference in the surface that couples the μLED light. Microscope images of the edge of a 0.5 mm and 1 mm thick PDMS membrane are shown in Figure 5.19.

It can be seen that the edges of the 0.5 mm thick membrane are smoother than those of the 1 mm thick membrane. The smoother surface will scatter less light, therefore more light will be coupled at the injection end and the propagation loss along the length of the membrane will be reduced. This results in the increased irradiance seen with the extraction substrates. Both membranes are cut to size from a larger area of PDMS, using a single-use scalpel. The thinner membrane is easier to cut, so therefore the edge is more even, resulting in a surface more optically smooth than that of the thicker membrane.

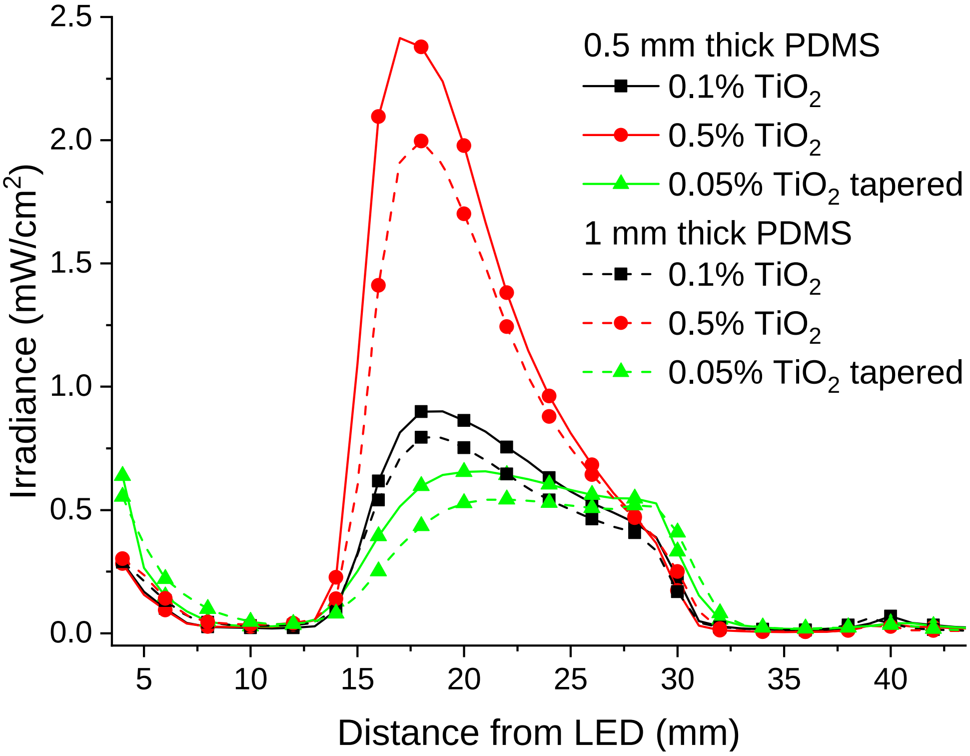

FIGURE 5.18: Irradiance results of different extraction substrates on the 500 μm thick PDMS membrane and the 1 mm thick PDMS membrane

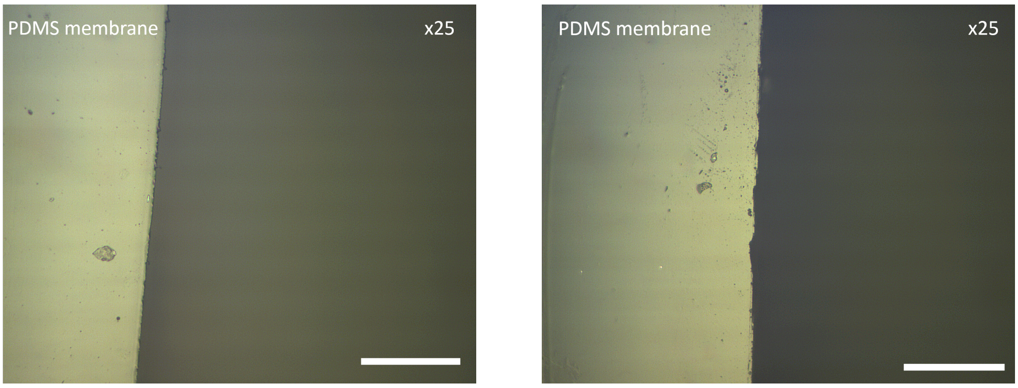

(a) (b)

FIGURE 5.19: Microscope images at 25 x magnification of the PDMS membrane edges, (a) 500 μm thick PDMS membrane and (b) 1 mm thick PDMS membrane, scale is 0.5 mm

5.5 Double-ended light injection

Another method for increasing the irradiance is to use more than one μLED array. By having an array at both ends of the membrane the flexibility of the device is decreased, however, more light can be extracted. Both of the μLED arrays from Section 3.1.3, Devices A1 and A2 are added to each end of the membrane like in Figure 5.20. Extraction substrates are then added to the centre surface of the PDMS membrane and the irradiance measured.

5.5.1 Method for double-ended injection

The extraction substrates with 0.05%, 0.1% and 0.5% TiO_2 in PDMS were added to the surface of the double-injected membrane. With single-ended injection these samples produced an initial high irradiance close to the μLED followed by a decay (as shown in Section 3.4.1). By injecting from both ends of the membrane, this increase should be seen at either end of the extraction substrate. These substrates were added to the centre of the PDMS membrane to determine if uniform light extraction could be achieved using double-ended injection.

5.5.2 Irradiance from double-ended injection

The irradiance was measured from the top surface of the membrane for each of the extraction substrates. The irradiance results are shown in Figure 5.21 with the irradiance from the single-injected devices for comparison. The irradiance increases when injecting

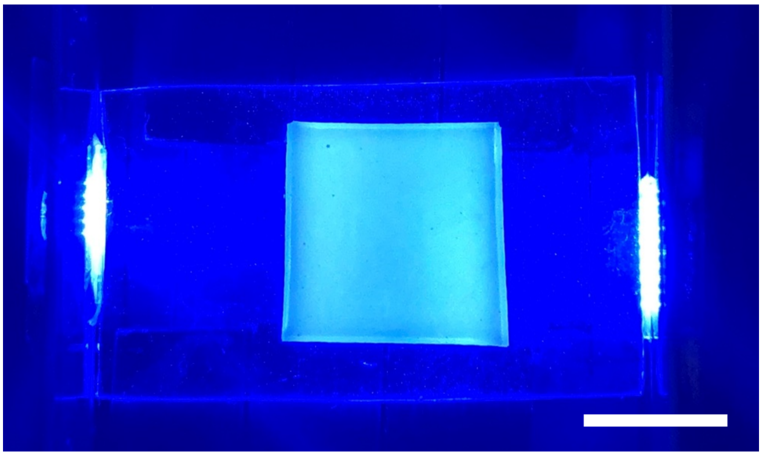

FIGURE 5.20: Image of a 1 mm thick PDMS membrane with 0.5% extraction substrate with μLEDs injecting light at either end of the membrane, scale is 10 mm

light from both ends of the membrane as expected. The extracted irradiance from the TiO_2 substrates is also more uniform than when injected with a single array.

The irradiance peaks at both ends of the extraction substrate with a slight dip in the middle for each concentration of TiO_2. However, for both the 0.05% and 0.1% TiO_2 substrates the mean irradiance is 1.4 and 1.5 mW/cm^2 respectively, with SD errors of 9% and 10%. Showing that over the length of the substrate the irradiance is uniform for these concentrations with double-ended injection. The irradiance dip is more pronounced for the 0.5% TiO_2 substrate. It also shows that a higher irradiance is obtained at the end of the substrate closest to array 2. Both arrays are run at optical powers of 10 mW, however, the scatter substrate is slightly closer to array 2 on the membrane, resulting in an irradiance maximum closer to array 2 than array 1. Although there is this small peak, the mean irradiance is uniform with an SD of 9% and a mean of 3.6 mW/cm^2. This is the highest uniform irradiance achieved with the device, of all the possible methods.

CCD images were taken of the double-ended injection membranes and analysed, as per Section 2.6.3. The resultant irradiance map of the 0.5% TiO_2 extraction substrate is shown in Figure 5.22 alongside the irradiance map for the same concentration with single-ended injection. It can be seen that the irradiance is more uniform over the entire

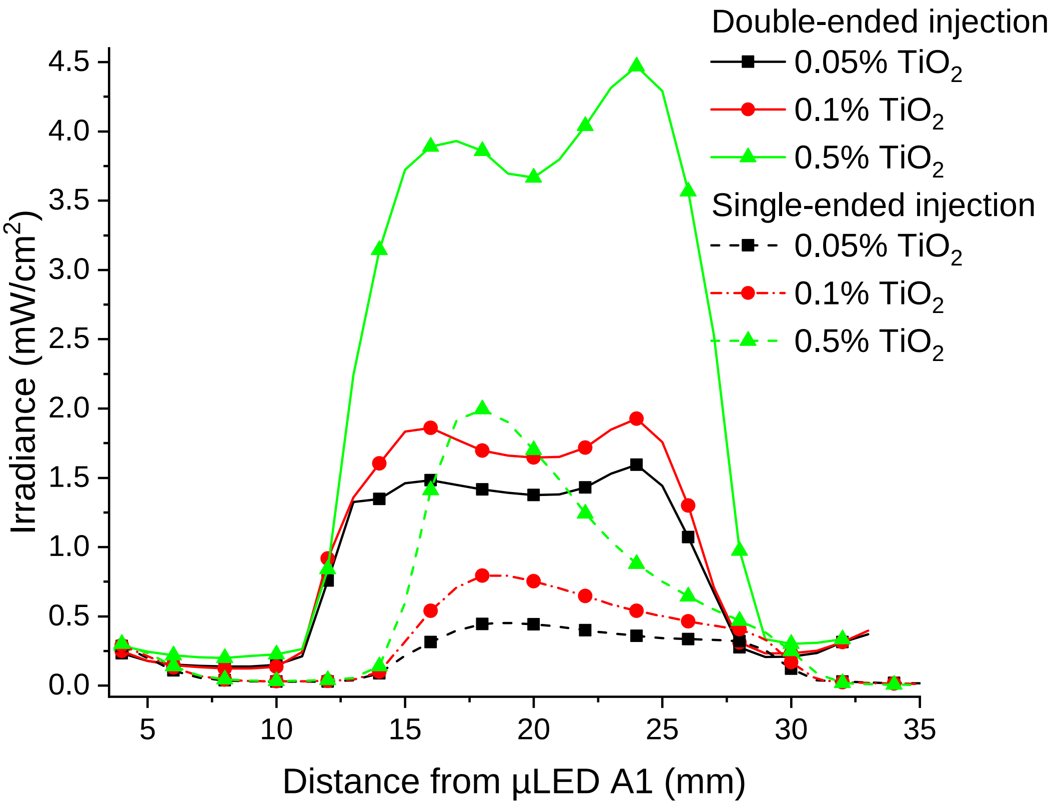

FIGURE 5.21: Irradiance results of different concentrations of TiO_2 extraction substrates injected with a single μLED array or with double-ended injection

substrate of the double-injected array. It is interesting that the end of the substrate closest to array 2, with all 10 pixels working, shows more irradiance over the area than the array with less pixels working. This shows that the results received up to this point with the defective device A1 are more likely to be less than those obtained with a fully working μLED array with the same output power. This is likely because the output power is spread over a larger area with the fully working device and not concentrated to certain regions as with the defective device.

From the irradiance maps, it can be seen that the double-injected sample outputs a much higher optical power of 9.8 mW compared to 2 mW for the single. This gives the double array a total efficiency of 49% as both arrays produce an output optical power of 10 mW. The single array only has an efficiency of 25% with an output power of 2.5 mW. Based on the results from Section 5.1.4, it is expected that the extracted light could be increased further by adding a reflective layer to one side of the PDMS membrane.

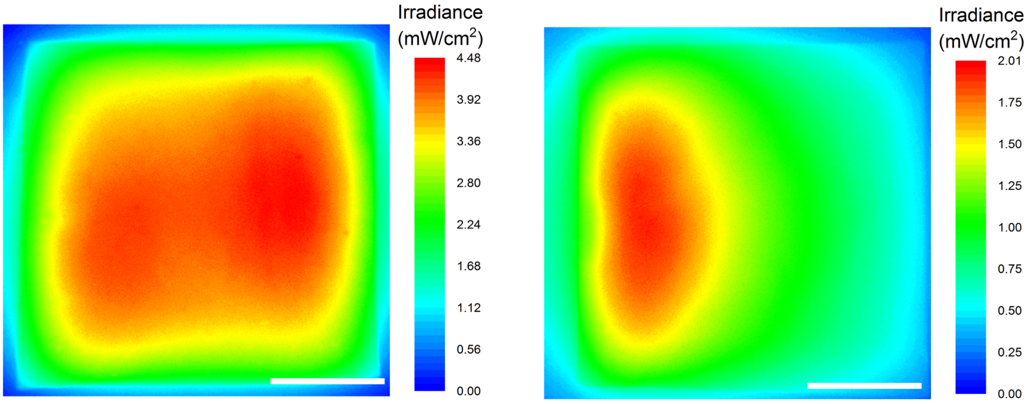

(a) (b)

Figure 5.22: Irradiance maps of the 0.5% TiO_2 extraction substrate injected with (a) a double μLED array or (b) a single μLED array, scale is 5 mm

5.6 Summary

This chapter showed the properties of the device and possible improvements to produce a higher light output. The use of a flexible reflective layer increased the measured irradiance output by almost 66% while maintaining flexibility. Specially fabricated curved pieces were utilised to determine the effect of curvature on irradiance output, with curvatures up to at least 55% producing uniform irradiance with an extraction substrate of 15 x 15 mm^2. Secondary waveguides were added to the PDMS membranes using an epoxy with a higher refractive index than PDMS. These waveguides were tested with a single μLED pixel to determine if light could be coupled into them before being coupled with the μLED array. The use of the secondary waveguides allows the treatment area to be moved further away from the source, this will help avoid excess heat reaching the treatment area. These secondary waveguides could also be used to increase the irradiance from the extraction substrate and also to produce structured emission over treatment areas by using individually active μLED pixels. The effect of decreasing the PDMS membrane thickness was tested to show that membranes as thin as 500 μm can be coupled to the designed μLED device effectively. This also showed the importance of optically smooth PDMS edges, as smoother edges will scatter less light and allow for lower guiding losses. Finally, two μLED arrays were used in combination, one at either end of the membrane, to produce uniform emission with a 0.5% TiO_2 extraction substrate. This double-injection method decreases the device flexibility, however, improves the fabrication process as concentration gradients are not required for uniform irradiance.

References

[1] H. C. Hulst and H. C. van de Hulst, *Light scattering by small particles.* Courier Corporation, 1981.

[2] A. Taylor and J. D. Edwards, "Ultraviolet and light reflecting properties of aluminum," *JOSA*, vol. 21, no. 10, pp. 677–684, 1931.

[3] J. Yuan, S. Chang, S. Li, and Y. Zhang, "Design and fabrication of micro-cube-corner array retroreflectors," *Optics communications*, vol. 209, no. 1-3, pp. 75–83, 2002.

[4] J. Schutt, J. Arens, C. Shai, and E. Stromberg, "Highly reflecting stable white paint for the detection of ultraviolet and visible radiations," *Applied optics*, vol. 13, no. 10, pp. 2218–2221, 1974.

[5] D. Bodas and C. Khan-Malek, "Hydrophilization and hydrophobic recovery of PDMS by oxygen plasma and chemical treatment—an SEM investigation," *Sensors and Actuators B: Chemical*, vol. 123, no. 1, pp. 368–373, 2007.

[6] C. Xu and X. Wang, "Fabrication of flexible metal-nanoparticle films using graphene oxide sheets as substrates," *Small*, vol. 5, no. 19, pp. 2212–2217, 2009.

[7] E. Kharlampieva, V. Kozlovskaya, R. Gunawidjaja, V. V. Shevchenko, R. Vaia, R. R. Naik, D. L. Kaplan, and V. V. Tsukruk, "Flexible silk-inorganic nanocomposites: From transparent to highly reflective," *Advanced Functional Materials*, vol. 20, no. 5, pp. 840–846, 2010.

[8] J. A. Hutchison, "Corrosion resistant flexible reflective film for solar energy applications," June 2 1992. US Patent 5,118,540.

[9] H. Moseley, "Light distribution and calibration of commercial PDT LED arrays," *Photochemical & Photobiological Sciences*, vol. 4, no. 11, pp. 911–914, 2005.

[10] S.-W. Lee, J.-W. Park, Y.-E. Kwon, S. Kim, H.-J. Kim, E.-A. Kim, H.-S. Woo, and J. Swiderska, "Optical properties and UV-curing behaviors of optically clear semi-interpenetrated structured acrylic pressure sensitive adhesives," *International journal of adhesion and adhesives*, vol. 38, pp. 5–10, 2012.

[11] Z. Cai, W. Qiu, G. Shao, and W. Wang, “A new fabrication method for all-PDMS waveguides,” *Sensors and Actuators A: Physical*, vol. 204, pp. 44–47, 2013.

[12] J. W. Parks and H. Schmidt, “Flexible optofluidic waveguide platform with multi-dimensional reconfigurability,” *Scientific reports*, vol. 6, no. 1, pp. 1–8, 2016.

[13] “Norland Epoxies NOA65.” `https://www.norlandprod.com/adhesives/NOA65.html`. Accessed: 28-04-2020.

[14] J. Herrnsdorf, Y. Wang, J. J. McKendry, Z. Gong, D. Massoubre, B. Guilhabert, G. Tsiminis, G. A. Turnbull, I. D. Samuel, N. Laurand, *et al.*, “Micro-LED pumped polymer laser: A discussion of future pump sources for organic lasers,” *Laser & Photonics Reviews*, vol. 7, no. 6, pp. 1065–1078, 2013.

[15] F. H. Dill, “Optical lithography,” *IEEE transactions on electron devices*, vol. 22, no. 7, pp. 440–444, 1975.

[16] “MicroChem SU-8 formulations.” `https://kayakuam.com/products/su-8-photoresists.html`. Accessed: 30-04-2020.

[17] B. Bohl, R. Steger, R. Zengerle, and P. Koltay, “Multi-layer SU-8 lift-off technology for microfluidic devices,” *Journal of micromechanics and microengineering*, vol. 15, no. 6, p. 1125, 2005.

[18] M. Widmer, “Constant bevel Doctor Blade and method and apparatus using same,” Jan. 22 1980. US Patent 4,184,429.

[19] R. X. Ferreira, E. Xie, J. J. McKendry, S. Rajbhandari, H. Chun, G. Faulkner, S. Watson, A. E. Kelly, E. Gu, R. V. Penty, *et al.*, “High bandwidth GaN-based micro-LEDs for multi-Gb/s visible light communications,” *IEEE Photonics Technology Letters*, vol. 28, no. 19, pp. 2023–2026, 2016.

[20] L. Zhu, C. Ng, N. Wong, K. K.-Y. Wong, P. Lai, and H. Choi, “Pixel-to-pixel fiber-coupled emissive micro-light-emitting diode arrays,” *IEEE Photonics Journal*, vol. 1, no. 1, pp. 1–8, 2009.

Chapter 6

Sensor

In the previous chapters, the design of a light emitting, mechanically flexible device for area illumination at visible and UV wavelengths has been discussed. This device consists of an edge-lit elastomeric membrane with added scattering films to extract light. This chapter discusses an alternative use for the edge-lit elastomeric membrane, using it as an evanescent waveguide sensor to determine the presence of fluorescent markers. The design of the waveguide device allows for a large sensing surface area whilst maintaining an overall compact structure. By using an imaging device as the sensor, data can be captured over the entire waveguide surface in a single shot with no scanning required. These properties make the device suitable for point of care use, or for use in the field.

For this proof of concept test, different molar concentrations of colloidal quantum dots are utilised as the markers. Two different imaging systems are used to measure the fluorescence, a CCD system and a smart phone camera. Finally, the quantum dot concentration at the limit of detection for the smart phone system is measured.

6.1 Fluorescent sensing

Fluorescent sensing is a well-established biochemical sensing technique used for diagnostics [1]. It is typically based on biomolecular processes whereby analytes are captured on a surface and coupled to fluorescent tags. The tags are then excited using a light source and the resulting fluorescence is measured to assess the presence and quantity of analytes.

The most sensitive and specific tests to determine the presence or concentration of analytes is immunoassays. These capture analytes on specific antibodies and then identify them with fluorescent markers. There are a number of different ways to employ this

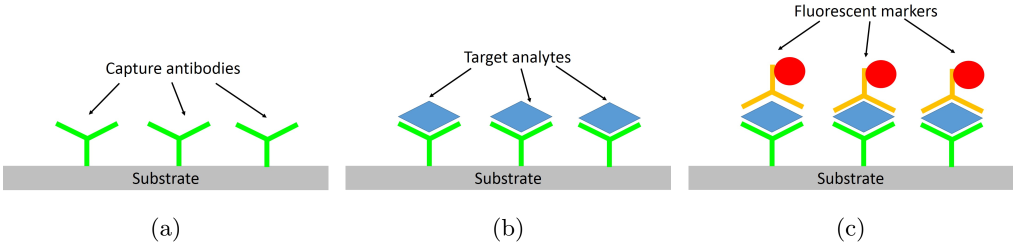

(a) (b) (c)

Figure 6.1: Basic steps in a sandwich immunoassay, (a) the capture antibodies on the test surface, (b) the capture of the target analytes from a biological sample and (c) the fluorescently labelled antibody capture to identify analyte presence

technique, however, the most common is a sandwich immunoassay [2]. The test surface (glass, paper or metal) contains specific antibodies required to capture certain analytes (Figure 6.1(a)). A biological sample (blood, saliva or urine) is then added to the surface. If the analytes are present, they will be captured by the antibodies. The remainder of the fluid is generally then washed off to avoid any non-specific binding (Figure 6.1(b)). A fluorescent marker solution is then added to the surface. These markers consist of the antibody molecule, coupled to a fluorescent tag, this tag will fluoresce when irradiated with a light source. The excess markers are rinsed from the surface and the resultant fluorescence from the sample can be used to determine the presence and/or concentration of the target analyte (Figure 6.1(c)).

Common fluorescent analytes are rhodamine dyes, which are used extensively in fluorescent sensing applications. These have varying limits of detection from 400 to 100 nM [3, 4] depending upon the methods used. For a POC sensor, the design utilised in this thesis has to detect to limits of at least these values.

One challenge with fluorescent sensing and biological samples is autofluorescence [5]. This effect occurs due to non-specific molecules fluorescing naturally under certain wavelengths of visible and UV light. Autofluorescence is a source of noise in sensors and can severely affect the limit of detection, decreasing the efficacy of the sensor. It can be mitigated by using evanescent waves to excite fluorescent labels instead of direct illumination, known as evanescent fluorescence sensing or total internal reflection fluorescence (TIRF) [5]. There are a range of different types of evanescent waveguide sensors based on different techniques, for example planar waveguides [6, 7], optical fibres [8] and capillary waveguides [9].

6.1.1 Evanescent waveguide sensors

Evanescent wave excitation is based on the principle of total internal reflection. When the refractive index of the waveguide is higher than that of the surrounding media, light

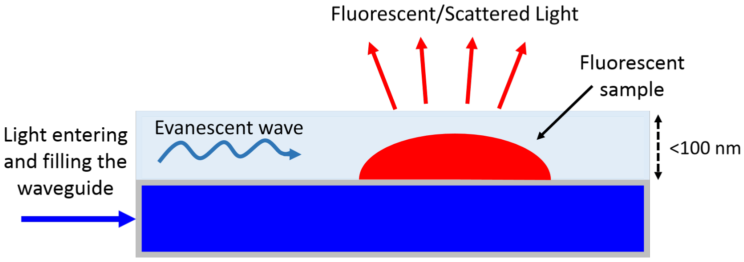

Figure 6.2: Schematic showing evanescent wave generation and subsequent fluorescence of a sample

that interacts with the surface of the waveguide at an angle larger than the critical angle will be totally reflected within the waveguide. When the light undergoes total internal reflection, an electromagnetic field is generated on the waveguide surface, known as an evanescent wave. This wave decays in power exponentially from the waveguide surface over a distance of a few 10s to 100s of nm [5]. Evanescent optical waveguide sensors have been used to detect additives in petrol, bacteria in food samples and proteins/antibodies in biological samples [10]. The technique has also been used in fluorescence microscopy to reduce background scattering and observe the binding of single fluorescent objects [11] as only materials on or very near the surface can be excited by the evanescent field. A schematic of how an evanescent waveguide sensor works is given in Figure 6.2. The evanescent waveguide method normally utilises bulky laser sources and optics, meaning they are typically used in centralised laboratories instead of point of care (POC) devices at patients' bedsides. However, the effect of miniaturising this setup for point of care applications has been shown, for example in [12] where a laser diode was coupled, through micro-optics, to a glass plate that acts as the waveguide.

6.2 Our design

The micro-LED light source described in Section 3.1.3, is coupled to a PDMS slab waveguide 40 x 20 x 1 mm^3. PDMS has been shown to be a suitable waveguide due to its material properties, including its high transparency to UV and visible light.

PDMS is also often used in microfluidic structures due to its cost-effective moulding properties [13]. This makes the material an attractive platform to directly incorporate micro-wells and channels into the waveguide structure, making the future device suitable for multiplexing. Compared to previously reported POC evanescent waveguide devices, the light sources used here directly couple into the PDMS waveguide without the need for optics or specialised coupling structures [7, 12]. The small size of μLEDs enables efficient coupling to thin waveguides, with a maximum coupling efficiency of 88% for a 1 mm thick waveguide. The 1D array geometry of the μLED array also permits near filling of the waveguide which is important for TIRF. It allows the field to be generated over the entire surface of the waveguide, increasing the sensing area [14]. This filling is shown in Figure 6.3 from optical simulation of the design using Zemax OpticStudio [15].

6.2.1 Quantum dots as fluorophores

A whole range of different fluorophores are utilised in fluorescent biosensors including fluorescent proteins, organic dyes and more recently, semiconductor quantum dots (QDs). The recent interest in QDs is due to their functionalisation capability, high stability and adaptable photophysical properties [16]. Fluorescent dyes and proteins typically have narrow excitation bands and broad fluorescence spectra, whereas QDs generally have a much broader excitation profile and narrower emission spectra [17]. The narrow emission profiles make QDs a suitable fluorophore for multiplexing capabilities [18]. The relatively large surface area of QDs make them ideal for adding functionalised surfaces and many biological molecules form strong non-specific binding interactions with QDs relatively easily [19]. These properties make QDs effective fluorophores, in particular in low power instruments due to their high efficiencies. For this reason, QDs are used in this proof of concept device as the fluorescent labels.

6.2.2 Fabrication

For these proof of concept tests, colloidal quantum dots (CQDs) were used as fluorescent labels (630nm-emitting CdSSe/ZnS, 6nm mean diameter, Cytodiagnostics). A range of concentrations were produced by diluting the CQDs in toluene. Using an autopipette, 0.2 μL of each concentration was drop-coated onto the PDMS membrane, spaced at least 2 mm apart in each direction to avoid the samples mixing upon addition to the waveguide

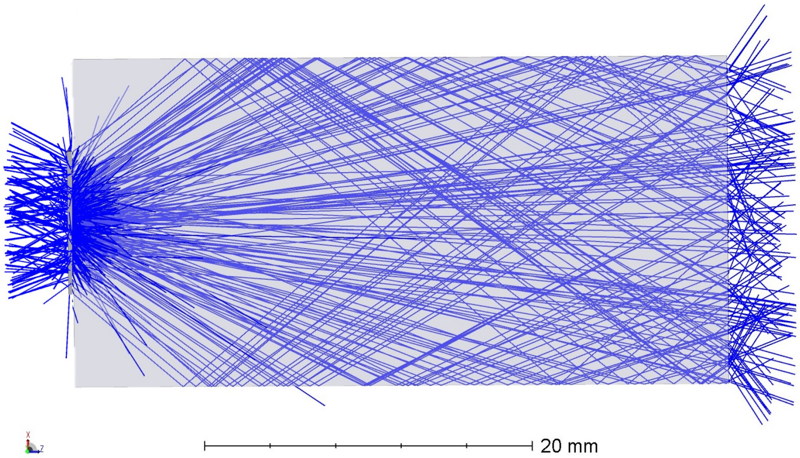

FIGURE 6.3: Optical simulation of the μLED device filling the PDMS waveguide

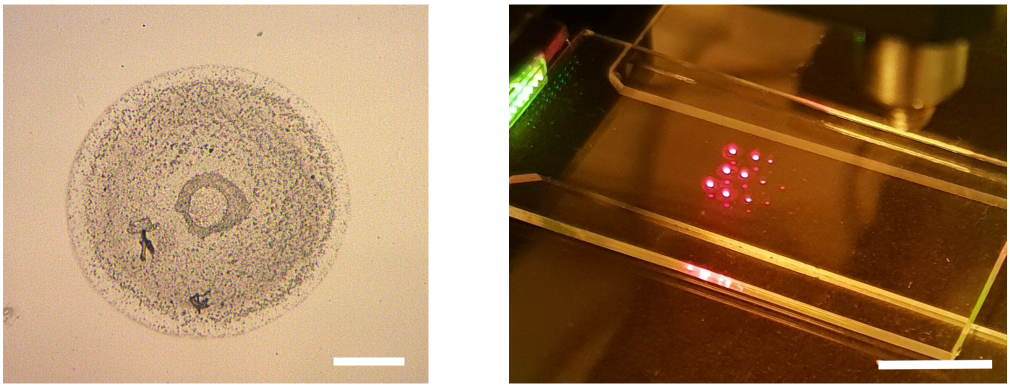
(a) (b)

Figure 6.4: (a) Microscope image of a 300 nM QD region under 10x magnification, scale is 100 μm and (b) an image of a PDMS sensor coupled to the μLED, a 500 nm cut-on filter is added to the camera to show the fluorescent samples, the green light is due to the wavelength tail of the blue μLED not removed by the filter, scale is 10 mm

surface. The toluene was evaporated in air, leaving CQD molar concentrations ranging from 770 nM to 0.4 nM for proof of concept tests. This was repeated for three PDMS membranes in triplicate to determine if the measured fluorescence was repeatable. The dried samples were analysed under a microscope to determine the size of each remaining quantum dot region. The quantum dot regions were an average of 0.8 mm^2 in size with an average diameter of 320 μm ± 18 μm. A microscope image of a 300 nM quantum dot region is shown under 10x magnification in Figure 6.4(a).

6.2.3 Test setup

The end of the PDMS membrane was placed in contact with the μLED device and the LED ran at a current of 120 mA, producing an output optical power of 10 mW. An image of one sensor coupled to the LED is shown in Figure 6.4(b), the red luminescence of the CQD labels can be seen. One of the most common methods for identifying/measuring fluorescence is imaging systems. The fluorescence results of the fabricated sensors are discussed below using either a CCD or smart phone camera to image the samples.

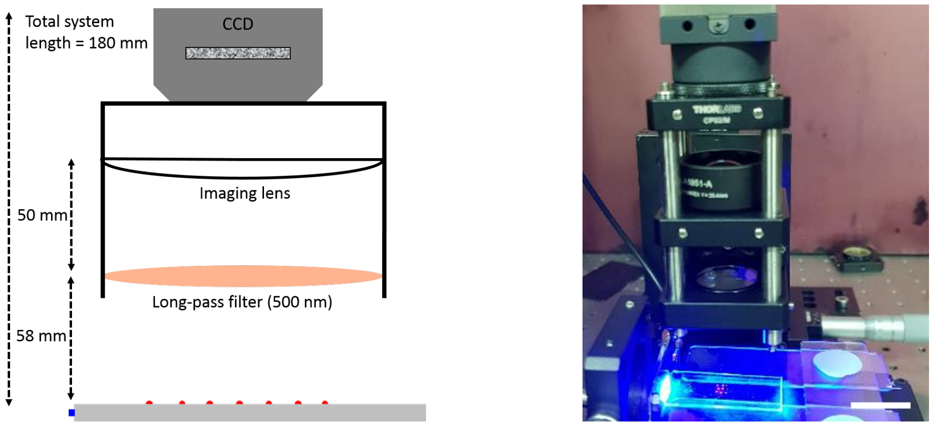

(a) (b)

Figure 6.5: (a) Schematic of the CCD imaging system components (not to scale) and (b) image of the system with the μLED on, scale is 20 mm

6.3 Imaging the sensor with a CCD

A similar imaging system to that described in 2.6.3 was utilised to test the fluorescence capability of the fabricated sensors. A long-pass filter (Thorlabs, FEL0500), with a cut-on wavelength of 500 nm, was fixed 60 mm above the sensor surface. An imaging lens was placed 50 mm above this, followed by a CCD (Thorlabs, DCU244M). The height of the entire system including the sensor and CCD device was 180 mm. The long pass filter was added to the setup to avoid any scattered LED light being detected by the monochromatic sensor. Figure 6.5(a) has a schematic of the sensor setup with the CCD sensor and Figure 6.5(b) shows an image of this setup in the laboratory. The CCD settings were maintained at a gain level of 1 and an exposure time of 100 ms. The sensors were imaged with both the LED switched on and off, producing ‘on’ and ‘dark’ images. Images are saved in a TIFF format to avoid any losses with compression. The images consist of intensity values ranging from 0 to 255 relative counts, with 0 representing no light reaching the sensor and 255 representing pixel saturation.

6.3.1 Image analysis

The resultant sensor image and dark image were imported into MATLAB and the difference between them taken as the true sample image, shown in Figure 6.6(a). This image is then binarized using an adaptive thresholding method. The resultant regions of pixels with a reading of 1 are then closed and filled like shown in Figure 6.6(b). These regions are overlapped with the original image (a) and the average intensity of each region on the original image is recorded.

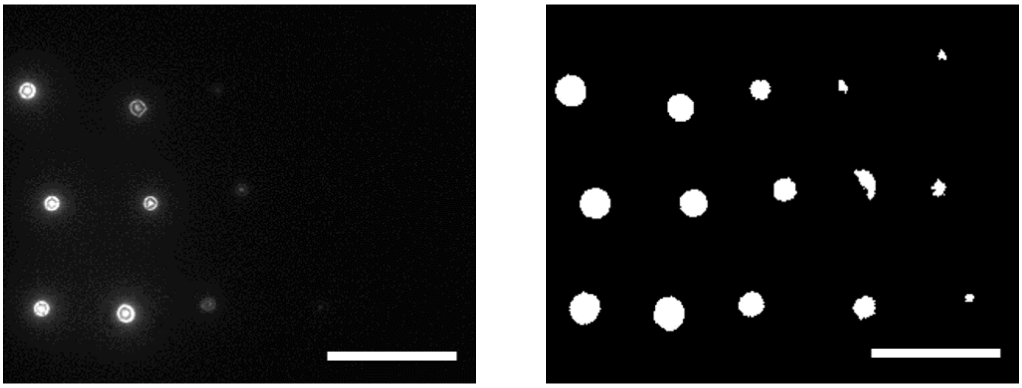

(a) (b)

FIGURE 6.6: (a) Image taken of a sensor surface using the CCD and (b) the subsequently analysed image highlighting the regions of fluorescence, scale is 5 mm

6.3.2 Results

The mean pixel intensity for each CQD region was plotted against the molar concentration, shown in Figure 6.7. The mean intensity for each region was averaged for each concentration over the three waveguides, the errors represent the SD of these averages. For concentrations of 100 to 770 nM, each region has a mean intensity value between 120 and 160, with an average SD of 6%. There is a small increasing trend in mean intensity with increasing concentration. Between 100 nM and 40 nM there is a large drop in mean intensity down to 50 units. Inset of Figure 6.7 shows the low concentration region of the graph on a larger scale with concentrations ranging from 0.4 nM to 40 nM. This region again follows a trend of decreasing intensity values with decreasing CQD molar concentrations. It can be seen that the overall trend is a linear increase in intensity with increasing CQD concentration, saturating at high intensity levels due to the sensitivity of the CCD sensor. Concentrations of more than 100 nM cause the sensor to saturate, while concentrations below this level follow the linear trend.

From these results, it can be seen that the designed platform works effectively as a fluorescent sensor and a CCD imaging system can be utilised to qualify that there is a fluorescent sample present on the waveguide. The CCD imaging system has been shown to detect CQDs down to a molar concentration of 0.4 nM. It is worth noting that concentrations less than 20 nM are not visible to the eye.

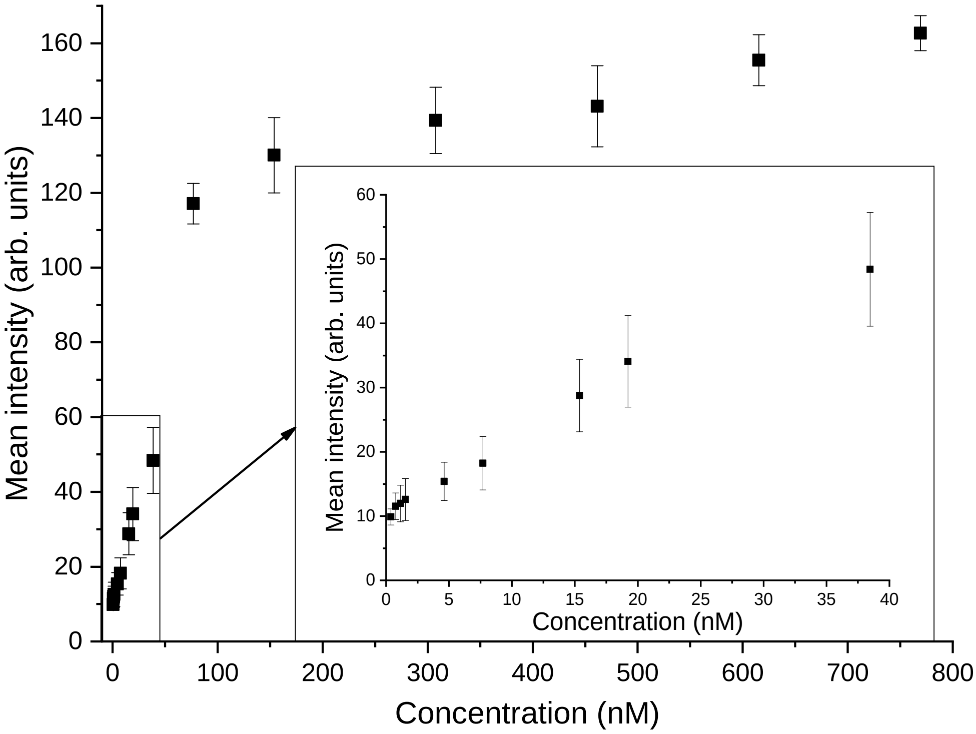

Figure 6.7: Mean pixel intensity of fluorescent regions sensors plotted against the CQD molar concentration of these regions, inset is a scaled graph of the 0 to 40 nM results

6.4 Smart phone imaging

A CCD sensor was utilised to image the fluorescent sensor. CCDs are effective and sensitive to light, however, they are expensive. The CCD utilised throughout this thesis costs over £2000. As the miniaturised design of the waveguide is ideal for POC diagnostic systems, the imaging device should also be small, portable and sturdy. An ideal imaging system which is widely available is the camera in a smart phone [20]. Smart phones use CMOS sensors due to their lower power consumption and higher integration with smaller components. Due to the widespread use of CMOS sensors, heavy investments were made in the fabrication and manufacturing processes resulting in these sensors being almost as sensitive as their CCD counterparts [21]. Smart phone based imaging platforms have been shown to detect bacteria and proteins from a range of samples [18, 22].

6.4.1 Smart phone setup

A Samsung Galaxy S9 [23] was utilised as the camera. This smart phone was placed 100 mm from the PDMS sensor surface. A long pass filter (Thorlabs, FEL0500) with a cut-on wavelength of 500 nm was secured over the camera lens to avoid any scattered

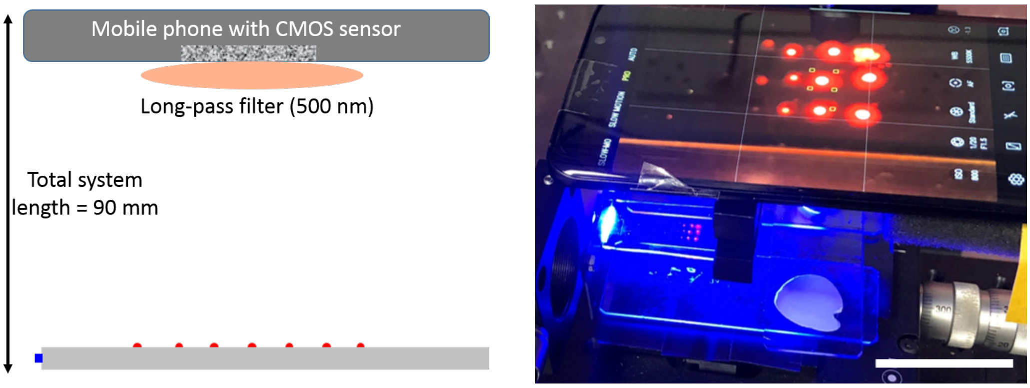

(a) (b)

Figure 6.8: (a) Schematic of the smart phone imaging system components (not to scale) and (b) image of the system with the μLED on, scale is 50 mm

LED light reaching the camera. The phones inbuilt camera application was used in PRO-mode to allow the exposure time, ISO setting and focus to be manually adjusted.

The exposure time determines how long the sensor collects light for, and ranges from 41 μs to capture very high light images all the way through to 10 seconds to capture very low light images. The ISO value ranges from 50 to 800, with an increasing value being more sensitive to light, so therefore useful in dark environments. The exposure time for the camera was fixed at 250 ms, the ISO value was set to 800, the camera was fixed at a 2x zoom to capture as little background as possible. With these settings the background pixel noise was determined to be 2.1 ± 0.8 relative intensity units. The sensors were imaged with both the LED switched on and off, producing 'on' and 'dark' images. Unlike the CCD, these images were saved in a compressed format, JPEG as this is the only save setting available using the inbuilt camera application. The images consist of intensity values ranging from 0 to 255 relative counts, with 0 representing no light reaching the sensor and 255 representing pixel saturation.

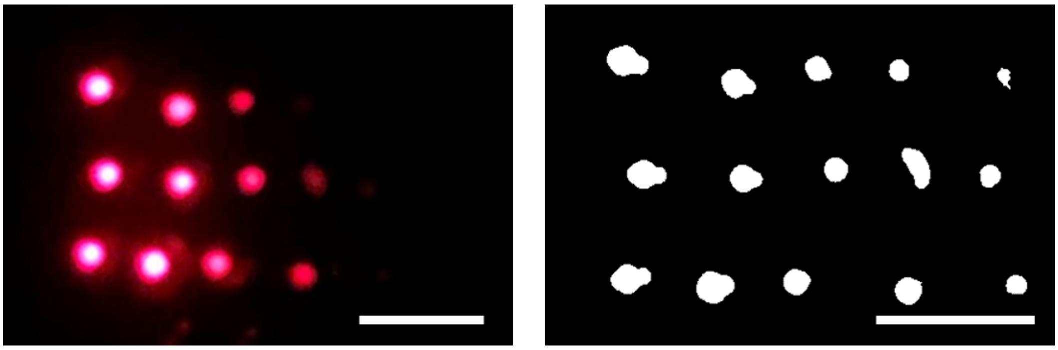

(a) (b)

Figure 6.9: (a) Image taken of a sensor surface using the smart phone camera and (b) the subsequently analysed image highlighting the regions of fluorescence, scale is 5 mm

6.4.2 Image analysis

The resultant sensor image and dark image were imported into MATLAB and the difference between them taken as the true sample image, shown in Figure 6.9(a). Unlike the CCD sensor which was a monochrome detector, the camera captures the image in red-green-blue (RGB) with the CQDs showing as red. The resultant RGB image is then converted to grey-scale to allow image binarization to take place. This image is binarized using an adaptive thresholding method and remaining regions with less than 100 pixels are also set to zero. The remaining regions of pixels with a reading of 1 are then closed and filled like shown in Figure 6.9(b). These regions are overlapped with the original image (a) and the average intensity of each region in the true sample image is recorded.

6.4.3 Smart phone results

The mean pixel intensity for each CQD region was plotted against the molar concentration, shown in Figure 6.10. The mean intensity for each region was averaged for each concentration over the three waveguides, the errors represent the standard deviation of these averages. For higher concentrations of CQDs, 100 nM and more, the mean intensity is clearly saturated. This is different from the CCD due to the exposure time of the camera being 1.5x longer than that of the CCD. This allows for more light to be captured resulting in pixels with higher intensity values. The inset of Figure 6.10 shows the pixel intensity for the lower CQD concentrations of 0.4 nM to 40 nM.

This follows a trend of hyperbolic saturation, a response seen in many biological reactions. From these results, it can be seen that the smart phone camera is an effective imaging system for the designed TIRF platform. Using images taken of sensors fabricated with CQDs, concentrations down to 0.4 nM have been detected.

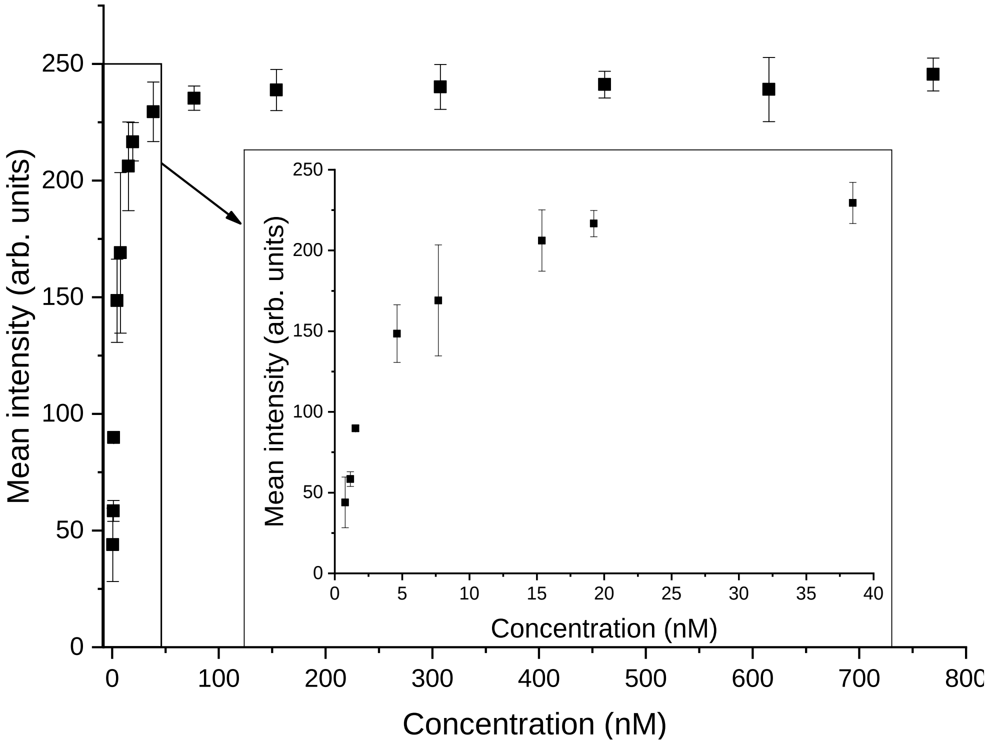

Figure 6.10: Mean pixel intensity of fluorescent regions sensors taken with the smart phone plotted against the CQD molar concentration of these regions, inset is a scaled graph of the 0 to 40 nM results

6.5 Limit of detection

The smart phone camera system was effective at detecting CQDs with concentrations as low as 0.4 nM, producing a mean intensity value of 45 units. As this value is higher than the dark pixel count of 2.1 ± 0.8, it is natural to assume that lower concentrations of CQDs could also be detected. In order to determine the limit of detection of the device, a new sensor was fabricated with lower concentrations. The sensor was fabricated as described in 6.2.2, with CQD molar concentrations of 16 nM to 20 pM.

6.5.1 Results

Three images were taken of the sensor using the protocols described in 6.4.1. The resultant images were analysed with the same MATLAB script and the mean intensity values plotted against the concentration as shown in Figure 6.11. The image processing code was able to identify 14 regions of fluorescence, the lowest concentration region of the sensor, 20 pM, was not identifiable on the images. The resultant response shows hyperbolic saturation as before with an increase in mean intensity with increased concentration of the CQD region. Inset shows the concentration below 2 nM, on a pico-Molar scale for

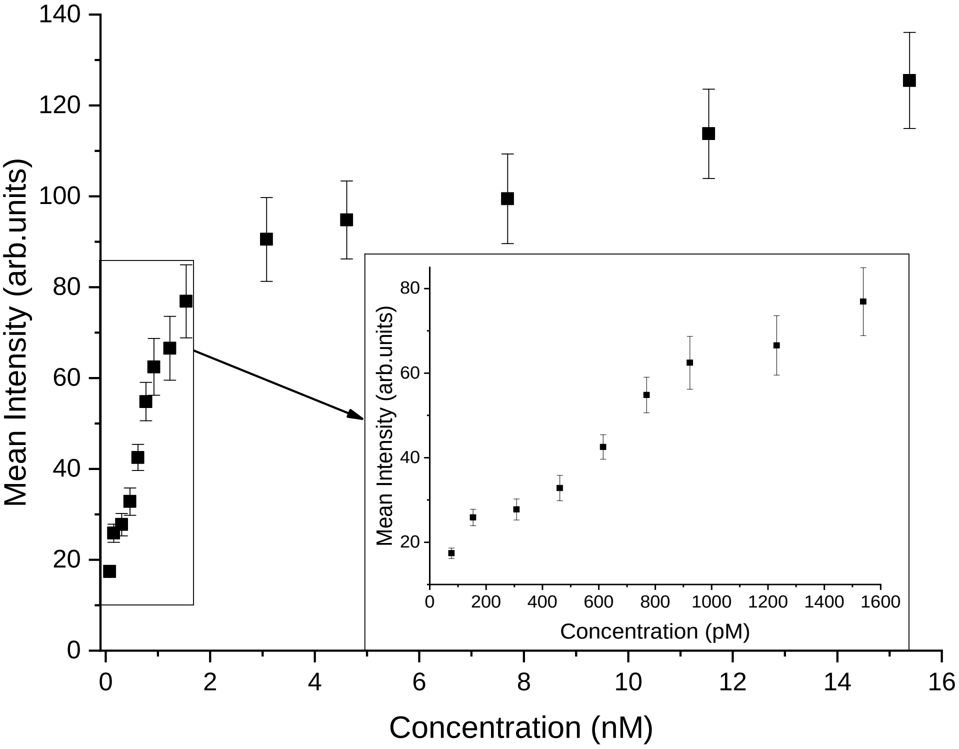

FIGURE 6.11: Mean pixel intensity of the limit of detection fluorescent sensors taken with the smart phone plotted against the CQD molar concentration of these regions, inset is a scaled graph of the 0 to 1600 pM region

ease of reading. It can be seen that the CQDs were detectable down to 80 pM using the smart phone camera on the chosen settings. This is a much lower detection limit that what has been published with similar CQDs on a typical fluorescence imaging method using a smart phone [24].

6.6 Summary

The edge-lit elastomeric membrane has been shown to be an effective platform for a POC evanescent waveguide sensor. The system was used effectively to detect CQD molar concentrations down to 80 pM using a smart phone camera to image the device. Multiple improvements could be made to the device, and the analysis, to possibly detect lower concentrations. The current method of analysis depends on MATLAB software identifying regions of higher pixel intensity than the background. Although this was effective, a better method of doing this would be to have the samples in a micro-well structure on the PDMS surface. PDMS is widely fabricated into both micro-wells and channels due to its material properties. These micro-wells would always be in the same place; therefore the software could highlight the identifying regions to be the same size. This would produce a more repeatable analysis method and may allow for identification of lower concentration regions that may not have been identified due to the limits of the current method. The use of micro-wells could allow for device multiplexing, an essential capability of POC devices [25].

As well as improving the fluorescent sensor device, the imaging system could also be improved upon. The images from the smart phone are currently saved as JPEGs, this means the images are compressed when taken therefore, valuable information may be getting lost. Applications are available and can be produced to allow for smart phones to take RAW images - these images have larger file sizes, however, none of the pixel data is compressed and therefore lost. In order for the device to be used as a biosensor, these capabilities have to be introduced.

Ultimately, this proof of concept device was effective in identifying fluorescent CQD markers to a concentration of 80 pM, lower that any reported in literature [24]. Further improvements to the system itself, via the incorporation of micro-wells, image capture and analysis improvements and the use of CQD markers to identify biological analytes makes the device a possible sensor to be used at POC and in the field.

References

[1] J. R. Lakowicz, *Principles of fluorescence spectroscopy.* Springer Science & Business Media, 2013.

[2] I. A. Darwish, “Immunoassay methods and their applications in pharmaceutical analysis: basic methodology and recent advances,” *International journal of biomedical science: IJBS*, vol. 2, no. 3, p. 217, 2006.

[3] K. Kolmakov, V. N. Belov, J. Bierwagen, C. Ringemann, V. Müller, C. Eggeling, and S. W. Hell, “Red-emitting rhodamine dyes for fluorescence microscopy and nanoscopy,” *Chemistry–A European Journal*, vol. 16, no. 1, pp. 158–166, 2010.

[4] S. Roy, A. Maity, N. Mudi, M. Shyamal, and A. Misra, “Rhodamine scaffolds as real time chemosensors for selective detection of bisulfite in aqueous medium,” *Photochemical & Photobiological Sciences*, vol. 18, no. 6, pp. 1342–1349, 2019.

[5] C. R. Taitt, G. P. Anderson, and F. S. Ligler, “Evanescent wave fluorescence biosensors,” *Biosensors and Bioelectronics*, vol. 20, no. 12, pp. 2470–2487, 2005.

[6] C. Murphy, E. Stack, S. Krivelo, D. A. McPartlin, B. Byrne, C. Greef, M. J. Lochhead, G. Husar, S. Devlin, C. T. Elliott, *et al.*, “Detection of the cyanobacterial toxin, microcystin-LR, using a novel recombinant antibody-based optical-planar waveguide platform,” *Biosensors and Bioelectronics*, vol. 67, pp. 708–714, 2015.

[7] R. Asquini, A. Buzzin, D. Caputo, and G. de Cesare, “Integrated evanescent waveguide detector for optical sensing,” *IEEE Transactions on Components, Packaging and Manufacturing Technology*, vol. 8, no. 7, pp. 1180–1186, 2018.

[8] X.-A. Ton, V. Acha, P. Bonomi, B. T. S. Bui, and K. Haupt, "A disposable evanescent wave fiber optic sensor coated with a molecularly imprinted polymer as a selective fluorescence probe," *Biosensors and Bioelectronics*, vol. 64, pp. 359–366, 2015.

[9] J. Balsam, H. A. Bruck, and A. Rasooly, "Capillary array waveguide amplified fluorescence detector for mHealth," *Sensors and Actuators B: Chemical*, vol. 186, pp. 711–717, 2013.

[10] C. R. Taitt, G. P. Anderson, and F. S. Ligler, "Evanescent wave fluorescence biosensors: Advances of the last decade," *Biosensors and Bioelectronics*, vol. 76, pp. 103–112, 2016.

[11] B. Agnarsson, A. Lundgren, A. Gunnarsson, M. Rabe, A. Kunze, M. Mapar, L. Simonsson, M. Bally, V. P. Zhdanov, and F. Hook, "Evanescent light-scattering microscopy for label-free interfacial imaging: from single sub-100 nm vesicles to live cells," *ACS nano*, vol. 9, no. 12, pp. 11849–11862, 2015.

[12] P. Kozma, A. Lehmann, K. Wunderlich, D. Michel, S. Schumacher, E. Ehrentreich-Förster, and F. Bier, "A novel handheld fluorescent microarray reader for point-of-care diagnostic," *Biosensors and Bioelectronics*, vol. 47, pp. 415–420, 2013.

[13] S. Halldorsson, E. Lucumi, R. Gómez-Sjöberg, and R. M. Fleming, "Advantages and challenges of microfluidic cell culture in polydimethylsiloxane devices," *Biosensors and Bioelectronics*, vol. 63, pp. 218–231, 2015.

[14] F. S. Ligler and C. R. Taitt, *Optical biosensors: present & future.* Gulf Professional Publishing, 2002.

[15] "Zemax OpticStudio." `https://www.zemax.com/products/opticstudio`. Accessed: 22-01-2020.

[16] K. D. Wegner and N. Hildebrandt, "Quantum dots: bright and versatile in vitro and in vivo fluorescence imaging biosensors," *Chemical Society Reviews*, vol. 44, no. 14, pp. 4792–4834, 2015.

[17] V. Biju, T. Itoh, and M. Ishikawa, "Delivering quantum dots to cells: bioconjugated quantum dots for targeted and nonspecific extracellular and intracellular imaging," *Chemical Society Reviews*, vol. 39, no. 8, pp. 3031–3056, 2010.

[18] M. Chern, J. C. Kays, S. Bhuckory, and A. M. Dennis, "Sensing with photoluminescent semiconductor quantum dots," *Methods and Applications in Fluorescence*, vol. 7, no. 1, p. 012005, 2019.

[19] K. E. Sapsford, W. R. Algar, L. Berti, K. B. Gemmill, B. J. Casey, E. Oh, M. H. Stewart, and I. L. Medintz, "Functionalizing nanoparticles with biological molecules: developing chemistries that facilitate nanotechnology," *Chemical reviews*, vol. 113, no. 3, pp. 1904–2074, 2013.

[20] A. Ozcan, "Mobile phones democratize and cultivate next-generation imaging, diagnostics and measurement tools," *Lab on a Chip*, vol. 14, no. 17, pp. 3187–3194, 2014.

[21] J. Ohta, *Smart CMOS image sensors and applications.* CRC press, 2017.

[22] E. Petryayeva and W. R. Algar, "Multiplexed homogeneous assays of proteolytic activity using a smartphone and quantum dots," *Analytical chemistry*, vol. 86, no. 6, pp. 3195–3202, 2014.

[23] "Samsung Galaxy S9." `https://www.samsung.com/global/galaxy/galaxy-s9/`. Accessed: 31-03-2020.

[24] E. Petryayeva and W. R. Algar, "A job for quantum dots: use of a smartphone and 3D-printed accessory for all-in-one excitation and imaging of photoluminescence," *Analytical and bioanalytical chemistry*, vol. 408, no. 11, pp. 2913–2925, 2016.

[25] V. Gubala, L. F. Harris, A. J. Ricco, M. X. Tan, and D. E. Williams, "Point of care diagnostics: status and future," *Analytical chemistry*, vol. 84, no. 2, pp. 487–515, 2012.

Chapter 7

Conclusions

The work presented here focused on the design of a wearable device for phototherapy. The device utilised a PDMS membrane, edge-lit with LEDs or μLEDs with blue or UV wavelengths. Nanoparticle substrates were used to extract light from the surface of the membrane.

Chapter 1 gave an introduction into the use of light therapy as a treatment for skin disorders and other conditions. The different dermatological conditions which can be treated with different wavelengths of light were discussed as was the use of photosensitisers with light treatment to increase the effect. The benefits of at-home phototherapy and phototherapy devices that have previously been, or are currently on, the market were discussed and compared. The use of devices with LED arrays were mentioned and the challenges associated with these arrays were discussed. This led into the benefits of other system designs, for example, the use of polymer optical fibres, which allow for conformability over treatment areas [1].

The first chapter then discussed our design for a wearable phototherapy device. The device utilised LEDs due to their low-cost design, miniaturisation capability and high efficiency. These LEDs are used in an edge-lit format to avoid light uniformity issues as seen with LED arrays [2]. The background physics of LEDs and their fabrication was presented. The use of μLEDs were introduced as these allow for thin elastomeric membranes to be utilised, improving the wearability of the device.

The second chapter focused on validating the device design using a broad area blue LED. The LED was coupled into the edge of a 1 mm thick PDMS membrane. The use of PDMS made the device flexible. The effect of coupling the LED into the PDMS membrane was shown by optical simulation software. The system for measuring the light output from the top surface as irradiance (mW/cm^2) was described with the laboratory setup and the methods required. The light output from the top surface of the membrane when coupled to the LED was low, as most of the light was guided in the membrane via total internal reflection.

This chapter then introduced the use of various methods to extract light from an edge-lit device. The effect of high refractive index light scattering nanoparticles was tested experimentally, using 20 nm TiO_2 particles. These particles were homogenously mixed with PDMS at different concentration weights to create extraction substrates. These substrates were then used to effectively extract light from the membrane; however, it was not extracted uniformly over the area of the scatter substrate (15 x 15 mm^2). A CCD imaging system was introduced as a method of producing irradiance maps of the extraction substrates. This allowed for the irradiance over the entire extraction substrate to be shown. This method was discussed and irradiance maps for each concentration of TiO_2 were produced. From these irradiance maps the output optical power of the substrates was estimated, and in turn, the efficiency of each substrate based on the LED optical power. This chapter closed with a method of obtaining uniform irradiance using a TiO_2 substrate of increasing thickness with increasing distance from the LED.

Chapter 3 utilised similar methods to Chapter 2, however, used a blue-emitting μLED array. The array consisted of a 1 x 10 linear geometry with each pixel being 100 x 100 μm^2. The design of the μLED array and the PCB for electrical contacting of the array were discussed in detail. The electrical and optical characteristics of the μLED array were presented. The effect of coupling the array to a 1 mm thick PDMS membrane was shown by optical simulations. The same extraction substrates of Chapter 2 were used to extract the μLED light and the output irradiance measured by spectrometer and imaging methods. The results were compared to the broad LED results and produced an increased efficiency with the μLED due to more of the light being coupled into the membrane. Extraction substrates with increasing concentrations of TiO_2 were fabricated to obtain uniform emission from a thinner device. A uniform irradiance of 1 mW/cm^2 was obtained with this sample, at a μLED input current of 120 mA and supply voltage of 3.24 V. The chapter then finished with a mathematically derived equation for determining the concentration gradient for different lengths of extraction substrate.

The ability of the device platform to operate at other wavelengths was shown in Chapter 4. Firstly, a broad area UVA LED, with a peak wavelength of 383 nm, was used as the source and light extracted using the TiO_2 substrates. This extraction was compared to the blue LED results and it was determined that the wavelength of the source light changed the effect of the concentration of TiO_2. This is due to light scattering being dependent upon wavelength, more light is scattered with a shorter wavelength than a longer wavelength [3]. For uniform irradiance with a tapered substrate the concentration of TiO_2 had to be lowered to 0.04% compared to the blue LEDs which showed uniform irradiance with a 0.05% tapered substrate. Therefore, although not tested, the concentration gradient of TiO_2 required for uniform emission from a flat substrate would be different than that of the blue device. For the wavelength to be decreased further, for example 311 nm UVB, the extraction substrate may need to be changed. TiO_2 begins to absorb in the UV [4], so the extraction effect would decrease. Other nanoparticles with larger band gaps or a porous PDMS substrate could be utilised to maintain a high light extraction.

Colour converter films were fabricated using CQDs and PDMS. These films were used to convert the blue μLED light into red light through down-conversion. By utilising a combination of a TiO_2 extraction substrate and a colour converting substrate, uniform emission peaking at 634 nm was achieved. Furthermore, by using a different concentration of extraction substrate, uniform emission at blue and red wavelengths was obtained simultaneously. This demonstrates the potential of the device for multiwavelength emission, used in some treatments to get the benefits of both [5]. Although colour converters were effective in producing a different wavelength, the samples fabricated here were made from cadmium-based quantum dots. These are toxic to the human body, they are contained in a polymer matrix, however, it would be a necessity to use quantum dots that do not contain cadmium [6].

In Chapter 5, more properties of the μLED device were discussed. The extraction was increased greatly by applying a reflective layer to the under-side and end of the PDMS membrane. A flexible mirror-like substrate was used to maintain device conformability, while providing an average increase of 66% in the output irradiance. A uniform irradiance of 1.7 mW/cm^2 was obtained using the concentration gradient extraction substrate and the reflective layer, an increase from 1.0 mW/cm^2. The effect of curvature on the uniform irradiance output was tested at different curvature values. This determined that, with an extraction substrate of 15 x 15 mm^2, a uniform irradiance was obtained down to at least 55% curvature.

In this chapter, further device improvements were tested, including the use of a secondary waveguiding layer. The waveguiding layer couples the μLED light so it is emitted further down the PDMS membrane. This resulted in less light being lost initially close to the μLED and allows for the source to be moved further away from the treatment area, reducing the pain effect caused by excess heating [7]. Another possibility for this design is for structured illumination over different treatment areas, reducing the areas of skin being treated unnecessarily.

Here, the μLED device was shown to couple effectively to a 500 μm thick PDMS membrane. As well as showing that coupling to thinner membranes was possible, this also showed the importance of the surface properties of the membrane input facet. The optical clarity is very important when coupling light as a rough surface will scatter more light, reducing the amount of light that can be extracted.

Double-ended injection was also looked at as a method of increasing the irradiance output. It was a very effective method and produced a uniform irradiance of 3.6 mW/cm^2 over the 15 mm length of extraction substrate. However, by adding sources at either end of the PDMS membrane, the flexibility was decreased. This reduced the conformability of the device for treatment areas. Nonetheless, it is a viable option for producing uniform emission with less fabrication time required as it utilises a single concentration of TiO_2, rather than a concentration gradient.

The final chapter introduced an alternative use for the edge-lit PDMS membrane. Instead of extracting light from the membrane surface, it was used as an evanescent waveguide to detect fluorescent materials. This proof of concept test was used to identify CQD molar concentrations down to 80 pM. A smart phone camera was used as the sensor with image processing being carried out in MATLAB to identify the CQD regions and measure the intensity associated with each region. This identified lower CQD concentrations than what has been detected with similar CQDs and direct illumination and fluorescent measurement using a smart phone [8]. This method of fluorescence sensing could be utilised as a biosensor to detect certain biomarkers for clinical use.

7.1 Future work

The device designed in this thesis has been shown to have potential for a phototherapy device at a range of different wavelengths (UVA, blue and/or red). In order to be accessible to the full phototherapy market, the device also has to be effective at UVB wavelengths, in particular 311 nm, which is the gold-standard for psoriasis treatment [9]. UV wavelengths are also being explored for other benefits including the localised production of nitric oxide which leads to benefits with the cardiovascular system [10].

The results presented in this thesis utilised butt-coupling of the μLED device and the PDMS membrane requiring alignment in a laboratory set up. For a flexible device that can be used outwith the laboratory, the PDMS membrane and the array have to be aligned and “glued”. Different methods could be used to achieve this, with the most obvious connection layer being a glue, such as an epoxy. However, epoxy has a higher refractive index than PDMS and would lead to a change in the coupled μLED light. An alternative is to use PDMS to stick the two components together, reducing any refractive index losses. A thin layer of uncured PDMS can be applied to the input facet

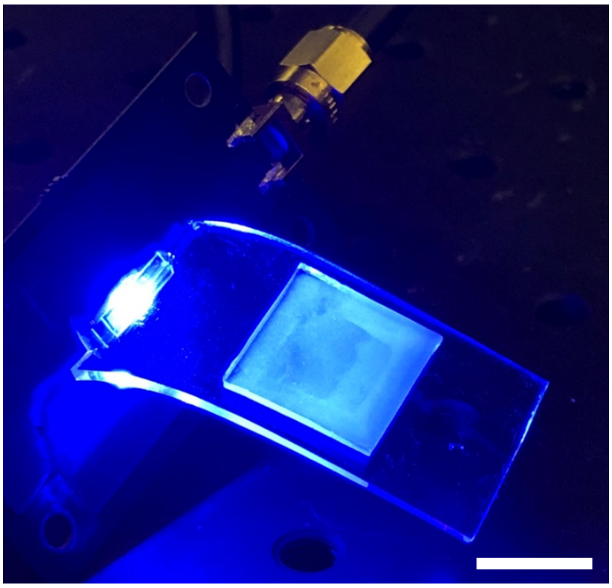

Figure 7.1: Image of a PDMS membrane attached to the μLED with a PDMS interface, scale is 10 mm

of the PDMS membrane. PDMS has a working time of at least 2 hours before it cures. The membrane can then be aligned to the μLED using the same setup described in Chapter 2. When the μLED is aligned with the membrane the PDMS can be cured by increasing the current supplied to the device. This increased current leads to an increased surface temperature of the sapphire, resulting in the PDMS curing, attaching the PDMS membrane and μLED array. An image of a PDMS membrane attached to the μLED array is given in Figure 7.1. As can be seen, the PDMS membrane remains in contact with the μLED device when not held on a flat surface and the light within the PDMS membrane is still guided and can be extracted with a TiO_2 extraction substrate as shown.

The device designed produces a uniform optical power of more than 1 mW, over an area more than 2 cm^2 when the blue μLED is utilised as the source. This has been shown to increase to 9.8 mW over the area when light is injected from both ends of the PDMS membrane. A similar increase could be produced by utilising a μLED device with more pixels. This would result in a higher current needed to produce the same optical power output from the individual pixels, but would also result in more light being coupled into the membrane which could then be extracted.

For the device to become truly wearable the electronics themselves would have to also be flexible. The μLED device has been tested when bonded to a rigid PCB to allow electrical contacting. Future contacting of the device will utilise a flexible circuit board, these circuit boards are made from a flexible polyimide substrate [11]. The design of these boards is given in Figure 7.2 and consists of a 25 mm long flexible substrate with

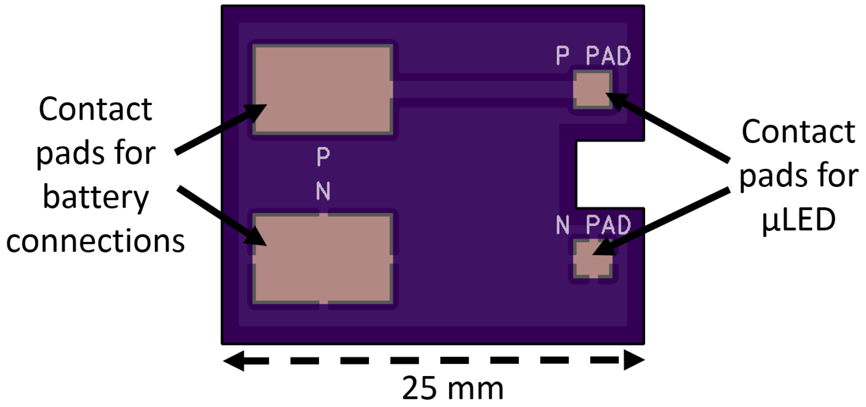

Figure 7.2: Schematic of the flexible PCBs for contacting the μLED arrays and battery supply

contact pads to connect a battery power supply and contact pads for the μLED array at the end of the board to allow the edge of the device to be flush with the skin.

The use of flexible PCBs will increase the wearability of the device, however, it will still have to be connected to a battery to supply the voltage required to power the μLEDs. A more wearable alternative would be to use a wireless power supply, like those used in [12] and [13]. These devices work by using near-field communication between two antennas, a transmitting antenna on a nearby power supply and receiving antenna on the flexible device. This method allows for completely flexible substrates, however, the power transfer is not fully efficient. Maximum power transfer efficiencies of 21.5% with a 5 mm distance between the antenna have been demonstrated [12]. The efficiency of power transfer decays with increasing distance between the antenna. Further improvements in power transfer and increased antenna distance would have to be made before the method could be fully utilised in our wearable device design.

Though not discussed the device designed could also be used for non-healthcare related illumination. For example, structured illumination using secondary embedded waveguides, colour converters and/or light extracting substrates.

7.2 Discussion on an optimal device

In Section 1.6, the device design and aims were discussed. The initial device objectives were to have an irradiance output of at least 1 mW/cm^2 over an area of 1 cm^2 with a uniformity error of less than 15% over the emission area. This was achieved with different device designs utilising the μLED array. Although this irradiance value is less than other devices on the market [14, 15]. The device is less obtrusive than these other devices, allowing it to be worn for longer to reach the required light dose. Throughout this thesis, a range of different devices utilising the edge-lit illumination technique have been discussed. A number of future improvements could be made to finalise the optimal device.

Based on the results produced, the ideal device would have μLEDs at one end of the elastomeric membrane. Although much higher device irradiances were obtained when light is input from both ends of the device, the flexibility of the device was decreased. As one of the main design identifiers for the device is flexibility, this would not be as suitable.

For a blue light emissive device, the best irradiance with light input at one side was 1.0 mW/cm^2. The ideal device would also have a reflective layer, this was shown in Section 5.1.5 to increase the irradiance by over 65% to 1.7 mW/cm^2. This is lower than the irradiance value of currently available visible light phototherapy devices. For example, the Ambulight device produced an irradiance of 7 mW/cm^2. In order to meet the required maximum light dosage of 75 J/cm^2, the device had to be worn for 3 hours [15]. With our maximum irradiance of 1.7 mW/cm^2, the device would have to be worn for 12 hours to meet the required maximum dose. This could be improved upon by adding additional μLED arrays to the same side of the device, as more light is added to the device, more can be extracted. Using a best-case scenario, with an additional 10 pixel array the irradiance output would be doubled to 3.4 mW/cm^2. With this irradiance, the device could be worn for 6 hours to maintain the required maximum light dose for PDT, 75 J/cm^2.

In order for a device to be worn for this required dose, the correct power would have to be supplied. As discussed in Section 7.1, the power supply to the device also has to be wearable. Though inductive charging of a nearby battery could provide a wearable option, this is not yet efficient enough to power this wearable device for a long time. The most reasonable solution is to use a rechargeable lithium-ion battery with wired recharging. For example, a 3.2 V lithium ion battery with a volume of 5 x 3 x 1 cm^3 and a charge of 1800 mAh, would run one μLED array for 18 hours at the output current of 100 mA. This would be enough to produce the required light dose for PDT.

The ideal device would also be available at UV wavelengths. Although not carried out as part of this thesis, μLED arrays with UVC wavelengths have been fabricated [16]. These are less efficient than their blue counterparts, but research on UV band gap semiconductors suggests that the efficiency is improving. For a UVA wavelength of 360 nm, the maximum light dosage utilised for PUVA treatment in the UK is 15 J/cm^2 [17]. Assuming the improvements in UV semiconductors and the use of a concentration gradient similar to that used with the blue μLEDs, and a similar reflectivity effect, the maximum irradiance of the device could be 1.7 mW/cm^2. With this irradiance the device would be worn for 2.5 hours to reach the maximum light dose of 15 J/cm^2. The initial starting dose for Type I skin is 0.5 J/cm^2, to reach this the device would be required to be worn for only 5 minutes. Although these values are more realistic for a wearable device, further optimisation has to be carried out and the final UV device will require much input from clinicians due to the risk/benefit nature of UV phototherapy.

Ideally, market research should be employed to determine the device potential and help guide the future work to produce an ideal wearable phototherapy device that meets the requirements of both patients and clinicians.

References

[1] C. Cochrane, S. R. Mordon, J. C. Lesage, and V. Koncar, "New design of textile light diffusers for photodynamic therapy," *Materials Science and Engineering: C*, vol. 33, no. 3, pp. 1170–1175, 2013.

[2] H. Moseley, "Light distribution and calibration of commercial PDT LED arrays," *Photochemical & Photobiological Sciences*, vol. 4, no. 11, pp. 911–914, 2005.

[3] A. Cox, A. J. DeWeerd, and J. Linden, "An experiment to measure Mie and Rayleigh total scattering cross sections," *American Journal of Physics*, vol. 70, no. 6, pp. 620–625, 2002.

[4] M. M. Khan, S. A. Ansari, D. Pradhan, M. O. Ansari, J. Lee, M. H. Cho, *et al.*, "Band gap engineered TiO_2 nanoparticles for visible light induced photoelectrochemical and photocatalytic studies," *Journal of Materials Chemistry A*, vol. 2, no. 3, pp. 637–644, 2014.

[5] P. Papageorgiou, A. Katsambas, and A. Chu, "Phototherapy with blue (415 nm) and red (660 nm) light in the treatment of acne vulgaris," *British journal of Dermatology*, vol. 142, no. 5, pp. 973–978, 2000.

[6] G. Xu, S. Zeng, B. Zhang, M. T. Swihart, K.-T. Yong, and P. N. Prasad, "New generation cadmium-free quantum dots for biophotonics and nanomedicine," *Chemical reviews*, vol. 116, no. 19, pp. 12234–12327, 2016.

[7] K. Langmack, R. Mehta, P. Twyman, and P. Norris, "Topical photodynamic therapy at low fluence rates–theory and practice," *Journal of Photochemistry and Photobiology B: Biology*, vol. 60, no. 1, pp. 37–43, 2001.

[8] E. Petryayeva and W. R. Algar, "A job for quantum dots: use of a smartphone and 3D-printed accessory for all-in-one excitation and imaging of photoluminescence," *Analytical and bioanalytical chemistry*, vol. 408, no. 11, pp. 2913–2925, 2016.

[9] A. Campanati and A. Offidani, *Phototherapy in Dermatology.* Nova Biomedical, Nova Science Publishers, Inc, 2017.

[10] C. V. Suschek, T. Schewe, H. Sies, and K.-D. Kröncke, "Nitrite, a naturally occurring precursor of nitric oxide that acts like a 'prodrug'," *Biological chemistry*, vol. 387, no. 5, pp. 499–506, 2006.

[11] "OSH Park." `https://oshpark.com/`. Accessed: 28-02-2020.

[12] H. E. Lee, D. Lee, T.-I. Lee, J. H. Shin, G.-M. Choi, C. Kim, S. H. Lee, J. H. Lee, Y. H. Kim, S.-M. Kang, *et al.*, “Wireless powered wearable micro light-emitting diodes,” *Nano Energy*, vol. 55, pp. 454–462, 2019.

[13] A. J. Bandodkar, P. Gutruf, J. Choi, K. Lee, Y. Sekine, J. T. Reeder, W. J. Jeang, A. J. Aranyosi, S. P. Lee, J. B. Model, *et al.*, “Battery-free, skin-interfaced microfluidic/electronic systems for simultaneous electrochemical, colorimetric, and volumetric analysis of sweat,” *Science advances*, vol. 5, no. 1, p. 3294, 2019.

[14] D. R. Opel, E. Hagstrom, A. K. Pace, K. Sisto, S. A. Hirano-ALi, S. Desai, and J. Swan, “Light-emitting diodes: a brief review and clinical experience,” *The Journal of clinical and aesthetic dermatology*, vol. 8, no. 6, p. 36, 2015.

[15] S. H. Ibbotson and J. Ferguson, “Ambulatory photodynamic therapy using low irradiance inorganic light-emitting diodes for the treatment of non-melanoma skin cancer: an open study,” *Photodermatology, Photoimmunology & Photomedicine*, vol. 28, no. 5, pp. 235–239, 2012.

[16] X. He, E. Xie, M. S. Islim, A. A. Purwita, J. J. McKendry, E. Gu, H. Haas, and M. D. Dawson, “1 Gbps free-space deep-ultraviolet communications based on III-nitride micro-LEDs emitting at 262 nm,” *Photonics Research*, vol. 7, no. 7, pp. 41–47, 2019.

[17] T. Ling, T. Clayton, J. Crawley, L. Exton, V. Goulden, S. Ibbotson, K. McKenna, M. Mohd Mustapa, L. Rhodes, R. Sarkany, *et al.*, “British Association of Dermatologists and British Photodermatology Group guidelines for the safe and effective use of psoralen–ultraviolet A therapy 2015,” *British Journal of Dermatology*, vol. 174, no. 1, pp. 24–55, 2016.

List of publications

Conference proceedings

(Presenter highlighted by bold letters)

[1] **Francesca Farrell**, Enyuan Xie, Benoit Guilhabert, Anne-Marie Haughey, Martin D Dawson, Nicolas Laurand *Micro-LED waveguide for fluorescence applications* (oral), IEEE Photonics Conference, Texas 2019

[2] **Francesca Farrell**, Enyuan Xie, Benoit Guilhabert, Anne-Marie Haughey, Patricia Connolly, Martin D Dawson, Nicolas Laurand *A wearable phototherapy device utilising micro-LEDs* (oral), IEEE Engineering in Medicine and Biology Conference, Berlin 2019

[3] Francesca Farrell, Enyuan Xie, Benoit Guilhabert, Anne-Marie Haughey, Patricia Connolly, Martin D Dawson, **Nicolas Laurand** *Hybrid GaN LED/elastomer membrane for uniform area illumination* (oral), IEEE Photonics Conference, Virginia 2018

Conferences

(Presenter highlighted by bold letters)

[4] **Francesca Farrell**, Natalie Bruce, Xiangyu He, Enyuan Xie, Anne-Marie Haughey, Martin D Dawson, Nicolas Laurand, *Hybrid GaN micro-LED platform for fluorescence sensing* (oral), UKNC Winter Meeting, Cardiff 2020

[5] **Francesca Farrell**, Benoit Guilhabert, Anne-Marie Haughey, Patricia Connolly, Martin D Dawson, Nicolas Laurand, *Wearable μLED based device for phototherapy applications* (oral), BioMedEng19, London 2019

[6] **Francesca Farrell**, Enyuan Xie, Benoit Guilhabert, Anne-Marie Haughey, Patricia Connolly, Martin D Dawson, Nicolas Laurand, *A flexible phototherapy device utilising GaN μLEDs* (oral), UKNC Winter Meeting, Glasgow 2019

[7] **Francesca Farrell**, Benoit Guilhabert, Anne-Marie Haughey, Patricia Connolly, Martin D Dawson, Nicolas Laurand, *Design of a wearable LED-based device for phototherapy applications* (poster), BioMedEng18, London 2018

[8] **Francesca Farrell**, Benoit Guilhabert, Anne-Marie Haughey, Patricia Connolly, Martin D Dawson, Nicolas Laurand, *Wearable LED-based phototherapy device* (invited speaker), International Conference on UV LED Technologies and Applications, Berlin 2018

[9] **Francesca Farrell**, Benoit Guilhabert, Anne-Marie Haughey, Patricia Connolly, Martin D Dawson, Nicolas Laurand, *Irradiance of an LED edge-lit elastomeric light guide* (poster), SU2P, Edinburgh 2017